

FROM MOUNTAINS TO BEDFORMS: MULTISCALE GROUNDWATER DYNAMICS AND ITS
INFLUENCE ON SOLUTE AND ENERGY FATE AND TRANSPORT

By

Daniel Gonzalez-Duque

Dissertation

Submitted to the Faculty of the
Graduate School of Vanderbilt University

in partial fulfillment of the requirements

for the degree of

DOCTOR OF PHILOSOPHY

in

Environmental Engineering

May 10, 2024

Nashville, Tennessee

Approved:

Jesus Gomez-Velez, Ph.D.

Shihong Lin, Ph.D.

Mark Person, Ph.D.

Sankaran Mahadevan, Ph.D.

John Ayers, Ph.D.

George Hornberger Ph.D.

Copyright © 2024 Daniel Gonzalez Duque
All Rights Reserved

To my grandmother, Beatriz Gonzalez,
my parents, Hernan Gonzalez Cardona and Diana Duque Gonzalez, my brother, Miguel Gonzalez Duque,
and most importantly, to my beloved wife, Ferna Alvarez-Carrascal.
without your constant support and love, this work would not have been possible.

ACKNOWLEDGMENTS

I want to express my deepest gratitude to my supervisor, Dr. Jesus D. Gomez-Velez, for his invaluable guidance, support, and insightful feedback throughout my Doctorate studies. His expertise, encouragement, and commitment have been instrumental in shaping this dissertation and my academic growth.

I am also immensely thankful to Dr. Mark Person, Dr. Gorge Hornberger, Dr. Sankaran Mahadevan, Dr. Shihong Lin, and Dr. John Ayers for their constructive criticism, suggestions, and encouragement during the development and completion of this dissertation. Their expertise and feedback have significantly enriched the quality of this work.

I sincerely appreciate the faculty and staff of Vanderbilt University, with special thanks to Dr. David J. Furbish, whose dedication and resources have provided me with a conducive environment for academic exploration and learning.

I would also like to acknowledge Dr. Shari Kelley, Dr. Kerry Key, Dr. Jay Zarnetske, Dr. Xingyuan Chen, Dr. Timothy Scheibe, and Dr. Scott Painter for their time, cooperation, and willingness to share their insights throughout the development of this research.

Special acknowledgment is due to the founding agencies, including the National Science Foundation (NSF) (awards EAR-1830172, OIA-2020814, and OIA-2312326) and the AGU Horton Research Grant. Additional support was provided by the U.S. Department of Energy, Office of Science, Biological and Environmental Research, The Oak Ridge National Laboratory (ORNL), through the Watershed Dynamics and Evolution (WaDE) Science Focus Area, and the Pacific Northwest National Laboratory (PNNL), through the Environmental System Science Program as part of the River Corridor Scientific Focus Area project.

I sincerely thank my beloved wife, Ferna Alvarez-Carrascal, for her support and encouragement throughout my academic and professional journey. Your intelligence, love, and understanding have been my source of strength and inspiration.

My heartfelt thanks go to my family for their unconditional love, encouragement, and unwavering belief in my abilities. Their support has been my anchor throughout this journey.

I am indebted to my friends and colleagues for their encouragement, understanding, and moral support during moments of doubt and difficulty, with special thanks to Oscar Alvarez, Gabriel Perez, and Madeline Allen for countless hours of constructive feedback and scientific discussions.

Finally, I express my gratitude to all those individuals whose names may not appear here but whose contributions, in various ways, have been integral to completing this dissertation.

Thank you.

TABLE OF CONTENTS

	Page
LIST OF TABLES	viii
LIST OF FIGURES	ix
I Imaging the Multiscale, Nested Structure of Groundwater Flow in Mountainous Terrains	1
1 Introduction	2
2 Groundwater Circulation within the Mountain Block: Combining Flow and Transport Models with Magnetotelluric Observations to Untangle Its Nested Nature	4
2.1 Introduction	5
2.2 Methods	10
2.2.1 Conceptual Model	10
2.2.2 Model for Fluid Flow and Transport of Heat and Solutes	12
2.2.3 Model for Residence Time Distribution	15
2.2.4 Model for Bulk Electrical Resistivity	15
2.2.5 Scenarios Explored	17
2.3 Results	19
2.3.1 Role of Topography and Geology in Groundwater Dynamics and Residence Times	19
2.3.2 Can We Image the Nested Nature of Hydrologic Systems Using Electromagnetic Methods?	26
2.3.3 Dosit River Resistivity	31
2.4 Discussion	31
2.5 Conclusions	34
3 Exploring The Multiscale Nature of Flow in the Sacramento Mountains and Their Influence on Brackish Groundwater Resources Distribution in the Tularosa Basin in New Mexico	36
3.1 Introduction	37
3.2 Study Area	39
3.3 Methods	41
3.3.1 Groundwater Flow	42
3.3.2 Transport of Heat and Solutes Model	43
3.3.3 Water Age Model	45
3.3.4 Bulk Resistivity Model	46
3.3.5 Scenarions To Explore	46
3.4 Results	48
3.4.1 Groundwater Flow and Transport	48
3.4.2 Bulk Resistivity and Extended Cross-Section	50
3.5 Discussion	51
3.6 Conclusions	53
4 Conclusions and Future Work	55

II	The Multiscale, Nested Nature of River Corridor Connectivity and Their Influence on Ecosystem Services	57
5	Introduction	58
6	Sinuosity-driven Hyporheic Exchange: Hydrodynamics and Biogeochemical Potential	60
6.1	Introduction	61
6.2	Methods	64
6.2.1	Reduced-complexity Model	64
6.2.1.1	Flow Model	66
6.2.1.2	Water Age	67
6.2.1.3	Reactive Transport of Solutes Involved in Nitrogen Transformations	69
6.2.2	Selection of Scenarios: Exploring the Parameter Space	73
6.2.2.1	Meander Topology	73
6.2.2.2	System parameters	74
6.3	Results and Discussion	76
6.3.1	Meander topology drives hyporheic exchange and conditions the modulating effects of regional groundwater flow	77
6.3.1.1	Implications for flow	77
6.3.1.2	Implications for transport time scales	79
6.3.2	The Biogeochemical Potential of Sinuosity-Driven Hyporheic Zones	82
6.3.2.1	Master dimensionless variables for biogeochemical potential: $\Pi_{C,e}$ and Da_O	83
6.3.2.2	The role of Particulate Organic Carbon	90
6.4	Conclusions	92
7	<i>WigglyRivers</i>: A Tool to Characterize the Multiscale Nature of Meandering Channels	94
7.1	Introduction	94
7.2	The <i>WigglyRivers</i> tool	96
7.2.1	Data preparation	98
7.2.1.1	NHDPlus HR information processing	98
7.2.2	Transect characterization	99
7.2.2.1	Resampling and smoothing the river transect	99
7.2.2.2	Characterization of planimetry curvature and direction-angle	100
7.2.2.3	River and meander bend definitions	100
7.2.3	Unsupervised identification of meandering features	102
7.2.3.1	Continuous Wavelet Transform	102
7.2.3.2	Multiscale meandering signal identification	104
7.2.3.3	Meander identification	105
7.2.4	Supervised identification of meanders	106
7.2.5	Meander Metrics	107
7.3	Applications	109
7.3.1	Periodic river transect example	109
7.3.2	Idealized channel example	113
7.3.3	Natural river channels examples	116
7.3.3.1	Validation of unsupervised detection	116
7.3.4	Catchment analysis	116
7.4	Conclusions	122
8	Conclusions and Future Work	123
A	Supplemental Material for Chapter 2: "Groundwater Circulation within the Mountain Block:	

Combining Flow and Transport Models with Magnetotelluric Observations to Untangle Its Nested Nature”	126
A.1 Additional Figures	126
B Supplemental Material for Chapter 3: ”Exploring The Multiscale Nature of Flow in the Sacramento Mountains and Their Influence on Brackish Groundwater Resources Distribution in the Tularosa Basin in New Mexico”	135
B.1 Additional Figures	135
B.2 Additional Tables	137
C Supplemental Material for Chapter 6: ”Sinuosity-driven Hyporheic Exchange: Hydrodynamics and Biogeochemical Potential”	139
C.1 Model Sensitivity Analysis	139
C.2 Flow, Transport, and Reaction Models	139
C.2.1 Nondimensionalization of the flow model	139
C.2.2 Nondimensionalization of the Cumulative Age Distribution	142
C.2.3 Nondimensionalization of Transport and Reaction Model	143
C.3 Additional Figures	146
D Supplemental Material for Chapter 7: ”WigglyRivers: A Tool to Characterize the Multiscale Nature of Meandering Channels”	154
D.1 Interpolation of drainage area and channel width	154
D.2 Additional Tables	155
D.3 Additional Figures	156
E Supplemental Material for Chapter 8: 2D Heterogeneous and Homogeneous Model Conceptualization	163
E.1 Model Conceptualization	163
References	165

LIST OF TABLES

Table		Page
2.1	Parameter values for numerical simulations	17
3.1	Scenarios explored for permeability and porosity in the Tularosa Basin.	47
6.1	Microbial Reaction Processes in the Transport Model ^a	69
6.2	Parameters for the Monte Carlo analysis. This table includes information on the typical range of the parameter and the probability distribution function used for the generation of independent realizations. <i>ECDF</i> is the Empirical Cumulative Distribution Function, and <i>Uniform</i> is a uniform probability distribution function (i.e., uninformative prior).	76
B.1	Parameter values used in the numerical simulations of the Tularosa Basin	137
D.1	River and meander variables used in the <i>WigglyRivers</i> package with their dimensionless form.	155

LIST OF FIGURES

Figure	Page	
2.1	(a) after Binley et al. (2015), comparison of horizontal and vertical survey scales for electrical resistivity tomography (ERT) with 1, 5, and 10 m electrode array spacing Bernard (2003), frequency domain electromagnetics (FDEM) with 3.5 m coil instrument, time domain electromagnetics (TDEM) with 50 and 500 m loop soundings at multiple stations along a transect (Bear et al., 2013), and magnetotellurics (MT) with 1 km spacing between stations. MT can survey deeper than 2 km, and its investigation depth depends on the conductivity, duration and sampling rate of the deployment, and the upper and lower frequency limits Spies (1989); Chave et al. (2012). (b) Histogram for groundwater borehole logging depth in the U.S. Qi and Harris (2017); Stanton et al. (2017)	9
2.2	(a) Conceptual model of the mountain-to-valley transition. The mountain system is a subdued replica of the water table described by $Z_s(x)$, and a fault characterizes the transition from mountain to valley at the base of the mountain range. The Roman numbers separate the system regions: (I) upper basin-floor alluvium, (II) lower alluvium, (III) upper proximal-piedmont alluvium, and (IV) mountain block. (b) Permeability variations with depth, the red and blue lines denote the permeability variation in the z and x direction, respectively. (c) Porosity variations with depth. The solid and dashed lines in (b) and (c) represent the two permeability scenarios explored for the mountain block (region IV). The dotted lines represent the permeability and porosity used for the alluvium (region II).	11
2.3	Spatial variability of the Darcy flux magnitude. The first column (panels a, c, e, and g) denotes scenarios with low permeability, and the second column (panels b, d, f, and h) denotes scenarios with high permeability. The rows present different degrees of topographic relief, starting with low relief and low regional slope (panels a and b), high relief and low regional slope (panels c and d), low relief and high regional slope (panels e and f), and high relief and high regional slope (panels g and h). The black lines show uniformly spaced streamlines. The streamlines in the mountain block show the distinct separation between the local and regional flowpaths recharging the lowland aquifers. The flow through the fault is preferentially downward in all the simulations.	23
2.4	Spatial variability of groundwater age. The first column (panels a, c, e, and g) denotes scenarios with low permeability, and the second column (panels b, d, f, and h) denotes scenarios with high permeability. The rows present different degrees of topographic relief, starting with low relief and low regional slope (panels a and b), high relief and low regional slope (panels c and d), low relief and high regional slope (panels e and f), and high relief and high regional slope (panels g and h). The colors separate water ages. Each color denotes the water that has 60% of water in that specific range. In the mountain block, the water ages increase with increased depth. In the alluvium, the water ages combine young water from local flowpaths and old water from regional sources.	24
2.5	Solute concentration for a high reaction rate ($k_{m10} = 1 \times 10^{-13}$). The first column (panels a, c, e, and g) denotes scenarios with low permeability, and the second column (panels b, d, f, and h) denotes scenarios with high permeability. The rows present different degrees of topographic relief, starting with low relief and low regional slope (panels a and b), high relief and low regional slope (panels c and d), low relief and high regional slope (panels e and f), and high relief and high regional slope (panels g and h). The contours separate freshwater, brackish water, and saline water. The solute concentration increases with depth, delineating the multi-scale nature of flow in the mountain block. In the alluvium, the interaction of local and regional flowpaths produces the presence of brackish water in the upper alluvium.	25
2.6	Solute concentration for low permeability (a and c) and high permeability (b and d), and high dissolution rate (a and b) and low dissolution rate (c and d) scenarios. The contours separate water between fresh, brackish, and saline. Lower dissolution rates cause freshwater to penetrate deeper into the mountain block and alluvium.	26

2.7	Bulk resistivity predicted from the model results using Eq. (2.11) for a high reaction rate ($k_{m0} = 1 \times 10^{-13}$). The first column (panels a, c, e, and g) denotes scenarios with low permeability, and the second column (panels b, d, f, and h) denotes scenarios with high permeability. The rows present different degrees of topographic relief, starting with low relief and low regional slope (panels a and b), high relief and low regional slope (panels c and d), low relief and high regional slope (panels e and f), and high relief and high regional slope (panels g and h). The contours separate freshwater, brackish water, and saline. The resistivity fields show the location of stagnation points present in the mountain block, separating the local and regional flowpaths.	27
2.8	Bulk resistivity predicted from the model results using Eq. (11) for low permeability (a and c) and high permeability (b and d), and high dissolution rate (a and b) and low dissolution rate (c and d) scenarios. The contours separate freshwater, brackish water, and saline. Lower dissolution rates cause the loss of contrasting resistivity values within the mountain block.	28
2.9	Synthetic inversion tests assessing the ability of MT data to image the resistivity of the groundwater system features. The columns denote the forward (a, c, e, and g) and inverse (b, d, f, and h) models. In (a) and (b), the inversion of the idealized system is presented with receivers spacing every 200 meters. The following three rows denote the same system with receivers spacing every 200 meters (c and d), ~ 1.5 km (e and f), and 26 receivers placed on top of structures of interest (g and h). The inverted white triangles show the location of the receivers in each inversion. The low resistivity pockets in the mountain block are captured with good sensor placement.	30
2.10	Simulations of the Dosit River transect. The panels show the results of solute concentration (a), residence times (b), and bulk resistivity (c). The contours denote the separation of fresh, brackish, and saline groundwater. The vertical dashed lines show the area where Jiang et al. (2014) performed their MT survey (Figure A.1).	32
3.1	Water Supply Sustainability Risk Index for the year 2050. Roy et al. (2012) calculates the index values based on the development of renewable water supply, the susceptibility to drought, the growth in water withdrawal, the increased need for storage, and the groundwater use. The New Mexico state and the Tularosa Basin are colored with red contours. .	37
3.2	(Left) Tularosa Basin area with water quality and Carbon-14 measurements. The solid black line shows the (right) cross-section A-A'-A'' geology (based on Newton and Land, 2016). The blue line denotes the water table used in the simulations, and the red square shows the inset of the cross-section shown in the results. The conceptual model used in the simulations is a replica of this cross-section. It is bounded by the west boundary ($\partial\Omega_w$), the east boundary ($\partial\Omega_e$), the water table boundary in the alluvium ($\partial\Omega_{wt,a}$) and in the San Andres and Sacramento Mountains ($\partial\Omega_{wt,m}$), and the basement boundary ($\partial\Omega_b$). The water quality measurements were provided by the New Mexico Environment Department (NMED), the New Mexico Bureau of Geology and Mineral Resources (NMBGMR), and the US Geological Survey (USGS). The information was downloaded from the NMBGMR interactive map (NMBGMR et al., 2016). The Carbon-14 age measurements were taken from Eastoe and Rodney (2014) and Mamer et al. (2014).	40
3.3	z -direction permeability (κ_z in (a), (b), (c)), and simulation results for groundwater flow (\mathbf{q} in (d), (e), (f)), water ages (τ in (g), (h), (i)), and solute concentration (c in (j), (k), (l)). The streamlines are the black lines in the groundwater flow panels ((d), (e), (f)). The solute concentration is discretized between fresh, brackish, and saline water. The triangle within the (g), (h), and (i) shows a C^{14} age measurement from a well less than 3 km from the cross-section (Mamer et al., 2014). The points in (j), (k), and (l) show the water quality wells that are located less than 3 km away from the cross-section (NMBGMR et al., 2016).	49
3.4	Porosity of the system (ϕ in a, b, c) and simulation results for bulk resistivity calculated with equation (3.10) ($\rho_{r,bulk}$ in (d), (e), (f)). The back contours in (d), (e), and (f) separate fresh, brackish, and saline water in the Sacramento Mountains and brackish and saline water in the basin fill.	51

3.5	Simulation results for groundwater flow (\mathbf{q} in a), water ages (τ in b), temperature (T in c), solute concentration (c in d), and bulk resistivity ($\rho_{r,bulk}$ in e). The streamlines are the black lines in the groundwater flow panel (a). The solute concentration is discretized between fresh, brackish, and saline water. The triangle within (b) shows the C^{14} age measurement from a well less than 3 km from the cross-section (Mamer et al., 2014). The points in (c) show the water quality wells located less than 3 km from the cross-section (NMBGMR et al., 2016). The back contours in (d) separate fresh, brackish, and saline water in the Sacramento Mountains and brackish and saline water in the basin fill.	52
6.1	Conceptualization of the reduced-complexity model for sinuosity-driven hyporheic exchange. (A) Examples of meandering channels at different scales (images taken from Google Earth). The river in the upper image illustrates the alluvial valley axis (solid black line), the alluvial belt (dashed black line), and the flow field of a single meander bend dictated by the interaction of sinuosity-driven hyporheic exchange (cyan arrows) and regional groundwater flow (orange arrows). (B) Examples of meanders generated with a Kinoshita curve for different values of the maximum angular amplitude θ_0 . In these synthetic meanders, the wavelength ($\lambda = 100$), flatness coefficient ($J_f = 1/192$), and skewness coefficient ($J_s = 1/32$) are constant, except for the last meander where $J_s = 1/10$. Planimetric view (C) and longitudinal view along the channel (D) of the domain used in the model. The model focuses on a single meander bend described by a Kinoshita curve ($\partial\Omega_c$). To minimize boundary effects, we repeat this meander unit three times and assume periodic boundary conditions for flow and transport in the downstream ($\partial\Omega_d$) and upstream ($\partial\Omega_u$) boundaries. Our analyses focus on the meander bend in the middle of the domain. The alluvial valley length is $B = 3\lambda$, which is selected to minimize numerical artifacts in the simulated hyporheic flow field caused by the influence of the valley-side boundary ($\partial\Omega_v$).	65
6.2	Meander topologies used in the analysis. Four Kinoshita topologies generated with parameters, from left to right, $\theta_0 = [90, 105, 115, 120]^\circ$, $J_s = [0, 0.014, 0.020, 0.020]$, and $J_f = [0.0048, 0, 0, 0]$. Axes are in dimensionless coordinates $x^* = x/\lambda$ and $y^* = x/\lambda$, resulting in meanders with a unitary dimensionless arc wavelength. The red dots denote the inflection points, and the dashed lines represent the characteristic lengths of the meander neck (red) and lobe (blue). These lengths are estimated as the longest distance within the neck or lobe along a line parallel to the line defined by the inflection points. Each meander shows the sinuosity (σ) and funneling factor (FF).	74
6.3	Flow field and sinuosity-driven hyporheic zone within the alluvial aquifer. The magnitude of the dimensionless flux (\mathbf{Q}^* ; colors), dimensionless hydraulic head (white contours), and hyporheic streamlines (black lines) for four meander topologies (columns) under neutral ($\Pi_{J_y} = 0$), moderate ($\Pi_{J_y} = 1$), and strong ($\Pi_{J_y} = 10$) regional groundwater flow conditions (rows).	78
6.4	Total dimensionless hyporheic exchange flux (Q^*) as a function of meander topology (σ) and regional groundwater flow (Π_{J_y}). The funneling factor (FF) for each meander topology is included as a reference. Also, notice that the green solid line ($\Pi_{J_y} = 1$) is on top of the red line ($\Pi_{J_y} = -1$).	80
6.5	Cumulative residence times (CRTD). CRTD of all meander topologies separated by the colors shown above, the line styles denote the stream conditions, from strong gaining ($\Pi_{J_y} = 10$) to strong losing ($\Pi_{J_y} = -10$) conditions, passing through neutral conditions ($\Pi_{J_y} = 0$).	81
6.6	Potential for the biogeochemical transformation of nitrate in a meander under neutral conditions ($\Pi_{J_y} = 0$) with $\Pi_{C,c} = 1$. The colors denote the potential P_{NO} (calculated with Equation (6.18)), the thick black line denotes the zero contour value (transition from source to sink of nitrate), and the thin black lines denote streamlines. The two first columns show simulations for pristine conditions, while the last two show polluted conditions.	83

6.7	Biogeochemical potential in the $\Pi_{C,c} - Da_O$ domain (Panel A). Each point in this domain represents potential P_i for a single meander with dimensionless parameters $\Pi_{C,c}$ and Da_O (e.g., Panel B). The x-axis separates the domain into meanders exposed to carbon-limited ($\Pi_{C,c} < 1$) and oxygen-limited ($\Pi_{C,c} > 1$) boundary conditions, while the y-axis separates the domain into meanders characterized by reaction-limited ($Da_O < 1$) and transport-limited ($Da_O > 1$) conditions. For reference, we include histograms for typical values of the dimensionless variables found across the Conterminous US and their corresponding 5%, 25%, 50%, 75%, and 95% percentiles (yellow boxes and point). Generally, this diagram results in two characteristic zones: one for hyporheic zones that act as net sources of the constituent ($P_i < 0$; red colors) and one for meanders that act as net sinks ($P_i > 0$; blue colors).	84
6.8	Potential of retention of nitrates for the pristine river channel case and $P_0 = 0.02\%$. The columns denote different meander topologies described by the sinuosity (σ). The rows separate the regional gradient Π_{J_y} . The colors show the potential for biogeochemical retention. The solid black line shows the zero contour line. The horizontal dashed line is the division between transport-limited ($\log(Da_O) > 0$) and reaction-limited systems ($\log(Da_O) < 0$). The vertical dashed lines is the division between carbon-limited ($\Pi_{C,c} < 0$) and oxygen-limited systems ($\Pi_{C,c} > 0$). For reference, we include histograms for typical values of the dimensionless variables found across the Conterminous US and their corresponding 5%, 25%, 50%, 75%, and 95% percentiles (yellow boxes and point). . . .	87
6.9	Potential of retention of nitrates for the polluted river channel case and $P_0 = 0.02\%$. The columns denote different meander topologies described by the sinuosity (σ). The rows separate the regional gradient Π_{J_y} . The colors show the potential for biogeochemical retention. The solid black line shows the zero contour line. The horizontal dashed line is the division between transport-limited ($\log(Da_O) > 0$) and reaction-limited systems ($\log(Da_O) < 0$). The vertical dashed lines is the division between carbon-limited ($\Pi_{C,c} < 0$) and oxygen-limited systems ($\Pi_{C,c} > 0$). For reference, we include histograms for typical values of the dimensionless variables found across the Conterminous US and their corresponding 5%, 25%, 50%, 75%, and 95% percentiles (yellow boxes and point). . . .	89
6.10	Effect on POC concentration in the biogeochemical potential for DOC and NO_3^- transformations for meanders of moderate sinuosity ($\sigma = 3.1$) and neutral regional groundwater flow ($\Pi_{J_y} = 0.0$). Columns correspond to labile POC of 0%, 0.02%, and 0.2%. The figure includes meanders under pristine (rows one and two) and polluted (rows three and four) channel conditions. The solid black line shows the zero contour line. The horizontal dashed line is the division between transport-limited ($\log(Da_O) > 0$) and reaction-limited systems ($\log(Da_O) < 0$). The vertical dashed lines is the division between carbon-limited ($\Pi_{C,c} < 0$) and oxygen-limited systems ($\Pi_{C,c} > 0$). For reference, we include histograms for typical values of the dimensionless variables found across the Conterminous US and their corresponding 5%, 25%, 50%, 75%, and 95% percentiles (yellow boxes and point). . . .	91
7.1	Structure of the <i>WigglyRivers</i> Python package. The blue boxes represent the main classes of the package. The yellow boxes represent the classes and functions that make river-related computations, such as river extractions, scaling, and resampling, among others. The red boxes represent wavelet-related functions, the magenta boxes represent plotting-related functions, and the green boxes are utility-based functions. The lines show the connection between the package sections and where to expect the computations to be made. . . .	97

7.2	(a) Idealized river planimetry is shown in the black solid line in the first panel. (b) and (c) show the curvature and direction-angle calculated from the river planimetry. The half-meander is bounded by the inflection points (red dots and red dashed line), and the full-meander is bounded by the maximum points in the curvature (blue dots and green dashed line). The half-meander is characterized by the half-meander arc-wavelength (λ_{hm}), valley length (L_{hm}), and amplitude (A_{hm}). Similarly, the full-meander is characterized by the full-meander arc-wavelength (λ_{fm}), valley length (L_{fm}), and amplitude (A_{fm}). The radius of curvature (R_{hm}) is calculated for the half-meander. The gold solid line denotes the distance in the neck (L_n), and the solid magenta line denotes the largest distance within the meander lobe (L_l). The distances between the inflection points and the maximum points in the curvature upstream ($\lambda_{hm,u}$) and downstream ($\lambda_{hm,d}$) of the half-meander are denoted by the magenta and cyan lines.	101
7.3	Process for automatic detection of meanders. (a) resampled and smoothed river planimetry. (b) curvature of the planimetry. (c) CWT of the curvature. (d) Construction of the scale space tree in the CWT plane. (e) zoomed in planimetry with the projected tree where individual half-meanders are identified. The blue lines in (a) and (b) denote the zoomed-in river section presented in (e).	103
7.4	Spectral characterization of a regular river transect planform. (a) river transect generated with equation (7.15) with $\theta_0 = 37^\circ$, $\theta_s = 0.344$, $\theta_f = 0.031$, and $\lambda = 100$. (b) curvature calculated with equation (7.2), CWT of the curvature below, the GWS on the right is calculated with equation (7.6), and SAWP at the bottom is calculated with equation (7.7). The same arrangement is given on (c) direction-angle, calculated with equation (7.3). The hatch areas are the cone of influence of the CWT calculations.	110
7.5	Comparison between GWS values (a) for curvature and (c) for direction-angle, and SAWP (b) for curvature and (d) for direction-angle on periodic river transects with a wavelength (λ) of 100 m (dashed line in a and c).	111
7.6	Spectral characterization of a regular river transect planform with changing wavelength ($\lambda = [50, 100, 200, 500]$). (a) river transect with $\theta_0 = 115^\circ$, $\theta_s = 0.344$, and $\theta_f = 0.031$. (b) curvature calculated with equation (7.2), CWT of the curvature below, the GWS on the right is calculated with equation (7.6), and SAWP at the bottom is calculated with equation (7.7). The same arrangement is given on (c) direction-angle, calculated with equation (7.3). The hatch areas are the cone of influence of the CWT calculations.	112
7.7	Unsupervised identification of meander bends in the regular river transect planform with changing wavelength ($\lambda = [50, 100, 200, 500]$). (a) river transect with $\theta_0 = 115^\circ$, $\theta_s = 0.344$, and $\theta_f = 0.031$ with the projected scale space tree. (b) CWT of the curvature with the scale space tree. The blue dots denote the location of the meander nodes, the red dots denote parent nodes, and the green node represents the root node. These nodes are connected by the branches (red lines). The blue dashed lines denote the peaks in the wavelength found in the GWS.	113
7.8	Spectral characterization of a river transect modeled with <i>meanderpy</i> . (a) river transect. (b) curvature calculated with equation (7.2), CWT of the curvature below, the GWS on the right is calculated with equation (7.6), and SAWP at the bottom is calculated with equation (7.7). The same arrangement is given on (c) direction-angle, calculated with equation (7.3). The hatch areas are the cone of influence of the CWT calculations.	114
7.9	Unsupervised identification of meander bends of a river transect modeled with <i>meanderpy</i> . (A) river transect with the projected scale space tree. (B) CWT of the curvature with the scale space tree. The blue dots denote the location of the meander nodes, the red dots denote parent nodes, and the green node represents the root node. These nodes are connected by the branches (red lines). The blue dashed lines denote the peaks in the wavelength found in the GWS.	115

7.10	(a) hexbin plot of the overlapping fractions (F_{oa} and F_{ma}) of the automatic and manual identification of full-meander bends, calculated with equation (7.8). The color scale represents the number of full-meander bends in each hexbin. The dashed lines are the set thresholds for the zone separation. The insets show examples of the identification of meander for each zone, where the blue line is the river centerline, the red line is the automatic identification, the green dots show the manual identification, and the gold dots show the overlapping points. (b) histogram of the classification of the overlapping fractions discretized by stream order (SO).	117
7.11	Spectral characterization of a river transect within the 0602 subregion river network. (a) river transect. (b) curvature calculated with equation (7.2), CWT of the curvature below, the GWS on the right is calculated with equation (7.6), and SAWP at the bottom is calculated with equation (7.7). The same arrangement is given on (c) direction-angle, calculated with equation (7.3). The hatch areas are the cone of influence of the CWT calculations.	118
7.12	Relationships between meander length metrics and (a) radius of curvature (R_{hm}), (b) full-meander amplitude (A_{fm}), (c) meander neck distance (L_n), (d) full-meander sinuosity (σ_{fm}), (e) funneling factor (FF), and (f) asymmetry (a_{hm}). The colors denote the stream order.	119
7.13	Tennessee River Region (HUCs-4 0601, 0602, 0603, and 0604) maps showing the distribution of (a) the full-meander arc-wavelength (λ_{fm}), (b) the radius of curvature (R_{hm}), (c) the full-meander amplitude (A_{fm}), (d) the full-meander asymmetry (a_{hm}), (e) the full-meander sinuosity (σ_{fm}), and (f) the funneling factor. The watershed outlet is located on the top left corner. Notice that the main stem was not captured by the unsupervised detection and is illustrated here in gray for representation purposes.	121
8.1	Denitrification potential comparison between (a) heterogeneous and (b) homogeneous porous matrix. The 15 black lenses in the heterogeneous system (a) are the location of liable particulate organic carbon (POC) where the dissolution of organic carbon will occur. The integrated denitrification potential is calculated with equation (6.18) using the integrated mass of nitrates coming from the left and the integrated mass of nitrates leaving the porous media on the right.	124
A.1	MT survey crossing Dosit River, China. (a) topography and location of survey profile. (b) distribution of apparent resistivity and schematic streamlines along with profile DD', the pink numbers and triangles denote the location of MT stations, the black dashed line is the boundary of the Cretaceous and Jurassic formations, the solid black arrows are streamlines of local flow systems, the solid blue lines with arrows are streamlines old regional flow systems, and the white circles are internal hydraulic traps (stagnation zones). Modified from Jiang et al. (2014).	126
A.2	Water quality and Carbon-14 measurements within the Tularosa Basin. The water quality measurements were provided by the New Mexico Environment Department (NMED), the New Mexico Bureau of Geology and Mineral Resources (NMBGMR), and the US Geological Survey (USGS). The information was downloaded from the NMBGMR interactive map (NMBGMR et al., 2016). The Carbon-14 age measurements were taken from Eastoe and Rodney (2014) and Mamer et al. (2014). The map shows old and saline groundwater systems in the basin west of the Sacramento Mountains mountain block. The geology of the cross-section profile A-A' is presented in Figure A.3.	127
A.3	Geologic cross-section through the Tularosa Basin. Modified from Newton and Land (2016). 128	128

A.4	Comparison between five empirical models for the fluid electrical resistivity. The first row shows the comparison between the models for a range of values of concentration of solutes (c) (NaCl, in this case) and temperature (T). The black dots denote the concentration and temperature location of the measured values for resistivity collected by Pepin (2019). The middle row compares calculated resistivity ($\rho_{r,c}$) and measured resistivity ($\rho_{r,m}$). The bottom row shows the histogram of the residuals between the calculated and measured resistivity. Notice that the scales of Pepin (2019), Ucock et al. (1980), and Sen and Goode (1992) have a different scale from the Becker et al. (1982) and Constable et al. (2009) models to provide a better comparison of the errors. The first three models reasonably fit the data, showing the importance of temperature variations in fluid resistivity.	129
A.5	Effective resistivity ($\rho_{r,bulk} = 1/\sigma_{r,bulk}$) resulting from variations in porosity (ϕ) and fluid resistivity ($\rho_{r,f}$) for Glover’s model $\sigma_{r,bulk} = \sigma_{r,f}\phi^{m_r} + \sigma_{r,s}(1 - \phi)^{p_r}$ (Glover et al., 2000). The solid resistivity is assumed to be 500 $\Omega\cdot m$. Results show that low resistivity water (lower than 3.1 $\Omega\cdot m$), associated with hot saline water, can be detected in systems porosities lower than 5%.	130
A.6	(left) Fluid resistivity using the model by Sen and Goode (1992). (right) Effective resistivity calculated with Glover et al. (2000) for different rock groups and porosities within those values. High solid resistivity mediums provide a higher contrasting factor between fresh and saline water.	130
A.7	The MARE2DEM forward and inverse MT simulations use a telescopic meshing approach to minimize artificial boundary effects. In this case, we combine an unstructured mesh outside the area of interest (panel a) and a structured mesh for the mountain-to-valley system (panel b). The red polygon in panel (a) corresponds to the location of the mountain-to-valley system.	131
A.8	Scenarios of permeability on the z direction (κ_z). The only changes in permeability are present in the mountain block.	132
A.9	Temperature fields of the mountain-to-valley transition systems. In the figure, the columns denote the two scenarios for permeability, increasing from left to right, the rows present different topographic relief systems, and the contours represent the isotherms. The temperature follows the multi-scale nature of flow in the mountain block and increases with depth, agreeing with previous studies (Gleeson and Manning, 2008; Jiang et al., 2009; Smith and Chapman, 1983; Tóth, 1963).	133
A.10	Profiles of permeability, velocity, mass flux, and heat flux at the fault. The colors show the difference in permeability for the simulations. The line styles show the combination of systems with high regional slope and high relief (H-S, H-R), low regional slope and high relief (L-S, H-R), high regional slope and low relief (H-S, L-R), and low regional slope and low relief (L-S, L-S).	134
A.11	RMS misfit for each iteration of all the inversions performed with MARE2DEM. The dashed line denotes the target misfit value of 1.0.	134
B.1	Interpolated water table for the Tularosa Basin. The solid black line shows the cross-section A-A’-A’’ used for the simulations. The water table was interpolated from water-level maps from the Sacramento Mountains (Land et al., 2014), the basin-fill (Embid et al., 2011), and the San Andres Mountains (Horne, 2019).	135
B.2	Comparison between measured and computed total dissolved solutes (TDS). The measured salinities were obtained from NMBGMR et al. (2016). The computed information comes from the modeled Scenario 2.	136

C.1	Sensitivity analysis on the number of meanders. While panels (A) through (D) show the dimensionless vertical integrated fluxes (Q^*), panels (E) through (H) show the potential of denitrification (P_{NO}) for one, two, three, and four meander sequential bends. The black streamlines show the extent of the hyporheic zone, the black solid contour line shows the places where $P_{NO} = 0$, the white contour lines denote the dimensionless hydraulic head, and the red square boxes point to the extent of the hyporheic zone through the neck of the meander.	140
C.2	Sensitivity analysis on the extent of the alluvial valley. The panels (A) through (D) show the dimensionless vertical integrated fluxes (Q^*) for $B = 0.1L, 0.2L, 0.5L$, and L . The black streamlines show the extent of the hyporheic zone, the white contour lines denote the dimensionless hydraulic head, and the red square boxes point to the extent of the hyporheic zone through the neck of the meander.	141
C.3	Comparison of the numerical solutions for the transient (solid lines) and steady-state (dots) versions of the reactive transport model in equations (6.7)-(6.11) from Chapter 6. In this case, we use relative concentrations in a one-dimensional domain. The transient solution corresponds to the long-term relative concentrations predicted by the system of PDEs from equations (6.7)-(6.11), which are transient in nature and account for the coupled dissolution of POC. The steady-state solution corresponds to the relative concentrations predicted by the system of PDEs from equations (6.7)-(6.11) when $\partial(\epsilon_p HC_i)/\partial t \rightarrow 0$ and $P(t) = P_0$.	146
C.4	Monte Carlo simulations of hydraulic conductivity (K), slope (J_x), and meander arc length (λ). The hydraulic conductivity was obtained from the <code>Hydr1CondCat</code> variable in the StreamCat dataset (Hill et al., 2016), the slope was obtained from the NHDPlus High-Resolution dataset (Moore et al., 2019), and we assumed a uniform distribution in log space from 10 meters to 50 kilometers for the arc length of the meanders, similar to what can be found from exploration in river planimetries in satellite images.	146
C.5	Monte Carlo simulations of channel concentration in oxygen ($C_{O,c}$), ammonium ($C_{NH,c}$), nitrate ($C_{NO,c}$), dissolved organic carbon (DOC, $C_{C,c}$), and particulate organic carbon (POC, P_0). We use CAMELS-Chem dataset, provided in Sterle et al. (2022), for oxygen, DOC, and nitrate. The ammonium concentration was assumed uniform with a range between pristine and polluted streams, presented in Zheng et al. (2016), with values of $C_{NH,c}$ between (0.05, 5). Finally, we assumed a uniform distribution in log space for the particulate organic carbon exploring ranges where POC is low 1×10^{-6} , and where is high 1×10^{-2}	147
C.6	Monte Carlo simulations of reaction rates for oxygen (V_O), ammonium (V_{NH}), and nitrates (C_{NO}), and the first-order mass transfer rate to dissolve organic carbon (α). We assumed a uniform distribution for all the rates with the ranges presented in Zarnetske et al. (2012).	147
C.7	Monte Carlo simulations of high-saturation constant for oxygen (K_O), ammonium (K_{NH}), nitrates (K_{NO}), and dissolved organic carbon (DOC, K_C), and histogram of the linear distribution of coefficient for sediments (K_d) and the inhibition constant for denitrification (K_I). We assumed a uniform distribution for all the concentration constants with the ranges presented in Zarnetske et al. (2012).	148
C.8	Monte Carlo simulations for the advection time scale (τ_c), and the Damköhler numbers for oxygen (Da_O), ammonium (Da_{NH}), nitrates (Da_{NO}), and the particulate organic carbon (POC, Da_P). The values within the red lines show the range of values explored in the biogeochemical simulations.	149
C.9	Monte Carlo simulations for the scaled concentrations of dissolved organic carbon (DOC, $\Pi_{C,c}$), ammonium ($\Pi_{NH,c}$), nitrate ($\Pi_{NO,c}$), and particulate organic carbon (POC, Π_{P-c}). The solid red lines show the range of values explored in the biogeochemical simulations. The dashed lines show the values explored for pristine and polluted streams in ammonium and nitrates. Finally, the solid green and blue lines show the ranges of values explored for POC cases.	150
C.10	Monte Carlo simulations for the ratios of reaction rates of ammonium (V_{NH}/V_O) and nitrate (V_{NO}/V_O). The green solid line shows the mean, and the blue line is the ratio from the values used in Zarnetske et al. (2012).	150

C.11	Monte Carlo simulations for the ratios of reaction rates of ammonium (M_{NH}) and nitrate (M_{NO}). The green solid line shows the mean, and the blue line is the ratio from the values used in Zarnetske et al. (2012).	151
C.12	Potential of retention of dissolved organic carbon for the pristine case and $P_0 = 0.02\%$. The columns denote different meander topologies described by the sinuosity (σ). The rows separate the regional gradient Π_y . The colors show the potential for biogeochemical retention. The solid black line shows the zero contour line. The horizontal dashed line is the division between transport-limited ($\log(Da_O) > 0$) and reaction-limited systems ($\log(Da_O) < 0$). The vertical dashed lines is the division between carbon-limited ($\Pi_{C,c} < 0$) and oxygen-limited systems ($\Pi_{C,c} > 0$). For reference, we include histograms for typical values of the dimensionless variables found across the Conterminous US and their corresponding 5%, 25%, 50%, 75%, and 95% percentiles (yellow boxes and point).	152
C.13	Potential of retention of dissolved organic carbon for the polluted case and $P_0 = 0.02\%$. The columns denote different meander topologies described by the sinuosity (σ). The rows separate the regional gradient Π_y . The colors show the potential for biogeochemical retention. The solid black line shows the zero contour line. The horizontal dashed line is the division between transport-limited ($\log(Da_O) > 0$) and reaction-limited systems ($\log(Da_O) < 0$). The vertical dashed lines is the division between carbon-limited ($\Pi_{C,c} < 0$) and oxygen-limited systems ($\Pi_{C,c} > 0$). For reference, we include histograms for typical values of the dimensionless variables found across the Conterminous US and their corresponding 5%, 25%, 50%, 75%, and 95% percentiles (yellow boxes and point).	153
D.1	Computation of curvature and direction angle. Comparison between normal, noisy, and spline-fitted planimetry coordinates in a kinoshita-type river.	156
D.2	Spectral characterization of a regular river transect planform. (a) river transect generated with equation (7.15) with $\theta_0 = 115$, $\theta_s = 0.344$, $\theta_f = 0.031$, and $\lambda = 100$. (b) curvature, CWT of the curvature below, the GWS on the right, and SAWP at the bottom. The same arrangement is given on (c) direction-angle. The hatch areas are the cone of influence of the CWT calculations.	157
D.3	Spectral characterization of a regular river transect planform. (a) river transect generated with equation (7.15) with $\theta_0 = 115^\circ$, $\theta_s = 0.344$, $\theta_f = 0.031$, and $\lambda = 100$. (b) curvature calculated with equation (7.2), CWT of the curvature below, the GWS on the right is calculated with equation (7.6), and SAWP at the bottom is calculated with equation (7.7). The same arrangement is given on (c) direction-angle, calculated with equation (7.3). The hatch areas are the cone of influence of the CWT calculations.	158
D.4	Spectral characterization of a regular river transect planform with changing wavelength ($\lambda = [50, 100, 200, 500]$). (a) river transect with $\theta_0 = 115^\circ$, $\theta_s = 0$, and $\theta_f = 0$. (b) curvature and CWT of the curvature. The same arrangement is given on (c) direction-angle. The hatch areas are the cone of influence of the CWT calculations.	159
D.5	Spectral characterization of a river transect modeled with <i>meanderpy</i> . (a) river transect. (b) curvature, CWT of the curvature below, the GWS on the right, and SAWP at the bottom. The same arrangement is given on (c) direction-angle. The hatch areas are the cone of influence of the CWT calculations.	160
D.6	Spectral characterization of a river transect modeled with <i>meanderpy</i> . (a) river transect. (b) curvature, CWT of the curvature below, the GWS on the right, and SAWP at the bottom. The same arrangement is given on (c) direction-angle. The hatch areas are the cone of influence of the CWT calculations.	161
D.7	Spectral characterization of a river transect within the 0604 subregion river network. (a) river transect. (b) curvature, CWT of the curvature below, the GWS on the right, and SAWP at the bottom. The same arrangement is given on (c) direction-angle. The hatch areas are the cone of influence of the CWT calculations.	162

E.1 Conceptualization of the 2D model for the (a) heterogeneous and (b) homogeneous porous matrix. The 15 black lenses in the heterogeneous system (a) are the location of liable particulate organic carbon (POC) where the dissolution of organic carbon will occur. . . . 163

Part I

Imaging the Multiscale, Nested Structure of Groundwater Flow in Mountainous Terrains

CHAPTER 1

Introduction

Mountains are ubiquitous water sources vital to humans and ecosystems (Viviroli et al., 2007). In the face of unprecedented climate and land-use changes, natural and anthropogenic stresses can significantly impact these water sources and increase the risk of water scarcity in lowland areas, especially in arid and semiarid regions, where the water supply is insufficient to meet the increasing demand (Viviroli et al., 2007; Hare et al., 2021; Messerli et al., 2004; Pimentel et al., 1999; Qadir et al., 2007; Rijsberman, 2006; Cuthbert et al., 2019; Scanlon et al., 2012a; Kang and Jackson, 2016). The sustainable use of “unconventional” water resources, like brackish aquifers (Stanton and Dennehy, 2017), has emerged as an alternative to offset the ever-increasing deficit of water in these arid environments. However, these sources are intimately linked and cannot be assessed independently as the quantity and quality of brackish resources depend on the mountain sources that replenish them. In other words, sustainable management of water resources in arid regions requires a detailed understanding of the unobserved and typically underappreciated flow field within the mountain-to-valley transition. This part of the dissertation offers a novel approach to address this challenge.

Traditional conceptualizations assume that the role of groundwater in mountainous terrains is relatively shallow (less than 100 meters deep) (Condon et al., 2020b; Fan, 2015), partly due to the lack of information on deeper systems (Condon et al., 2020b; Carroll et al., 2020; Markovich et al., 2019). However, recent studies have combined geophysical and geochemical observations to show that deep regional groundwater flow can play a crucial role in the overall water, solute, and energy budgets of mountain systems (Carroll et al., 2020; Frisbee et al., 2017; McIntosh and Ferguson, 2021; Gabrielli et al., 2012; White et al., 2021; Kim et al., 2022a). The limited nature of these resulting shallow conceptualizations has crucial implications for assessing conventional and unconventional water resources, as traditional modeling approaches tend to ignore regional groundwater contributions, potentially misinterpreting water, solutes, and energy fluxes, and therefore the importance of biogeochemical processes occurring at multiple scales (Condon et al., 2020b; Frisbee et al., 2017; Riebe et al., 2017).

This part of the dissertation addresses these limitations by combining geophysical and geochemical observations with flow and transport models to characterize the nested nature of groundwater flow in mountain-to-valley systems. This characterization offers crucial insight into the quality and recharge rates of water resources in lowland aquifers. Given the nature of these systems, the characterization can be achieved by using geophysical methods, particularly electromagnetic methods like magnetotellurics (MT), as they can image at depths of kilometers (Spies, 1989; Meqbel et al., 2013; Egbert et al., 2022).

To show the potential of an MT geophysical survey, we use idealized groundwater flow and transport of heat and solutes simulations to explore a range of mountain-to-valley settings with variations on geological characteristics in Chapter 2. Then, in Chapter 3, we used a cross-section of the Tularosa Basin in New Mexico and modeled the transport of water, energy, and solutes through the system and explore the potential of MT surveys in the study area to describe the multiscale nature of flow in the Sacramento Mountains and their influence on brackish groundwater resources distribution in the Tularosa Basin. We picked the Tularosa basin because it has been proposed as a potential source of water for Las Cruces and Alamogordo, NM, and hosts the U.S. Bureau of Reclamation's National Inland Desalination Research Center, a critical testbed to assess the potential of brackish aquifers as an "unconventional" resource (Bureau of Reclamation, 2022; Newton and Land, 2016).

As shown throughout Part I, this approach can potentially image the nested nature of flow within the mountain-to-valley system feeding this testbed and offer a novel tool to characterize water sources in similar landscapes. Furthermore, the characterization of these deep groundwater systems is essential for understanding the multiscale hydrologic processes occurring in mountain systems (Markovich et al., 2019; Robinson et al., 2008; Wilson and Guan, 2004).

CHAPTER 2

Groundwater Circulation within the Mountain Block: Combining Flow and Transport Models with Magnetotelluric Observations to Untangle Its Nested Nature

This chapter is a modified version of a paper submitted to Water Resources Research. Gonzalez-Duque, D., Gomez-Velez, J. D., Person, M. A., Kelley, S., Key, K., & Lucero, D. (2023). Groundwater Circulation within the Mountain Block: Combining Flow and Transport Models with Magnetotelluric Observations to Untangle Its Nested Nature (Accepted). Water Resources Research.

Abstract

Mountains are vital water sources for humans and ecosystems, continuously replenishing lowland aquifers through surface runoff and mountain recharge. Quantifying these fluxes and their relative importance is essential for sustainable water resource management. However, our mechanistic understanding of the flow and transport processes determining the connection between the mountain block and the basin aquifer remains limited. Traditional conceptualizations assume groundwater circulation within the mountain block is predominantly shallow. This view neglects the role of deep groundwater flowpaths significantly contributing to the water, solute, and energy budgets. Overcoming these limitations requires a holistic characterization of the multiscale nature of groundwater flow along the mountain-to-valley continuum. As a proof-of-concept, we use a coupled groundwater flow and transport model to design a series of numerical experiments that explore the role of geology, topography, and weathering rates in groundwater circulation and their resulting resistivity patterns. Our results show that accumulating solutes near stagnation zones create contrasting electrical resistivity patterns that separate local, intermediate, and regional flow cells, presenting a target for magnetotelluric observations. To demonstrate the sensitivity of magnetotelluric data to features in our resistivity models, we use the MARE2DEM electromagnetic modeling code to perform forward and inverse simulations. This study highlights the potential of magnetotelluric surveys to image the resistivity structure resulting from multiscale groundwater circulation through relatively impervious crystalline basement rocks in mountainous terrains. This capability could change our understanding of the critical zone, offering a holistic perspective that includes deep groundwater circulation and its role in conveying solutes and energy.

Plain-text Summary

Mountains are vital water sources for humans and ecosystems, continuously replenishing lowland aquifers through surface runoff and mountain recharge. Quantifying these fluxes and their relative importance is essential for sustainable water resource management. Here, we present a novel approach to characterize the nested nature of groundwater flow along the mountain-to-valley continuum by combining flow and transport models and magnetotelluric (MT) geophysical surveys. We assess the approach's potential by creating virtual realities that mimic realistic patterns of subsurface electrical resistivity. Then, using an inverse modeling approach, we test the ability of different MT survey configurations to reconstruct the resistivity fields. Our analysis shows that the accumulation of solutes in subsurface low-velocity zones (i.e., stagnation zones) results in resistivity fields with enough contrast to image the local, intermediate, and regional groundwater flow cells. While this study is conceptual in nature, we aim to offer a framework for geophysical exploration that can characterize the critical zone without neglecting deep groundwater circulation and its role in conveying solutes and energy.

2.1 Introduction

Mountains are an abundant source of surface and subsurface water vital to humans and ecosystems (Viviroli et al., 2007). Natural and anthropogenic stresses, a product of unprecedented climate change, population growth, and land use, critically impact these water sources, increasing the risk of water scarcity in lowland areas, especially in arid and semi-arid environments where water supply is insufficient to meet the increasing demand (Messerli et al., 2004; Viviroli et al., 2011, 2020). The sustainable use of “unconventional” water resources, like brackish aquifers, has emerged as an alternative to offset the ever-increasing water deficit in these arid environments (Robinson et al., 2019; Stanton and Dennehy, 2017; Stanton et al., 2017). However, these sources are intimately linked and cannot be assessed independently, as the quantity and quality of brackish resources depend on the mountain source that replenishes them. In other words, sustainable management of water resources in arid regions requires a detailed understanding of the flow and transport along the mountain-to-valley transition, particularly the unobserved and typically underappreciated flow field within the mountain block.

The mountain block is an area with significant topographic relief primarily formed by a bedrock matrix with fractured and unfractured regions (Wilson and Guan, 2004). How these mountain systems recharge lowland aquifers has been an active area of research for groundwater hydrologists over the past decades, with significant advances made in the mechanistic understanding of this process (Markovich et al., 2019). One characteristic approach divides the water that enters the lowland aquifer originating from the mountain block, known as mountain-front recharge (MFR), into two main components: (i) water-table recharge at the

mountain-front zone (direct MFR) and (ii) mountain-block recharge (MBR) (Wilson and Guan, 2004). MBR represents only the portion directly of the MFR that comes from the regional groundwater sources moving within the mountain block (Markovich et al., 2019; Wilson and Guan, 2004). Both of these processes provide significant amounts of water to lowland areas and can be the primary source of recharge in arid regions (Scanlon et al., 2006, 2012b). Over the past two decades, the hydrologic community has made fundamental advances in MBR science (Markovich et al., 2019). However, there is still considerable uncertainty when it comes to identifying and measuring the depth of groundwater circulation through mountain blocks (Condon et al., 2020a; Markovich et al., 2019). This uncertainty is exacerbated by the scarcity of data for hydrogeologic parameters, such as hydraulic conductivity, porosity, and flow rates for deeper groundwater flow systems in various geologic settings (Carroll et al., 2020).

Traditional conceptualizations of groundwater circulation through the mountain block have evolved over the years (Markovich et al., 2019; Somers and McKenzie, 2020). Early ones assumed the groundwater flow only occurred in the permeable soil above the bedrock (Fan, 2019; Mosley, 1979; Tani, 1997); however, this assumption has been challenged in the light of new data. For example, irrigation experiments performed in the Panola Mountain Watershed in Georgia (Tromp-van Meerveld et al., 2007) and the western Cascade Range in Oregon (Graham et al., 2010) found considerable infiltration of water into the bedrock (91% in the Panola Mountain and 27% in the Cascade Range). This infiltration can circulate at different depths within the mountain block. A recent study for the Copper Creek watershed in Colorado used a hydrologic model and baseflow age estimates from dissolved gas tracers to constrain these depths, suggesting that circulation can exceed 100 meters (Carroll et al., 2020). Another study estimated circulation depths from 0.2 km to over 1.2 km using quartz-silica geothermometry for two watersheds in New Mexico and Colorado, thus challenging existing hydrogeological models in these areas (Frisbee et al., 2017). Similar depth ranges of groundwater circulation were presented in another study that used the stable isotopes of water ($\delta^2\text{H}$ and $\delta^{18}\text{O}$) in wells across North America to determine the extent of meteoric water circulation, indicating that water can flow deeper than 2 km in areas with high topographic relief (McIntosh and Ferguson, 2021). Similarly, analog studies using residence time data from environmental tracers have shown the important contribution of old groundwater to streamflow (Meyers et al., 2021; White et al., 2019, 2021). Person et al. (2024) argued that in mountainous terrains of the Paradox Plateau, USA enhanced mountain front recharge occurs where the crystalline basement cropped out. These findings are consistent with a permeable (10^{-14} to 10^{-16} m²) crystalline basement and supported groundwater age dates (¹⁴C, ⁸¹Kr) and salinity inversions within lowland basal sedimentary aquifer systems (Kim et al., 2022b). Hydrothermal investigations within the desert southwest of the United States suggest MBR fluid circulation depths of 3-6 km (Barroll and Reiter, 1990; Mailloux et al., 1999; Pepin et al., 2014). Lastly, simulations performed in the Swiss Alps suggest meteoric

water recharge through faults of depths of ~ 10 km to explain thermal anomalies (Alt-Epping et al., 2021).

From a modeling perspective, significant contributions have been made in determining the features controlling deep groundwater circulation. We know that water flowpaths through the mountain block are multi-scale and nested in nature. This behavior results from the interaction between local, intermediate, and regional flowpaths driven by the topographic features of the mountain (Tóth, 1963). While local and intermediate flowpaths recharge streams in sub-catchments within the mountain block, regional flowpaths move large amounts of water, energy, and solutes through deep systems contributing to MBR (Gomez and Wilson, 2013; Markovich et al., 2019). The latter has substantial implications on streamflow generation and the water budgets at catchment scales (Fan, 2019; Flerchinger and Cooley, 2000; Frisbee et al., 2017; Fujimoto et al., 2016; Voeckler et al., 2014). Frisbee et al. (2017) showed that the streamflow is not an accumulation of near-surface hillslope responses but a combination of the latter and flow through bedrock. Studies have used 2D and 3D numerical simulations of groundwater flow through mountainous terrains to investigate the most prominent features affecting this nested nature. These studies have determined that the vertical extent of local and regional flowpaths and their relative recharge are highly dependent on the topographic relief, the depth of the water table, and the hydraulic parameters of the mountain block (Gleeson and Manning, 2008; Welch et al., 2012; Welch and Allen, 2012, 2014). The interaction of these flowpaths also produces a mixing between young and old water within the mountain block that is translated to the lowland aquifers, producing longer tails in the residence time distributions (Frisbee et al., 2013a; Gomez and Wilson, 2013). This behavior has also been shown to depend on topographic relief and variations in hydraulic parameters (Cardenas and Jiang, 2010; Jiang et al., 2010). Lastly, the interplay between flowpaths produces stagnant zones in the meeting branches of local and regional flowpaths, where solutes and heat accumulate within the mountain block (An et al., 2014; Jiang, 2012; Jiang et al., 2011, 2014). As expected, topographic relief and hydraulic conductivity also play an essential role in the location of the stagnation zones within the mountain block (Jiang et al., 2011).

Samples from hydrologic systems (i.e., streams, lakes, and wells) encapsulate the effects of a myriad of flowpaths, representing a wide range of spatial and temporal time scales (Frisbee et al., 2013b). To interpret these samples, we typically divide the catchment into active and inactive zones (e.g., Mayo et al., 2003), conceptualizing the effective circulation occurring within the shallow active region and therefore ignoring the role of deeper flowpaths (Frisbee et al., 2017), which might not be a reasonable assumption. The samples from these systems represent the interaction between the local, intermediate, and regional flow systems. Conceptualizing a shallow circulation through the mountain block will likely result in an underestimation of the transport processes occurring within the system, leading to deceptive simulation results that do not conform with the samples taken.

The use of geophysical measurements is promising, as they constitute an extensive, cost-efficient, and non-invasive vertical exploration tool of shallow and deep subsurface characteristics. Novel inversion techniques (e.g., Binley et al., 2010, 2015; Ferré et al., 2009; Rubin and Hubbard, 2005) have shown that geophysical surveys can go beyond the mapping of petrophysical properties (e.g., electrical conductivity, seismic velocities, and dielectric constant) to the inference of spatiotemporal variations of hydraulic parameters (i.e., porosity and hydraulic conductivity) and state variables (i.e., solute concentration and water content, among others), providing fundamental information about hydrogeological parameters and processes (Rubin and Hubbard, 2005). The ability to detect groundwater through geophysical methods depends on the degree of saturation and how this saturation causes contrasts of bulk petrophysical properties for different lithological settings. For instance, in fully saturated systems, the p-wave velocities tend to be larger, resistivity values tend to be smaller, and permittivity values positively correlate with the water content (Kirsch, 2009). The range of probable values for each property relies on the lithological setting, the chemistry of water, and the method used (Kirsch, 2009). The use of electrical resistivity-based geophysical methods has allowed the identification of water infiltration through the vadose zone (Daily and Ramirez, 1995) and fractured bedrock (Cassiani et al., 2009), the quantification of spatial patterns of groundwater recharge (Behroozmand et al., 2019; Cook et al., 1992), the estimation of subsurface hydraulic parameters and state variables (Herckenrath et al., 2013; Hinnell et al., 2010; Pollock and Cirpka, 2012), mapping submarine and subglacial groundwater saline aquifers (Gustafson et al., 2019, 2022), mapping the saline lithology in the Dead Sea Basin (Meqbel et al., 2013), studying fluid transport in the lithology of the crust (Egbert et al., 2022), and the exploration of geothermal systems (Blake et al., 2016; Marwan et al., 2021; Peacock et al., 2016, 2020), among other applications. The vertical investigation extent of a survey strongly depends on the geophysical method used. For example, while electrical resistivity tomography (ERT) data allow for a shallow exploration (generally less than 500 m), magnetotelluric (MT) data can be sensitive to depths of order 100 m to more than 10 km (Figure 2.1a), depending on the frequency bandwidth of the data (Chave et al., 2012). Furthermore, the current borehole information across the United States, extracted from the Geochemical Database for the Brackish Groundwater Assessment (Qi and Harris, 2017; Stanton et al., 2017), shows abundant information above 150 m deep, leaving deeper systems unmeasured all across the U.S. (Figure 2.1b). The latter shows the potential of using MT to provide additional information in the deeper parts of the hydrological systems.

Information gathered from MT surveys in mountainous terrains can provide crucial information about the subsurface fluid flow and geology of the system. With fluid flow in mind, a crucial question is whether electromagnetic data can detect regional to local groundwater flow systems in mountain blocks. A study on the Dosit River in China (Jiang et al., 2014) seems to point in that direction. MT surveys performed in a cross-section of the Dosit River show contrasting resistivities that decrease with depth in areas where brackish

groundwater is present (see Figures 2 and 3 in their study and Figure A.1 in the Appendix A). The authors argue that the differences in resistivities are not related only to the geology but to the saline groundwater circulating at those depths. This study provides important insight into how the nested nature of the flow system in mountainous terrains produces distinct resistivity patterns on MT surveys.

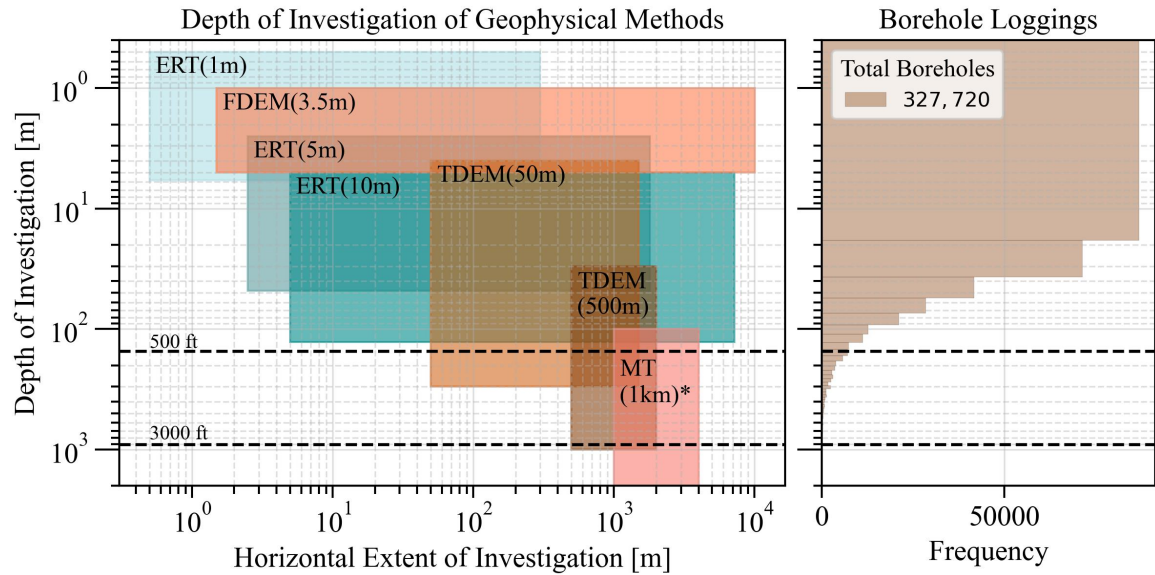


Figure 2.1: (a) after Binley et al. (2015), comparison of horizontal and vertical survey scales for electrical resistivity tomography (ERT) with 1, 5, and 10 m electrode array spacing Bernard (2003), frequency domain electromagnetics (FDEM) with 3.5 m coil instrument, time domain electromagnetics (TDEM) with 50 and 500 m loop soundings at multiple stations along a transect (Bear et al., 2013), and magnetotellurics (MT) with 1 km spacing between stations. MT can survey deeper than 2 km, and its investigation depth depends on the conductivity, duration and sampling rate of the deployment, and the upper and lower frequency limits Spies (1989); Chave et al. (2012). (b) Histogram for groundwater borehole logging depth in the U.S. Qi and Harris (2017); Stanton et al. (2017)

This work explores how MT surveys can provide information about the nested nature of flow in mountain-to-valley systems recharging lowland aquifers through regional circulation paths. To achieve this objective, we propose a handful of idealized mountain-to-valley conceptual models similar to the geologic setting of the Tularosa Basin in south-central New Mexico (see Figures A.2 and A.3 in the Appendix A). Water chemistry measurements performed in this area points to recharge from the Sacramento Mountains (Mamer et al., 2014), where water in the basin becomes older and more saline further away from the mountain block (Figure A.2 in the Appendix A). We explore various numerical experiments that account for different types of hydrological systems, exploring the role of topography, geology, and weathering rates. The groundwater flow and transport models we used are fully coupled by equations of state that connect variations in density and viscosity with changes in temperature and pressure. We also investigated the environmental age distribution at discharge sections of the watershed and compared the predicted distribution to previous observations made

in the Tularosa Basin by Eastoe and Rodney (2014) and Mamer et al. (2014) (Figure A.2 in the Appendix A). Lastly, we used a modified version of Archie’s Law proposed by Glover et al. (2000) to explore how flow and transport affect the electrical resistivity of the system. 2D forward and inverse models of resistivity computed from flow and transport were investigated using MARE2DEM, a freely-available adaptive finite element code for the 2D EM modeling (Key, 2016).

2.2 Methods

2.2.1 Conceptual Model

Our groundwater system is a simplified conceptualization of a mountain-to-valley transition within an extensional tectonic setting. We used the Sacramento Mountains and the Tularosa Basin in south-central New Mexico as inspiration (Figures A.2 and A.3). This modeling approach is intended as a sensitivity study within an idealized rift basin, and it is in the spirit of previous efforts that draw fundamental insight from simplified domain conceptualizations (e.g., Forster and Smith, 1988; Freeze and Witherspoon, 1967; Garven and Freeze, 1984; Person and Garven, 1994). Bedrock in the Sacramento Mountains is comprised of Paleozoic carbonates, sandstone, shale, and gypsum about 1.2 km thick overlying Proterozoic metasedimentary and crystalline basement (Kelley et al., 2014a; Newton and Land, 2016). The mountain block represented within our model is idealized and does not consider evaporite beds such as gypsum. No layers of Paleozoic strata are considered, and we assume that basement permeability is controlled by fracture networks. Our alluvium is divided into an alluvial fan (domain III in Figure 2.2a), a distal alluvial fan (domain I in Figure 2.2a), and an old alluvium that is cemented and hence we did not include a high permeability zone adjacent to the fault (domain II in Figure 2.2a). The horizontal extent of the conceptual model (Figure 2.2a) is 65 km divided between alluvium ($L_v = 52$ km) and a mountain block ($L_m = 13$ km). A fault zone characterizes the transition from mountain to valley at the piedmont of the mountain range. The fault zone has a dip angle of 55° and a thickness of 100 m. The alluvium surface has a constant slope of $S_v = 0.0001$ from the proximal piedmont deposits near the mountain front to basin floor deposits toward the left boundary ($\partial\Omega_l$). The mountain block is simplified to follow a Tóthian-like system (Tóth, 1963, 2009) described with a sinusoidal function. The complete surface topography (i.e., boundary $\partial\Omega_s$) in the model is represented with the following stepwise expression,

$$Z_s(x) = \begin{cases} S_v x, & \text{for } -L_v \leq x \leq 0 \\ A + S_m x + A \sin \left[\frac{2\pi}{\lambda} \left(x - \frac{\lambda}{4} \right) \right], & \text{for } 0 < x \leq L_m \end{cases} \quad (2.1)$$

where λ is the valley wavelength [L], A is the valley amplitude [L], and S_v and S_m are the alluvium

and mountain regional slope, respectively [-]. In this case, we assume that the surface topography, $Z_s(x)$, coincides with the water table, consistent Tóth's model (Tóth, 1963, 2009) where the water table is a subdued replica of the topography. From the surface of the lowest valley, the domain extends a distance B vertically [L]. We assume $B = 5$ km with five valleys. The domain is bounded laterally by $\partial\Omega_l$ and $\partial\Omega_r$, and at the bottom by $\partial\Omega_b$.

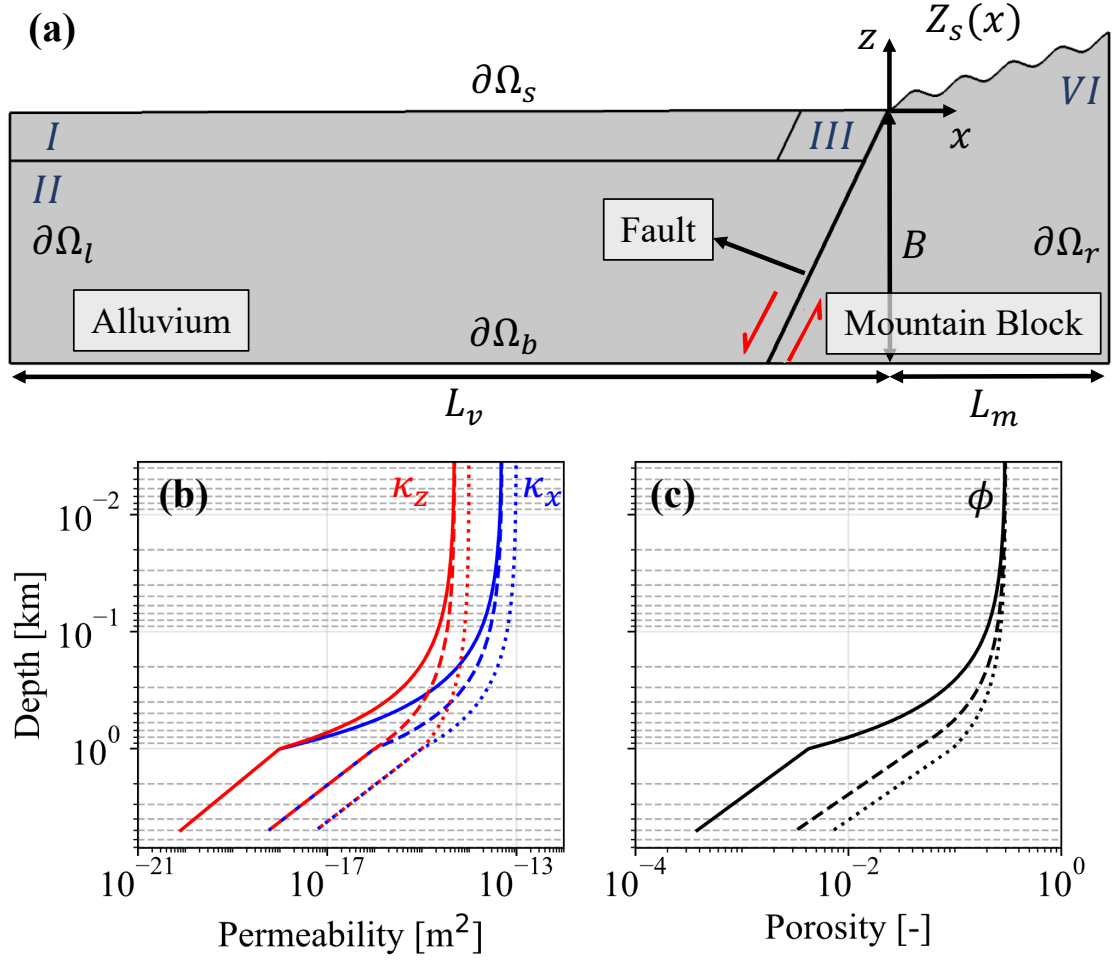


Figure 2.2: (a) Conceptual model of the mountain-to-valley transition. The mountain system is a subdued replica of the water table described by $Z_s(x)$, and a fault characterizes the transition from mountain to valley at the base of the mountain range. The Roman numerals separate the system regions: (I) upper basin-floor alluvium, (II) lower alluvium, (III) upper proximal-piedmont alluvium, and (IV) mountain block. (b) Permeability variations with depth, the red and blue lines denote the permeability variation in the z and x direction, respectively. (c) Porosity variations with depth. The solid and dashed lines in (b) and (c) represent the two permeability scenarios explored for the mountain block (region IV). The dotted lines represent the permeability and porosity used for the alluvium (region II).

We also assume a decreasing permeability (κ_z and κ_x ; [L^2]) and porosity (ϕ ; [-]) with depth for both the alluvium and the mountain block. The only exception is the proximal piedmont alluvium (III), which

is assumed to have a constant permeability higher than the rest of the systems, as suggested by Paola et al. (1992). For permeability in the remaining subdomains, a number of models have been used to describe this behavior (Ingebritsen and Manning, 2010; Jiang et al., 2009; Manning and Ingebritsen, 1999; Saar and Manga, 2004). Here, we use the piecewise permeability decay model presented in Saar and Manga (2004), which uses an exponential function for the shallow system and a potential function for the deep system. This model allows for a smaller decrease in permeability at lower depths, preventing singularities deep in the bedrock.

$$\kappa_z = \begin{cases} \kappa_s \exp[-A_s(Z_s(x) - z)], & \text{for } Z_s(x) - z < d_l \\ 10^{-A_d} \left(\frac{Z_s(x) - z}{D_d}\right)^{-B_d}, & \text{for } Z_s(x) - z \geq d_l \end{cases} \quad (2.2)$$

where κ_s is the permeability at the surface, A_s [m^{-1}] and B_d [-] are the decaying exponents that represent the decreased rate of permeability with depth, d_l is a defined depth (1 km for all the simulations) that separates the shallow from the deep systems, $D_d = 1$ km, and A_d can be calculated as follows,

$$A_d = B_d \log_{10} \left[\frac{\kappa_s \exp -A_s d_l}{d_l^{B_d}} \right] \quad (2.3)$$

Equation (2.2) calculates the permeability in the z direction, and we explore the effects of anisotropy in the shallow system with $\kappa_x = \eta \kappa_z$, where $\eta = 10$ is the anisotropy value. We assume anisotropic behavior only occurs above d_l in the upper alluvium (I) and in the mountain block (VI) (see Figure 2.2b). The value of $A_s = d_l^{-1} \log(\kappa_s) - \log(\kappa_{d_l})$, where κ_{d_l} is the permeability at the distance d_l that is extracted from Saar and Manga (2004) and Ingebritsen and Manning (2010).

For porosity, we assume $\kappa_z/\kappa_s = (\phi/\phi_s)^m$, where ϕ_s is the porosity at the surface and m is a medium and process-dependent coefficient. This expression has been used in earlier studies (see Bernabé et al., 2003; Cardenas and Jiang, 2010; Jiang et al., 2010). Replacing the permeability values with porosity in (2.2) yields the expression below. The behavior of the porosity within the system is illustrated in Figure 2.2c.

$$\phi(x, z) = \begin{cases} \phi_s \exp \left[-\frac{A_s(Z_s(x) - z)}{m} \right], & \text{for } Z_s(x) - z < d_l \\ \phi_s \left(\frac{10^{-A_d}}{\kappa_s} \right)^{\frac{1}{m}} \left(\frac{Z_s(x) - z}{D_d} \right)^{-B_d/m}, & \text{for } Z_s(x) - z \geq d_l \end{cases} \quad (2.4)$$

2.2.2 Model for Fluid Flow and Transport of Heat and Solutes

The simulations presented in this work solve the following governing equations for groundwater flow and transport of heat and solutes (Bear, 1972; Fetter, 2001; Nield and Bejan, 2013),

$$\frac{\partial(\phi\rho_f)}{\partial t} = -\nabla \cdot (\rho\mathbf{q}) \text{ with } \mathbf{q} = -\frac{\kappa\rho_f g}{\mu_f} \nabla \left(\frac{p}{\rho_f g} - z \right) \quad (2.5)$$

$$p(\mathbf{x}, t = 0) = \rho_{f,0}g [Z_s(x) - z]$$

$$p(\mathbf{x}, t) = 0 \text{ on } \partial\Omega_s$$

$$z(x = -L_v, y = -S_v L_v, t) = -S_v L_v \text{ on } \partial\Omega_l$$

$$-\mathbf{n} \cdot \rho_f \mathbf{q} = 0 \text{ on } \partial\Omega_r \wedge \partial\Omega_b$$

$$(\rho_f C_p) \frac{\partial T}{\partial t} = -\nabla \cdot (K_{eff} \nabla T) - \rho_f C_{p,f} \mathbf{q} \cdot \nabla T \quad (2.6)$$

$$T(\mathbf{x}, t = 0) = T_{profile} = T_s(x) + \frac{q_{Hb}}{K_{eff}} [Z_s(x) - z]$$

$$T(\mathbf{x}, t) = T_s \text{ on } \partial\Omega_s$$

$$\mathbf{n} \cdot K_{eff} \nabla T = 0 \text{ on } \partial\Omega_l \wedge \partial\Omega_r$$

$$\mathbf{n} \cdot K_{eff} \nabla T = q_{Hb} \text{ on } \partial\Omega_b$$

$$\frac{\partial(\phi c)}{\partial t} = -\nabla \cdot (\mathbf{D} \nabla c) - \nabla \cdot (\mathbf{q}c) + R \quad (2.7)$$

$$c(\mathbf{x}, t = 0) = c_{max}$$

$$c(\mathbf{x}, t) = c_0 \text{ on } \partial\Omega_{s,in}$$

$$\mathbf{n} \cdot (\mathbf{D} \nabla c) = 0 \text{ on } \partial\Omega_{s,out} \wedge \partial\Omega_l$$

$$\mathbf{n} \cdot (\mathbf{D} \nabla c - \mathbf{q}c) = 0 \text{ on } \partial\Omega_r \wedge \partial\Omega_b$$

Beginning with the groundwater flow equation (2.5), \mathbf{q} is the Darcy's flux [LT^{-1}], $\mathbf{x} = [x, z]$ is the coordinate vector [L], \mathbf{n} is an outward vector normal to the boundary [-], ρ_f and $\rho_{f,0}$ are the water density and the water reference density [ML^{-3}], respectively, μ_f is the dynamic viscosity of water [$\text{ML}^{-1}\text{T}^{-1}$], g is the gravity acceleration constant [LT^{-2}], and p is pressure [$\text{ML}^{-1}\text{T}^{-2}$]. As an initial condition in the system, we use the hydrostatic equation. As boundary conditions, we use a constant head boundary on the left ($\partial\Omega_l$), a no-flow condition on the right ($\partial\Omega_r$), and bottom ($\partial\Omega_b$) boundaries, and a pressure boundary is set at the surface ($\partial\Omega_s$).

In the heat (T ; [Θ]) transport equation (2.6), $(\rho_f C_p)_{eff} = \phi \rho_f C_{pf} + (1 - \phi) \rho_s C_{ps}$ is the effective heat

capacity [$L^2MT^{-2}\Theta^{-1}$], $K_{eff} = \phi K_f + (1 - \phi)K_s$ is effective thermal conductivity [$MLT^{-3}\Theta^{-1}$], $T_s(x) = T_0 - \Gamma Z_s(x)$ is the surface temperature profile (at $\partial\Omega_s$), Γ is the atmospheric lapse rate, C_{pf} and C_{ps} are the water and solid heat capacity, ρ_s is the solid density and q_{Hb} is the basal heat flux imposed along the bottom boundary ($\partial\Omega_b$). The system has a $T_{profile}$ as the initial condition, and a thermal insulation boundary condition was set in the lateral boundaries ($\partial\Omega_l, \partial\Omega_r$).

In the solute transport equation (2.7), c is the volumetric concentration of salinity (NaCl) [ML^{-3}], $D = D_{i,j}$ is the dispersion-diffusion tensor [L^2T^{-1}] defined as (Bear, 1972)

$$D_{i,j} = \alpha_T |\mathbf{q}| \delta_{i,j} + (\alpha_L - \alpha_T) \frac{q_i q_j}{|\mathbf{q}|} + \frac{\phi}{\xi_m} D_m \quad (2.8)$$

with α_T and α_L the transverse and longitudinal dispersivities [L], D_m the effective molecular self-diffusion coefficient, $\xi_m = \phi^{-1/3}$ is the fluid tortuosity (defined here with the Millington and Quirk (1961) model), and $\delta_{i,j}$ is the Kronecker delta function. In equation (2.7), $R = k_{mt}(c_{max} - c)$ is a first-order reaction solute mass rate of dissolution of precipitation (solute source term), used in Lemieux et al. (2008a) and Provost et al. (2012) to mimic the buildup of salinity due to fluid-rock interactions. In this expression, c_{max} is the maximum allowable fluid concentration, and k_{mt} is the mass transfer reaction rate [T^{-1}] that is temperature dependent and can be described through the Arrhenius expression (Langmuir, 1997),

$$k_{mt} = A_0 \exp\left(-\frac{E_0}{R_0 T}\right) \quad (2.9)$$

where A_0 is a temperature-independent coefficient [T^{-1}], E_0 is the activation energy [L^2MT^{-2}] and R_0 is the ideal gas constant [$ML^2T^{-2}\Theta^{-1}$]. To obtain a reasonable value of A_0 we explore a range of values of $k_{mt} \rightarrow k_{mt_0}$ used by Lemieux et al. (2008b) and Provost et al. (2012) and solve for A_0 in (2.9) assuming a mean temperature of $160^\circ C$ for those values (temperature at a depth of 5 km). It is worth noting that although this representation might not be appropriate for all environments, it allows for the consideration of realistic and applicable salinity scenarios. As an initial condition, we set the concentration to be equal to c_{max} , because the system will flush out the excess of solute as the simulation progresses. As boundary conditions, we set a no flux condition on the right and bottom boundaries ($\partial\Omega_r$ and $\partial\Omega_b$), a symmetry boundary condition on the left boundary ($\partial\Omega_l$), and an open boundary condition is set at the surface ($\partial\Omega_s$), with a reference concentration c_0 .

Lastly, we use empirical approximations for density and dynamic viscosity derived by Kestin et al. (1981), based on Rowe and Chou (1970), as they provide a reasonable approximation to experimental data (Adams and Bachu, 2002). The empirical expressions vary the density and viscosity according to variations in pressure (p), temperature (T), and volumetric concentration of solutions (mainly NaCl) (c). These equations are

presented in more detail in Adams and Bachu (2002) equations (1) and (15).

2.2.3 Model for Residence Time Distribution

We model the residence time distribution (RTD) of water molecules $\psi(\mathbf{x}, \tau)$ [T^{-1}] using the approach described in Gomez-Velez (2013). From a numerical perspective, it is more stable to simulate the evolution of the cumulative residence time distribution (CRTD), $F(\mathbf{x}, t, \tau) \int_0^\tau \psi(\mathbf{x}, t, \xi) d\xi$, and then estimate the RTD by differentiation as $\psi(\mathbf{x}, \tau) = \partial F / \partial \tau$. The CRTD is described by the following mathematical statement,

$$\begin{aligned} \frac{\partial(\phi F)}{\partial \tau} &= \nabla \cdot (\mathbf{D}\nabla F) - \nabla \cdot (\mathbf{q}F) & (2.10) \\ F(\mathbf{x}, t = 0) &= 0 \\ F(\mathbf{x}, t) &= H(t) \text{ on } \partial\Omega_{s,in} \\ \mathbf{n} \cdot (\mathbf{D}\nabla F) &= \text{ on } \partial\Omega_{s,out} \\ \mathbf{n} \cdot (\mathbf{D}\nabla F - \mathbf{q}F) &= 0 \text{ on } \partial\Omega_l \wedge \partial\Omega_r \wedge \partial\Omega_b \end{aligned}$$

where $\tau(\tau \geq 0)$ is age [T] and $H(t)$ is the Heaviside step function.

2.2.4 Model for Bulk Electrical Resistivity

We estimate the electrical conductivity (the inverse of resistivity) for each simulation result using a modified version of Archie's Law, published by Glover et al. (2000). This modification is a mixing model that estimates the bulk electrical conductivity ($\sigma_{r,bulk}$, S/m; [$\text{M}^{-1}\text{L}^{-3}\text{T}^3\text{A}^2$]) of the medium with its porosity (ϕ) and both, fluid and solid, electrical conductivities ($\sigma_{r,f}$, $\sigma_{r,s}$), as

$$\sigma_{r,bulk} = \sigma_{r,f}\phi^{m_r} + \sigma_{r,s}(1 - \phi)^{p_r} \quad (2.11)$$

where m_r is the cementation exponent (common values range from 1.5 to 2.5 for sedimentary rocks containing saline aqueous fluids) and $p_r = \log(1 - \phi)^{m_r} / \log(1 - \phi)$. Observations show that the fluid's electrical conductivity primarily depends on salinity and temperature (Arps, 1953; Pepin, 2019; Sen and Goode, 1992; Uco et al., 1980). Empirical models have been used to calculate fluid resistivity ($\rho_{r,f}(T, c) = 1/\sigma_{r,f}(T, c)$); some of the models use solute concentration and temperature (Pepin, 2019; Sen and Goode, 1992; Uco et al., 1980), and others use only temperature with an assumed seawater salinity (Becker et al., 1982; Constable et al., 2009). We tested each model, comparing them with information on fluid resistivity collected by Pepin (2019) from reported measurements (Ho et al., 2000; Lide and Haynes, 2009; National Research

Council, 1930; Noyes, 1907; Quist and Marshall, 1968; Ucock et al., 1980; Zimmerman et al., 1995). We decided to use the model presented in Sen and Goode (1992) for the comparison, as it provides a reasonable approximation to the data while having low model complexity (see the comparison in Figure A.4 in the Appendix A). The model form is the following,

$$\sigma_{r,f} = (5.6 + 0.27T - 1.5 \times 10^{-4}T^2)M - \frac{2.36 + 0.099T}{1.0 + 0.214M}M^{3/2} \quad (2.12)$$

where M is the molality, and the temperature (T) is in Celsius.

Glover’s model (Eq. (2.11)) shows that as porosity decreases, solid resistivity becomes the dominant value in the system. However, the change in bulk resistivity depends on the water salinity. The transition between fluid and solid resistivity preponderance on the total bulk resistivity happens below a porosity of 5%, suggesting that we will be able to see saline water in systems with relatively low porosity (see Figures A.5 and A.6 in the Appendix A).

Lastly, we create a forward model using MARE2DEM (Key, 2016), a code that uses an Occam’s inversion approach (Constable et al., 1987), to perform forward and inverse MT modeling. In that sense, we created forward models using the bulk resistivity ($\rho_{r,bulk}$) from the simulation results and populating the surface with three different arrangements of magnetotelluric (MT) receivers that explore 49 frequencies between 10^{-2} to 103 Hz (skin depth, δ , between 5 to 112 km with the lowest frequency and assuming resistivities of 1 and 500 $\Omega \cdot m$, respectively, using the equation $\delta = 503\sqrt{\rho_{r,bulk}/f}$ from Chave et al. (2012)). We then created synthetic noisy observations by adding a 5% relative Gaussian error. That is, a random error with mean zero and standard deviation of 5% of the simulated value for the variable of interest (bulk resistivity and phase) at each frequency. This means the error floor of our data is within the range of 5% for all of our synthetic observations, mimicking good-quality field data. We inverted both TE and TM modes as bulk resistivity and phase data to test whether an MT survey can capture the dynamics of the systems we are exploring. For the inversions, we used a telescopic meshing strategy that combines structured and unstructured meshes (see Figure A.7 in the Appendix A). Within the mountain-to-valley system ($x \in [-51, 13]$ km and $z \in [-3, 1.6]$ km), we used a structured mesh with quadrilateral elements of size 0.1×0.05 km (width \times depth). The idea is to use mesh with enough resolution to capture the complex spatial patterns expected from a nested regional groundwater flow system. For reference, the horizontal separation between the local topographic ridges is approximately 2.8 km. Then, enclosing the domain of interest, we use an unstructured mesh large enough to minimize artificial boundary effects ($x \in [-100, 100]$ km and $z \in [-100, 1.6]$ km). The final mesh has 68,273 elements (24,376 structured and 43,897 unstructured). Finally, we set a root-mean-square (RMS) misfit target of 1.0 for all our synthetic inversions.

2.2.5 Scenarios Explored

Although the conceptual model presented above is idealized, we strive to explore realistic scenarios that resemble shallow, intermediate, and deep circulation systems. With this in mind, we investigate two local and regional topographic systems, changing the regional slope (S_m) and the amplitude (A) of Eq. (2.1). For permeability in the shallow region (depths larger or equal than d_l), we set the surface value (κ_s) and the value at d_l (κ_{d_l}), from this information, we back-calculate A_s in Eq. (2.2) using two values for κ_{d_l} that account for fast and slow decaying permeability cases and then use the anisotropy (η) to calculate κ_x . In the deep region (depths larger or equal than d_l), we use two values for the deep decaying exponent (B_d) (the resulting permeability for both systems can be seen in Figure A.8 in the Appendix A). For solute concentration, we look at two reaction rates (k_{m_0}) that encompass some of the variability presented in Lemieux et al. (2008b). To estimate the resistivity fields, we use the porosity of the system, a constant value for the cementation factor (m_r), and explore constant values for solid resistivity ($\rho_{r,s}$), assuming distinct medium resistivity values for the system regions described in Figure 2.2. Lastly, we ran the simulations for $t = 10^6$ years to achieve steady-state conditions (less than 0.1% change), running a transient solution with the coupled model helps in a smooth convergence of the simulation.

The values for all parameters used in our analysis are presented in Table 2.1. We check the following physical requirements in all our simulations. (i) recharge rates between 10^{-2} and 100 m/yr, as presented in other studies (Gleeson et al., 2011; Schaller and Fan, 2009; Wilson and Guan, 2004), (ii) temperature profiles that follow realistic scenarios coming from previous simulations (Smith and Chapman, 1983), and (iii) age distributions similar to the ones found in analogous systems (Figure 2.3) (Eastoe and Rodney, 2014; Frisbee et al., 2013b,a; Mamer et al., 2014).

Table 2.1: Parameter values for numerical simulations

Symbol	Variable Name	Values Explored	Units
A	Valley Amplitude ^{a,b}	0.01λ ; 0.04λ	m
L_v	Alluvium Horizontal Distance	52	km
L_m	Mountain Block Horizontal Distance ^{a,b}	13	km
B	Vertical Distance	5	km
S_m	Mountain Regional Slope	0.02; 0.1	-
S_v	Alluvium Slope	0.0001	-

Continued on next page

Table 2.1: Parameter values for numerical simulations (Continued)

Symbol	Variable Name	Values Explored	Units
n	Number of Valleys	5	-
d_l	Depth of Change in Permeability ^{c,d}	1	km
κ_s^I	Surface Permeability of Upper Basin-floor Alluvium ^{c,d}	1×10^{-14}	m^2
κ_s^{III}	Surface Permeability of Alluvial Piedmont ^{c,d}	1×10^{-15}	m^2
κ_s^{IV}	Surface Permeability of Mountain Block ^{c,d}	5×10^{-15}	m^2
$\kappa_{d_l}^{II}$	Permeability at d_l of Lower Alluvium ^{c,d}	1×10^{-16}	m^2
$\kappa_{d_l}^{III}$	Permeability at d_l of Alluvial Piedmont ^{c,d}	1×10^{-13}	m^2
$\kappa_{d_l}^{VI}$	Permeability at d_l of Nountain Block ^{c,d}	1×10^{-18} ; 1×10^{-16}	m^2
$\kappa_{f,z}$	Permeability of the fault in the z -direction ^{c,d}	5×10^{-14}	m^2
$\kappa_{f,x}$	Permeability of the fault in the x -direction ^{c,d}	5×10^{-15}	m^2
B_d	Depth Permeability Coefficient ^{c,d}	3; 3.2	-
η	Anisotropy Coefficient ^{d,e}	10	-
ϕ_s	Surface Porosity ^{b,f}	0.3	-
m	Medium and Process Dependent Coefficient ^{b,f}	2	-
T_0	Temperature at the First Valley ^g	20	$^{\circ}C$
Γ	Thermal Lapse Rate	6.5	$^{\circ}C/km$
q_{Hb}	Basal heat Flux ^g	60	mW/m^2
$\mu_{f,0}$	Initial Fluid Viscosity	0.001	$kg/(m \cdot s)$
$\rho_{f,0}$	Initial Fluid Density	0.998.2	kg/m^3
C_{pf}	Fluid Specific Heat Capacity ^g	4,183	$J/(kg \cdot K)$
K_f	Fluid Thermal Capacity ^g	1	$W/(m \cdot K)$
ρ_s	Solid (Rock) Density	2,600	kg/m^3
C_{ps}	Solid Specific Heat Capacity	836.8	$J/(kg \cdot K)$
K_s	Solid Thermal Capacity ^g	3	$W/(m \cdot K)$

Continued on next page

Table 2.1: Parameter values for numerical simulations (Continued)

Symbol	Variable Name	Values Explored	Units
c_{max}	Maximum Salinity ^{h,i}	0.3	kg/kg
R_0	Ideal Gas Constant ^j	1.9871×10^{-3}	kcal/(mol·K)
E_0	Activation Energy ^j	10.0	kcal/mol
k_{m0}	Dissolution Rate at $T = 160^\circ\text{C}$	1×10^{-13} ; 1×10^{-16}	1/s
α_L	Longitudinal Dispersivity ^{k,l}	100	m
α_T	Transversal Dispersivity ^{k,l}	10	m
$\rho_{r,s}^I$	Solid (Rock) Resistivity of Upper Alluvium ^m	100	$\Omega \cdot \text{m}$
$\rho_{r,s}^{II}$	Solid (Rock) Resistivity of Upper Alluvium ^m	500	$\Omega \cdot \text{m}$
$\rho_{r,s}^{III}$	Solid (Rock) Resistivity of Alluvial Piedmont ^m	200	$\Omega \cdot \text{m}$
$\rho_{r,s}^{IV}$	Solid (Rock) Resistivity of Mountain Block ^m	500	$\Omega \cdot \text{m}$
m_r	Cementation Factor	2	-
M_{NaCl}	NaCl Molar Mass	58.442	g/mol

^aGleeson and Manning (2008), ^bCardenas and Jiang (2010), ^cIngebritsen and Manning (2010), ^dSaar and Manga (2004),

^eDeming and Baross (1993), ^fJiang et al. (2010), ^gSmith and Chapman (1983), ^hLemieux et al. (2008b), ⁱProvost et al. (2012),

^jLangmuir (1997), ^kFetter (2001), ^lGelhar et al. (1992), ^mPalacky (1988).

2.3 Results

2.3.1 Role of Topography and Geology in Groundwater Dynamics and Residence Times

This section explores the topographic features and role of geology in groundwater system dynamics and residence times. In all our simulation results, the recharge rates in the mountain block systems vary between 0.35 to 0.9 m/yr in the peaks of the mountains and the discharge rates from 0.1 to 0.6 m/yr in the valleys, with the highest recharge rates occurring in the high regional slope systems. These rates are comparable to values explored in other systems (Gleeson et al., 2011; Schaller and Fan, 2009).

First, we focus on the flow system with high local and regional relief systems with low permeability (panel g in Figures 2.3, 2.4, and 2.5). In this mountain-to-valley transition system, we can see a distinct separation of local and regional flowpaths, where stagnation points are made visible by the lower Darcy velocities in the meeting branches of the local and regional flowpaths (panel g in Figure 2.3). The regional flow travels 0.5

to 2 km deep within the mountain block until it reaches the fault. In the fault, the water moves upwards in the first 400 meters and then switches downward, recharging the alluvial piedmont and the lower alluvium. The recharge of the alluvial piedmont comes preferentially from the first local relief systems of the mountain block. This flow behavior strongly impacts the age distribution of this mountain-to-valley transition system (panel g in Figure 2.4), as water flowing through the local flowpaths ranges from less than one year to 100 years old, with increasing ages as depth increases. In the alluvium, the old regional groundwater flow mixes with younger water coming from the local flowpaths, increasing the water ages with increased distance from the piedmont into the alluvium, reaching ages older than 1,000 years. Finally, the production of solutes is strongly related to the water age, as greater ages involve a longer contact time of water with minerals that could potentially dissolve, increasing the total dissolved solute (TDS) content of the groundwater. The solute concentrations presented for these systems (Figure 2.5) are divided into fresh ($< 1,000$ mg/L), brackish (1,000 - 10,000 mg/L), and saline ($> 10,000$ mg/L) water to make an easier comparison (with values from Stanton et al., 2017). The solute concentration increases with depth, following the multi-scale nature of the flow field in the mountain block with brackish and saline water present in the stagnation points (panel g in Figure 2.5). In the alluvium, the solute distribution is a consequence of the interaction between the local and regional flow systems from the mountain block, with freshwater present at the alluvial piedmont and brackish water appearing nine kilometers away from the mountain block, where young water mixes with older water. The appearance of brackish water on the alluvium surface is a consequence of the solute reaction rate, the interaction of the mountain flowpaths, and the change in permeability between the alluvial piedmont and the upper alluvium sections.

Reducing the local topographic relief of the mountain block (panel e in Figures 2.3, 2.4, and 2.5) produces shallower regional flowpaths with depths of 200 meters, where the stagnation points disappear. In these systems, the regional groundwater flow travels at a higher rate through the mountain block, recharging the lowland aquifers through the alluvial piedmont and the lower alluvium. The water age increases linearly with depth, following the regional groundwater streamlines, and freshwater is present in the first kilometer of the mountain block due to the fast-moving regional flow. On the other hand, reducing the regional topography (panel c in Figures 2.3, 2.4, and 2.5) leads to systems with enhanced local flowpaths that can reach 2 km deep. In these cases, the upper alluvium is predominantly recharged by the first peak of the mountain system, leaving the regional flow system to recharge the deeper parts of the lower alluvium. This behavior influences the water ages as younger water penetrates deeper into the mountain block, moving the stagnation points deeper where the concentration of solutes increases. Lastly, increasing the permeability of the mountain block (panels b, d, f, and h in Figures 2.3, 2.4, and 2.5) produces faster and shallower regional groundwater fluxes, reducing the residence times of the overall mountain block and increasing the amount of freshwater

present in the system. Furthermore, the recharge of water in the alluvial piedmont and upper alluvium shifts to a predominantly regional source, which increases the amount of brackish groundwater present in the upper alluvium. In addition to the presented results, we also estimated the temperature distribution (Figure A.9 in the Appendix A). The resulting temperature fields follow the multi-scale nature of flow in the mountain block and increase with depth, agreeing with results presented in previous studies (Gleeson and Manning, 2008; Jiang et al., 2009; Smith and Chapman, 1983; Tóth, 1963).

The latter simulation results explore a range of probable geologic and topographic features. The resulting behavior of the high local and regional relief systems agrees with age dating and geochemical analysis measurements performed in the Tularosa Basin (Figure A.2 in Appendix A). For instance, Carbon-14 age estimates show water ages between 1,340 and 27,500 years in the alluvium, increasing with increased distance from the mountain block (Eastoe and Rodney, 2014; Mamer et al., 2014). Similarly, TDS measurements in the area show freshwater present in the alluvial piedmont and brackish and saline water in sections of the basin-floor alluvium further away from the mountain system, attributed to the dissolution of gypsum (Orr and Myers, 1986; Newton and Land, 2016; NMBGMR et al., 2016). However, not all mountain-to-valley transition systems have a high accumulation of solutes close to the surface. By decreasing the reaction rate of one of the systems, freshwater penetrates deeper into the mountain block, causing freshwater to extend into the upper part of the alluvium (Figure 2.6). In these systems, the downward movement of water through the fault is apparent, recharging fresh and brackish water to deeper parts of the alluvial valley. To illustrate the importance of multiscale circulation within the mountain block, we estimated water, solute, and energy fluxes passing through the fault from the mountain block to the alluvium (Figure A.10). Water flux decreases with depth due to decreasing permeability (Figure A.10a, b). For systems with high reaction rates (red and blue lines), the solute fluxes are characterized by two peaks. The shallowest one is associated with local and intermediate circulation cells and occurs at approximately 50 meters. This peak is more subtle for the cases with low permeability (blue lines). The deepest peak is linked to regional groundwater flowpaths that move brackish and brine water from the mountain block to the alluvium and occur at approximately 500 meters and 750 meters for the low- and high-permeability cases, respectively. Similarly, the peak flux is lower for the low-permeability cases. After the second peak, we see a decrease of about an order of magnitude as we move to the deeper parts of the mountain block. However, these deeper contributions of solute mass still enter the fault and are eventually redistributed to the alluvium. For low reaction rate systems (green lines), we see a sharp decrease in solute flux with a shallow minimum at around 450 meters. Because these systems do not have enough time to accumulate significant amounts of solutes in the upper regions of the mountain block (Figure 2.6b), we see freshwater entering the lower sections of the mountain block that are then moved through local and regional flowpaths to the alluvium. Lastly, the heat flux (Figure A.10d) only shows strong

variations in the first 200 meters (associated with local flowpaths), with heat fluxes varying between 0.05 to 0.25 W/m². The lowest values are associated with low regional slope and low relief systems, whereas the highest values correspond to high regional slope and low relief systems. As we move deeper into the domain, these fluxes decrease to 10⁻² W/m².

In summary, the multi-scaled nested flow in mountain systems strongly depends on the topography and geology of the mountain block, where regional flowpaths drive water and solutes further into the alluvium in systems with high local and regional relief and high permeability. The interaction of local and regional flowpaths produces stagnation points in the mountain block. These points are delineated by brackish and saline water in systems with high dissolution rates, analogous to mountains with geologic material that can be easily dissolved, like evaporites. The following section explores how resistivity patterns give insight into the multi-scale nested nature of flow in the mountain block and how magnetotelluric (MT) measurements can be used to study this behavior.

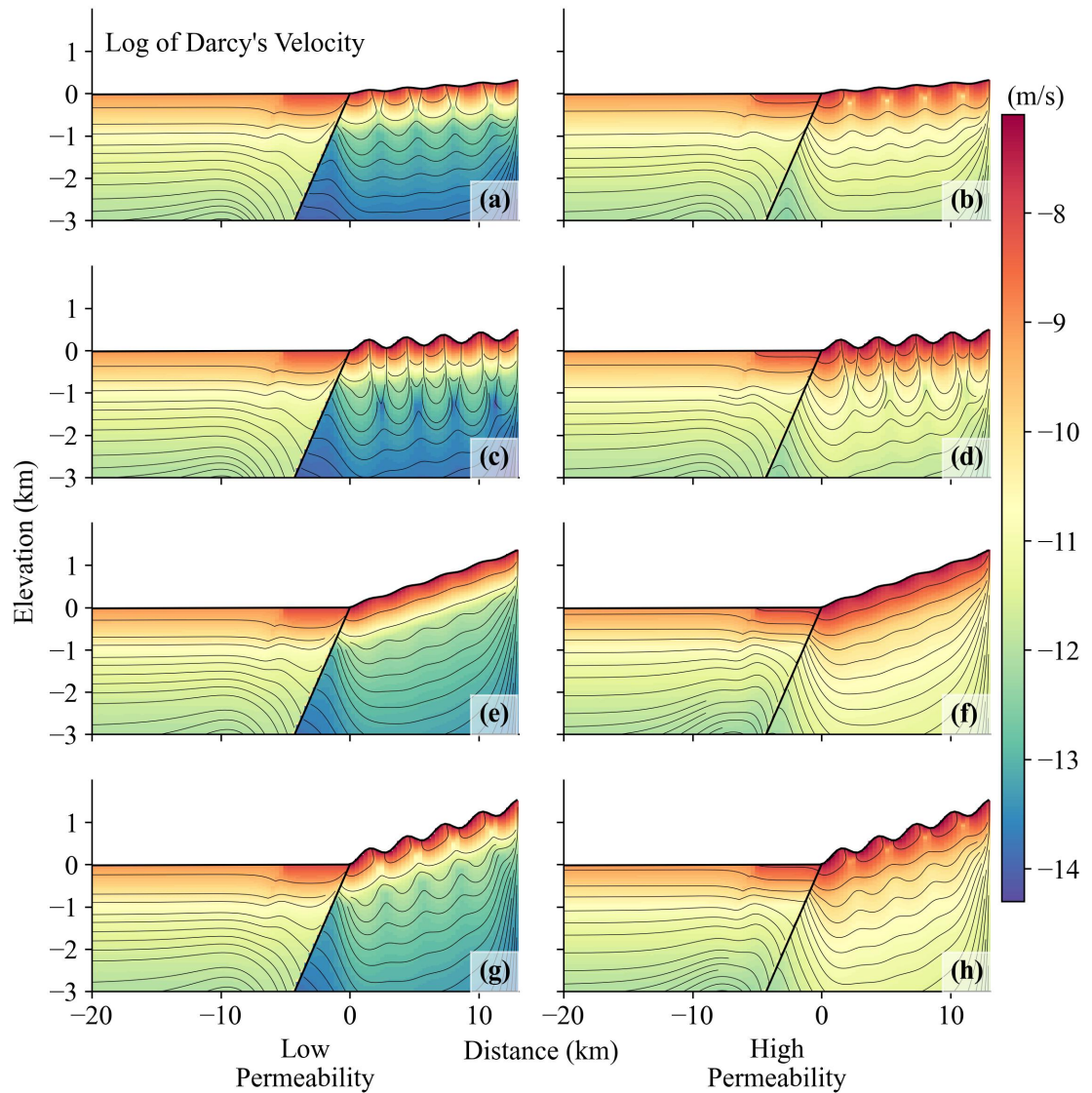


Figure 2.3: Spatial variability of the Darcy flux magnitude. The first column (panels a, c, e, and g) denotes scenarios with low permeability, and the second column (panels b, d, f, and h) denotes scenarios with high permeability. The rows present different degrees of topographic relief, starting with low relief and low regional slope (panels a and b), high relief and low regional slope (panels c and d), low relief and high regional slope (panels e and f), and high relief and high regional slope (panels g and h). The black lines show uniformly spaced streamlines. The streamlines in the mountain block show the distinct separation between the local and regional flowpaths recharging the lowland aquifers. The flow through the fault is preferentially downward in all the simulations.

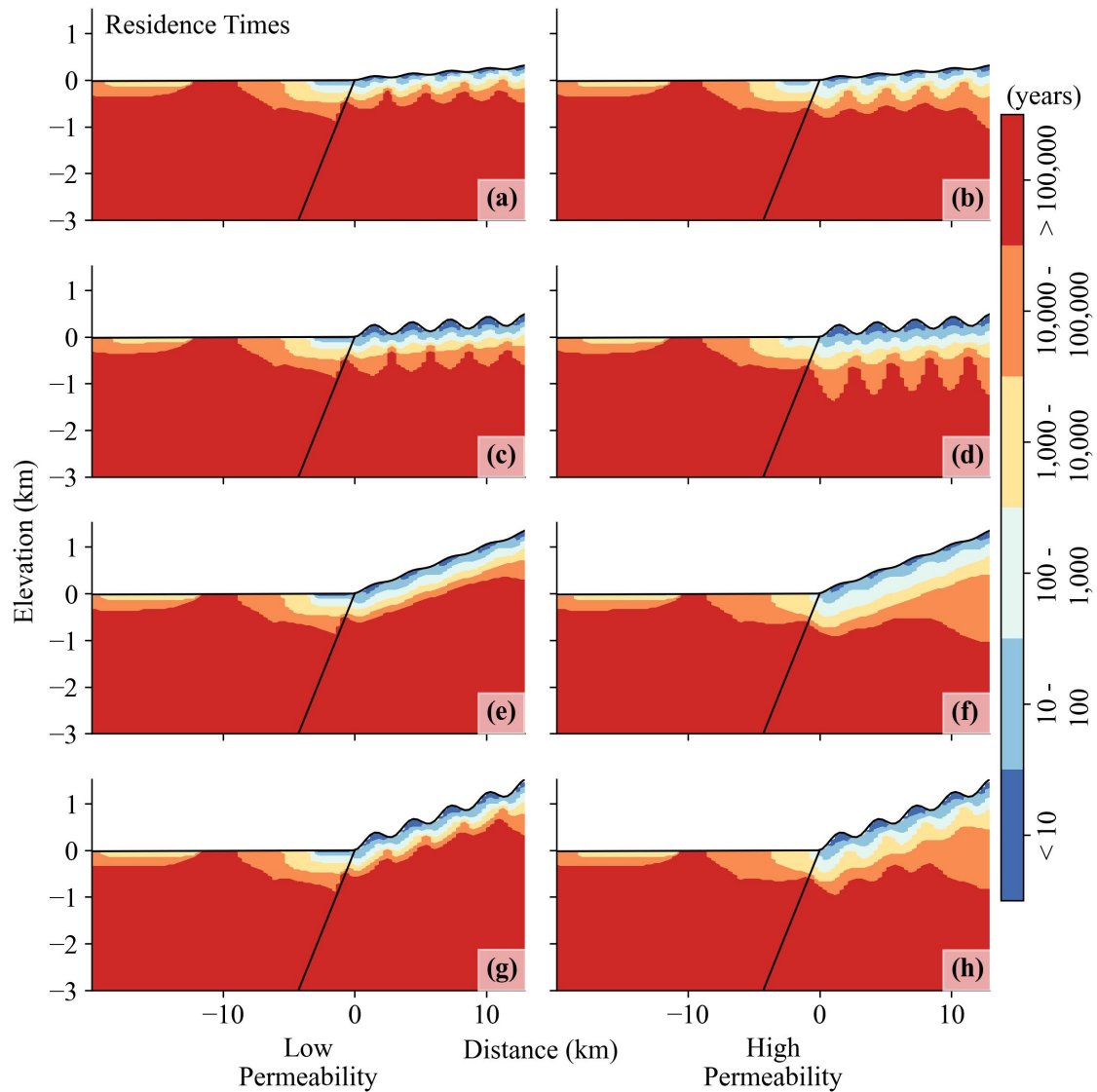


Figure 2.4: Spatial variability of groundwater age. The first column (panels a, c, e, and g) denotes scenarios with low permeability, and the second column (panels b, d, f, and h) denotes scenarios with high permeability. The rows present different degrees of topographic relief, starting with low relief and low regional slope (panels a and b), high relief and low regional slope (panels c and d), low relief and high regional slope (panels e and f), and high relief and high regional slope (panels g and h). The colors separate water ages. Each color denotes the water that has 60% of water in that specific range. In the mountain block, the water ages increase with increased depth. In the alluvium, the water ages combine young water from local flowpaths and old water from regional sources.

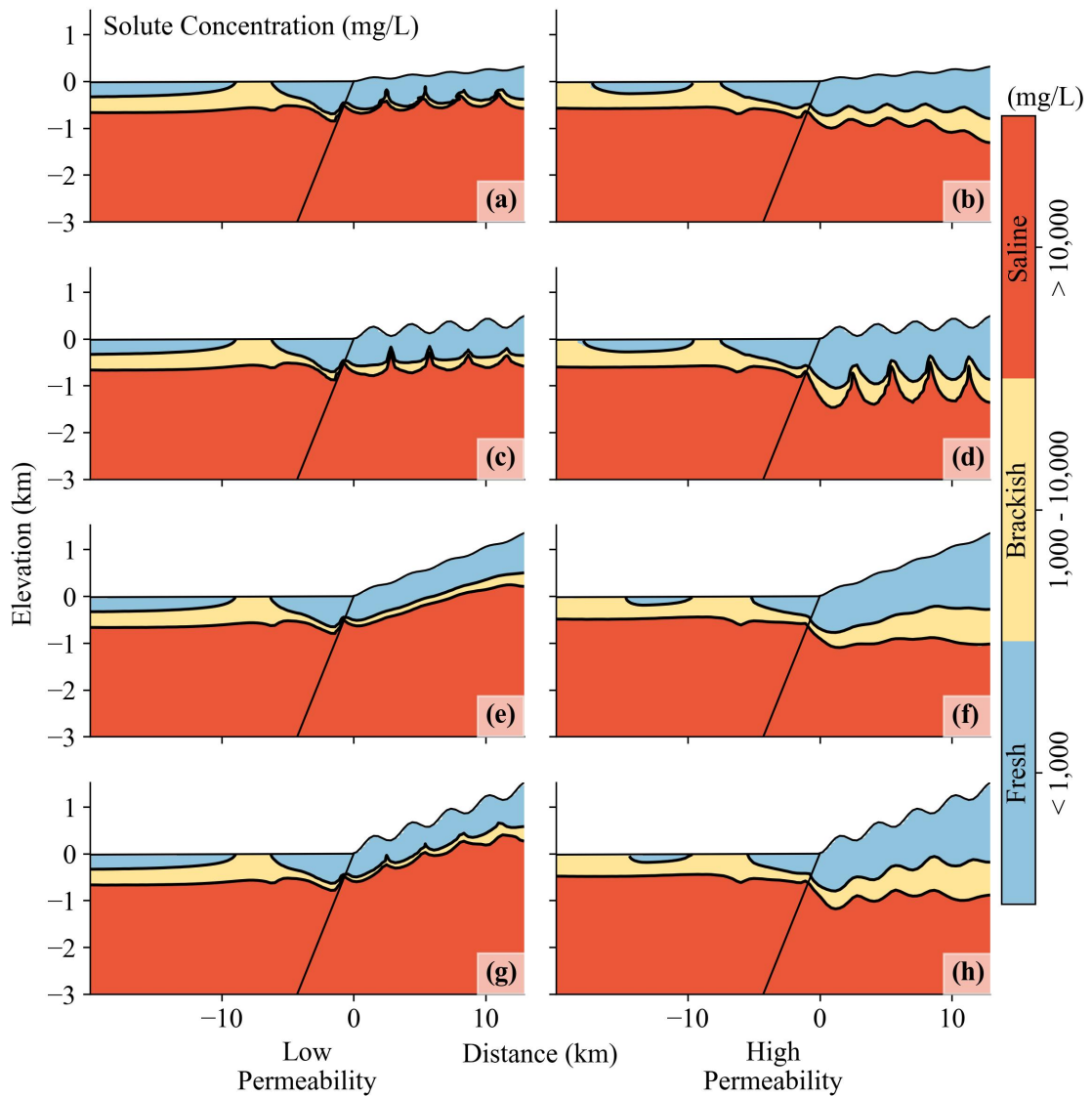


Figure 2.5: Solute concentration for a high reaction rate ($k_{mt_0} = 1 \times 10^{-13}$). The first column (panels a, c, e, and g) denotes scenarios with low permeability, and the second column (panels b, d, f, and h) denotes scenarios with high permeability. The rows present different degrees of topographic relief, starting with low relief and low regional slope (panels a and b), high relief and low regional slope (panels c and d), low relief and high regional slope (panels e and f), and high relief and high regional slope (panels g and h). The contours separate freshwater, brackish water, and saline water. The solute concentration increases with depth, delineating the multi-scale nature of flow in the mountain block. In the alluvium, the interaction of local and regional flowpaths produces the presence of brackish water in the upper alluvium.

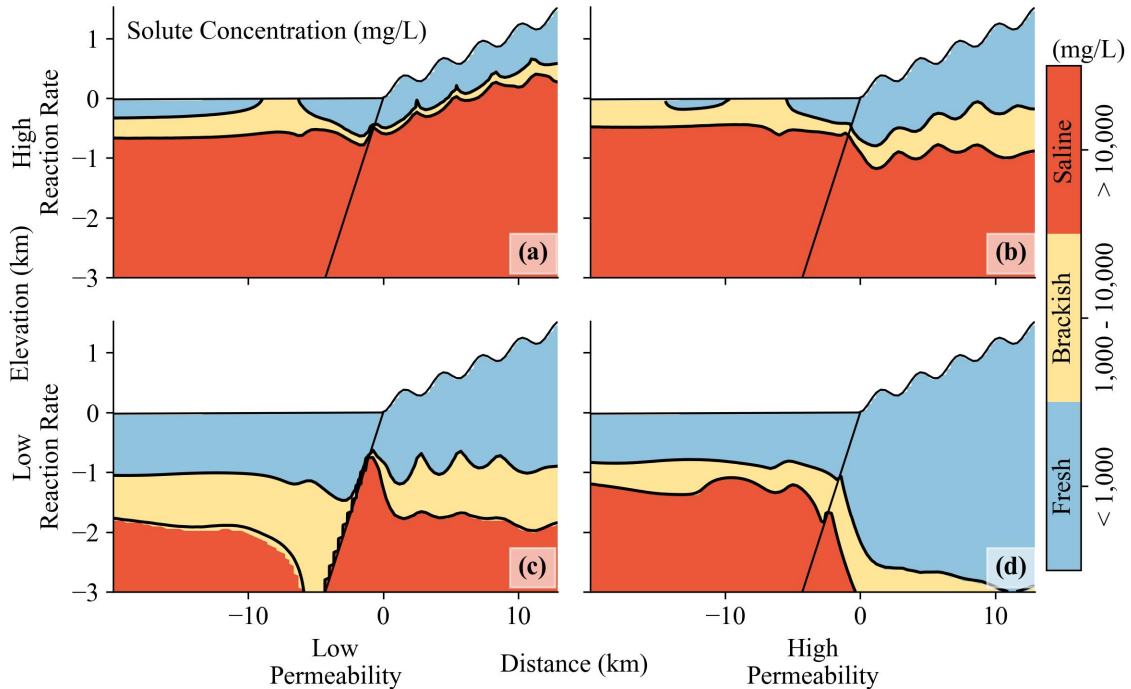


Figure 2.6: Solute concentration for low permeability (a and c) and high permeability (b and d), and high dissolution rate (a and b) and low dissolution rate (c and d) scenarios. The contours separate water between fresh, brackish, and saline. Lower dissolution rates cause freshwater to penetrate deeper into the mountain block and alluvium.

2.3.2 Can We Image the Nested Nature of Hydrologic Systems Using Electromagnetic Methods?

As suggested by Glover et al. (2000), the resistivity patterns are a mixture that depends on fluid conductivity and lithology linked through the porous media (Equation (2.11)). We also see that fluid conductivity is linked to heat and solute concentration, where systems with high temperature and solute concentration tend to be more conductive and, thus, less resistive. Our results show a clear distinction in the resistivity values of fresh and saline water in parts of the system with high porosity values (Figure 2.7). These patterns vary with permeability, where systems with low permeability and porosity are associated with increasing resistivity with depth in the mountain block. As a result, we see pockets of low resistivity close to the stagnation zones, where regional circulation meets the local flowpaths accumulating solutes. These zones appear below the valleys of the mountain system. On the other hand, high permeability systems are linked to a slower decaying porosity. The results show a distinct decrease in resistivity as water becomes saline, starting at the interface between the local and regional flowpaths in the mountain block. Lastly, the bulk resistivity in the alluvium is primarily conductive, with resistivity values lower than $100 \Omega \cdot m$. This behavior is linked to a higher porosity, the presence of saline and brackish water, and a lower solid resistivity in the upper part of

the alluvium. However, we also see contrasting resistivity values in the alluvial piedmont, where freshwater is being recharged from the mountain block.

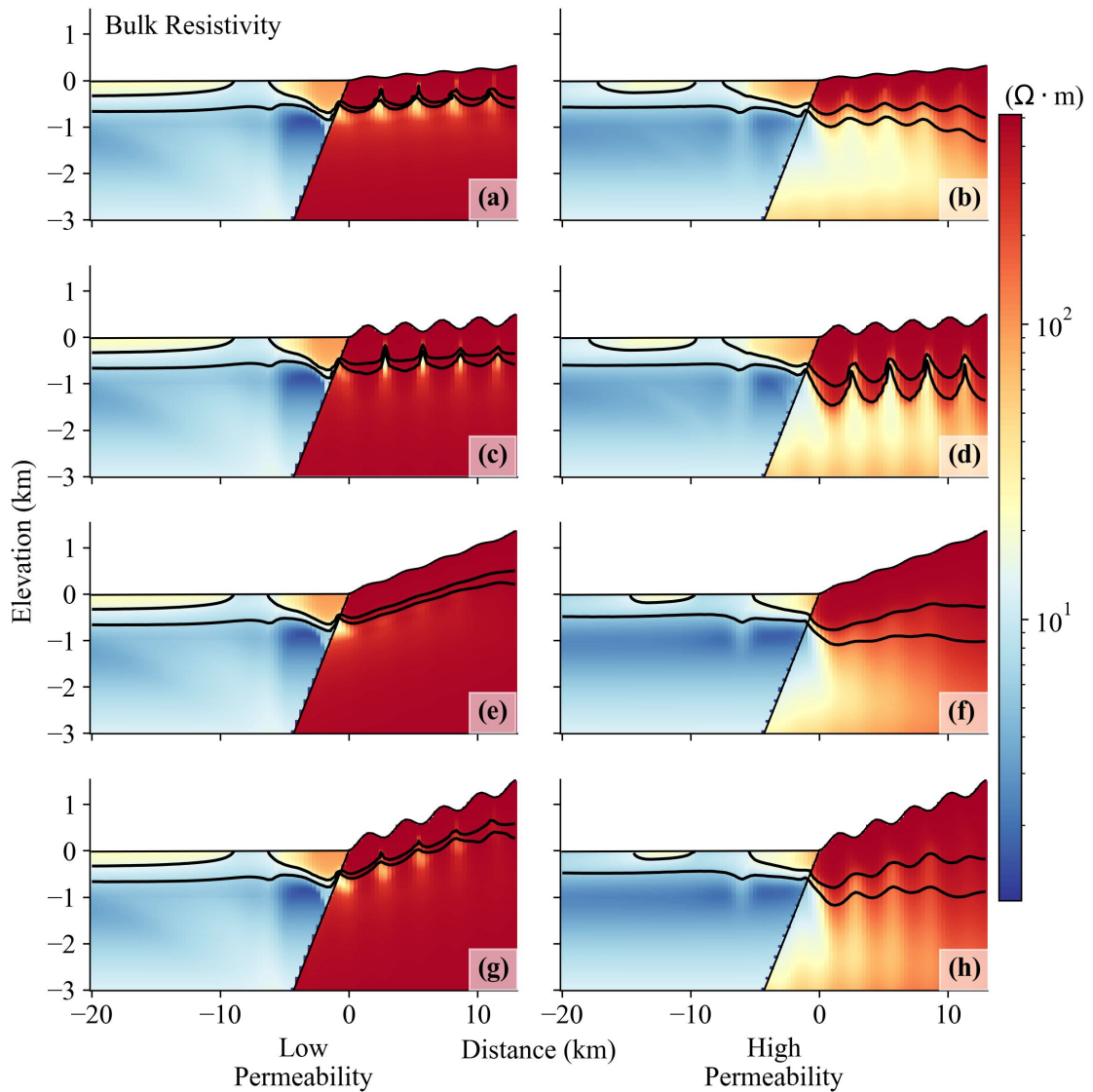


Figure 2.7: Bulk resistivity predicted from the model results using Eq. (2.11) for a high reaction rate ($k_{m0} = 1 \times 10^{-13}$). The first column (panels a, c, e, and g) denotes scenarios with low permeability, and the second column (panels b, d, f, and h) denotes scenarios with high permeability. The rows present different degrees of topographic relief, starting with low relief and low regional slope (panels a and b), high relief and low regional slope (panels c and d), low relief and high regional slope (panels e and f), and high relief and high regional slope (panels g and h). The contours separate freshwater, brackish water, and saline. The resistivity fields show the location of stagnation points present in the mountain block, separating the local and regional flowpaths.

As we mentioned earlier, the accumulation of solutes is linked to dissolution rates. If we reduce the dissolution rates of the system, we reduce the amount of solute buildup close to the stagnation zones (Figure 2.8).

Thus, we also lose our ability to see notable changes in the bulk resistivity of the mountain block and the alluvium, especially in systems with low permeability, where most resistivity values are associated with the solid phase. These results also show the importance of geology, as systems with clay, shales, or other conductive materials could be mistaken for brackish or saline water when the resistivity is larger than $10 \Omega \cdot \text{m}$.

Apparent field electrical resistivity measurements in the Dosit River in China (Jiang et al., 2014) and the Tularosa Basin in New Mexico, USA (Newton and Allen, 2014; Newton and Land, 2016; Orr and Myers, 1986; Zohdy et al., 1969) have shown similar results. In these studies, the authors detected brackish and saline water in areas with low resistivity values and freshwater in areas with high resistivity values. It is worth remembering that the electrical resistivity strongly depends on the solid phase resistivity, porosity, and chemical composition of water (see Figures A.5 and A.6 in the Appendix A illustrate the tight connection between the bulk resistivity and the porous media and the fluid resistivities). Our results suggest that geophysical methods, especially electromagnetic surveys, can serve as a tool for imaging mountain flow separation, where local and regional flow paths can be distinguished given the right solute concentration and geologic conditions.

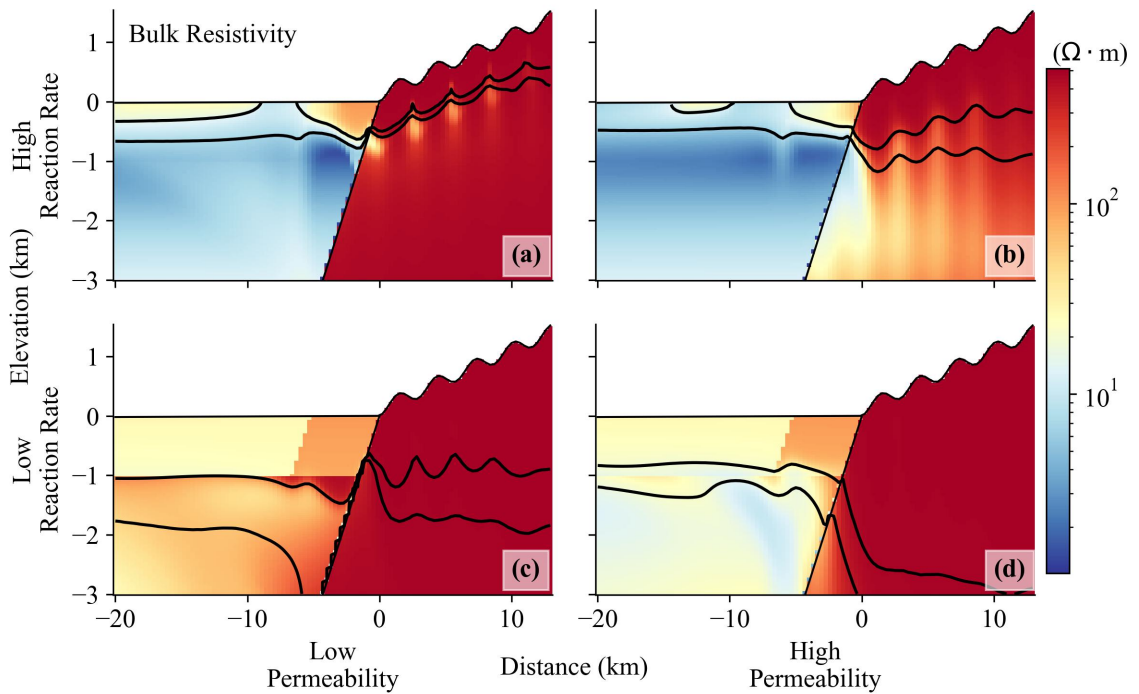


Figure 2.8: Bulk resistivity predicted from the model results using Eq. (11) for low permeability (a and c) and high permeability (b and d), and high dissolution rate (a and b) and low dissolution rate (c and d) scenarios. The contours separate freshwater, brackish water, and saline. Lower dissolution rates cause the loss of contrasting resistivity values within the mountain block.

Although these results are promising, there have not been, to our knowledge, electromagnetic measure-

ments done in mountain systems that address the behavior we see in our simulations, partly due to the difficulty in performing such observations in these settings. Another concern is whether MT field data, which involve electromagnetic diffusion, can resolve the complex resistivity patterns shown in predictions in Figures 2.7-2.8. To that end, we designed a series of experiments on one of the groundwater flow and transport synthetic models, where we performed forward and synthetic data inverse MT simulations for variable receiver spacing densities using MARE2DEM. The main goal of this synthetic inversion approach is to test if MT data can detect and image the resistivity patterns found in the system, especially the Tóthian patterns found in the mountain block.

The forward and inverse models were tested on the model with low permeability and high topographic features (Figure 2.7g). We first performed an inversion using only the solid resistivity (porous media without fluids such as water or air) to see if we get back the general behavior of the system. Next, we changed the number of receivers in the system, first spacing the stations every 200 m, then we used 26 receivers spaced ~ 1.5 km, and lastly, we used the same 26 receivers placed on top of structures we are interested in mapping in the mountain block. In our inversions, we used a unique initial condition of $1 \Omega \cdot \text{m}$. This strategy was reasonable given the good performance of the inversion results, as illustrated by all models reaching the target RMS misfit of one (see Figure A.11 in the Appendix A). In addition, as described in the methods section, we used a telescopic modeling mesh that extends to a depth of 100 km. The idea is to avoid artificial boundary effects by refining the mesh in the area of interest (Figure A.7 in the Appendix A). Furthermore, this depth selection is consistent with the skin depth range of 5-112 km estimated for our analysis. The oversampled inversion can capture the general behavior of the system; however, as expected with this type of inversion problems, the recovered model presents some smearing due to limited resolution Aster et al. (2016); see, for example, the resistivity patterns in the alluvium (Figure 2.9). When fluid is considered in the resistivity calculation, the resistivity values in the alluvial valley change considerably due to a combination of higher porosity and saline water. The oversampled inversion, in this case, can capture the overall changes in resistivity in the alluvium and the location of the small pockets of low resistivity in the mountain block close to the stagnation zones. The inversion also recovers part of the fault's low resistivity values. The inversions show a higher resistivity than the true models at the bottom of the system. These overestimated values can be attributed to a plurality of reasons that include the extent of the MARE2DEM model, the initial conditions for the inversions, the non-uniqueness in the inversion arising from limitations in the inherent resolution of MT data, the Gaussian noise added to the data, along with the impact of the smoothing operator used to stabilize the inversion process. Decreasing the number of receivers (and hence increasing the receiver spacing) hinders the ability of the inversion to delineate some of the low resistivity pockets in the mountain block. However, placing sensors directly over these pockets allows us to characterize some of the structures of interest within

the mountain block (Figure 2.9h). This modeling approach, coupled with optimization methods for sensor placement design Hu et al. (2017); Robertson and Saad (2019) and expert advice, can give the best initial location of receivers in future studies.

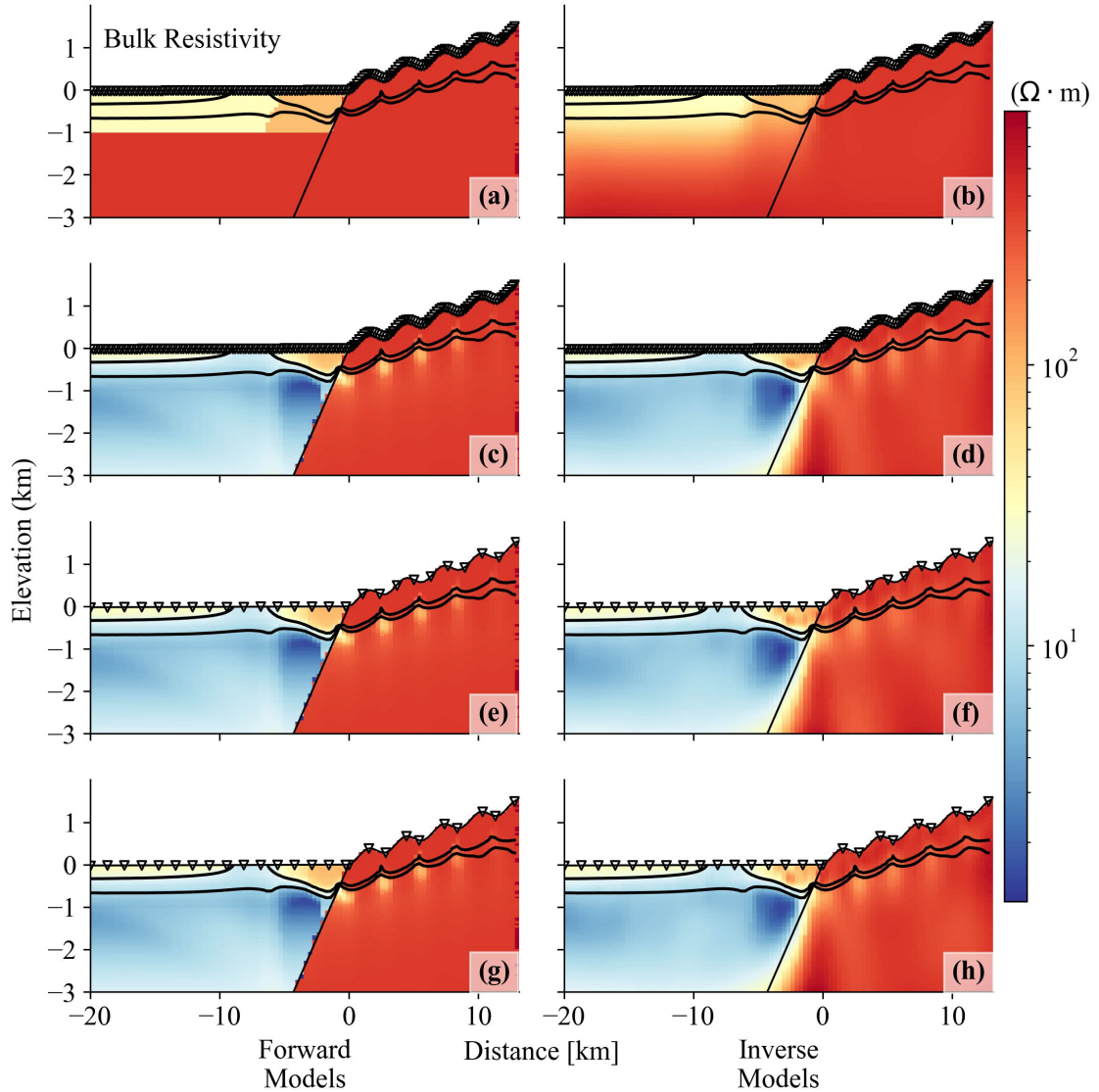


Figure 2.9: Synthetic inversion tests assessing the ability of MT data to image the resistivity of the ground-water system features. The columns denote the forward (a, c, e, and g) and inverse (b, d, f, and h) models. In (a) and (b), the inversion of the idealized system is presented with receivers spacing every 200 meters. The following three rows denote the same system with receivers spacing every 200 meters (c and d), ~ 1.5 km (e and f), and 26 receivers placed on top of structures of interest (g and h). The inverted white triangles show the location of the receivers in each inversion. The low resistivity pockets in the mountain block are captured with good sensor placement.

These results show that an MT survey will be able to capture the overall behavior of the resistivity patterns in the investigated systems, especially the Tóthian patterns in the mountain block. Furthermore, the use of

this method will allow us to see the pockets of saline water produced by the interaction of local, intermediate, and regional flowpaths, thus giving us a sense of how deep local and regional circulation occurs in mountain systems.

2.3.3 Dosit River Resistivity

As an additional analysis, we extracted the N-S cross-sectional area of the Dosit River, China, explored by Jiang et al. (2014), and used the coupled 2D groundwater flow and transport model applied in our idealized simulations to model the bulk resistivity of the system. This area was selected because Jiang et al. (2014) previously performed an MT survey of the region covering 38 km of the cross-section that can be used as a qualitative comparison for the bulk resistivity results.

The model was built using a smoothed cross-section of a Digital Elevation Model (DEM) downloaded from the SRTM dataset of the region (Earth Resources Observation And Science (EROS) Center, 2017). We also used a decaying permeability and porosity with depth, using a surface permeability, $\kappa_s = 5 \times 10^{-15} \text{ m}^2$, a permeability at d_l , $\kappa_{d_l} = 1 \times 10^{-16} \text{ m}^2$, a decaying permeability exponent, $B_d = 3.2$, a surface porosity, $\phi_s = 0.3$, and a first-order reaction rate, $k_{m_0} = 1 \times 10^{-13}$. The cross-section results show an accumulation of solutes near the river discharge, where the groundwater flow coming from both mountain systems converges (see Figure 2.10). This system also separates fresh, brackish, and saline water and gives a contrasting feature on the electrical resistivity patterns, similar to the patterns observed in the idealized case scenarios.

Measurements of total dissolved solutes at the surface of the river give 2,037 mg/L, other measurements near the area show values of concentration higher than a 1,000 mg/L below 150 meters deep and values up to 8,499 mg/L at 1,400 meters deep near the river basement (Jiang et al., 2014), similar to the results of concentration calculated in our simulations. Although the model used does not include a detailed lithology of the site, and the resistivity values obtained are higher than those presented in the article, the resistivity patterns are similar to those obtained by the authors (Figure S1 in the SI). The system shows low resistivity near the river discharge and in the basement, where brackish and saline water is accumulating, and higher resistivity values where freshwater is located. These results reinforce the idea that the low resistivity values present at the system's bottom are likely attributed to variations in the groundwater solute concentration, as the authors also mention.

2.4 Discussion

Our simulations follow the nested nature of hydrologic systems expected in topographic-driven flow through mountainous systems (as presented in Tóth, 2009), with water age and brackish groundwater patterns within the alluvium comparable to the ones found in the Tularosa Basin (Eastoe and Rodney, 2014; Mamer et al.,

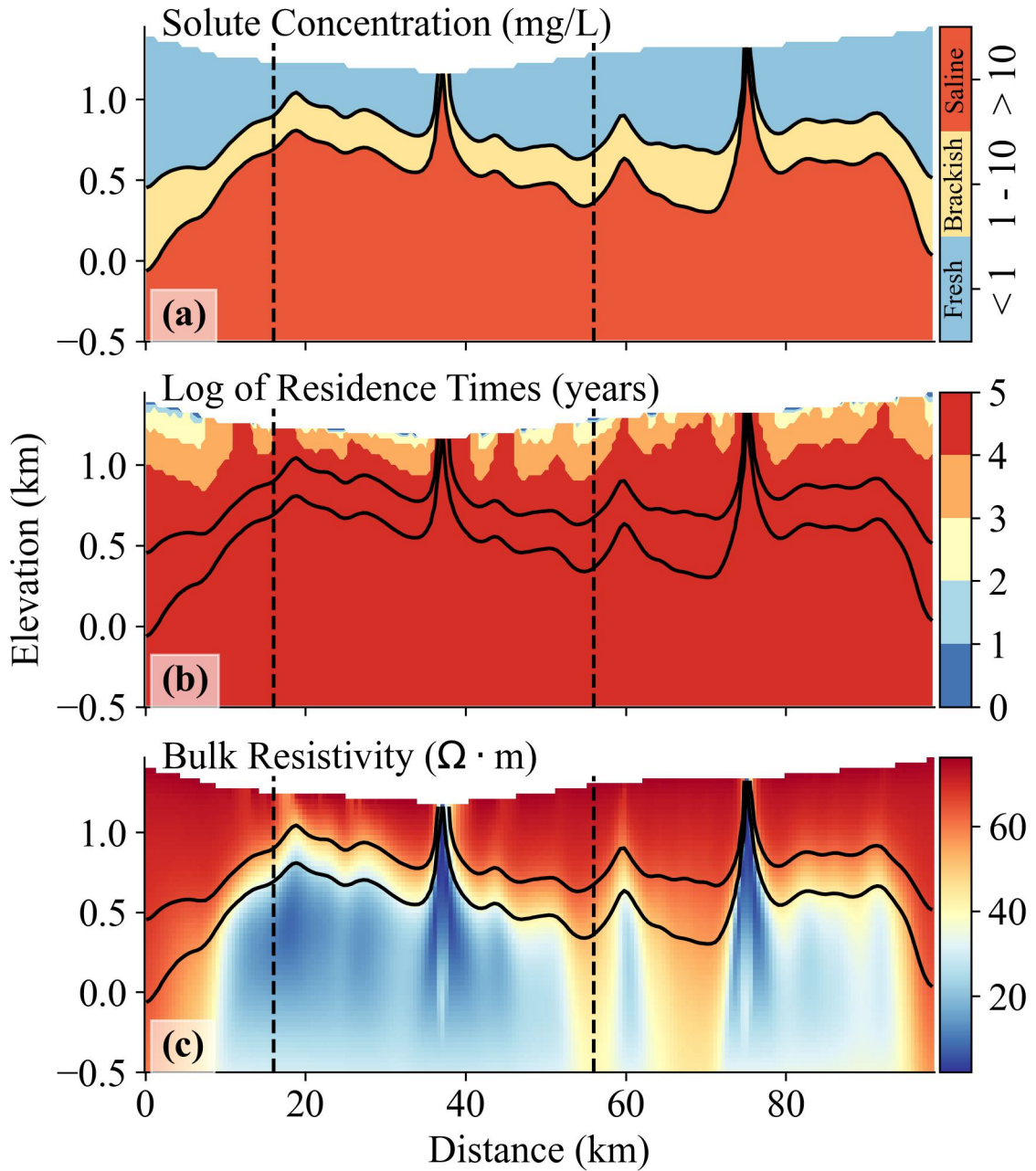


Figure 2.10: Simulations of the Dosit River transect. The panels show the results of solute concentration (a), residence times (b), and bulk resistivity (c). The contours denote the separation of fresh, brackish, and saline groundwater. The vertical dashed lines show the area where Jiang et al. (2014) performed their MT survey (Figure A.1).

2014; Newton and Land, 2016). This range of patterns in the alluvium is a consequence of the mixing between local and regional flowpaths in the mountain block that are sensible to the topographic and geologic

characteristics of the mountain system. In all the simulations explored, we can see the importance of the regional groundwater flow in providing water and solutes to the alluvial aquifers and delineating the depth of local flowpaths in the mountain block. These regional flowpaths reach the alluvium with a high variation in depth, from hundreds of meters to kilometers deep, as other studies have suggested (e.g., Barroll and Reiter, 1990; Carroll et al., 2020; Frisbee et al., 2017; Mailloux et al., 1999; McIntosh and Ferguson, 2021; Pepin et al., 2014).

Our results also suggest that the water chemistry and lithological and geological conditions present in the mountain block provided the best conditions for the use of magnetotelluric surveys to map the nested groundwater circulation patterns. Mapping these patterns is crucial for characterizing the depth and the chemical and weathering processes occurring in the critical zone (Ackerer et al., 2021; Anderson et al., 2007; Condon et al., 2020b; Holbrook et al., 2014; Riebe et al., 2017), and can also provide estimates of the mountain block recharge (Markovich et al., 2019; Wilson and Guan, 2004). Furthermore, inverse modeling of MT surveys, as presented here, could help to constrain the permeability structure of the crystalline basement to depths of up to 10 km, assuming that the survey acquired reliable information at depth and proper hydrogeophysical inversions methods are implemented (e.g., Rubin and Hubbard, 2005; Hinnell et al., 2010; Herckenrath et al., 2012). This is an important opportunity as there is a dearth of deep (> 1km) subsurface permeability information (Carroll et al., 2020; Ingebritsen and Manning, 2010; Manning and Ingebritsen, 1999). The available deep borehole data shows a wide standard deviation for metamorphic and igneous rocks forming the crystalline basement Stober and Bucher (2007). We expect a lateral variation in crystalline basement formation resistivity between the recharge and discharge areas as salinity builds up along the flow path at depths due to water-rock interactions (Specifically fluid inclusion dissolution Nordstrom et al., 1989b,a).

As presented in this study, the contrasting resistivity pattern comes from the interaction between fluid chemistry and the subsurface matrix properties (porosity and resistivity), where brackish and saline water is less resistive. Mapping these “unconventional” water resources is critical in arid and semi-arid environments where the water supply is inadequate to meet the ever-increasing demand (Kang and Jackson, 2016; Qadir et al., 2007; Stanton et al., 2017; Viviroli et al., 2007). Stanton et al. (2017) note that there is about $300 \times 10^3 \text{ km}^3$ of brackish water within the United States. As shallow, young groundwater resources become increasingly depleted, brackish water appears to represent an essential resource for municipalities. In Israel and Spain, desalinated brackish water is currently being used in the production of high-value crops (Aparicio et al., 2017; Ghermandi and Minich, 2017). Similarly, the Tularosa Basin has been proposed as a potential source of water for Las Cruces and Alamogordo, NM, and hosts the U.S. Bureau of Reclamation’s National Inland Desalination Research Center, a critical testbed to assess the potential of brackish aquifers as an “unconventional” resource (Bureau of Reclamation, 2022; Newton and Land, 2016; Stephens, 2015). Mag-

netotelluric field campaigns may be of benefit in identifying deep subsurface brackish water resources within unconventional aquifer systems near the margins of basins.

Our study focuses on an idealized two-dimensional system without exogenous factors affecting the MT surveys. Field MT applications, however, must consider potential complicating factors such as 3D electrical structure and potential distortions arising from any strong near-surface gradients in conductivity (e.g., Ledo, 2006; Ledo et al., 1998). We refer the reader to Chapter 6 in Chave et al. (2012) for a detailed look at these complicating factors in interpreting MT field data and strategies for deployment. Furthermore, additional considerations should account for the cation exchange capacity (CEC) of clays that can play a crucial role in the electrical conduction of shales and shaly sands (Schön, 2015), using other formulations of Archie's law, like the one presented by Waxman and Smits (1968), as found in other studies (Armadillo et al., 2020; Rizzello et al., 2022).

2.5 Conclusions

This work explores the influence of topographic and geologic variations on active groundwater circulation of mountain-to-valley transition systems and discusses optimum electromagnetic geophysical survey designs needed to detect the resultant flow paths. Our simulations show that groundwater ages and solute concentration patterns strongly depend on topography, geological and lithological structures, and dissolution rates. In the mountain block, solutes accumulate near the stagnation zones located in the meeting branches of local, intermediate, and regional flowpaths close to the valleys of the mountain. These solutes are then transported to the alluvial valley, where brackish water is diffused close to the surface in systems with high dissolution rates. This behavior is also observed in the distribution of groundwater ages in the alluvium, where a combination of young water from local flowpaths and old water from regional mountain circulation converged in the simulations. Although our systems are idealized, similar behavior can be seen in the Tularosa Basin in New Mexico, where young freshwater from the Sacramento Mountains system follows local and regional circulation patterns, increasing the water ages and dissolving gypsum that increases the total dissolved solids content in the alluvium (see Figure A.2 and Mamer et al. (2014) and Newton and Land (2016)). These results show the importance of characterizing deep circulation in mountain systems, as water movement through relatively deep systems (> 500 m) transports heat and solutes close to the alluvial valley surface.

The distribution of solutes in the mountain block and the alluvium strongly affects the bulk resistivity patterns. Contrasting resistivity values occur in parts of the system where there is a change from freshwater to saline and where porosity becomes low. These changes in resistivity occur near the stagnation zones in the mountain block, allowing us to map the depth where regional circulation meets the local flowpaths. We hypothesize that rigorous inversion techniques that couple electromagnetic geophysical surveys and ground-

water flow and transport models could allow us to isolate the effects of nested flow processes in mountain systems. These techniques can also be used to estimate hydraulic parameters and state variables of these systems where information is scarce (Carroll et al., 2020). Note that this contrast of resistivity values can only be detected in systems with considerably high dissolution rates.

Lastly, we perform an idealized magnetotelluric inversion in one of the resulting scenarios to determine if electromagnetic surveys can detect resistivity patterns. Our results show that realistic low-noise MT data and 2D inversion can capture the depth and overall extent of the low resistivity structure in the mountain block. Our results also show that even sparsely spaced receivers (1.5 km spacing) can recover the low resistivity zones when carefully positioned with respect to local topographic high and low points. Our results give us confidence that carefully planned and executed MT measurements would be able to capture these structures in real systems. It is worth mentioning that the complexity of natural mountain systems can produce 3D circulation patterns that are not captured by our idealized cross-sectional scenarios. Future modeling and field studies should explore the potential implications three-dimensional topographic structure on the characterization of subsurface resistivity patterns with MT techniques.

CHAPTER 3

Exploring The Multiscale Nature of Flow in the Sacramento Mountains and Their Influence on Brackish Groundwater Resources Distribution in the Tularosa Basin in New Mexico

This chapter is a manuscript in preparation that will be submitted to Water Resources Research. Gonzalez-Duque, D., Gomez-Velez, J. D., Person, M. A., Kelley, S., & Lucero, D. (2023). Exploring The Multiscale Nature of Flow in the Sacramento Mountains and Their Influence on Brackish Groundwater Resources Distribution in the Tularosa Basin in New Mexico (In Preparation). Water Resources Research.

Abstract

In the United States, the use of brackish water for municipal water supplies is growing at a near-exponential rate. Using well geochemistry data from sedimentary basin aquifers and unconsolidated deposits, the US Geological Survey estimates that the nation's brackish water resources are on the order of 3×10^5 km³, providing an unconventional water resource with the potential to offset the depletion of fresh aquifers in arid and semi-arid environments. With this in mind, new desalination plants are being constructed to extract these resources. One of them is located in Alamogordo, a city within the Tularosa Basin in New Mexico. Geochemical data from wells within the Tularosa Basin have documented the presence of saline water (TDS between 3,400 to 5,900 mg/L) at depths of 80 meters, likely explained by the dissolution of Gypsum. Carbon-14 measurements in the area show millennia-old water, suggesting that the groundwater circulation recharging these aquifers through the Sacramento Mountains is likely greater than 1 km deep, flowing through fractured, permeable crystalline basement rocks. In this study, we used groundwater flow and transport models to assess the circulation patterns and crystalline basement permeability for the Tularosa Basin. We validated our results with the sites' current geochemical and water age data. We also calculated the effective resistivity patterns using the simulated information and petrophysical relationships. Our models provide a general framework for characterizing groundwater circulation depth through the Tularosa Basin's mountain blocks. Furthermore, the simulated resistivity patterns produced by the movement of solutes and heat in the groundwater system can open the door for future geophysical exploration in these regions to assess the availability of brackish groundwater resources and gain a mechanistic understanding of the multiscale nature of flow in the Sacramento Mountains.

3.1 Introduction

Water resources are essential for life and socioeconomic development. Primary uses include agriculture, energy generation, and industrial activities. Their availability is given by the balance between water storage and recharge fluxes that are affected by natural and anthropogenic stresses, such as climate change, population growth, and land use (Qadir et al., 2007; Roy et al., 2012; Vorosmarty, 2000). Projections in population growth suggest that water supply in water-deficit areas (i.e., arid and semi-arid) is not adequate to meet the increasing demand (Pimentel et al., 1999; Qadir et al., 2007; Rijsberman, 2006). In the southwestern U.S., this problem is compounded by the fact that dryer conditions are becoming more likely in the 21st century due to climate change forcings, which increases the water supply risk index to conditions between moderate to extreme (see Figure 3.1) (Cayan et al., 2010; Seager et al., 2007, 2017; Stanton et al., 2017; The National Drought Mitigation Center, 2019; Roy et al., 2012).

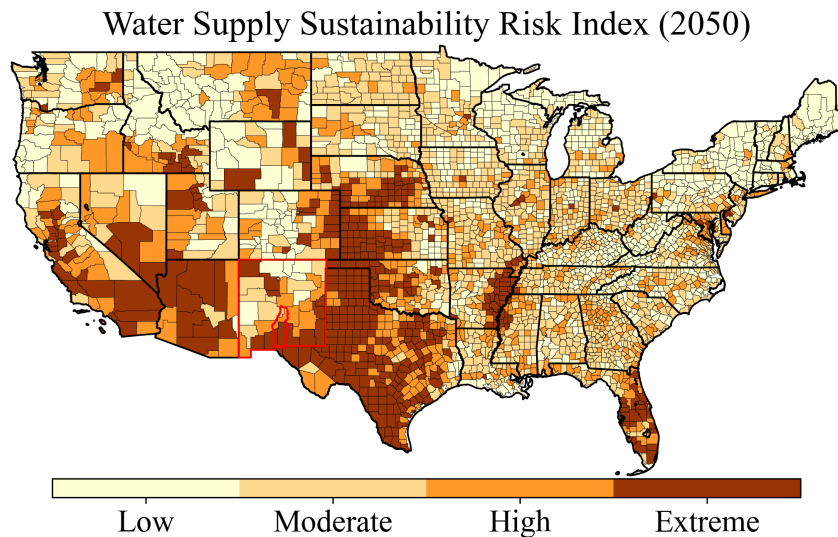


Figure 3.1: Water Supply Sustainability Risk Index for the year 2050. Roy et al. (2012) calculates the index values based on the development of renewable water supply, the susceptibility to drought, the growth in water withdrawal, the increased need for storage, and the groundwater use. The New Mexico state and the Tularosa Basin are colored with red contours.

Finding solutions to this problem involves the sustainable use of unconventional water resources. These resources are defined as water that comes as a by-product of specialized processes or water that needs a suitable pre-use treatment or unique technologies to collect or access it (UNU-INWEH, 2019), one of them is brackish groundwater reservoirs. By definition, brackish groundwater resources have total dissolved solids (TDS) content between 1,000 to 10,000 mg/L (Stanton et al., 2017), which can be used for consumption

after a desalination process (Graham, 2015; Ahdab and Lienhard, 2021). In the United States, the size of this unconventional resource has been estimated to be on the order of $3 \times 10^5 \text{ km}^3$ (Stanton et al., 2017). Thus, the adoption of this resource has been growing exponentially with new technical and economic considerations (Person and Sazeed, 2022), and the inclusion of new regulations for its use (e.g., Buono et al., 2016).

The exploration and evaluation of brackish groundwater systems have been the focus of several studies that show the potential use of these resources for municipalities in New Mexico (i.e., Huff, 2004; Graham, 2015; Land, 2016; Land and Timmons, 2016; Newton and Land, 2016), Arizona (i.e., McGavock and Montgomery, 2016; Cáñez, 2019), Texas (i.e., Andrews and Croskrey, 2019; Croskrey et al., 2019; Robinson et al., 2019), and other states across the conterminous US (i.e., Anning et al., 2018; Stanton and Dennehy, 2017). As an example, the Tularosa Basin, New Mexico, contains several million cubic meters of groundwater in basin-fill aquifers (Land, 2016), where more than 90% of this resource is estimated to be saline due to the dissolution of Gypsum present in the area (McLean, 1970; Orr and Myers, 1986; Land, 2016; Newton and Land, 2016). The remaining fresh groundwater aquifers are used by the municipalities of Alamogordo, Carrizozo, Tularosa, La Luz, and other small communities, located within the basin that are experiencing noted declines in water levels and a diminished water quality (Mamer et al., 2014).

In the Tularosa Basin, the primary and secondary sources of recharge for the alluvial aquifers come from runoff from ephemeral and perennial mountain streams that infiltrate into adjacent basin sediments, and the regional groundwater flow from the Sacramento Mountains on the east and the San Andres Mountains on the west (Mamer et al., 2014; Land, 2016; Huff, 2002). Part of the water from the streams that reach the basin-fill evaporates, depositing dissolved solids in the basin-fill playas, which increases the saline content of the water contained in these low-permeability layers (McLean, 1970; Land, 2016). This increase in saline content in the playas eventually increases the TDS content of the water that reaches the groundwater aquifers. Considering the latter, we can see that this basin can be regarded as a critical testbed for assessing brackish groundwater resources in the area. It also hosts the U.S. Bureau of Reclamation's National Inland Desalination Research Center, located in the city of Alamogordo, NM, that does research in desalination techniques for public water supply (Bureau of Reclamation, 2022).

The use of unconventional water resources in the Tularosa Basin is a challenging endeavor that requires the study of a handful of factors in order to potentially offset the depletion of freshwater resources. The water sources, recharge rates, and water quality are some of these important factors. Previous studies on the regional hydrogeology of sections within the basin have shown that the primary source of water comes from the Sacramento Mountains, where water ages increase with increasing distance from the mountain-front (Mamer et al., 2014; Eastoe and Rodney, 2014; Huff, 2002). Recharge rates estimated for the northeastern part of the basin are of the order of $228,000 \text{ m}^3/\text{day}$, where 66% of the water is calculated to come from streams and

33% from deeper flowpaths or mountain-block recharge (Mamer et al., 2014). Other studies have looked into the water quality in wells located in the basin-fill and have shown that the TDS content in the water increases from the mountain-front to the middle of the basin-fill (Orr and Myers, 1986; Newton and Allen, 2014; Land, 2016). Finally, simulations in the area show the flow of water coming from the Sacramento Mountains recharge the basin-fill and project a decline in water levels of 15 meters in the city of Alamogordo for the year 2040 (Huff, 2005). The water ages and quality gradients between the mountain-front and the alluvium suggest that regional water sources from the Sacramento Mountains could move considerable amounts of water, energy, and solutes that reach the deeper basin-fill aquifers.

Previous idealized simulations done in mountain-to-valley transition systems show how topographical gradients in the mountain block move considerable amounts of water, energy, and solutes from regional sources to the alluvium and how Magnetotelluric (MT) surveys could be used to describe the interaction of flowpaths in within the mountain system (Gonzalez-Duque et al., 2024a) (Chapter 2 in this document). This work builds on Gonzalez-Duque et al. (2024a) and performs numerical simulations on a west-to-east cross-section of the Tularosa Basin (see Figure 3.2) to assess the circulation patterns and crystalline basement permeability of the Sacramento Mountains and their influence on the brackish groundwater resources reaching the alluvium. We also used the simulation results to calculate resistivity patterns, allowing the mapping of brackish and saline groundwater in the alluvium and the interaction of flowpaths within the Sacramento Mountains. This work provides a general framework for characterizing the depth of circulation in the Sacramento Mountains and the sources and distribution of solutes in the basin fill.

3.2 Study Area

This work focuses on groundwater flow and the transport of solutes and heat in a west-to-east cross-section of the central portion of the Tularosa Basin (right Figure 3.2). As presented in Newton and Land (2016), the basin is bounded on the west by the Oscura, San Andres, and Franklin Mountains and on the east by the Sacramento Mountains and Otero Mesa, covering a drainage area of around 17,000 km. Within the basin, we can find the communities of Alamogordo, La Luz, Tularosa, Oscuro, and Carrizozo, which rely heavily on groundwater for public water supply, livestock, commercial, and industrial use (Magnuson et al., 2019). The cross-section selected for the study passes through, from west to east, the San Andres Mountains, White Sands National Monument (WSNM), the Holloman Air Force Base, the city of Alamogordo, and the Sacramento Mountains (left Figure 3.2).

The Tularosa Basin was formed around 30 million years ago from periods of tectonic activity associated with the Rio Grande rift and extensive erosion (U.S. National Park Service, 2020). The complex structure of the basin consists of two half-grabens that are bounded on the west by the San Andres fault zone, on the east

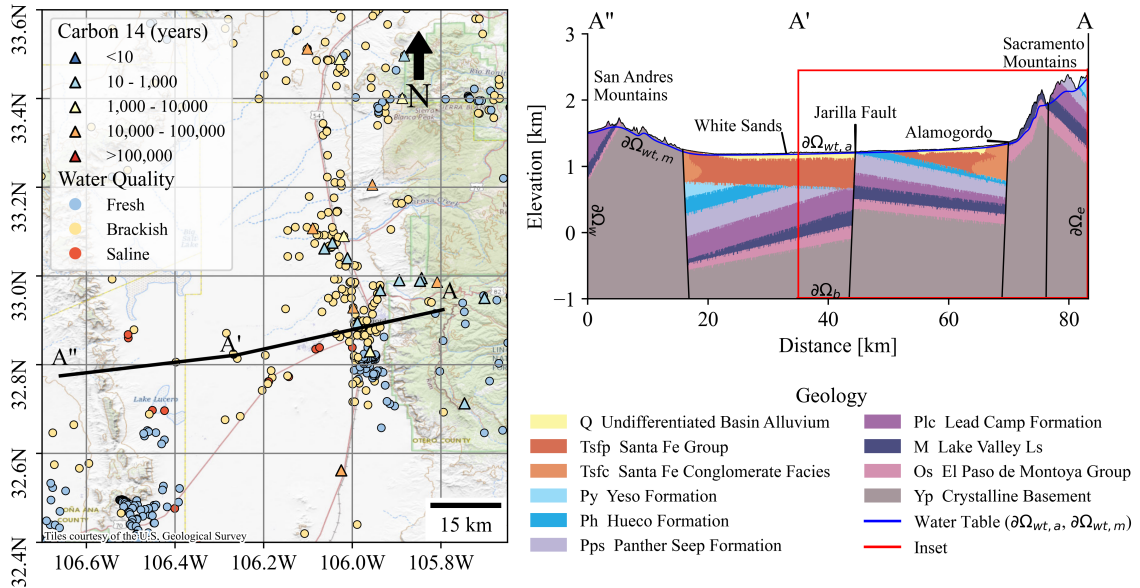


Figure 3.2: (Left) Tularosa Basin area with water quality and Carbon-14 measurements. The solid black line shows the (right) cross-section A-A'-A'' geology (based on Newton and Land, 2016). The blue line denotes the water table used in the simulations, and the red square shows the inset of the cross-section shown in the results. The conceptual model used in the simulations is a replica of this cross-section. It is bounded by the west boundary ($\partial\Omega_w$), the east boundary ($\partial\Omega_e$), the water table boundary in the alluvium ($\partial\Omega_{wt,a}$) and in the San Andres and Sacramento Mountains ($\partial\Omega_{wt,m}$), and the basement boundary ($\partial\Omega_b$). The water quality measurements were provided by the New Mexico Environment Department (NMED), the New Mexico Bureau of Geology and Mineral Resources (NMBGMR), and the US Geological Survey (USGS). The information was downloaded from the NMBGMR interactive map (NMBGMR et al., 2016). The Carbon-14 age measurements were taken from Eastoe and Rodney (2014) and Mamer et al. (2014).

by the Alamogordo fault zone, and in the middle by the Jarilla fault zone (Lozinsky and Bauer, 1991). The geology of the basin varies extensively from north to south. A stratigraphy study in the east-front of a south-center section in the San Andres Mountains shows Mississippian rocks of the Lake Valley Formation close to the top of the mountain that is followed east-ward by Cambrian and Ordovician strata with El Paso and Montoya groups, to end with Precambrian outcrops present in large areas of the east-bounding escarpment of the San Andres mountain range (Kottlowski, 1975). On the south-west, the Sacramento Mountains geology is characterized by highly faulted and fractured Paleozoic sedimentary rocks that include the San Andres, Yeso, Hueco, and Abo Formations (Kelley et al., 2014b; Koning et al., 2014; Newton and Land, 2016). These rocks contain significant amounts of carbonates and evaporites, which impact the water chemistry in the area (Newton and Land, 2016). The basin is estimated to have a basin-fill thickness of around 900 to 1,200 m near Tularosa, composed of alluvial-fan, piedmont-slope, alluvial-flat, and playa deposits of the Santa Fe Group that become finer with increasing distance from the mountain front (Mamer et al., 2014; Newton and Land, 2016). In the western region of the basin, we can find the White Sands gypsum dune field that

sits on top of recrystallized gypsum deposits and lacustrine deposits, mainly composed of clays (Orr and Myers, 1986). As can be seen from the geology, the water chemistry within the basin is highly variable, with freshwater moving through different highly permeable sediments close to the mountains and old brackish and saline water residing in finer sediments that are rich with carbonates and evaporites, primarily present in the Permian layers (Newton and Land, 2016).

The region is a semi-arid climate environment with mean annual precipitation ranging from 254 mm in the basin's center to 635 mm in the surrounding mountains (McLean, 1970). The precipitation is maximum during the summer monsoonal season from July to September and decays significantly during winter from January to March (Bourret, 2015) with a maximum during the summer monsoonal season from July to September and decays significantly during winter from January to March (Bourret, 2015). The potential evapotranspiration (PET), estimated with the modified Thornthwaite method, is around 430 mm in the basin's center, which is larger than the precipitation in the area (Bourret, 2015). The estimated mean annual recharge to the basin-fill ranges from 143,000 to 228,000 m³/day (Huff, 2005; Mamer et al., 2014). This recharge is estimated to be only 4 to 8.9% of the precipitation, and it is primarily supplied by perennial and ephemeral streams and regional flows from the Sacramento Mountains; the rest of the water leaves through evapotranspiration, runoff, and public use (Huff, 2005; Mamer et al., 2014). Water-level interpolations show groundwater flowing from the northeastern portion of the basin to the southwestern region (see Figure B.1 in Appendix B). The construction of the water table used in our simulation is interpolated between water-level maps from the Sacramento Mountains (Land et al., 2014), the basin-fill (Embid et al., 2011), and the San Andres Mountains (Horne, 2019). The interpolated water table had issues in the cross-section in the San Andres Mountains, so we corrected these values with the DEM.

3.3 Methods

We explore the groundwater system in an east-to-west cross-section of the Tularosa Basin with a conceptualized geology of the cross-section based on Newton and Land (2016) (left in Figure 3.2). The system is bounded by the alluvial and mountain interpolated water tables at the top ($\partial\Omega_{wt,a}$, $\partial\Omega_{wt,m}$), the west and east boundaries ($\partial\Omega_w$, $\partial\Omega_e$), and the basement boundary at the bottom ($\partial\Omega_b$). The conceptualization includes the San Andres Fault on the west with a dip angle of 60° eastward, the Jarilla Fault in the middle with a dip angle of 60° westward, the Alamogordo fault zone with a dip angle of 60° westward, and the Sacramento fault with a dip angle of 80° westward.

The following subsections describe the physical and mathematical conceptualization of the groundwater flow and transport of heat and solutes in the cross-section of the Tularosa Basin.

3.3.1 Groundwater Flow

In our simulations, we model a two-dimensional heterogeneous and anisotropic groundwater flow system that is similar to the one explored in Gonzalez-Duque et al. (2024a) (Chapter 2). First, for groundwater flow, we solved the following governing equation (Bear, 1972),

$$\begin{aligned}
0 &= -\nabla \cdot (\rho \mathbf{q}) \quad \text{with} \quad \mathbf{q} = -\frac{\kappa \rho_f g}{\mu_f} \nabla \left(\frac{p}{\rho_f g} - z \right) & (3.1) \\
p(\mathbf{x}, t = 0) &= \rho_f g [wt(x) - z] \\
p(x, z = wt(x)) &= 0 \quad \text{on} \quad \partial\Omega_{wt,a} \wedge \partial\Omega_{wt,m} \\
p(x = 0, z) &= wt(x = 0) - z \quad \text{on} \quad \partial\Omega_w \\
p(x = L_e, z) &= wt(x = L_e) - z \quad \text{on} \quad \partial\Omega_e \\
-\mathbf{n} \cdot \rho_f \mathbf{q} &= 0 \quad \text{on} \quad \partial\Omega_b
\end{aligned}$$

where \mathbf{q} is the Darcy's flux [LT^{-1}], $\mathbf{x} = [x, z]$ is the coordinate vector [L], $\kappa = [\kappa_x, \kappa_z]$ is the diagonal permeability tensor [L^2] with components in x and z , ρ_f is the water density [ML^{-3}], μ_f is the dynamic viscosity of water [$\text{ML}^{-1}\text{T}^{-1}$], g is the gravity acceleration constant [LT^{-2}], p is pressure [$\text{ML}^{-1}\text{T}^{-2}$], \mathbf{n} is an outward vector normal to the boundary [-], $wt = f(x)$ is the interpolated water table surface through the cross-section, and L_e is the length of the cross-section. We assumed steady-state conditions with a constant water table elevation as the top boundary ($\partial\Omega_{wt,a}$ and $\partial\Omega_{wt,m}$), constant head boundary on the west and east boundaries ($\partial\Omega_w$ and $\partial\Omega_e$), and a no-flow condition on the basement boundary ($\partial\Omega_b$).

The geologic layers discretize the homogeneous permeability (κ_x and κ_z) in the basin fill and have an anisotropy of $\eta = 10$, such that $\kappa_x = \eta \kappa_z$. In the basement geologic layer and the San Andres and Sacramento Mountains, the permeability decays with depth and has an anisotropic of 10 in the first kilometer. The model used to describe the decay of permeability with depth is the same piecewise equation as the one used in Gonzalez-Duque et al. (2024a) (Chapter 2) that is based in Saar and Manga (2004),

$$\kappa_z = \begin{cases} \kappa_s \exp[-A_s(wt(x) - z)], & \text{for } wt(x) - z < d_l \\ 10^{-A_d} \left(\frac{wt(x) - z}{D_d} \right)^{-B_d}, & \text{for } wt(x) - z \geq d_l \end{cases} \quad (3.2)$$

where κ_s is the permeability at the surface, A_s [m^{-1}] and B_d [-] are the decaying exponents that represent the decreased rate of permeability with depth, $d_l = 1$ km is a defined depth that separates the shallow from the deep systems, $D_d = 1$ km, and A_d can be calculated as follows,

$$A_d = B_d \log_{10} \left[\frac{\kappa_s \exp -A_s d_l}{d_l^{B_d}} \right] \quad (3.3)$$

Similar to Gonzalez-Duque et al. (2024a), the value of $A_s = d_l^{-1} \log(\kappa_s) - \log(\kappa_{d_l})$, where κ_{d_l} is the permeability at the distance d_l . We explored a range of permeability values used in previous simulations of the area (Huff, 2005; Bourret, 2015), and values explored in other systems (Saar and Manga, 2004; Ingebritsen and Manning, 2010; Gonzalez-Duque et al., 2024a).

3.3.2 Transport of Heat and Solutes Model

We used similar models as the ones used in Gonzalez-Duque et al. (2024a) (Chapter 2) to simulate the transport of heat and solutes in the groundwater system. The model for the transport of heat uses the following equation (Nield and Bejan, 2013),

$$\begin{aligned} 0 &= -\nabla \cdot (K_{eff} \nabla T) - \rho_f C_{p,f} \mathbf{q} \cdot \nabla T & (3.4) \\ T(\mathbf{x}, t = 0) &= T_{profile} = T_{wt}(x) + \frac{q_{Hb}}{K_{eff}} [Z_s(x) - z] \\ T(\mathbf{x}) &= T_{wt}(x) \text{ on } \partial\Omega_{wt,a} \wedge \partial\Omega_{wt,m} \\ \mathbf{n} \cdot K_{eff} \nabla T &= 0 \text{ on } \partial\Omega_w \wedge \partial\Omega_e \\ \mathbf{n} \cdot K_{eff} \nabla T &= q_{Hb} \text{ on } \partial\Omega_b \end{aligned}$$

where T is temperature [Θ], $K_{eff} = \phi K_f + (1 - \phi) K_s$ is the effective thermal conductivity [$\text{MLT}^{-3}\Theta^{-1}$] with porosity ϕ ; $C_{p,f}$ is the specific heat of water [$\text{ML}^{-1}\text{T}^{-2}\Theta^{-1}$], $T_{profile}$ is the initial temperature in the groundwater system, $T_{wt} = T_a - \Gamma wt(x)$ is the temperature along the water table boundary ($\partial\Omega_{wt,a}$ and $\partial\Omega_{wt,m}$) that is assumed to decrease linearly from the temperature in the alluvium (T_a) with an atmospheric lapse rate (Γ); and q_{Hb} is the basal heat flux imposed along the basement boundary ($\partial\Omega_b$). The system has outflow boundaries at the west and east boundaries ($\partial\Omega_w$ and $\partial\Omega_e$).

Similar to permeability, the porosity (ϕ) is discretized in the geologic layers within the basin fill and decays with depth in the basement geologic layer and in the San Andres and Sacramento Mountains. In the depth-decaying model, we assumed that $\kappa_z/\kappa_s = (\phi/\phi_s)^m$, with ϕ_s being the porosity at the surface and $m = 2$ being a medium and process-dependent coefficient (Bernabé et al., 2003; Cardenas and Jiang, 2010; Jiang et al., 2010; Gonzalez-Duque et al., 2024a). The resulting model for the porosity is the following,

$$\phi(x, z) = \begin{cases} \phi_s \exp \left[-\frac{A_s(Z_s(x)-z)}{m} \right], & \text{for } wt(x) - z < d_l \\ \phi_s \left(\frac{10^{-A_d}}{\kappa_s} \right)^{\frac{1}{m}} \left(\frac{wt(x)-z}{D_d} \right)^{-B_d/m}, & \text{for } wt(x) - z \geq d_l \end{cases} \quad (3.5)$$

To simulate the transport of solutes, we used the following equation (Fetter, 2001),

$$\begin{aligned} 0 &= -\nabla \cdot (\mathbf{D}\nabla c) - \nabla \cdot (\mathbf{q}c) + R & (3.6) \\ c(\mathbf{x}, t = 0) &= c_{max} \\ c(18.5 \leq x \leq 48 \text{ km}, z) &= c_{0,WS} \text{ on } \partial\Omega_{wt,a,in} \\ c(48 \leq x \leq 73 \text{ km}, z) &= c_{0,Al} \text{ on } \partial\Omega_{wt,a,in} \\ c(\mathbf{x}) &= c_{0,m} \text{ on } \partial\Omega_{wt,m,in} \\ \mathbf{n} \cdot (\mathbf{D}\nabla c) &= 0 \text{ on } \partial\Omega_{wt,m,out} \wedge \partial\Omega_{wt,a,out} \wedge \partial\Omega_w \wedge \partial\Omega_e \\ \mathbf{n} \cdot (\mathbf{D}\nabla c - \mathbf{q}c) &= 0 \text{ on } \partial\Omega_b \end{aligned}$$

where c is the volumetric concentration of salinity (NaCl) [ML^{-3}] and $D = D_{i,j}$ is the dispersion-diffusion tensor [L^2T^{-1}] defined as (Bear, 1972),

$$D_{i,j} = \alpha_T |\mathbf{q}| \delta_{i,j} + (\alpha_L - \alpha_T) \frac{q_i q_j}{|\mathbf{q}|} + \frac{\phi}{\xi_m} D_m \quad (3.7)$$

with transversal dispersivity (α_T) and longitudinal dispersivity (α_L) [L], effective molecular self-diffusion coefficient (D_m) [L^2T^{-1}], fluid tortuosity based in the Millington and Quirk (1961) model ($\xi_m = \phi^{-1/3}$) [-], and the kronecker delta function ($\delta_{i,j}$). The first-order reaction solute mass rate of dissolution ($R = k_{mt}(c_{max} - c)$) used in equation (3.6) is a solute source term that mimics the buildup of salinity due to fluid-rock interactions (Lemieux et al., 2008a; Provost et al., 2012) with a maximum allowable concentration of c_{max} and a temperature-dependent mass transfer reaction rate (k_{mt}) [T^{-1}]. The k_{mt} can be described through the Arrhenius expression (Langmuir, 1997),

$$k_{mt} = A_0 \exp \left(-\frac{E_0}{R_0 T} \right) \quad (3.8)$$

where A_0 is a temperature-independent coefficient [T^{-1}], E_0 is the activation energy [L^2MT^{-2}], and R_0 is the ideal gas constant [$\text{ML}^2\text{T}^{-2}\Theta^{-1}$]. Similar to Gonzalez-Duque et al. (2024a) (Chapter 2), we calculate the value of $A_0 = k_{mt_0} \exp(E_0/(R_0 T))$ using a value of $T = 165^\circ\text{C}$ and setting values of k_{mt_0} similar to the ones used in Lemieux et al. (2008b) for all the geologic layers but the one in the Yeso Formation (Py in Figure 3.2)

where we use the dissolution rate for gypsum $k_{m0} = 2 \times 10^{-6} \text{ s}^{-1}$ (Langmuir, 1997). For the simulations, we start with a saturated system ($c = c_{max}$) and let the simulations flush the excess of solutes. We used an open boundary condition for the water table boundaries, where we divided the system into three regions: the San Andres and Sacramento Mountains, the White Sands region ($48 \leq x \leq 73 \text{ km}$), and the Alamogordo region ($18.5 \leq x \leq 48 \text{ km}$). If the water enters the system, we impose a different solute concentration for each region. For instance, the San Andres and Sacramento Mountains have a set solute concentration ($c_{0,m}$) on the mountain water table boundary ($\partial\Omega_{wt,m}$) of 9.98 mg/L. Similarly, the White Sands and Alamogordo regions have a set solute concentration of $c_{0,WS} = 5,000 \text{ mg/L}$ and $c_{0,Al} = 3,000 \text{ mg/L}$ on the alluvial water table boundary ($\partial\Omega_{wt,a}$), these values were obtained from previous measurements in the areas (Newton and Allen, 2014; Newton and Land, 2016; NMBGMR et al., 2016). The system has outflow west and east boundary conditions ($\partial\Omega_w$ and $\partial\Omega_e$) and a no-flux condition on the basement boundary ($\partial\Omega_b$).

3.3.3 Water Age Model

To model the water age distribution ($\psi(\mathbf{x}, \tau)$) [T^{-1}] we used the same approach described in Gonzalez-Duque et al. (2024a) that is based in Ginn (1999) and Gomez-Velez (2013). In this approach, we simulate the advection-diffusion equation to obtain the cumulative age distribution ($\Psi(\mathbf{x}, \tau)$; [-]) as follows,

$$\begin{aligned} \frac{\partial(\phi\Psi)}{\partial\tau} &= \nabla \cdot (\mathbf{D}\nabla\Psi) - \nabla \cdot (\mathbf{q}\Psi) & (3.9) \\ \Psi(\mathbf{x}, t = 0) &= 0 \\ \Psi(\mathbf{x}, t) &= H(t) \text{ on } \partial\Omega_{wt,m,in} \wedge \partial\Omega_{wt,a,in} \\ \mathbf{n} \cdot (\mathbf{D}\nabla\Psi) &= 0 \text{ on } \partial\Omega_{wt,m,out} \wedge \partial\Omega_{wt,a,out} \\ \mathbf{n} \cdot (\mathbf{D}\nabla\Psi - \mathbf{q}\Psi) &= 0 \text{ on } \partial\Omega_w \wedge \partial\Omega_e \wedge \partial\Omega_b \end{aligned}$$

where τ ($\tau \geq 0$) is age [T] and $H(t)$ is the Heaviside step function. We assumed that water entering through the water table boundary is young water ($\Psi(\mathbf{x}, \tau) = 1$), and the water leaving the water table boundary can be described by an advective boundary condition. Similar to the solute model, we use outflow boundaries at the west and east ($\partial\Omega_w$ and $\partial\Omega_e$) and a no-flux condition on the basement boundary ($\partial\Omega_b$). We can calculate a breakthrough curve at each point in the domain. As Mamer et al. (2014) and Eastoe and Rodney (2014) point out, the water in the Tularosa Basin is a mixture of old and young water. We estimated the water age at each location in the system by setting a threshold of 60% in the cumulative age distribution; that is, if the water age is 100 years, it is because at least 60% of the water located there has an age of 100 years or more.

3.3.4 Bulk Resistivity Model

The simulations provide the spatial distribution of solute concentration and temperature within the domain. We can use this information to calculate the Glover's bulk electrical resistivity ($\rho_{r,bulk} = 1/\sigma_{r,bulk}$, [ML³T⁻³A⁻²]) of the system using equation (3.10) (Glover et al., 2000).

$$\sigma_{r,bulk} = \sigma_{r,f}\phi^{m_r} + \sigma_{r,s}(1 - \phi)^{p_r} \quad (3.10)$$

where $\sigma_{r,f}$ is the fluid electrical conductivity, $\sigma_{r,s}$ is the solid electrical conductivity, $m_r = 2$ is the cementation exponent, and $p_r = \log(1 - \phi)^{m_r} / \log(1 - \phi)$. The fluid electrical conductivity ($\sigma_{r,f}$) is calculated using the following equation (Sen and Goode, 1992),

$$\sigma_{r,f} = (5.6 + 0.27T - 1.5 \times 10^{-4}T^2)M - \frac{2.36 + 0.099T}{1.0 + 0.214M}M^{3/2} \quad (3.11)$$

where M is the molality, and the temperature (T) is in Celsius. Further information about other fluid resistivity equations can be found in Gonzalez-Duque et al. (2024a) (Chapter 2 Section 2.2.4).

3.3.5 Scenarios To Explore

In this work, we explored three scenarios for permeability that look into the variability of flows in the mountain block and how they recharge the basin fill (Table 3.1). In the first scenario, we set the permeability to have similar values in the basin-fill and basement to the ones reported in the simulations done by Huff (2005) and Bourret (2015). It is worth noting that the 3D model done by Huff (2005) and Bourret (2015) did not simulate the flow within the San Andres or the Sacramento Mountains, and assumed a no-flow boundary condition in the contact between the basin fill and the surrounding mountains, arguing that the hydraulic conductivity in the mountain block is considerably lower than the one in the basin-fill. However, Gonzalez-Duque et al. (2024a) simulations suggest that regional groundwater flow from the mountain block can move considerable amounts of water, energy, and solutes into the basin-fill; thus we decided to use the permeability and porosity values from that work into the San Andres and the Sacramento Mountains. For the second scenario, we lower the permeability in the basin fill and increase the permeability in the first kilometer of the mountain blocks. Lastly, in the third scenario, we reduce the permeability of the basin fill and the mountain systems. These two last scenarios are used to explore the variability of flow, water age, and solutes in the domain and to check if we can match the water age and solute concentration values given by the wells in the area. The remaining parameters used in the simulations are presented in Table B.1 in the Appendix B.

Table 3.1: Scenarios explored for permeability and porosity in the Tularosa Basin.

Symbol	Variable Name	Scenario 1	Scenario 2	Scenario 3
κ_Q (m ²)	Perm. of the Undiff. Basin Alluvium ^{a,b,c}	5.29×10^{-13}	5×10^{-14}	5×10^{-14}
κ_{TsfP} (m ²)	Perm. of the Santa Fe Group ^{a,b,c}	1.06×10^{-12}	1×10^{-14}	1×10^{-14}
κ_{TsfC} (m ²)	Perm. of the Santa Fe Conglomerate Facies ^{a,b,c}	1.59×10^{-11}	1×10^{-13}	1×10^{-13}
κ_{Py} (m ²)	Perm. of the Yeso Formation ^{a,b,c}	1.06×10^{-12}	1×10^{-16}	1×10^{-16}
κ_{Ph} (m ²)	Perm. of the Hueco Formation ^{a,b,c}	1.06×10^{-12}	1×10^{-16}	1×10^{-16}
κ_{Pps} (m ²)	Perm. of the Panther Seep Formation ^{a,b,c}	1.06×10^{-14}	5×10^{-17}	5×10^{-17}
κ_{Plc} (m ²)	Permeability of the Lead Camp Formation ^{a,b,c}	1.06×10^{-14}	5×10^{-17}	5×10^{-17}
κ_M (m ²)	Perm. of the Lake Valley ^{a,b,c}	1×10^{-18}	1×10^{-18}	1×10^{-18}
κ_{Os} (m ²)	Perm. of the El Paso de Montoya Group ^{a,b,c}	1×10^{-18}	1×10^{-18}	1×10^{-18}
$\kappa_{s,b}$ (m ²)	Surf. Perm. of the Basement and Mountains ^{a,b,c}	5×10^{-15}	5×10^{-15}	5×10^{-15}
$\kappa_{dl,b}$ (m ²)	Perm. at d_l of the Basement and Mountains ^{c,d,e}	5.29×10^{-18}	1×10^{-16}	1×10^{-18}
B_d (-)	Depth Perm. Coefficient ^{c,d,e}	3.0	3.2	3.2
ϕ_Q (-)	Porosity of the Undiff. Basin Alluvium ^{a,b,c}	0.2	0.2	0.2
ϕ_{TsfP} (-)	Porosity of the Santa Fe Group ^{a,b,c}	0.25	0.25	0.25
ϕ_{TsfC} (-)	Porosity of the Santa Fe Conglomerate Facies ^{a,b,c}	0.3	0.3	0.3
ϕ_{Py} (-)	Porosity of the Yeso Formation ^{a,b,c}	0.1	0.1	0.1
ϕ_{Ph} (-)	Porosity of the Hueco Formation ^{a,b,c}	0.1	0.1	0.1
ϕ_{Pps} (-)	Porosity of the Panther Seep Formation ^{a,b,c}	0.1	0.1	0.1
ϕ_{Plc} (-)	Porosity of the Lead Camp Formation ^{a,b,c}	0.1	0.1	0.1
ϕ_M (-)	Porosity of the Lake Valley ^{a,b,c}	0.05	0.05	0.05
ϕ_{Os} (-)	Porosity of the El Paso de Montoya Group ^{a,b,c}	0.05	0.05	0.05
$\phi_{s,b}$ (-)	Surf. Porosity of the Basement and Mountains ^{a,b,c}	0.3	0.3	0.3

^aHuff (2005), ^bBourret (2015), ^c(Gonzalez-Duque et al., 2024a, Chapter 2)^dIngebritsen and Manning (2010), ^eSaar and Manga (2004)

3.4 Results

3.4.1 Groundwater Flow and Transport

This subsection explores the results for groundwater flow, water ages, and solute concentration for the three scenarios. The results are clipped to show only the eastern side of the cross-section (A'-A) because this region contains most of the water age and water quality measurements. To start, we look at the recharge rates resulting from the simulations, where the first scenario yields unreasonable recharge rates in the basin-fill, with values above 500 m/yr entering the basin-fill close to the faults, which are orders of magnitude higher than the ones presented in previous studies (i.e., Gleeson et al., 2011; Schaller and Fan, 2009). In the second and third scenarios, we see recharge values that range between 0.1 to 4 m/yr, with the highest values presented close to the faults that bound the basin fill. Although these values are large, they are comparable to values explored in Gleeson et al. (2011).

In the first scenario, while we see the interaction of local and regional flowpaths in the Sacramento Mountains enter the alluvium at 400 meters deep, the majority of the water that enters the alluvium in this scenario comes from the mountain front (Figure 3.3d). In the basin fill, the velocity increases by orders of magnitude in the Q, Tsfp, Tsfc, Ph, and Pps geologic layers. The fast-moving groundwater in the alluvium reduces the water ages to less than 100 years close to the water table (Figure 3.3g). It also lowers the solute concentration in the basin fill, resulting in brackish groundwater in the first kilometer of the alluvium (Figure 3.3j). Comparing these results with water age measurements (triangles in Figures 3.2 and 3.3g) we see that this scenario overestimates the water ages found in the basin-fill, where we can expect to reach water ages of 1,000 to 10,000 years with increasing distance from the mountain-front. In terms of solute concentration, the model matches the overall trend of water quality in the alluvium but misses some of the saline groundwater wells located at 55 km and 38 km in the cross-section (points in Figures 3.2 and 3.3j). In the Sacramento Mountains, we see the interaction between local and regional groundwater flow, producing a nested behavior with increasing water ages and solute concentration with depth. In summary, the permeability used for this scenario (Figure 3.3a) creates a fast-moving groundwater system in the basin-fill that produces unreasonably large recharge rates and generates water ages that do not match with the general behavior of measurements in the area. It is worth mentioning that the simulations performed by Huff (2005) and Bourret (2015) account for 3D structures that a 2D model cannot capture. Expanding this model to a 3D conceptualization might yield different results.

In the second scenario, we lower the permeability in the basin-fill and increase the permeability in the first kilometer of the mountain block (Figure 3.3b). The results yield deeper flow penetration of local and intermediate flowpaths in the Sacramento Mountains. This water enters the basin fill and moves upward,

reaching the water table surface at nearly 65 km in the cross-section (Figure 3.3e). This new flow pattern increases the water ages in the alluvium to ages that vary from 10 to 100,000 years (Figure 3.3h), following the behavior of younger water close to the mountain-front and older water located in the middle of the cross-section (Figure 3.3h). The solute concentration in the basin fill shows brackish groundwater close to the mountain-front and saline water traveling through the Ph and Pps geologic layers that reach the water table surface in the middle of the basin (Figure 3.3k). This solute concentration pattern is in better agreement with the water quality measurements in the area, but it still misses the location of the saline wells at 55 km and 38 km in the cross-section (points in Figures 3.2 and 3.3k). Flowpaths within the Sacramento Mountains show a nested behavior, with younger water ages reaching deeper into the system and a narrower freshwater window resulting from the movement of brackish and saline groundwater in the Py and Ph geologic layers at the top of the Sacramento Mountains (Figure 3.3h and k).

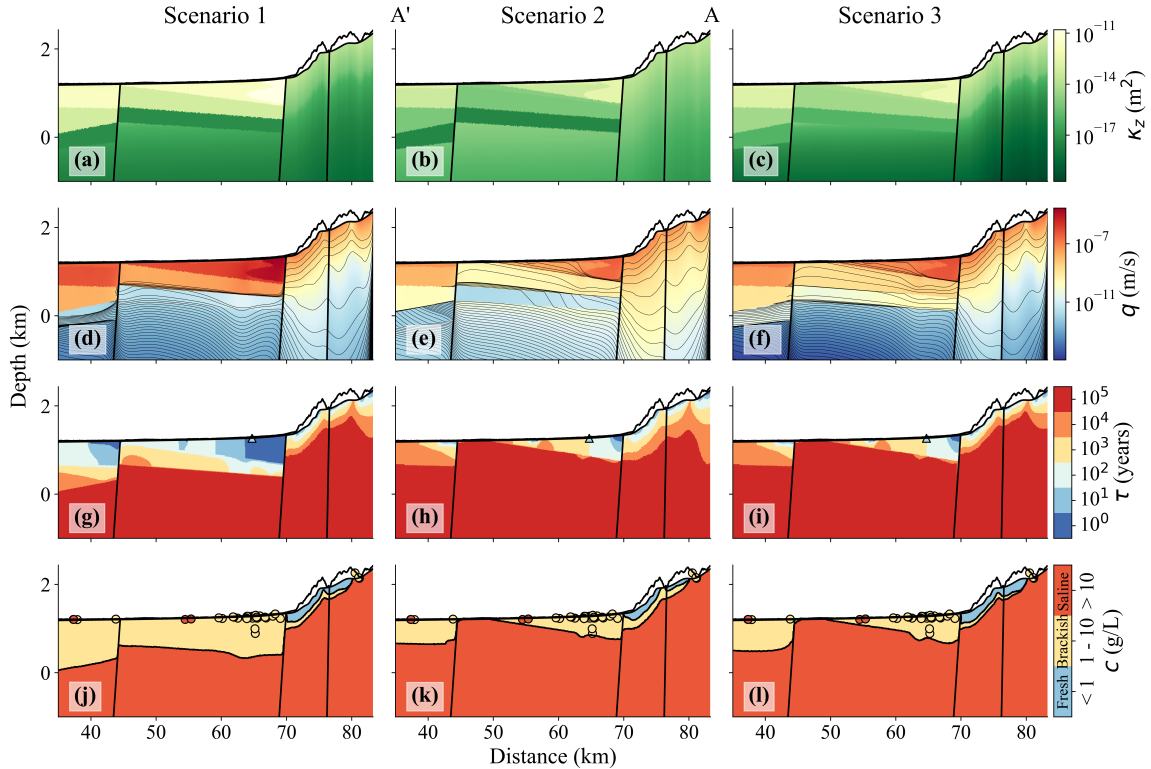


Figure 3.3: z -direction permeability (κ_z in (a), (b), (c)), and simulation results for groundwater flow (q in (d), (e), (f)), water ages (τ in (g), (h), (i)), and solute concentration (c in (j), (k), (l)). The streamlines are the black lines in the groundwater flow panels ((d), (e), (f)). The solute concentration is discretized between fresh, brackish, and saline water. The triangle within the (g), (h), and (i) shows a C^{14} age measurement from a well less than 3 km from the cross-section (Mamer et al., 2014). The points in (j), (k), and (l) show the water quality wells that are located less than 3 km away from the cross-section (NMBGMR et al., 2016).

In the third and last scenario, we reduce the permeability in the mountain block and use the same perme-

ability in the basin-fill as the second scenario (Figure 3.3c). In general, the resulting simulations are similar to the ones in the second scenario, where we see water entering the basin fill from the Sacramento Mountains through local, intermediate, and regional flowpaths that reach the water table surface at nearly 65 km in the cross-section (Figure 3.3f). We also see the increasing water ages and solute concentration in the alluvium with increasing distance from the mountain front (Figure 3.3i and l). The only notable difference between these scenarios is the patterns of solute concentration in the Sacramento Mountains, where the third scenario shows an increase in freshwater in the first 300 meters in the mountain block that results from a deeper penetration of the local flow paths. This scenario also agrees with the general behavior of water ages and solute concentration in the area. However, it still misses the location of the saline wells at 55 km and 38 km in the cross-section (points in Figures 3.2 and 3.3l). We also compared the total dissolved solutes (TDS) measured in wells extracted from NMBGMR et al. (2016) and the simulated results at the well locations (Figure B.2 in Appendix B). Although the scenarios qualitatively follow the general salinity patterns within the basin, the models still miss the exact salinity values when compared to wells in the area. This discrepancy can be attributed to a handful of factors. First, the proposed model has an idealized geology with large geologic layers that might need to be better represented in the alluvium. Secondly, the large scale of the model limits our ability to investigate specific details found where the majority of the well information is located. Lastly, the solute distribution close to the surface can be affected by the infiltration of brackish water at the surface that varies seasonally in the region, and it's not captured in our steady-state simulations. Future models should look into the local variability in the alluvium to better capture the local salinity patterns.

3.4.2 Bulk Resistivity and Extended Cross-Section

The simulated results of solute concentration and temperature allow us to calculate the bulk resistivity of the domain using equations (3.10) and (3.11). The results show resistivity values lower than $10 \Omega\cdot\text{m}$ in the Q, Tsfp, Tsfc, Ph, and Pps geologic layers in the basin-fill and values lower than $1 \Omega\cdot\text{m}$ in the Ph and Pps layer for the second scenario (Figures 3.4d, e, and f). At the basement of the basin fill, the resistivity increases by one order of magnitude due to the small values of porosity (Figure 3.4a, b, and c). In the mountain block, we see a window of low resistivity values (1 to $10 \Omega\cdot\text{m}$) occurring between 0.3 to 1 km deep, where the saline water travels through the regional flowpaths to reach the alluvium and supply solutes to the Ph and Pps geologic layers. This window is between resistivity values larger than $10 \Omega\cdot\text{m}$, produced by fresh and brackish water at the top and low porosity at the bottom. These results show that the bulk resistivity of the domain provides enough contrast to reveal the distribution of solutes in the basin fill and the interaction of local and regional flowpaths in the Sacramento Mountains.

The previous results show that scenarios two and three yield the results that agree the most with water age

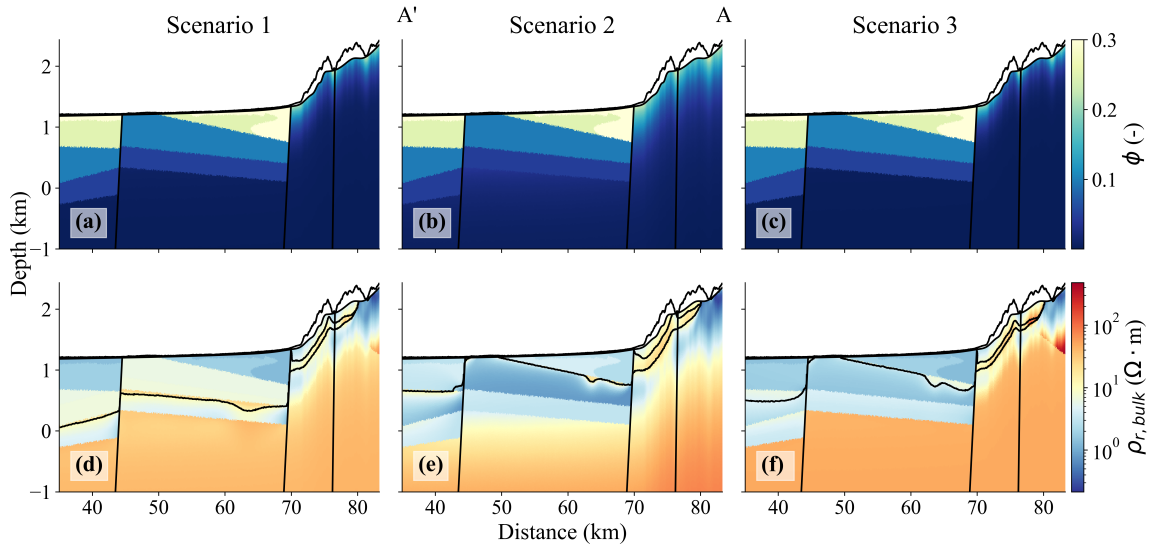


Figure 3.4: Porosity of the system (ϕ in a, b, c) and simulation results for bulk resistivity calculated with equation (3.10) ($\rho_{r,bulk}$ in (d), (e), (f)). The back contours in (d), (e), and (f) separate fresh, brackish, and saline water in the Sacramento Mountains and brackish and saline water in the basin fill.

and water quality measurements. So, we decided to present the whole cross-section for scenario two (Figure 3.5). These results show how the regional groundwater flow from the Sacramento Mountains recharges the White Sands region (left in the cross-section), providing old and salty water to the basin fill (Figure 3.5b and d). The system presents thermal anomalies in both mountain fronts, where colder water (less than 20°C) enters the alluvium in the first 500 meters depth, and as we move farther away from the mountain fronts, we see water at higher temperatures (larger than 20°C) moving close to the surface which falls within the range of values of temperature reported in Mamer et al. (2014) (Figure 3.5c). We also see deep regional groundwater flow coming from the San Andres Mountains, recharging part of the White Sands region. Regarding resistivity, there are not enough contrasting features to distinguish between the local and regional flowpaths in the San Andres Mountains due to the excess of freshwater in the system and the low porosity in the deeper sections of the mountain block (Figure 3.5e). However, we see a considerable decrease in resistivity (values of the order of $10^{-1} \Omega\cdot\text{m}$) in the White Sands region close to the San Andres mountain-front that are due to the excess of saline water present in the area.

3.5 Discussion

Our simulations agree with the solute concentration patterns suggested by Newton and Land (2016) conceptual model, where freshwater from the Sacramento Mountains becomes brackish and saline as it travels through the regional groundwater system and dissolves gypsum deposits in the Yeso and Hueco Formations.

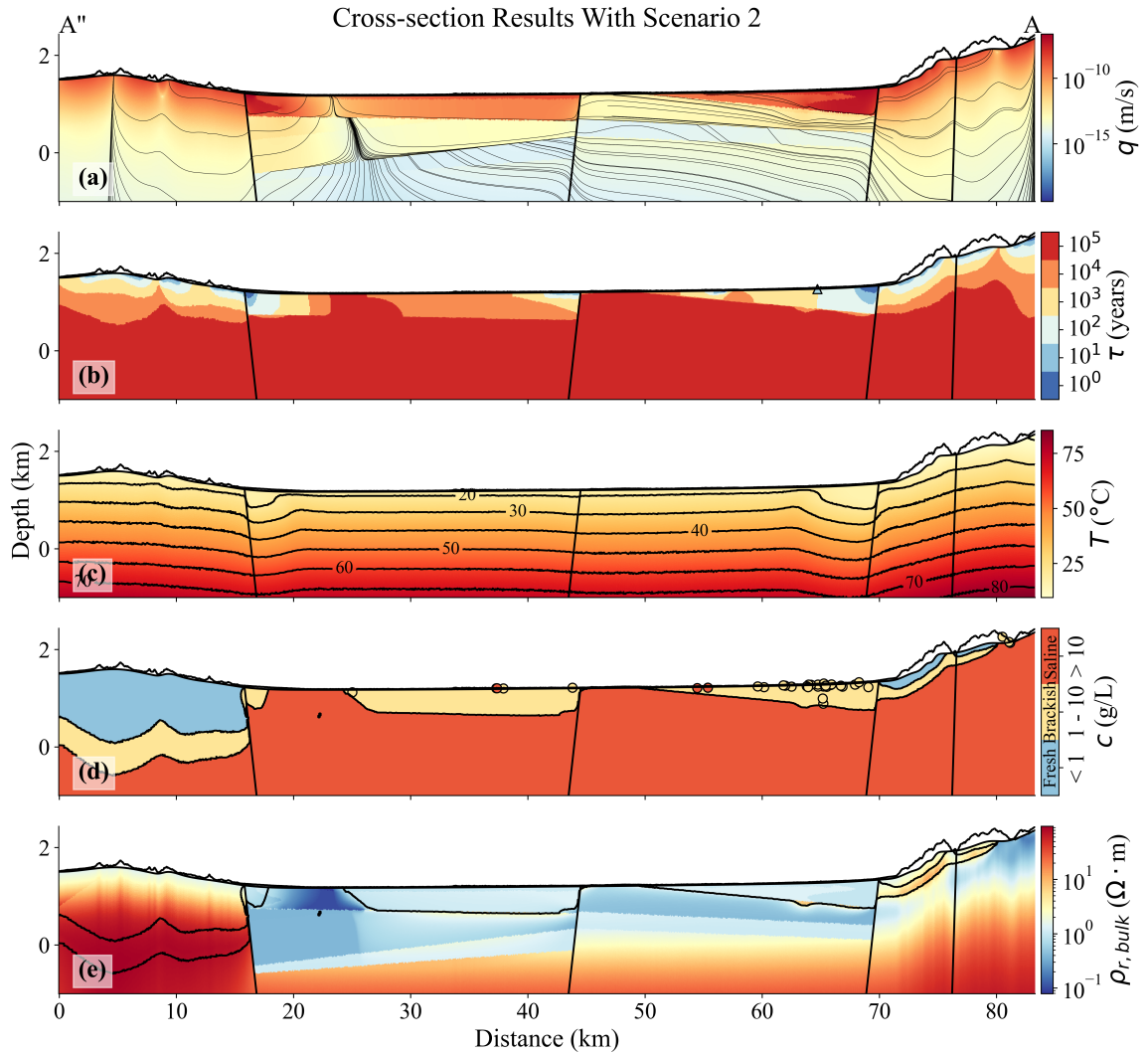


Figure 3.5: Simulation results for groundwater flow (q in a), water ages (τ in b), temperature (T in c), solute concentration (c in d), and bulk resistivity ($\rho_{r,bulk}$ in e). The streamlines are the black lines in the groundwater flow panel (a). The solute concentration is discretized between fresh, brackish, and saline water. The triangle within (b) shows the C^{14} age measurement from a well less than 3 km from the cross-section (Mamer et al., 2014). The points in (c) show the water quality wells located less than 3 km from the cross-section (NMBGMR et al., 2016). The back contours in (d) separate fresh, brackish, and saline water in the Sacramento Mountains and brackish and saline water in the basin fill.

This water then enters the alluvium at 1 km depth and moves upwards through the Permian geologic layers (Ph and Pps), supplying the alluvium with saline water close to the surface. These results also agree with the water age measurements as they increase as we move away from the mountain-front (Mamer et al., 2014; Eastoe and Rodney, 2014). Both of these results support the idea that regional groundwater fluxes can convey water, energy, and solutes to the groundwater budget, recharging deep brackish and saline groundwater aquifers that should be considered when managing the unconventional water resources in the area.

The bulk resistivity resulting from the simulations illustrates contrasting features in the basin fill that are a product of the changes in water salinity and the porosity of the basement. This behavior can allow magnetotelluric surveys to map the extent of the region's brackish and saline groundwater resources, providing an efficient and non-invasive assessing tool that can be used extensively to characterize the unconventional water resources in the basin. Furthermore, the resistivity patterns in the Sacramento Mountains create a low resistivity window between 0.3 to 1 km deep, where regional, old saline groundwater travels through the mountain block and enters the alluvium, similar to the contrasting resistivity patterns in the mountain block found in Gonzalez-Duque et al. (2024a) idealized simulations (Chapter 2 Section 2.3.2). This mountain block resistivity pattern is promising as it suggests that magnetotelluric surveys could potentially map the depth of regional groundwater traveling through the fractured mountains, opening the door for future characterization of flowpaths in the Sacramento Mountains system.

It is worth noting that these 2D steady-state simulations are still highly idealized, bringing important assumptions that limit the interpretation of these results. First, we are aware of the changes the Tularosa Basin has experienced in recent geologic times, with quaternary faulting events occurring at the San Andres and Alamogordo Fault zones (less than 35,000 years) (Machette, 1987) and the presence of the Lake Otero that developed over the past 45,000 years (Allen et al., 2009) and started an intensive deflation about 7,000 years ago (Langford, 2003; Kocurek et al., 2007; Allen et al., 2009). These events, as well as seasonality within the basin, led to important changes in the distribution of water, energy, and solutes. As Szykiewicz et al. (2009) reported, while the distribution of sulfates during wet episodes is the result of weathering of sulfides of hydrothermal and sedimentary origin, the sulfates in dry episodes are likely the result of the dissolution of marine evaporites present in Permian layers that are moved through the regional groundwater fluxes coming from the Sacramento and the San Andres Mountains. Secondly, our model does not account for the 3D nature of flow that can potentially move significant amounts of water, energy, and solutes in other directions within the basement, especially in the White Sands region where the water flows from north to south (Huff, 2005). Lastly, the use of an uncoupled numerical simulation neglects the role of possible convection through the system. Although our model is simplified, it shows some of the important flow and solute patterns presented in Szykiewicz et al. (2009), allowing us to have a general interpretation of the distribution and sources of solutes and energy for the Tularosa Basin. Also, these numerical simulations suggest that magnetotelluric surveys can be used to map the extent of the region's brackish and saline groundwater resources

3.6 Conclusions

This work explores the groundwater flow and transport of heat and solutes dynamics in an east-to-west cross-section within the Tularosa Basin, discusses the importance of regional groundwater flows from the Sacra-

mento Mountains to the alluvium, and explores the use of electrical resistivity measurements to assess the brackish and saline groundwater resources in the region. Our simulations generally agree with water ages and water quality measurements in the area and show how regional groundwater fluxes enter the basin fill at 1 km depth, moving considerable amounts of solutes to the alluvium through the Permian layers. These solute concentration patterns suggest that regional groundwater flow is an important source of water to the alluvium that should not be discarded as done in previous modeling in the area (e.g., Huff, 2005; Bourret, 2015).

The resulting distribution of solutes and heat in the basin fill and the mountain block strongly affects the resistivity patterns of the domain. Similar to Gonzalez-Duque et al. (2024a), we see contrasting patterns in the mountain block explained by old saline water traveling through the regional flowpaths. These resistivity patterns follow the behavior of solute concentration as it enters the basin-fill, with low resistivity values moving upwards through the Permian layers. Using geophysical surveys, such as magnetotelluric field campaigns, in the Sacramento Mountains could shed some light on the nested nature of flow in the mountain block and the extent of the regional groundwater flow system. Furthermore, these surveys can also be used to assess the extent of the brackish groundwater aquifers within the basin fill.

Future work should consider the use of a 3D conceptualization of the Tularosa Basin that incorporates the surrounding mountain systems and simulates the coupled groundwater flow and transport of heat and solutes. This model should also include an extended site geology and must be calibrated with the area's water table, ages, and solute concentration measurements. As an additional recommendation, these models should account consider looking into the saturation indices for gypsum from well information and along flowpaths to determine where the groundwater flowpath is dissolving or precipitating gypsum within the groundwater system, aiding in the interpretation of the solute patterns. The construction of this model and the assessment of resistivity patterns can open the door for determining future magnetotelluric measurements in the area, allowing the exploration of the regional groundwater flow system through the surrounding mountains and the assessment of the brackish groundwater "unconventional" resources.

CHAPTER 4

Conclusions and Future Work

In this part of the dissertation, we explore the importance of regional groundwater flow in mountain systems, how they convey significant amounts of water, energy, and solutes to the alluvium, and how we can use geophysical surveys (such as magnetotelluric campaigns) to assess the depth of circulation within the mountain block. We achieve this by implementing 2D coupled groundwater flow and transport numerical models that simulate mountain-to-valley transition systems. In our first work (Chapter 2), we explore the effects of topography, geology, and dissolution rate variations on idealized mountain-to-valley transition systems and show the strong dependence of water ages and solute concentration patterns on changes in these factors. These results also illustrate the presence of stagnation areas within the mountain block that accumulate considerable amounts of solutes and occur at the meeting branches of the local, intermediate, and regional flowpaths. Furthermore, the variations in solute concentration in the mountain block generate contrasting bulk resistivity patterns that allow the separation of local to regional flowpaths and the determination of the depth of circulation within the mountain block. These resistivity patterns could potentially be detected by magnetotelluric surveys, providing a crucial, non-invasive, and efficient tool to characterize the nested nature of flow in mountainous terrains.

In our second work (Chapter 3), we went one step further and implemented a 2D groundwater flow and transport model for an east-to-west cross-sectional area within the Tularosa Basin to assess the importance of regional groundwater flows in the distribution of solutes within the alluvium. For these simulations, we included a simplified geologic structure for the cross-section using the information provided in Newton and Land (2016) and simulated the flow and transport of water, heat, and solutes throughout the domain. Our results show regional flows from the Sacramento Mountains entering the alluvium at a depth of 1 km and moving upwards through the Permian layers in the basin fill. The water circulating through this regional system carries old saline water to the upper parts of the alluvium, which agrees with the region's water age and water quality measurements. Additionally, the bulk resistivity patterns produced by the distribution of solutes within the domain show a low resistivity window within the Sacramento Mountains that follows the regional groundwater flow in the mountain block. In the alluvium, the low resistivity patterns show the location of brackish and saline groundwater aquifers. These findings suggest that magnetotelluric surveys could be used to detect the depth of circulation within the Sacramento Mountains and assess the distribution of solutes within the alluvium.

Both works presented in this part provide valuable insight into the importance of regional groundwa-

ter flow in the mountain system and the potential of geophysical surveys to assess the depth of circulation within the mountain block. The use of groundwater flow and transport models coupled with magnetotelluric hydrogeophysical inversion techniques (e.g., Rubin and Hubbard, 2005; Herckenrath et al., 2013; Hinnell et al., 2010) can open the door for the estimation of hydraulic parameters (i.e., permeability and porosity) in mountain systems where direct measurements can be challenging. This approach can also provide valuable information about the distribution of solutes within the alluvium, which is crucial for the sustainable management of “unconventional” water resources in arid regions such as the Tularosa Basin.

Future work should consider the development of 3D models that include the geologic structure of the Tularosa Basin and its surrounding mountains and the calibration with water levels, water quality, and water age information. This conceptualization would provide a more realistic representation of the system and allow the assessment of the nested nature of flow in mountainous terrains. Finally, the implementation of a magnetotelluric survey in the Tularosa Basin would provide valuable data to validate the results of the numerical models and assess the potential of this geophysical survey to detect the depth of circulation within the mountain block and the distribution of solutes within the alluvium.

Part II

The Multiscale, Nested Nature of River Corridor Connectivity and Their Influence on Ecosystem Services

CHAPTER 5

Introduction

River corridor connectivity (RCC) provides ecosystem services that play a crucial role in regulating the ecosystemic health of rivers (Pringle, 2003) by driving surface water-groundwater exchange processes at multiple scales (Boano et al., 2014). Accelerated and uninformed anthropogenic-driven land changes have impacted this connectivity, degrading the health of ecosystems at a global scale (Décamps et al., 1988; Pringle, 2001, 2003). These ecosystems' preservation and remedial strategies rely on quantifying the exchange processes occurring in the RCC (Hancock, 2002; Harvey and Gooseff, 2015; Harvey et al., 2018; Lewandowski et al., 2019; Arora et al., 2022; Krause et al., 2022), complementing other management strategies provided in principle by the Clean Water Act (US Government, 1972). An essential part of this solution requires constructing modeling tools to assess the amount of exchange and the biogeochemical processes occurring at local and regional scales (Pringle, 2003; Harvey et al., 2018). This evaluation is often limited by the lack of standardized data collection and the complexity of models constraining aggregated estimations on a watershed scale (Boano et al., 2014; Ward and Packman, 2019; Krause et al., 2022). Lateral exchange processes, such as sinuosity-driven hyporheic exchange, are an integral part of the RCC processes that regulate the water quality of rivers (Gomez-Velez and Harvey, 2014; Krause et al., 2022). This part of the dissertation focuses on creating a novel tool for assessing meandering channels and their influence on RCC processes, specifically the sinuosity-driven hyporheic exchange processes.

The hyporheic exchange zone is hydrologically defined as the zone in which surface water and groundwater interact along river corridors (Tonina and Buffington, 2009; Cardenas, 2015). In meanders, the exchange is driven by the river morphology (Cardenas, 2008; Boano et al., 2006) and is modulated by regional groundwater fluxes (Cardenas, 2009b). Current parsimonious physics-based models have explored the relative contribution of a plurality of exchange processes occurring at a watershed (i.e., Gomez-Velez et al., 2015) and continental scale (i.e., Gomez-Velez and Harvey, 2014). These models have concluded that the relative contribution of intra-meander processes to the total exchange fluxes is small and limited to large rivers (Gomez-Velez and Harvey, 2014; Gomez-Velez et al., 2015). However, most models assume sinusoidal meander planimetry (i.e., Cardenas, 2009b; Gomez et al., 2012; Gomez-Velez and Harvey, 2014; Gomez-Velez et al., 2015, 2017), neglecting the important hydrodynamic and biogeochemical effect of complex meander geometries in natural streams (Peterson and Sickbert, 2006; Cardenas, 2008; Revelli et al., 2008; Boano et al., 2010b). The latter assumption can have substantial implications in estimating meanders' relative hyporheic exchange contribution, possibly underestimating the actual contribution of sinuosity-driven hyporheic ex-

change at a large scale.

This part addresses this limitation by providing a framework that combines groundwater flow and transport models with natural meander geometries to explore the role of sinuosity-driven hyporheic exchange at multiple scales. The framework includes a groundwater flow and transport model that explores the hydrodynamic effects of the meander geometry, the regional groundwater fluxes, and the availability of chemical constituents in the biogeochemical potential within the hyporheic exchange zone, with emphasis on nitrogen cycling (Chapter 6). The framework also includes an automated meander identification tool that characterizes meandering channels in river transects throughout the High-Resolution National Hydrography Dataset (NHDPlus HR), allowing the identification of individual meander geometries across catchments (Chapter 7).

As shown throughout Part II, the framework explores the biogeochemical potential of meanders to become sinks or sources of nitrates and the importance of particulate organic carbon in these biogeochemical processes. It also provides the modeling basis and the identification tools that allow the future quantification of the contribution of sinuosity-driven hyporheic exchange to the total hyporheic exchange fluxes throughout the Conterminous United States (CONUS). Lastly, the meander identification tool also incorporates methods that characterize sinuous channels throughout CONUS, opening the door for the future morphodynamic characterization of rivers at a national scale.

CHAPTER 6

Sinuosity-driven Hyporheic Exchange: Hydrodynamics and Biogeochemical Potential

This chapter is a modified version of a paper accepted to Water Resources Research. Gonzalez-Duque, D., Gomez-Velez, J. D., Zarnetske, J. P., Xingyuan, C., & Scheibe, T. D., (2024). Sinuosity-driven Hyporheic Exchange: Hydrodynamics and Biogeochemical Potential (Accepted). Water Resources Research.

Abstract

Hydrologic exchange processes are critical for ecosystem services along river corridors. Meandering contributes to this exchange by driving channel water, solutes, and energy through the surrounding alluvium, a process called sinuosity-driven hyporheic exchange. This exchange is embedded within and modulated by the regional groundwater flow (RGF), which compresses the hyporheic zone and potentially diminishes its overall impact. Quantifying the role of sinuosity-driven hyporheic exchange at the reach-to-watershed scale requires a mechanistic understanding of the interplay between drivers (meander planform) and modulators (RGF) and its implications for biogeochemical transformations. Here, we use a 2D, vertically integrated numerical model for flow, transport, and reaction to analyze sinuosity-driven hyporheic exchange systematically. Using this model, we propose a dimensionless framework to explore the role of meander planform and RGF in hydrodynamics and how they constrain nitrogen cycling. Our results highlight the importance of meander topology for water flow and age. We demonstrate how the meander neck induces a shielding effect that protects the hyporheic zone against RGF, imposing a physical constraint on biogeochemical transformations. Furthermore, we explore the conditions when a meander acts as a net nitrogen source or sink. This transition in the net biogeochemical potential is described by a handful of dimensionless physical and biogeochemical parameters that can be measured or constrained from literature and remote sensing. This work provides a new physically based model that quantifies sinuosity-driven hyporheic exchange and biogeochemical reactions, a critical step toward their representation in water quality models and the design and assessment of river restoration strategies.

Plain Language Summary

Meandering causes pressure gradients that induce water flow from the channel to the alluvial aquifer and back to the channel. This circulation process is known as sinuosity-driven hyporheic exchange, and it has traditionally been associated with ubiquitous and favorable impacts on ecosystem services. However, its presence and biogeochemical implications can vary across river networks and even result in detrimental conditions. Here,

we conducted a systematic modeling study to understand the hydrodynamics of sinuosity-driven hyporheic exchange and its implications for nitrogen transformations. Our results show that the compressing effect of regional groundwater flow can significantly reduce or vanish the hyporheic zone. Yet, narrow meander necks, characteristic of high-sinuosity channels, shield the hyporheic zone even under extreme regional gradients. This shielding effect has been previously ignored and highlights the persistent nature of the exchange and its resilience against external modulators. We also use our model to propose and evaluate a framework based on measurable physical and biogeochemical parameters to identify the conditions leading to a meander acting as a net source or sink of nitrogen. These mechanistic insights can guide the design and evaluation of river restoration strategies and provide a critical foundation for its representation in water quality models.

6.1 Introduction

Connectivity along river corridors plays a critical role in ecosystem services (Harvey and Gooseff, 2015; Harvey et al., 2018; Harvey and Schmadel, 2021). For example, it provides thermal (White et al., 1987; Holmes, 2000; Arrigoni et al., 2008; Wu et al., 2020, 2021) and nutrient regulation (Harvey et al., 2018; Holmes, 2000; Bencala, 2011) for streams and rivers. Connectivity encompasses exchange processes that move water, energy, and solutes between rivers and their surrounding surface and subsurface waters (Pringle, 2001), increasing the contact time with reactive environments and enhancing the biogeochemical processes supporting aquatic life (Dent et al., 2000, 2001; Pringle, 2003). Modeling these exchange processes in rivers at the local and catchment scales can provide useful tools for water management and remedial strategies (Arora et al., 2022; Hancock, 2002; Harvey and Gooseff, 2015; Lewandowski et al., 2019; Ward and Packman, 2019; Krause et al., 2022).

Hyporheic exchange is one connectivity process of particular interest as it circulates water, solutes, and energy through reactive environments, serving as a natural biogeochemical reactor modulating water quality across the river network (Boano et al., 2014). This exchange process occurs vertically and laterally and is driven by spatial variations in the hydraulic head (both the hydrodynamic and hydrostatic components) at the sediment-water interface, resulting in the circulation of water and the constituents it carries through the streambed and alluvium sediments before returning to the channel (Tonina and Buffington, 2009; Boano et al., 2014). The mechanisms that drive hyporheic exchange are dictated by river geomorphological features at various scales, influencing the direction, magnitude, and stability of the hyporheic flow (Buffington and Tonina, 2009; Poole et al., 2006) and controlling the residence times and biogeochemical processes (Buffington and Tonina, 2009). Previous efforts have proposed methodologies to quantify the relative role of different geomorphic features in the overall channel hyporheic exchange (e.g., Buffington et al., 2004; Gomez-Velez et al., 2015; Harvey et al., 2018; Kiel and Bayani Cardenas, 2014). These methodologies suggest that even

though both vertical and lateral exchange processes persist across river networks, vertical exchange plays a dominant role given the fragility of sinuosity-driven exchange to regional groundwater flow (Gomez-Velez et al., 2015). However, as shown in this study, sinuosity-driven exchange may be more resilient than previously thought due to the hydrodynamic shielding caused by the neck of high-sinuosity channels (more details in section 3.1).

Meanders are one of the ubiquitous geomorphic features driving channel water, solutes, and energy through the surrounding alluvium, a process called sinuosity-driven hyporheic exchange. Their planimetry is characterized by multiscale (Leopold and Wolman, 1960; Seminara, 2006; Lazarus and Constantine, 2013; Vermeulen et al., 2016) and self-similar (Snow, 1989; Montgomery, 1996) patterns, which further influence the nature of the exchange process. In fact, throughout river networks, from headwaters to coasts, similar topologies (i.e., shapes) can be found in channels of all sizes. Even though the meander geometry (i.e., length scales) differs drastically between small streams and large rivers, we can find similar meandering patterns at both scales (Anderson and Anderson, 2010; Leopold and Wolman, 1960). This topological commonality is fundamental to proposing a transferable understanding of sinuosity-driven hyporheic exchange.

Numerous studies have explored the underlying mechanisms and hydrodynamic effects behind the sinuosity-driven hyporheic exchange, addressing the importance of channel sinuosity in driving and regulating the hyporheic flow and its residence times (see review by Boano et al., 2014). Channel curvature produces hydraulic gradients between the channel and the alluvium that drive exchange and control the residence time of water (Boano et al., 2006; Cardenas, 2008; Peterson and Sickbert, 2006). For example, meanders with high sinuosity (i.e., sinuosities larger than approximately 2.5, typically characterized by a well-defined meander neck) produce low-velocity zones near the meander apex, allowing for longer contact times with the reactive environment (Boano et al., 2010b; Cardenas, 2008; Revelli et al., 2008). As meanders evolve, their planimetry elongates and closes, creating a neck in the base of the meander. This is a common feature of natural meanders that results in strong hydraulic gradients over the narrowest parts of the meander (Boano et al., 2006; Peterson and Sickbert, 2006), inducing faster hyporheic flow along the neck and, therefore, shorter residence times with important implications for biogeochemical transformations (Boano et al., 2010b; Revelli et al., 2008). A previous study for low-sinuosity meanders (i.e., sinuosities lower than approximately 2.5, idealized as sinusoidal shapes that cannot capture the formation of meander neck) has shown the tight connection between hyporheic exchange residence time distributions and sinuosity, valley slope, aquifer dispersivity, and hydraulic conductivity (Gomez et al., 2012). This analysis was later extended to account for the dynamics induced by river stage fluctuations (Gomez-Velez et al., 2017) and evaporation from riparian vegetation (Kruegler et al., 2020).

Sinuosity-driven hyporheic exchange is embedded within and modulated by the regional groundwater

flow (RGF), which compresses the hyporheic zone and potentially diminishes its overall impact. This modulating effect has been explored by Cardenas (2009b), where low-sinuosity meanders were exposed to varying degrees of RGF under gaining and losing conditions. His study focused on the net amount of exchange and the extent of the hyporheic zone, which are highly sensitive to RGF, with relatively small fluxes significantly compressing and, sometimes, obliterating the hyporheic zone. This high sensitivity to RGF is reflected in the cumulative effects of this exchange process at the catchment scale (Kiel and Bayani Cardenas, 2014; Gomez-Velez and Harvey, 2014; Gomez-Velez et al., 2015). However, these previous studies assessing the impacts of RGF do not explore the hydrodynamic effects of complex river planimetry on the compression of the hyporheic zone. As we show in this study, the strong hydraulic gradients induced by the meander neck can counteract the effects of regional groundwater gradients, resulting in a persistent sinuosity-driven hyporheic zone with implications for connectivity and water quality more important than we ever thought.

Although residence times are a critical indicator of biogeochemical reactions, this metric is not the only factor involved in the reaction processes. Reactivity strongly depends on the relative magnitude of the hyporheic transport time scale, the hyporheic zone reaction rates (Gu et al., 2007; Zarnetske et al., 2012), and on the availability of chemical constituents (Sawyer, 2015). From the perspective of nitrogen cycling and the role of hyporheic exchange in nutrient retention, a process that is critical for water quality, as it limits or enhances the chemical transformations (Harvey et al., 2018), these constraints have been studied in detail (e.g., Boano et al., 2010b; Gu et al., 2007; Zarnetske et al., 2011a). For example, the works of Gu et al. (2007) and Zarnetske et al. (2012) used a one-dimensional modeling framework to show how increasing values of the aerobic respiration Damköhler number, Da_O (ratio between the characteristic times of reaction and transport), enhance the removal of nitrates in the hyporheic zone of streambeds. Furthermore, nitrogen cycling is also limited by the availability of dissolved organic carbon (DOC) and ammonia (NH_4^+) (Zarnetske et al., 2011a, 2012), where the removal of nitrates (NO_3^-) is associated with the presence of DOC in the hyporheic zone either transported from the stream or locally dissolved from particulate organic carbon (POC) (e.g., Sawyer, 2015; Stelzer et al., 2015; Zarnetske et al., 2011b).

Quantifying the role of sinuosity-driven hyporheic exchange at the reach-to-watershed scale requires a mechanistic understanding of the interplay between drivers (e.g., meander planform) and landscape modulators (e.g., RGF) and its implications for biogeochemical transformations. This issue remains a gap in our knowledge, and this study aims to provide new insight from the perspective of flow hydrodynamics and the transformation of nitrogen with the sinuosity-driven hyporheic zone, allowing the systematic comparison to multiple scales of meanders in the river network. We propose a dimensionless framework to systematically explore hyporheic flow and residence times under different sinuosities and regional groundwater gradients while including the effects of reaction time scales and the availability of chemical constituents. In particular,

this study builds on the work of (Gomez-Velez et al., 2017) by representing more complex channel planimetrics that span the full spectrum of meanders observed in nature, describing the age distribution, not only its mean and explicitly modeling nitrogen transformations to estimate the hyporheic zone’s biogeochemical potential.

6.2 Methods

We use a reduced-complexity model to explore sinuosity-driven hyporheic exchange’s hydrodynamics, transport, and biogeochemical potential. Our approach explicitly represents the effects of (i) planform (meandering pattern), (ii) channel hydraulics, (iii) alluvium’s physical and biogeochemical properties, and (iv) the modulating effect of regional groundwater flow. We used COMSOL Multiphysics (COMSOL AB, 2024), a finite-element code for all simulations. We generated free-triangular meshes for the four meander geometries with significant refinement near the boundaries and within the meander. In all cases, the mesh quality was high (with a skewness average element quality of 0.90 (Gothäll, 2022), and the simulations are mesh-independent.

6.2.1 Reduced-complexity Model

The physical and biogeochemical process controlling sinuosity-driven hyporheic exchange and its biogeochemical potential in natural systems is highly complex (e.g., Dwivedi et al., 2018); however, in the spirit of Vušanović and Voller (2021), we use a reduced-complexity model, where only the first-order controls for flow and transport are represented. The assumption is that this simplification of the underlying mechanisms captures the general exchange patterns within the alluvium without compromising the predictive outcomes of the physical processes and highlights general and generalizable trends in the system’s response. Our conceptualization mimics an alluvial valley characterized by a meandering river that fully penetrates the alluvial valley aquifer, which overlies an older, horizontal, low-permeability river deposit (Figure 6.1C-D). The channel (boundary $\partial\Omega_c$ in Figure 6.1C) is described by a Kinoshita curve (Abad and Garcia, 2009; Kinoshita and Miwa, 1974; Seminara et al., 2001; Seminara, 2006), which is expressed as a parametric curve:

$$\theta(s) = \theta_0 \sin\left(\frac{2\pi}{\lambda}s\right) + \theta_0^3 \left[J_s \cos\left(\frac{6\pi}{\lambda}s\right) - J_f \sin\left(\frac{6\pi}{\lambda}s\right) \right], \quad (6.1)$$

where θ is the angle between the channel centerline and the down-valley direction [-], s is the streamwise coordinate [L], θ_0 is the maximum angular amplitude [-], λ is the arc wavelength [L], J_s is the skewness coefficient [-] and J_f is the flatness coefficient [-]. Given these parameters, we can calculate the length of the meander bend in the direction of the alluvial axis L [L] and estimate the sinuosity for an individual meander as $\sigma = \lambda/L$.

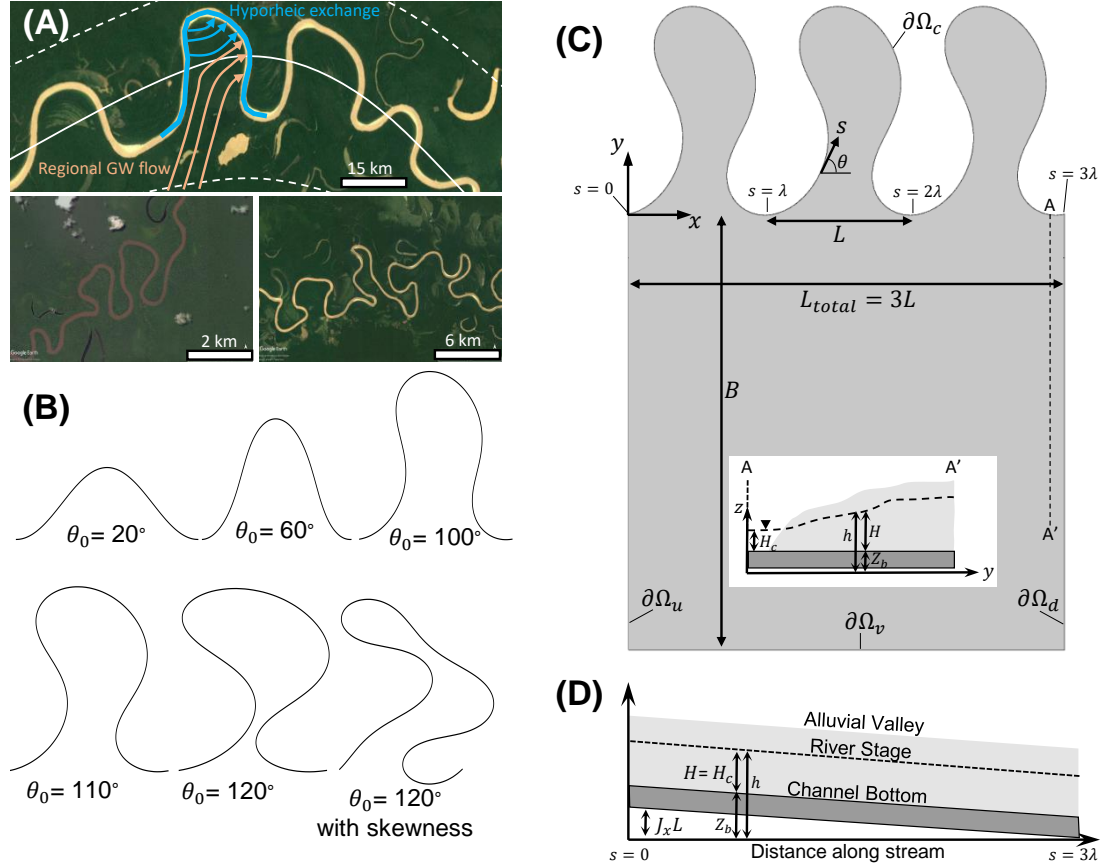


Figure 6.1: Conceptualization of the reduced-complexity model for sinuosity-driven hyporheic exchange. (A) Examples of meandering channels at different scales (images taken from Google Earth). The river in the upper image illustrates the alluvial valley axis (solid black line), the alluvial belt (dashed black line), and the flow field of a single meander bend dictated by the interaction of sinuosity-driven hyporheic exchange (cyan arrows) and regional groundwater flow (orange arrows). (B) Examples of meanders generated with a Kinoshita curve for different values of the maximum angular amplitude θ_0 . In these synthetic meanders, the wavelength ($\lambda = 100$), flatness coefficient ($J_f = 1/192$), and skewness coefficient ($J_s = 1/32$) are constant, except for the last meander where $J_s = 1/10$. Planimetric view (C) and longitudinal view along the channel (D) of the domain used in the model. The model focuses on a single meander bend described by a Kinoshita curve ($\partial\Omega_c$). To minimize boundary effects, we repeat this meander unit three times and assume periodic boundary conditions for flow and transport in the downstream ($\partial\Omega_d$) and upstream ($\partial\Omega_u$) boundaries. Our analyses focus on the meander bend in the middle of the domain. The alluvial valley length is $B = 3\lambda$, which is selected to minimize numerical artifacts in the simulated hyporheic flow field caused by the influence of the valley-side boundary ($\partial\Omega_v$).

The Kinoshita curve’s flexibility and simplicity make it ideal for exploring the similarities in meander planform across scales in river networks. This curve is flexible enough to reproduce the main planimetric features of individual meanders, including “flattening” and “skewing” of meander loops (Camporeale et al., 2007). For example, compare the meanders in Figure 6.1A with the curves in Figure 6.1B). Also, the curve only requires three parameters (θ_0 , J_s , and J_f), with the arc wavelength λ serving as a scaling factor. As

we show in the following sections, this is a major advantage to nondimensionalize the model, reducing the computational burden and generalizing our results.

We focus our analysis on the flow, transport, and reactivity of sinuosity-driven hyporheic exchange in a single meander bend; however, our numerical implementation uses a periodic modeling domain with three meanders to minimize boundary effects. The total length of the modeling domain in the direction of the alluvial axis (x) is $3L$. Boundary conditions for flow and transport processes along the downstream ($\partial\Omega_d$) and upstream ($\partial\Omega_u$) boundaries are assumed periodic to mimic an infinite domain. More specifically, for water flow, we maintain a constant hydraulic head drop, given by the slope of the channel, along these boundaries (the sensitivity analysis for the periodic heads is presented in Section C.1 and Figure C.1 in the Appendix C). For transport, we mirror concentrations along these boundaries. The boundary within the alluvial valley belt ($\partial\Omega_v$) is located at a distance $B = nL$ from the channel. Based on a sensitivity analysis (presented in Section C.1 and Figure C.2 in the Appendix C), the factor $n = 1$ was selected to minimize the influence of the alluvial belt boundary on the flow field.

In the following subsection, we describe the physics and mathematical conceptualization used to describe water flow, the evolution of the water age, and the fate and transport of key constituents involved in the denitrification process (nitrate, ammonium, oxygen, and dissolved organic carbon).

6.2.1.1 Flow Model

We model a two-dimensional homogeneous and isotropic alluvial aquifer bounded by a fully penetrating channel (Figure 6.1C-D). This assumption is fundamental for the Dupuit-Forchheimer approximation (predominantly horizontal flow) (Troch et al., 2013) and has been used in previous studies focusing on lateral sinuosity-driven hyporheic exchange (Boano et al., 2006, 2010a; Cardenas, 2009a,b; Gomez et al., 2012; Gomez-Velez et al., 2017). Although this assumption neglects the vertical flow induced by partially penetrating channel (e.g., Boano et al., 2010a), it is a reasonable approximation given the scale of the analysis and the focus on lateral circulation cells. With the latter in mind, we use the following continuity equation to describe the spatial distribution of hydraulic head ($h(\mathbf{x})$; [L]) under steady-state conditions (Bear, 1972; Bear and Cheng, 2010):

$$\nabla \cdot \mathbf{Q} = 0, \quad (6.2)$$

where $\mathbf{Q}(\mathbf{x}) = -KH\nabla h$ is the vertically integrated flux [L^2T^{-1}], $\mathbf{q}(\mathbf{x}) = \mathbf{Q}(\mathbf{x})/H = -K\nabla h$ is the Darcy flux [LT^{-1}], $\mathbf{x} = [x, y]$ is the spatial coordinate vector [L], K is the hydraulic conductivity [LT^{-1}], $H(\mathbf{x}) = h - Z_b$ is the saturated thickness [L], and $Z_b(x)$ is the vertical location of the impermeable layer elevation with respect

to a reference datum $z = 0$ [L]. See Figure 6.1C and inset for the cross-section A-A' for additional details. For simplicity, and without loss of generality, we assume $Z_b(x) = J_x(3L - x)$, with J_x [-] and L [L] the average valley slope and the meander wavelength in the direction parallel to the alluvial valley axis (x -direction), respectively.

Boundary conditions are imposed to resemble a periodic system of meander bends running along the alluvial valley axis. The hydraulic head along the meandering channel ($\mathbf{x} \in \partial\Omega_c$) is given by $h(\mathbf{x}) = H_c + (3L)J_x - \frac{J_x}{\sigma}s(\mathbf{x})$, where $\sigma = \lambda/L$ is the meander sinuosity [-], $s(\mathbf{x})$ is the arc length along the channel [L], and H_c is the channel saturated thickness [L]. The model is minimally affected by changes in H_c ; therefore, we assumed a typical value of 10 m characteristic of alluvial aquifers (Larkin and Sharp JR, 1992). A periodic boundary condition is assumed for the lateral boundaries ($\mathbf{x} \in \partial\Omega_u \vee \partial\Omega_d$), where a prescribed hydraulic head drop proportional to the average valley slope is imposed, resulting in $h(x = 3L, y) = h(x = 0, y) - (3L)J_x$. Finally, we assume that flow along the alluvial valley boundary ($\mathbf{x} \in \partial\Omega_v$) is given by $\mathbf{n} \cdot \mathbf{Q} = -KHJ_y$, with J_y [-] the average slope of the far-field water table perpendicular to the alluvial valley axis (y -direction) and \mathbf{n} an outward unit vector. In this case, we use J_y to capture the role of regional groundwater flow under neutral ($J_y = 0$), gaining ($J_y > 0$), or losing ($J_y < 0$) conditions.

To aid the interpretation and parameterization of scenarios, we recast the flow model in nondimensional terms. This is also done for all the processes that we model and is described in detail in the Supporting Information. After nondimensionalization, the solution to this problem for the dimensionless hydraulic head ($h^* = h/(J_x\lambda)$), vertically integrated flux ($\mathbf{Q}^* = \mathbf{Q}/Q_c = \mathbf{Q}/(KJ_x^2\lambda)$), Darcy flux ($\mathbf{q}^* = \mathbf{q}/q_c = \mathbf{q}/(KJ_x)$), or any boundary-integrated flux metric only depends on the following dimensionless variables (see Appendix C, Appendix C.2 for a detailed derivation):

$$\sigma = \sigma(\theta_0, J_f, J_s), \quad \Pi_{H_c} = \frac{H_c}{J_x\lambda} \quad \Pi_{J_y} = \frac{J_y}{J_x}, \quad (6.3)$$

where the sinuosity σ is a function of the Kinoshita curve parameters θ_0 , J_f , and J_s , defining the topology of the meander, Π_{H_c} is a dimensionless number that compares the stage at the river relative to the characteristic head drop along a meander, and Π_{J_y} reflects the magnitude and direction (positive for gaining and negative for losing channels) of the regional groundwater flow, the larger this number, the more important is the modulating role of regional groundwater on the hyporheic exchange process.

6.2.1.2 Water Age

The age of water (τ ; [T]) describes the time of exposure of water and its constituents to the subsurface re-active environment. In particular, the probability distribution function of age, known as the age distribution

$(\psi(\mathbf{x}, \tau); [\text{T}^{-1}])$, serves as a proxy metric for the hyporheic zone's biogeochemical potential. From a numerical perspective, it is easier to model the cumulative age distribution $(\Psi(\mathbf{x}, \tau); [-])$, which is described by the Advection-Dispersion Equation (ADE) (Ginn, 1999; Gomez and Wilson, 2013), and then estimate the probability distribution function as $\psi(\mathbf{x}, \tau) = \partial\Psi/\partial\tau$. Here, we expand on the mathematical formulation previously proposed by Gomez et al. (2012) and Gomez-Velez et al. (2017) for a vertically-integrated system:

$$\frac{\partial(\varepsilon_p(h - Z_b)\Psi)}{\partial\tau} = \nabla \cdot (\mathbf{D}\nabla\Psi) - \nabla \cdot (\mathbf{Q}\Psi) \quad (6.4)$$

where ε_p is porosity [-] and $\mathbf{D} = \{D_{i,j}\}$ is the vertically-integrated dispersion-diffusion tensor [L^3T^{-1}]. The dispersion-diffusion tensor is defined as

$$D_{i,j} = \alpha_T |\mathbf{Q}| \delta_{i,j} + (\alpha_L - \alpha_T) \frac{Q_i Q_j}{|\mathbf{Q}|} + \frac{\varepsilon_p H}{\eta} D_m \quad (6.5)$$

with α_T and α_L the transverse and longitudinal dispersivities [L], respectively, $\delta_{i,j}$ the Kronecker delta function [-], D_m the molecular diffusion [L^2T^{-1}], and $\eta = \varepsilon_p^{-1/3}$ the tortuosity factor approximated with the Millington and Quirk model (Millington and Quirk, 1961).

By definition, water inside the domain has already aged (i.e., $\tau > 0$). Mathematically, this corresponds to $\Psi(x = 0, y, \tau = 0) = 0$. We assume that water entering the alluvial aquifer from the channel (i.e., $\forall \mathbf{x} \in \partial\Omega_c \mid \mathbf{n} \cdot \mathbf{Q} \leq 0$) is “new,” and therefore $\Psi(\mathbf{x}, \tau) = 1$. In contrast, we assume water leaving the alluvial aquifer into the channel ($\forall \mathbf{x} \in \partial\Omega_c \mid \mathbf{n} \cdot \mathbf{Q} > 0$) can be described by an advective boundary condition, that is $-\mathbf{D}\nabla\Psi = 0$. Similar to the flow model, we assume a periodic boundary condition, $\Psi(x = 3L, y, \tau) = \Psi(x = 0, y, \tau)$, for the lateral boundaries ($\mathbf{x} \in \partial\Omega_u \vee \partial\Omega_d$). Finally, we prescribe boundary conditions for the alluvial valley boundary ($\mathbf{x} \in \partial\Omega_v$). Under gaining condition, when water enters the domain from the regional aquifer, we assume that the water age distribution at the boundary is characterized by an exponential distribution $\Psi(\mathbf{x}, \tau) = 1 - \exp(-\tau/\tau_v)$, with a mean age τ_v . Typical values for the mean age of water discharging to rivers from regional groundwater (τ_v) range from one to ten years (McGuire and McDonnell, 2006). With this in mind, and consistent with (Gomez-Velez et al., 2014), we selected $\tau_v = 10$ years for our simulations. On the other hand, under losing conditions, when the water leaves the domain, we assume an advective boundary condition along $\partial\Omega_v$, that is, $-\mathbf{D}\nabla\Psi = 0$.

The net cumulative age distribution for the water leaving the hyporheic zone, also known as the cumulative residence time distribution, is estimated by flux-weighting $\Psi(\mathbf{x}, \tau)$ along the boundary where hyporheic water returns to the channel ($\partial\Omega_{c,hz}$):

$$F(\tau) = \frac{\int_{\partial\Omega_{c,hz}} (\mathbf{n} \cdot \mathbf{Q}(\mathbf{x})) \Psi(\mathbf{x}, \tau) d\mathbf{x}}{\int_{\partial\Omega_{c,hz}} (\mathbf{n} \cdot \mathbf{Q}(\mathbf{x})) d\mathbf{x}}. \quad (6.6)$$

Finally, Eq. (6.4) can be nondimensionalized by introducing dimensionless age $\tau^* = \tau/\tau_c$, where $\tau_c = \lambda/(KJ_x)$ is a characteristic time scale (see C, Appendix C.2 for a detailed derivation).

6.2.1.3 Reactive Transport of Solutes Involved in Nitrogen Transformations

The Advection-Dispersion-Reaction Equation (ADRE) describes the spatiotemporal evolution of the reactive solutes involved in nitrogen transformations, including nitrate (NO_3^- ; subscript *NO*), ammonium (NH_4^+ ; subscript *NH*), oxygen (O_2 ; subscript *O*), and dissolved organic carbon (DOC; subscript *C*) (Molz et al., 1986; Hunter et al., 1998; Gu et al., 2007; Zarnetske et al., 2012). In particular, we recast the biogeochemical model used by Zarnetske et al. (2012) for the microbially mediated reactions in Table 6.1 for a vertically-integrated domain:

$$\frac{\partial(\varepsilon_p H C_i)}{\partial t} = \nabla \cdot (\mathbf{D} \nabla C_i) - \nabla \cdot (\mathbf{Q} C_i) + \varepsilon_p H R_i \quad (6.7)$$

where $C_i(\mathbf{x}, t)$ and R_i are the concentration [ML^{-3}] and reaction rate [$\text{ML}^{-3}\text{T}^{-1}$] for species i ($i = \text{NO}, \text{NH}, \text{O}$, or C), respectively. The reaction rates are described by Monod kinetics models (Zarnetske et al., 2012):

Table 6.1: Microbial Reaction Processes in the Transport Model^a

Reaction Processes	Stoichiometric Reaction Equation
Aerobic Respiration	$\text{CH}_2\text{O} + \text{O}_2 \rightarrow \text{CO}_2 + \text{H}_2\text{O}$
Nitrification	$\text{O}_2 + (1/2)\text{NH}_4^+ \rightarrow (1/2)\text{NO}_3^- + \text{H}^+ + (1/2)\text{H}_2\text{O}$
Denitrification	$\text{CH}_2\text{O} + (4/5)\text{NO}_3^- + (4/5)\text{H}^+ \rightarrow (7/5)\text{H}_2\text{O} + (2/5)\text{N}_2 + \text{CO}_2$
Microbial NH_4^+ Uptake	$5\text{CH}_2\text{O} + \text{HCO}_3^- + \text{NH}_4^+ \rightarrow \text{C}_5\text{H}_7\text{NO}_2 + 4\text{H}_2\text{O} + \text{CO}_2$

^aAdapted from Zarnetske et al. (2012); Gu et al. (2007)

$$R_O = -V_O y_O X_{AR} \left(\frac{C_C}{K_C + C_C} \right) \left(\frac{C_O}{K_O + C_O} \right) - V_O (1 - y_O) X_{NIT} \left(\frac{C_{NH}}{K_{NH} + C_{NH}} \right) \left(\frac{C_O}{K_O + C_O} \right), \quad (6.8)$$

$$R_{NH} = -V_{NH} y_{NH} X_{NIT} \left(\frac{C_{NH}}{K_{NH} + C_{NH}} \right) \left(\frac{C_O}{K_O + C_O} \right) - V_{NH} (1 - y_{NH}) X_{UP} \left(\frac{C_{NH}}{K_{NH} + C_{NH}} \right) \left(\frac{C_C}{K_C + C_C} \right), \quad (6.9)$$

$$\begin{aligned}
R_{NO} = & V_{NH} y_{NH} X_{NIT} \left(\frac{C_{NH}}{K_{NH} + C_{NH}} \right) \left(\frac{C_O}{K_O + C_O} \right) \\
& - V_{NO} X_{DN} \left(\frac{K_I}{K_I + C_O} \right) \left(\frac{C_C}{K_C + C_C} \right) \left(\frac{C_{NO}}{K_{NO} + C_{NO}} \right),
\end{aligned} \tag{6.10}$$

$$\begin{aligned}
R_C = & -V_O y_O X_{AR} \left(\frac{C_C}{K_C + C_C} \right) \left(\frac{C_O}{K_O + C_O} \right) \\
& - V_{NO} X_{DN} \left(\frac{K_I}{K_I + C_O} \right) \left(\frac{C_C}{K_C + C_C} \right) \left(\frac{C_{NO}}{K_{NO} + C_{NO}} \right) \\
& - V_{NH} (1 - y_{NH}) X_{UP} \left(\frac{C_{NH}}{K_{NH} + C_{NH}} \right) \left(\frac{C_C}{K_C + C_C} \right) \\
& + \frac{\rho_b}{\varepsilon_p} \alpha (P - K_d C_C)
\end{aligned} \tag{6.11}$$

where V_i is the maximum microbial process reaction rate [T^{-1}]; X_j is the biomass of the j -th functional microbial group [ML^{-3}] facilitating aerobic respiration ($j = AR$), nitrification ($j = NIT$), biological uptake ($j = UP$), or denitrification ($j = DN$); K_I is the inhibition constant for the denitrification reaction [ML^{-3}]; K_i is the half-saturation constant [ML^{-3}], ρ_b is the sediment bulk density [ML^{-3}], and y_O and y_{NH} are the dimensionless partition coefficients for oxygen and ammonium, respectively. These partition coefficients depend on the reaction of interest. More specifically, the partition coefficient for the oxygen demand process (y_O) is based on the known free energy yield between the two competing processes of aerobic respiration and nitrification Zarnetske et al. (2012). On the other hand, the ammonium partition coefficient (y_{NH}) is based on the bioenergetics and bacteria growth efficiencies (Zarnetske et al., 2012).

Finally, this model assumes that the dissolution of particulate organic carbon (POC, P) [$MM_{\text{sediment}}^{-1}$] is described by an irreversible, first-order process (Jardine et al., 1992; Robertson and Cherry, 1995):

$$\frac{\partial P}{\partial t} = -\alpha(P - K_d C_C), \tag{6.12}$$

where α is the first-order mass transfer coefficient [T^{-1}], K_d is the linear distribution coefficient for the sediment [$L^3 M_{\text{sediment}}^{-1}$].

Initial and boundary conditions are needed to complete the mathematical statement. An initial distribution of dissolved solutes ($C_i(\mathbf{x}, t = 0) = C_{i,0}(\mathbf{x})$) and POC ($P(t = 0) = P_0$) are prescribed. Because our focus is on the long-term behavior of the alluvial aquifer under the assumption of time-invariant flow, we explore the spatial distribution of reactive species after it reaches a steady-state equilibrium, where initial conditions are irrelevant. With this in mind, we can assume $C_i(\mathbf{x}, t = 0) = 0$. In the following, we will further specify this

model.

Boundary conditions along the meandering channel depend on flow direction. The concentration of dissolved species in rivers can have important and large variations in space and time (e.g., DOC and DO, Creed et al. (2015) and Diamond et al. (2023), respectively). To reduce the complexity of our model, for water entering the alluvial aquifer from the channel (i.e., $\{\forall \mathbf{x} \in \partial\Omega_c \mid \mathbf{n} \cdot \mathbf{Q} < 0\}$), we prescribe constant concentrations for all the dissolved species ($C_i = C_{i,c}$). On the other hand, for water leaving the alluvial aquifer and discharging into the channel (i.e., $\{\forall \mathbf{x} \in \partial\Omega_c \mid \mathbf{n} \cdot \mathbf{Q} > 0\}$), we assume an advective boundary condition of the form $-\mathbf{n} \cdot (-\mathbf{D}\nabla C_i) = 0$. A periodic boundary condition is assumed for the lateral boundaries ($\mathbf{x} \in \partial\Omega_u \vee \partial\Omega_d$), where the spatial distribution of the solute concentration along the upstream and downstream boundaries satisfies $C_i(x = 3L, y) = C_i(x = 0, y)$. Finally, the conditions along the alluvial valley boundary ($\mathbf{x} \in \partial\Omega_v$) depend on the regional groundwater flow direction. Under neutral conditions ($J_y = 0$) we impose a no-flux boundary condition, $-\mathbf{n} \cdot (\mathbf{Q}C_i - \mathbf{D}\nabla C_i) = 0$. Under gaining conditions ($J_y > 0$), we prescribe constant concentrations for all the dissolved species ($C_i = C_{i,v}$). And, under losing conditions ($J_y < 0$), we assume an advective boundary condition of the form $-\mathbf{n} \cdot (-\mathbf{D}\nabla C_i) = 0$.

To gain some perspective on the characteristic time scale for POC dissolution, we explore the following scenario. The maximum dissolution rate for POC is reached when $C_C = 0$, resulting in a simplified version of Eq. (6.12):

$$\frac{dP}{dt} = -\alpha P \quad (6.13)$$

The solution to this ordinary differential equation (ODE) is given by $P(t) = P_0 \exp(-\alpha t)$, with P_0 the initial concentration of POC within the sediment. In this case, $t_{c,POC} = \alpha^{-1}$ is a characteristic time scale for the dissolution of POC, which typically varies within the range 0.1-10 years (Zarnetske et al., 2012). In other words, the time required for a 10% decrease of the original POC available can be calculated as $t_{10\%} = -t_{c,POC} \ln(0.1)$, resulting in approximately 0.23-23 years. Again, this is a low-end estimate of the dissolution time scale, which is expected to be significantly longer given the availability of DOC. Furthermore, this estimate is consistent with the relatively recalcitrant nature of POC, and it is likely longer given the potential for replenishment of POC by hydrologic events taking place at time scales shorter of the order of magnitude of $t_{10\%}$ (see, e.g., Gu et al. (2007)). Based on these arguments, it is reasonable to assume that the change of POC concentration within the alluvium is insignificant during the modeling time scales (i.e., $P(t) \approx P_0$). This approximation simplifies the reaction rate for DOC, where the contribution of POC (see last term in Eq. (6.11)) can be replaced by $(\alpha \rho_b / \varepsilon_p)(P_0 - K_d C_C)$. We validated this assumption with a series of one-dimensional numerical experiments using typical values of the coefficients involved in the model. In this

case, we solved the system of PDEs from Eqs (6.7)-(6.11), which is transient in nature and accounts for the coupled dissolution of POC, and compare its long-term solution with the steady-state version of these equations, where $\partial(\varepsilon_p HC_i)/\partial t \rightarrow 0$ and $P(t) = P_0$. Both solutions converge to the same concentrations (see Figure C.3 for an example.)

Similar to the flow and water age models, we nondimensionalize the biogeochemical model. In addition to the dimensionless variables defined in Eq. (6.3), the solution to this fully-coupled system of PDEs only depends on the values of 18 dimensionless variables (see Appendix C, Section C.2 for a detailed derivation). First, a series of Damköhler numbers (Da_i) comparing the role of reaction and transport processes (expressed as the ratio of time scales characterizing advective transport and biogeochemical transformations) of the i -th constituent (Oldham et al., 2013):

$$Da_O = \frac{V_O \lambda}{KJ_x}, Da_{NO} = \frac{V_{NO} \lambda}{KJ_x}, Da_{NH} = \frac{V_{NH} \lambda}{KJ_x}, Da_P = \frac{\alpha \lambda}{KJ_x} \quad (6.14)$$

Transformation in systems where $Da_i \gg 1$ are likely limited by the transport of critical constituents (i.e., the supply) relative to the reaction demand. We refer to these systems as reaction-dominated or transport limited. In contrast, transformations in systems with $Da_i \ll 1$ are limited by the reaction rate. We refer to these systems as transport-dominated or reaction-limited.

Second, a series of dimensionless channel concentrations:

$$\Pi_{C,c} = \frac{C_{C,c}}{C_{O,c}}, \Pi_{NH,c} = \frac{C_{NH,c}}{C_{O,c}}, \Pi_{NO,c} = \frac{C_{NO,c}}{C_{O,c}}, \Pi_{P-c} = \frac{\rho_b P_0}{\varepsilon_p C_{C,c}} \quad (6.15)$$

and alluvial valley concentrations:

$$\Pi_{O,v} = \frac{C_{O,v}}{C_{O,c}}, \Pi_{C,v} = \frac{C_{C,v}}{C_{O,c}}, \Pi_{NH,v} = \frac{C_{NH,v}}{C_{O,c}}, \Pi_{NO,v} = \frac{C_{NO,v}}{C_{O,c}} \quad (6.16)$$

The dimensionless concentrations for the channel and the alluvial valley boundary ($\Pi_{i,c}$ and $\Pi_{i,v}$) i -th chemical constituent are scaled by channel oxygen concentration $C_{O,c}$. In particular, the dimensionless parameter $\Pi_{C,c} = C_{C,c}/C_{O,c}$ plays a central role in the denitrification process because it dictates the availability of oxygen and DOC for the aerobic respiration reaction within the hyporheic zone. This, at the same time, becomes a critical control in the nitrification and denitrification reactions that depend on this respiration reac-

tion (see Table 6.1). In other words, $\Pi_{C,c}$ is a master variable critical to identify the biogeochemical potential of hyporheic zones to process nitrate. If $\Pi_{C,c} > 1$, the reaction will be limited by the availability of oxygen, and we refer to these systems as oxygen-limited. On the other hand, if $\Pi_{C,c} < 1$, the availability of carbon limits the aerobic respiration process, and we refer to the system as carbon-limited. Among these dimensionless concentrations, the dimensionless initial POC content in the alluvium ($\Pi_{P-C} = (\rho_b P_0) / (\epsilon_p C_{C,c})$) is particularly important. Π_{P-C} can be understood as the ratio of the mass of carbon stored as POC per unit volume of alluvium to the maximum mass of carbon as DOC in the pores per unit volume of alluvium. The larger this number, the higher the potential of POC dissolution to offset the carbon limitation observed in systems with $\Pi_{C,c} < 1$. With this in mind, Π_{P-C} becomes a master dimensionless variable to evaluate the biogeochemical potential of hyporheic exchange.

Third, a series of dimensionless half-saturation (Π_{K_i}), inhibition (Π_{K_I}), and POC linear distribution (Π_{K_d}) coefficients:

$$\Pi_{K_C} = \frac{K_C}{C_{O,c}}, \Pi_{K_O} = \frac{K_O}{C_{O,c}}, \Pi_{K_{NH}} = \frac{K_{NH}}{C_{O,c}}, \Pi_{K_{NO}} = \frac{K_{NO}}{C_{O,c}}, \Pi_{K_I} = \frac{K_I}{C_{O,c}}, \Pi_{K_d} = \frac{K_d C_{O,c}}{P_0} \quad (6.17)$$

6.2.2 Selection of Scenarios: Exploring the Parameter Space

In the following, we describe the approach used to generate the simulation scenarios. In this case, we vary the meander topology and model parameters. In total, we performed 10,200 numerical simulations.

6.2.2.1 Meander Topology

The maximum angular amplitude (θ_0), flatness (J_f), and skewness (J_s) parameters of the Kinoshita curve (Eq. (6.1)) offer enough flexibility to capture the key aspects of the forms observed in single meanders (Seminara, 2006). Here, we explored the parameter space ($\theta_0 \in [30, 120]$, $J_s \in [0, 10]$, and $J_f \in [0, 10]$) to reproduce four types of meander planimetry similar to the ones studied by Revelli et al. (2008). As shown for the selected topologies in Figure 6.2, we progressively increased the sinuosity from 2.1 to 5.9, and the size of the meander neck (dashed red line) decreases with increasing θ_0 , while the degree of symmetry decreases with increasing skewness. To assess the importance of the meander neck, which significantly impacts the hydrodynamics of hyporheic exchange and biogeochemical transformation, we define the funneling factor $FF = L_n / L_l$, where L_n and L_l are the maximum distances within the meander neck and lobe, respectively, of lines parallel to the line defined by the meander inflection points. High FF values correspond to meanders with narrow necks and significant lobe space.

It is important to note that the topologies in Figure 6.2 are shown in the dimensionless space $x^* = x / \lambda$ and

$y^* = x/\lambda$, and therefore have a unitary channel length (i.e., arc wavelength). However, because the Kinoshita curve scales linearly with arc wavelength, we can obtain a meander with any value of λ without changing the topology simply by multiplying the axes x^* and y^* by a factor of λ .

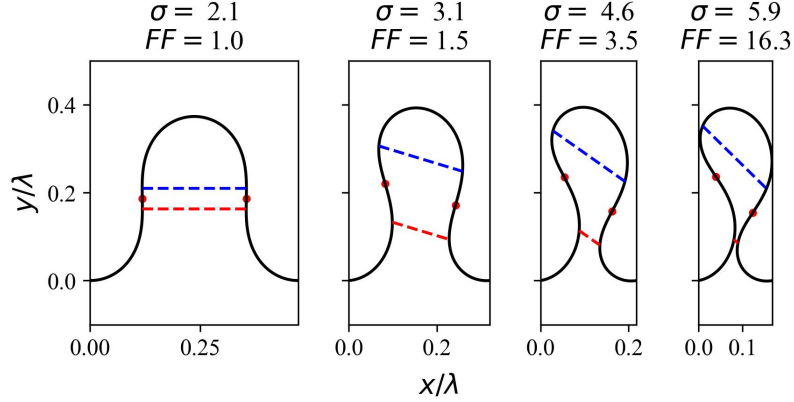


Figure 6.2: Meander topologies used in the analysis. Four Kinoshita topologies generated with parameters, from left to right, $\theta_0 = [90, 105, 115, 120]^\circ$, $J_s = [0, 0.014, 0.020, 0.020]$, and $J_f = [0.0048, 0, 0, 0]$. Axes are in dimensionless coordinates $x^* = x/\lambda$ and $y^* = x/\lambda$, resulting in meanders with a unitary dimensionless arc wavelength. The red dots denote the inflection points, and the dashed lines represent the characteristic lengths of the meander neck (red) and lobe (blue). These lengths are estimated as the longest distance within the neck or lobe along a line parallel to the line defined by the inflection points. Each meander shows the sinuosity (σ) and funneling factor (FF).

6.2.2.2 System parameters

Central to our analysis is the selection of scenarios that span a parameter space representative of natural systems. Values for all the parameters involved in our models can be found in the literature (e.g., Hedin et al., 1998; Bekins et al., 1998; Lindsey et al., 2003; Gu et al., 2007, 2008a,b, 2012; Liao et al., 2012; Stelzer and Bartsch, 2012; Zarnetske et al., 2012; Deng et al., 2015; Hester et al., 2014; Sawyer, 2015; Zheng et al., 2016; Dwivedi et al., 2018; Green et al., 2018). However, reported values typically consist of a handful of observations or only a range, limiting our ability to establish correlations or empirical probability distributions. To partially address this issue, we use a Monte Carlo simulation approach to assess the variability of the dimensionless parameters controlling the flow, transport, and reaction models.

Our Monte Carlo analysis generates 10,000 independent random realizations of each parameter to calculate 10,000 random realizations of the dimensionless parameters. These realizations are then used to propose a probability density function (PDF) for each dimensionless parameter. For some parameters, we have enough data to obtain an empirical PDF (see below). However, in several cases, especially for critical biogeochemical parameters, we only have information about the typical ranges reported in the literature. Therefore, we assume an “uninformative” uniform distribution bounded by the reported range in these cases. If the parameter

varies over orders of magnitude, we assumed that the logarithm of the parameter was uniformly distributed.

For channel slope (J_x), channel DOC ($C_{C,c}$) oxygen concentrations ($C_{C,c}$), nitrate concentration ($C_{NO,c}$), and hydraulic conductivity (K), we propose empirical PDFs with values reported for the conterminous US (CONUS). First, values for J_x and mean annual discharge (Q_{ma}) were taken from the NHD Plus High-Resolution dataset (Moore et al., 2019). Oxygen, DOC, and nitrate concentrations were obtained from the CAMELS-Chem dataset, provided in Sterle et al. (2024). Values of oxygen concentration higher than 20 mg/L were removed because it is uncommon to find natural channels with such a high concentration; they account for less than 0.001% of the dataset. Hydraulic conductivity values were taken from the StreamCat database version 2 (Hill et al., 2016), which reports mean reach catchment lithological hydraulic conductivity. Finally, all the other parameters were explored with a uniform distribution. Table 6.2.2 summarizes these ranges. The probability distribution functions for the input parameters are shown in Figures C.4, C.5, C.6, and C.7; and the resulting probability distribution functions are shown in Figures C.8 and C.9.

To explore the effects of regional groundwater flow, we simulated scenarios with $\Pi_{J_y} = J_y/J_x \in [-10, -1, 0, 1, 10]$, covering neutral, gaining, and losing conditions. Consistent with our Monte Carlo analysis, we also analyzed a wide range of oxygen Damköhler numbers, covering reaction-limited systems ($Da_O \in [10^{-2}, 1]$) and transport-limited or supply-limited systems ($Da_O \in (1, 10^{14}]$). Similarly, we explored Π_C values representative of covered carbon-limited ($\Pi_C \in [10^{-2}, 1]$) and oxygen-limited ($\Pi_C \in (1, 10^2]$) systems. In general, Da_O and Π_C can be understood as master variables that dictate the consumption of oxygen through aerobic respiration, which, at the same time, constraining the reaction ladder leading to the progression of nitrification, denitrification, and uptake (Table 6.1).

Lastly, we evaluated two scenarios of the channel concentrations for nitrate (NO_3^-) and ammonium (NH_4^+). Like Zheng et al. (2016), we explored a pristine channel with $C_{NO} = 1$ mg/L and $C_{NH} = 0.05$ mg/L and a contaminated channel with $C_{NO} = 8$ mg/L and $C_{NH} = 5$ mg/L. We also explored three cases for POC concentration: $P_0 = [0, 0.02, 0.2]\%$. POC within the alluvial aquifer can offset the DOC limitations, enhancing biogeochemical transformations (Sawyer, 2015).

To reduce the parameter space, we assume the ratios V_{NO}/V_O and V_{NH}/V_O are relatively stable for most alluvial systems. In other words, for the purposes of our analyses, we assume that these ratios, and therefore, the ratios of their corresponding Da numbers (Eq. (6.14)) are constant. Figures (C.10) and C.11 in the Appendix C show the distribution of these ratios from our Monte Carlo (MC) realizations. In this case, we compared the MC-derived PDF and its mean value with the values reported by Zarnetske et al. (2012) ($V_O = 1.97 \text{ h}^{-1}$, $V_{NH} = 1.08 \text{ h}^{-1}$, and $V_{NO} = 3.98 \text{ h}^{-1}$). The simulated mean ratios are close to the ratios from Zarnetske et al. (2012).

Now, for the half-saturation constants, we assumed that the ratio of the Monod Kinetics term remains

Table 6.2: Parameters for the Monte Carlo analysis. This table includes information on the typical range of the parameter and the probability distribution function used for the generation of independent realizations. *ECDF* is the Empirical Cumulative Distribution Function, and *Uniform* is a uniform probability distribution function (i.e., uninformative prior).

Symbol	Range	Domain	Distribution	Units
J_x^a	$10^{-5} - 73.36$	Logarithmic	ECDF	–
K^b	$10^{-10} - 10^{-3.3}$	Logarithmic	ECDF	m s^{-1}
λ^c	$1 - 4.70$	Logarithmic	Uniform	m s^{-1}
$C_{O,c}^d$	$0 - 20$	Linear	ECDF	mg L^{-1}
$C_{NH,c}^e$	$0.05 - 5$	Logarithmic	Uniform	mg L^{-1}
$C_{NO,c}^d$	$0 - 19.6$	Linear	ECDF	mg L^{-1}
$C_{C,c}^d$	$0.1 - 171$	Logarithmic	ECDF	mg L^{-1}
P_0^f	$10^{-6} - 0.02$	Logarithmic	Uniform	mg mg^{-1}
V_O^e	$0.1 - 10$	Logarithmic	Uniform	h^{-1}
V_{NH}^e	$0.36 - 4.2$	Logarithmic	Uniform	h^{-1}
V_{NO}^e	$0.26 \text{ to } 10$	Logarithmic	Uniform	h^{-1}
α^e	$10^{-5} - 10^{-3}$	Logarithmic	Uniform	h^{-1}
K_O^e	$0.2 - 5.8$	Logarithmic	Uniform	mg L^{-1}
K_{NH}^e	$0.1 - 1.1$	Logarithmic	Uniform	mg L^{-1}
K_{NO}^e	$0.21 - 3.1$	Logarithmic	Uniform	mg L^{-1}
K_C^e	$1 - 10$	Logarithmic	Uniform	mg L^{-1}
K_d^e	$5 - 100$	Logarithmic	Uniform	L mg^{-1}
K_I^e	$0.2 - 1$	Logarithmic	Uniform	mg L^{-1}

^aMoore et al. (2019), ^bHill et al. (2016), ^cNHDPlus High-Res dataset, ^dSterle et al. (2022),

^eZarnetske et al. (2012), ^fFrom Sawyer (2015), Zarnetske et al. (2012), and Gu et al. (2007).

relatively constant. This ratio can be expressed in terms of the metric $M_i = [(K_O/C_{O,c}) + 1][[(K_i/C_{i,c}) + 1]$ with $i = C, NH, NO$. The MC-derived PDFs are consistent with the estimates with the values reported by Zarnetske et al. (2012) ($K_{DOC} = 8.68 \text{ mg/L}$, $K_{NH} = 0.43 \text{ mg/L}$, and $K_{NO} = 1.64 \text{ mg/L}$).

6.3 Results and Discussion

In the following, we use our modeling framework to explore the role of meander topology (the exchange driver), regional groundwater flow (the exchange modulator), and alluvium physical and biogeochemical properties of sinuosity-driven hyporheic exchange and its potential for biogeochemical transformations. To this end, we use the key dimensionless variables described in Section 6.2 (and derived in the Appendix C Section C.2), which provide master variables to characterize the exchange process in terms of widely available hydrogeomorphic parameters and water quality observations. Using these master variables is critical to gain mechanistic understanding, transferability, and the integration of this mechanism into future generations of water quality models.

6.3.1 Meander topology drives hyporheic exchange and conditions the modulating effects of regional groundwater flow

First, we focus on the exchange hydrodynamics, specifically, the interplay between two master dimensionless variables: σ and Π_{J_y} . The former corresponds to sinuosity, which encapsulates the Kinoshita curve parameters, and the latter represents the magnitude and direction (positive for gaining and negative for losing channels) of the regional groundwater flow (RGF).

6.3.1.1 Implications for flow

We performed systematic simulations of the exchange process spanning typical ranges for the dimensionless master variables for flow. The results, summarized in Figures 6.3 and 6.4, include four sinuosity values ($\sigma = 2.1, 3.1, 4.6,$ and 5.9), which correspond to significant changes in the funneling factor (respectively, $FF = 1.0, 1.5, 3.5,$ and 16.3), and five Π_{J_y} values. The Π_{J_y} values represent RGF parallel to the channel axis ($\Pi_{J_y} = 0$), which we refer to as neutral conditions, moderate gaining ($\Pi_{J_y} = 1$) and losing ($\Pi_{J_y} = -1$) RGF, and strongly gaining ($\Pi_{J_y} = 1$) and losing ($\Pi_{J_y} = -1$) RGF. All simulations have unitary dimensionless channel wavelength (i.e., dimensionless distance along the channel).

Changes in the master variables result in significant changes in the velocity field (colors in Figure 6.3) and extent of the sinuosity-driven hyporheic zone (area delimited by the black streamlines in Figure 6.3). Under neutral conditions ($\Pi_{J_y} = 0$, third row in Figure 6.3), all the sinuosity scenarios (columns) have important commonalities: (i) the hyporheic zone extends slightly into the alluvial valley, (ii) the highest fluxes occur along neck flow paths, and (iii) the lowest fluxes occur within the lobe. However, as sinuosity increases and the neck narrows (increasing funneling factor), the magnitude of the flux along neck flow paths significantly increases due to the higher hydraulic gradients. Previous work by Revelli et al. (2008) and Boano et al. (2010b) show similar zonation and highlight its importance for constraining the dominant transport time scales within the meander and, therefore, the potential for specific biogeochemical transformation. For example, flow paths along the lobe are more likely to contribute to processes that require long time scales such as methanogenesis (e.g., Dahm et al., 1998; Baker et al., 1999). In contrast, neck flow paths have shorter time scales for reactions to take place but are likely enough to control aerobic respiration and denitrification processes (e.g., Boano et al., 2010b). Note that except for the studies mentioned above, most previous work has focused on low sinuosity meanders where the neck does not impact the timescales (e.g., Cardenas, 2009a,b; Gomez et al., 2012; Gomez-Velez et al., 2017).

We explore four conditions where regional groundwater flow has a component perpendicular to the channel axis: moderate gaining ($\Pi_{J_y} = 1$) and losing ($\Pi_{J_y} = -1$) and strong gaining ($\Pi_{J_y} = 10$) and losing ($\Pi_{J_y} = -10$). In this case, the hyporheic zone is compressed, and in some cases, it does not develop (rows 1,

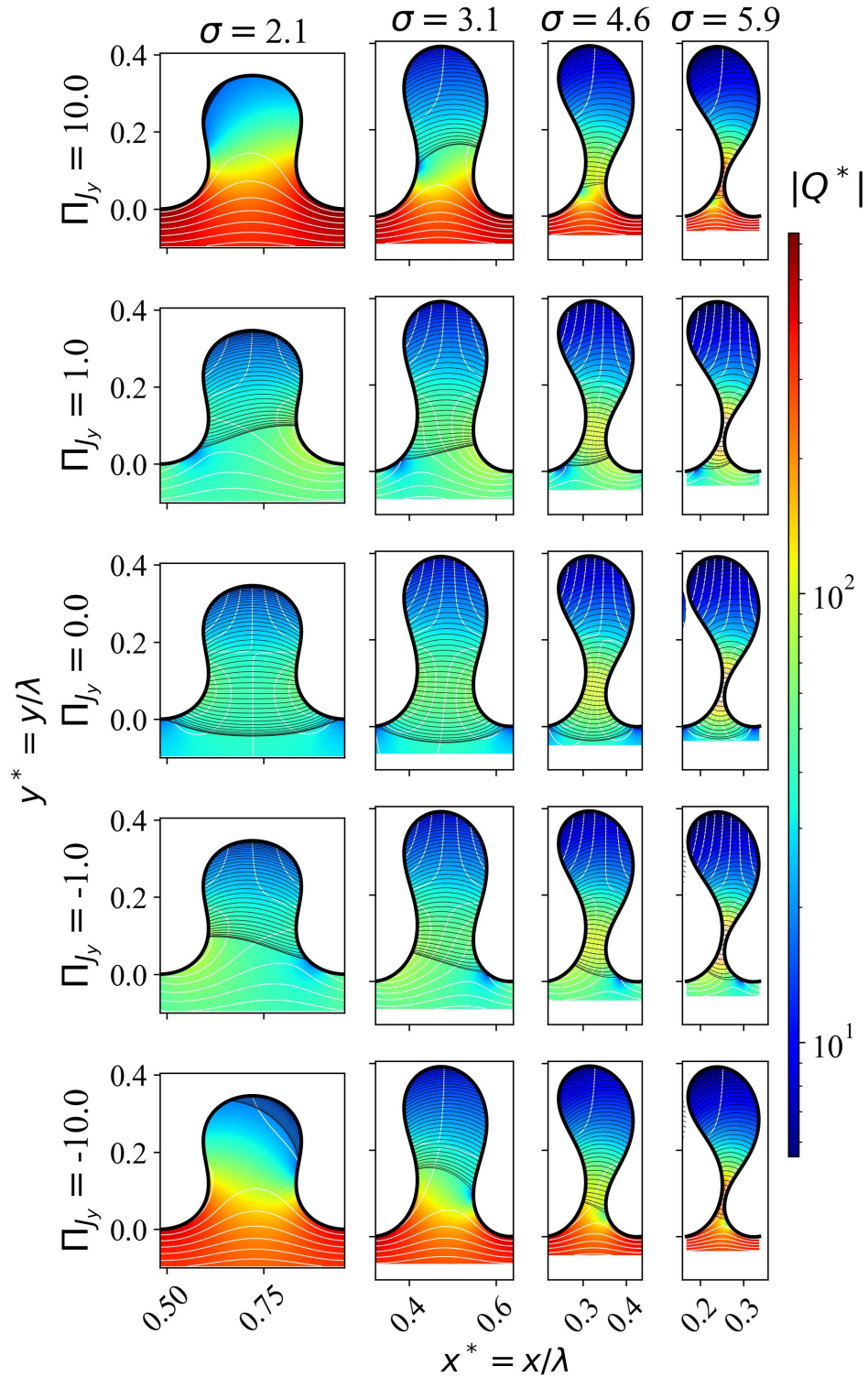


Figure 6.3: Flow field and sinuosity-driven hyporheic zone within the alluvial aquifer. The magnitude of the dimensionless flux (\mathbf{Q}^* ; colors), dimensionless hydraulic head (white contours), and hyporheic streamlines (black lines) for four meander topologies (columns) under neutral ($\Pi_{J_y} = 0$), moderate ($\Pi_{J_y} = 1$), and strong ($\Pi_{J_y} = 10$) regional groundwater flow conditions (rows).

2, 4, and 5 in Figure 6.3). Low sinuosity channels ($\sigma = 2.1$; first column in Figure 6.3) are susceptible to the compressing effect of regional groundwater flow. For example, for moderate RGF conditions ($\Pi_{J_y} = \pm 1$), the extent of the hyporheic zone decreases by about 30%, and a more significant proportion of the hyporheic zone is within the meander lobe. When this flux is further increased ($\Pi_{J_y} = \pm 10$), the exchange zone almost disappears, becoming confined to a small fraction of the meander lobe. These flow field changes reflect significant reductions in the total amount of water circulating through the hyporheic zone. For example, for $\sigma = 2.1$, the total hyporheic exchange flux can be reduced by a factor of 1.7 for moderate conditions and as much as a factor of 70 for strong conditions (Figure 6.4). As sinuosity (and funneling factor) increases, the compressing effect of regional gaining and losing conditions decreases (cases with $|\Pi_{J_y}| > 0$ and $3.1 \leq \sigma \leq 5.9$ in Figure 6.3). The meander neck offers a hydrodynamic shielding effect that protects the hyporheic zone, maintaining its general flow patterns and decreasing the differences in the total amount of hyporheic exchange (Figure 6.4).

Our findings highlight the critical role of meander topology to drive exchange and counteract the modulating effect of regional groundwater flow. This aspect has not been revealed in previous studies (e.g., Revelli et al., 2008; Boano et al., 2010b), where regional groundwater flow was not represented. Channels with low funneling factor and sinuosity are characterized by a fragile hyporheic zone that easily disappears under the influence of regional groundwater flow. This behavior is consistent with previous contributions by Cardenas (2009b) and Gomez-Velez et al. (2017). In contrast, channels with more significant funneling factors (and sinuosity) form a hydrodynamic shield that protects the sinuosity-driven hyporheic zone. Previous efforts to assess the cumulative biogeochemical potential of meanders along river corridors (e.g., Gomez-Velez et al., 2017; Gomez-Velez and Harvey, 2014; Gomez-Velez et al., 2015; Kiel and Bayani Cardenas, 2014) likely underestimate the importance of sinuosity-driven hyporheic exchange, which is more robust than previously thought.

6.3.1.2 Implications for transport time scales

Changes in the flow field result in changes in water residence time, which is a proxy for the time that solutes interact with the reacting environment and, therefore, for the biogeochemical potential within the hyporheic zone (Gomez and Wilson, 2013). We modeled the flux-weighted cumulative residence time distribution (CRTD) for the sinuosity-driven hyporheic zone. This distribution measures the characteristic time scales for hyporheic water discharging to the channel. While this is not the only constraint on reactivity, it is a fundamental metric that deserves attention. In particular, because it provides insight into the changes in transport mechanisms, in the following subsection, we summarize the results of a more detailed exploration of the biogeochemical transformation and the balance between residence times and reaction time scales.

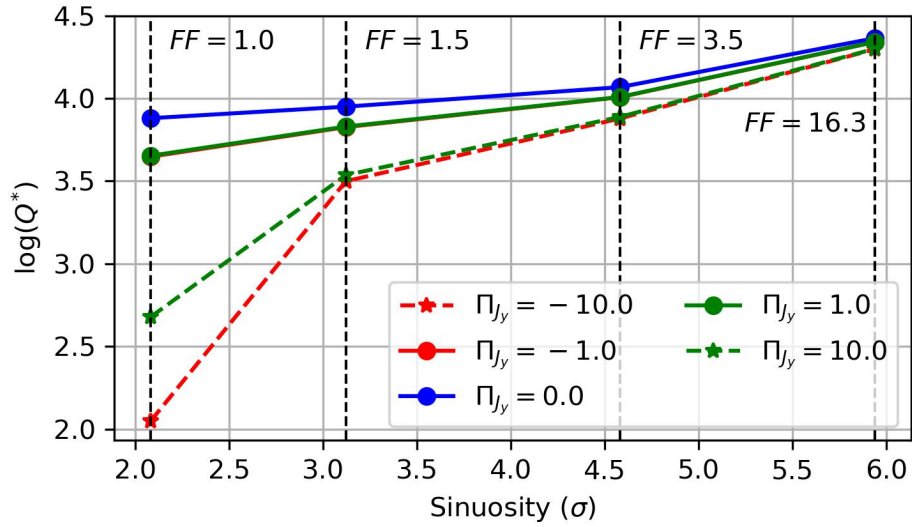


Figure 6.4: Total dimensionless hyporheic exchange flux (Q^*) as a function of meander topology (σ) and regional groundwater flow (Π_{J_y}). The funnelling factor (FF) for each meander topology is included as a reference. Also, notice that the green solid line ($\Pi_{J_y} = 1$) is on top of the red line ($\Pi_{J_y} = -1$).

As expected, increasing the funnelling factor (or sinuosity) shifts the CRTD left toward younger residence times (compare blue and red curves in Figure 6.5). This shift is expected because the relative contribution of meander neck flow paths, which have younger water, to the total exchange increases as sinuosity increases. For example, the median residence time for a meander with $\sigma = 5.9$ (blue lines in Figure 6.5) is about two orders of magnitude younger than the ones observed in low-sinuosity meanders ($\sigma = 2.1$, red lines in 6.5).

Interestingly, increasing the regional groundwater flow has relatively minor effects on the overall shape of the CRTD (notice the variability between lines of the same color, which correspond to different values of Π_{J_y} , in Figure 6.5). Differences are minimal for high-sinuosity cases, where the hyporheic zone is only slightly affected by the regional groundwater flow. For example, for $\sigma = 5.9$, increasing regional groundwater flow shifts the CRTD towards younger ages. In this case, the outer hyporheic flow paths within the alluvium are compressed (see the last column of Figure 6.3). Because these flow paths have lower velocities and travel longer distances, their removal results in a slightly younger CRTD. In other words, the role of the meander neck and its overall contribution to the total exchange flux is enhanced.

Meanders with $\sigma = 3.1$ and 4.6 behave somewhat differently because some of their neck flow paths are removed by the RGF, leading to an enhanced role of older residence times within the meander lobe. For example, when these meanders are exposed to moderate regional groundwater flow (dashed lines in Figure 6.5), their CRTD is biased towards younger residence times. This bias is explained by the prevalence

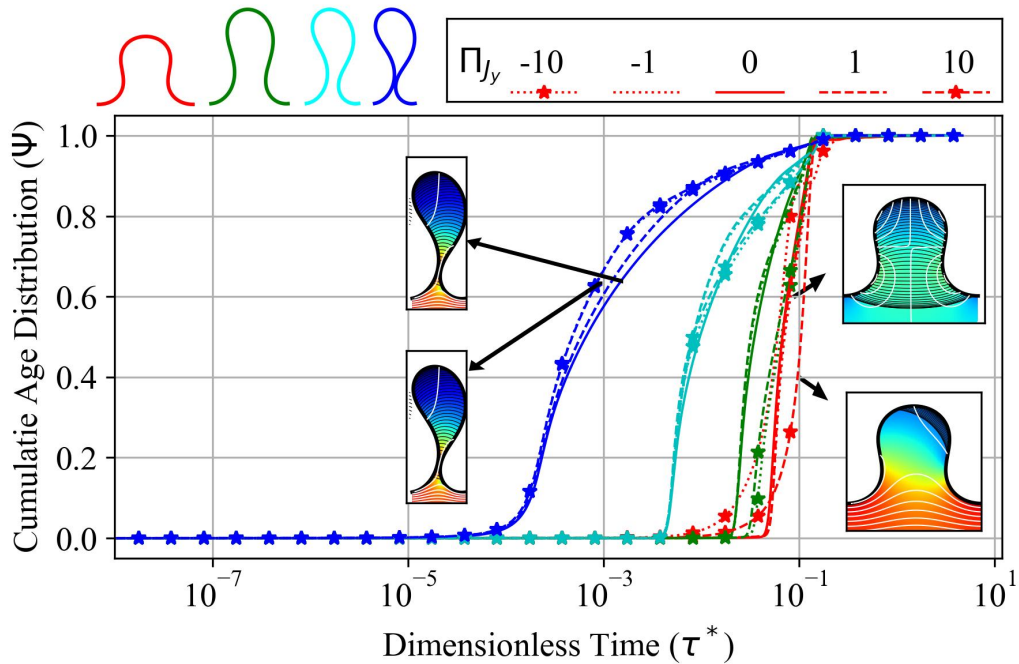


Figure 6.5: Cumulative residence times (CRTD). CRTD of all meander topologies separated by the colors shown above, the line styles denote the stream conditions, from strong gaining ($\Pi_{J_y} = 10$) to strong losing ($\Pi_{J_y} = -10$) conditions, passing through neutral conditions ($\Pi_{J_y} = 0$).

of neck flow paths, which remain dominant (see second and fourth rows in Figure 6.3). However, under strong regional groundwater flow ($|\Pi_{J_y}| = 10$), a more significant fraction of the neck flow paths are removed, resulting in a higher relative contribution of older water from the meander lobe and a shift the CRTD towards older residence times (see dashed lines with stars in Figure 6.5).

For the lowest sinuosity ($\sigma = 2.1$), the neck flow paths are readily removed under the modulating effect of RGF. In the case of strong RGF, only a small hyporheic zone with short flow paths and low velocities remains (see first and last row in the first column of Figure 6.3). This compression of the hyporheic zone results in younger residence times for low quantiles and older residence times for higher quantiles (Figure 6.5).

Previous efforts have highlighted the dominant role of neck flow paths in residence times distributions (Revelli et al., 2008; Boano et al., 2010b). However, these studies did not assess the role of regional groundwater flow. On the other hand, Cardenas (2009b) and Gomez-Velez et al. (2017) represent the role of regional groundwater flow but only explore low-sinuosity meanders. Here, we demonstrate the critical interplay between these two factors and how they affect transport time scales. Furthermore, it is important to highlight that while the effects of RGF in the CRTD are minor for moderate sinuosity, the changes in the total amount of exchange flux can be one to two orders of magnitude. In other words, two systems with the same sinu-

osity and different values of Π_y will have similar characteristic time scales for transport, but very different amounts of water (and solutes) will be exposed to the hyporheic reactive environment.

6.3.2 The Biogeochemical Potential of Sinuosity-Driven Hyporheic Zones

Flow and residence time are critical indicators of the potential for biogeochemical transformation; however, realizing this potential strongly depends on the reactions considered and their biogeochemical time scales. To further explore this issue, we focused our analysis on nitrogen transformations (see Table 6.1), and in particular on the net biogeochemical function of sinuosity-driven hyporheic zones to remove or produce nitrate (NO_3^- ; subscript *NO* in our model), given the widespread excess in streams and rivers across the globe (Smith et al., 2003; Dodds et al., 2013).

Our simulations are spatially explicit; however, to evaluate the net biogeochemical potential of sinuosity-driven hyporheic zones, we conceptualize this exchange zone as a biogeochemical reactor that processes inputs from the channel and delivers outputs back to the channel. With this aggregate perspective, we define the net biogeochemical potential for a constituent *i* (e.g., NO_3^- , NH_4^+ , O_2 , and DOC) as the net mass of the constituent removed ($P_i > 0$) or produced ($P_i < 0$) within the reactor relative to the input mass. Mathematically, this is given by

$$P_i = \frac{M_{i,in} - M_{i,out}}{M_{i,in}} = 1 - \frac{M_{i,out}}{M_{i,in}} \quad (6.18)$$

where $M_{i,in}$ and $M_{i,out}$ are the mass of constituent *i* entering and leaving the hyporheic zone, respectively.

We illustrate the spatial variation of the biogeochemical potential for nitrate (P_{NO}) by estimating the metric along flow paths (Figure 6.6). In this case, we explore eight scenarios with varying sinuosity and Da_O , which highlights the complex interplay between transport and biogeochemical time scales, substrate availability, and sinuosity. For example, systems with high Da_O values ($Da_O = 10^8$) are characterized by hyporheic flow paths with plenty of contact time with the reactive environment and, therefore, a tendency to fully consume the nitrate recharged from the channel within a short distance. When we aggregate the contribution from all the flow paths leaving the hyporheic zone, these meanders behave as a net sink for nitrate. In contrast, hyporheic flow paths in meanders with low Da_O ($Da_O = 10^4$) take longer distances to transition from source (red) to sink (blue). In fact, increasing sinuosity results in flow paths crossing the meander neck that remain as a sink (meander with $\sigma = 4.6$ and $Da_O = 10^4$ in Figure 6.6) and ultimately a system that behaves as a net source for nitrate. The net behavior can be explained by the large contribution of meander neck flow paths to the overall flux. In the following subsection, we explore a wide range of scenarios to better understand the controls on nitrogen retention/production within sinuosity-driven hyporheic zones.

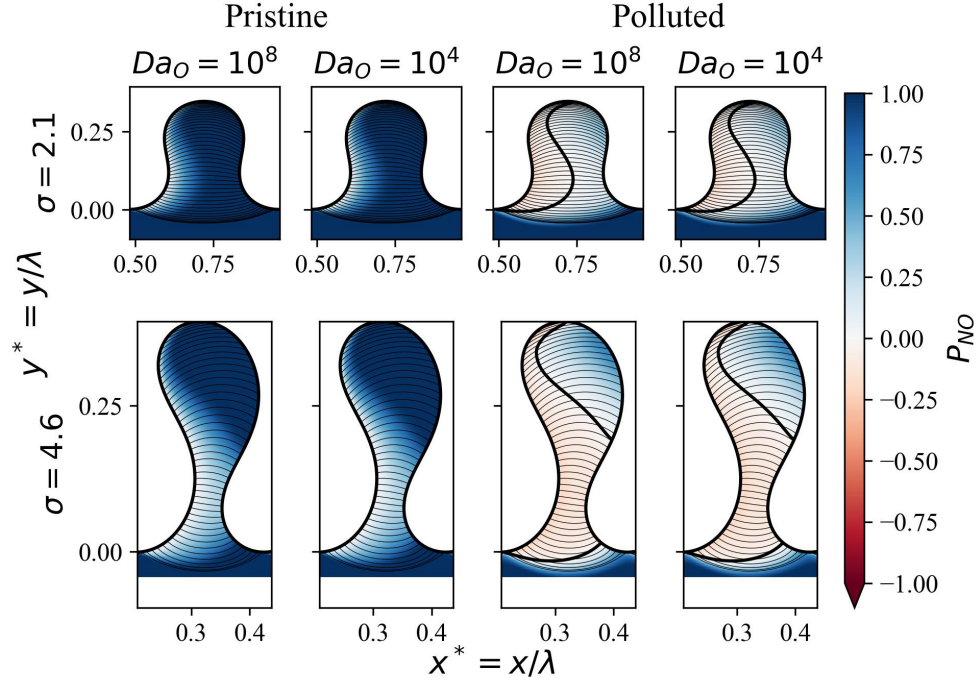


Figure 6.6: Potential for the biogeochemical transformation of nitrate in a meander under neutral conditions ($\Pi_{J_y} = 0$) with $\Pi_{C,c} = 1$. The colors denote the potential P_{NO} (calculated with Equation (6.18)), the thick black line denotes the zero contour value (transition from source to sink of nitrate), and the thin black lines denote streamlines. The two first columns show simulations for pristine conditions, while the last two show polluted conditions.

6.3.2.1 Master dimensionless variables for biogeochemical potential: $\Pi_{C,c}$ and Da_O

We explore the overall hyporheic potential for biogeochemical transformations by exploring two master dimensionless variables that emerged from our dimensional analysis: (i) the availability of DOC relative to dissolved oxygen for water entering the hyporheic zone ($\Pi_{C,c} = C_{C,c}/C_{O,c}$) and (ii) the Damköhler number for aerobic respiration ($Da_O = (V_O\lambda)/(KJ_x)$). These variables are expected to play a fundamental role in nitrogen transformations and can be easily calculated at the catchment to continental scales from readily available hydrogeomorphic and empirical data. Note, however, that previous studies have almost exclusively focused on exploring the role of Da_O as a master variable for other hyporheic exchange processes (e.g., Gu et al., 2007; Zarnetske et al., 2012) without a systematic analysis of $\Pi_{C,c}$. This dimensionless ratio naturally emerges as a critical quantity from the scaling analysis, yet it is seldom considered a master variable. As we show here, $\Pi_{C,c}$ varies significantly in river networks and plays a significant role in the biogeochemical potential of sinuosity-driven hyporheic zones.

In the following, we summarize our results using the $\Pi_{C,c} - Da_O$ domain (Figure 6.7A), where each

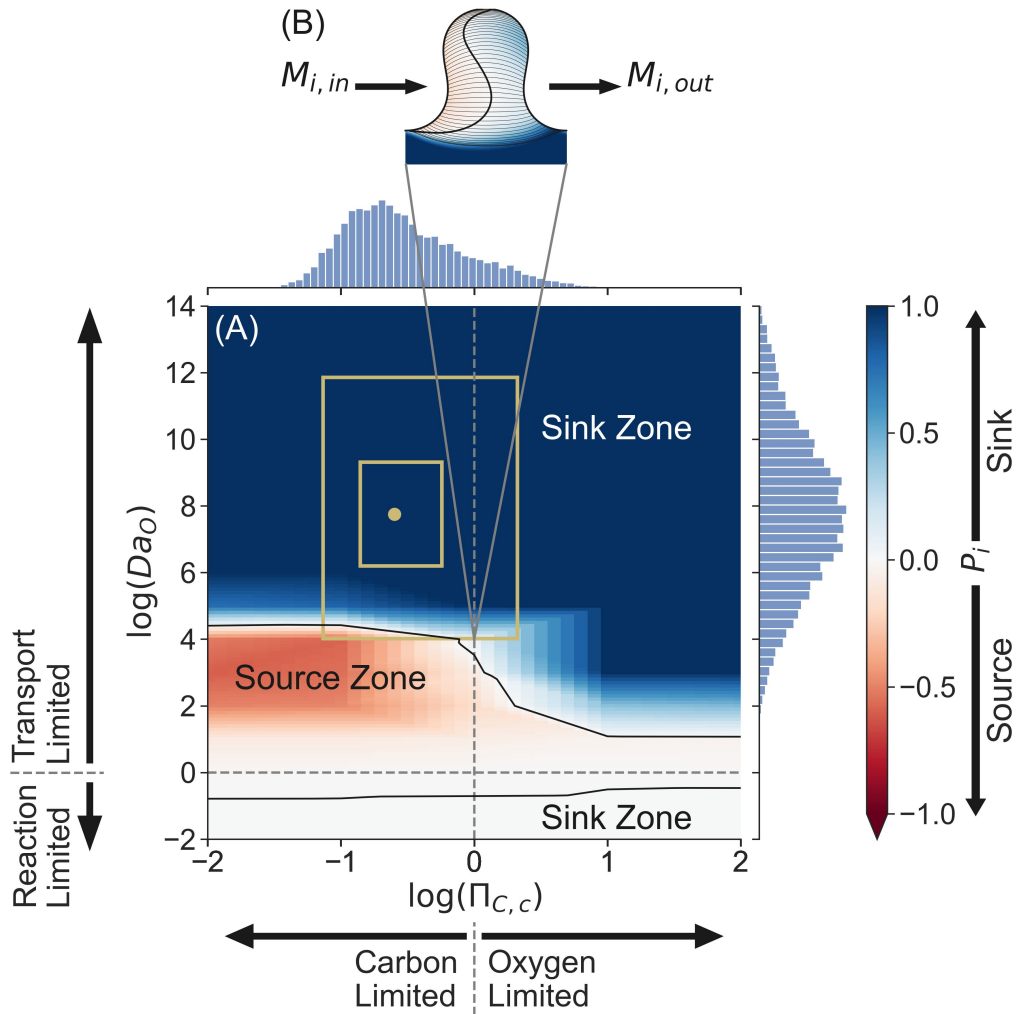


Figure 6.7: Biogeochemical potential in the $\Pi_{C,c} - Da_O$ domain (Panel A). Each point in this domain represents potential P_i for a single meander with dimensionless parameters $\Pi_{C,c}$ and Da_O (e.g., Panel B). The x-axis separates the domain into meanders exposed to carbon-limited ($\Pi_{C,c} < 1$) and oxygen-limited ($\Pi_{C,c} > 1$) boundary conditions, while the y-axis separates the domain into meanders characterized by reaction-limited ($Da_O < 1$) and transport-limited ($Da_O > 1$) conditions. For reference, we include histograms for typical values of the dimensionless variables found across the Conterminous US and their corresponding 5%, 25%, 50%, 75%, and 95% percentiles (yellow boxes and point). Generally, this diagram results in two characteristic zones: one for hyporheic zones that act as net sources of the constituent ($P_i < 0$; red colors) and one for meanders that act as net sinks ($P_i > 0$; blue colors).

point represents a meander with different dimensionless variables, and therefore net biogeochemical potential (Figure 6.7B). This domain can be discretized into quadrants based on typical thresholds of the master variables. The first quadrant (upper left) is characterized by meanders with carbon ($\Pi_{C,c} < 1$) and transport ($Da_O > 1$) limitations. The second quadrant (lower left) is characterized by meanders with carbon ($\Pi_{C,c} < 1$) and reaction ($Da_O < 1$) limitations. The third quadrant (upper right) is characterized by meanders with

oxygen ($\Pi_{C,c} > 1$) and transport ($Da_O > 1$) limitations. And lastly, the fourth quadrant (lower right) is characterized by meanders with oxygen ($\Pi_{C,c} > 1$) and reaction ($Da_O < 1$) limitations. From the Monte Carlo analysis, which leverages hydrogeomorphic and chemical information across the conterminous United States (CONUS) (Subsection 6.2.2.2) and the literature values reported in Table 6.2 2, we estimated a subdomain of the $\Pi_{C,c} - Da_O$ domain where the CONUS meanders are more likely to map (see histograms and yellow rectangles in Figure 6.7A). However, their net behavior can change depending on the other dimensionless variables, especially the amount of particulate organic matter, which serves as a potential source of DOC to offset the carbon limitations (e.g., Sawyer, 2015).

Figure 6.7 illustrates a typical pattern of nitrate's biogeochemical potential (P_{NO}) for meanders in the $\Pi_{C,c} - Da_O$ domain. Using this figure as an example, we can discriminate meanders as sinks (blue colors) or sources (red colors) for nitrate. More specifically, reaction-limited ($Da_O < 1$) meanders tend to be mild sinks with $P_{NO} \gtrsim 0$. These meanders have characteristic time scales for reactant supply that are shorter than the time scales for reaction. In other words, the hyporheic zone does not provide enough time to consume oxygen, so denitrification is limited or has significant nitrification, which is equivalent to having a reactor where nitrate NO_3^- is transported without significant transformations. As Da_O exceeds unity, a source zone typically develops. This source zone eventually transitions to a strong sink zone as Da_O increases, where the transition threshold differs for carbon-limited ($\Pi_{C,c} < 1$) and oxygen-limited ($\Pi_{C,c} > 1$) systems. Oxygen-limited systems tend to transition after small values of Da_O , and, in some cases, the source zone does not develop. On the other hand, for carbon-limited systems, a large value of Da_O is needed before the system behaves as a nitrate sink.

To better understand the key controls on the $\Pi_{C,c} - Da_O$ zonation, we performed a systematic analysis for 800 meanders (i.e., scenarios) in pristine (low inorganic N) and polluted (high inorganic N) systems (Zheng et al., 2016) and with varying sinuosity, magnitudes of regional groundwater flow, and availability of labile POC. First, we will focus on the effects of sinuosity and regional groundwater flow for systems with a constant POC of 0.02%. Then, we will explore the implications of POC on the patterns observed.

Pristine systems. Meanders in pristine systems (Figure 6.8; POC = 0.02%) are predominantly sinks for nitrate, with typical meanders across CONUS (yellow rectangles) having $P_{NO} \approx 1$. In some cases, small areas of the $\Pi_{C,c} - Da_O$ domain are classified as sources; however, P_{NO} is still close to zero, implying that these meanders behave as a net conveyor of nitrate with minimal transformations. In fact, systems with gaining conditions ($\Pi_{J_y} > 0$) do not develop a source zone.

The transition interface from mild to strong sink in the $\Pi_{C,c} - Da_O$ domain (transition from light to dark blue in Figure 6.8) is minimally affected by the magnitude of the regional groundwater flow (i.e., similar patterns for all rows in a column). This transition, however, changes significantly with the degree of sinu-

osity. Systems with high funneling factor transition to strong sinks at higher Da_O numbers, resulting in a larger proportion of CONUS meanders within the mild sink domain (area enclosed by the yellow rectangle). In other words, the likelihood of systems with conservative transport behavior for NO_3^- increases with sinuosity. These findings are at odds with the common assumption that increasing sinuosity leads to increasing river corridor and hyporheic complexity and, therefore, a likely increase in river corridor biogeochemical processing – the basis for the design of typical hyporheic restoration efforts (Hester and Gooseff, 2010, 2011). Our model shows that the reduction of the net denitrification in high sinuosity meanders results from the higher velocities around the neck of the meander that transport a significant amount of water and solutes at higher rates, reducing the amount of time in contact with the reactive sediments for the majority of the flow. Based on the histograms derived for natural channels across CONUS (Figure 6.7), a predominant portion of channels will be sink zones in all cases for these conditions. As we show later, this transition can be highly sensitive to POC availability, completely changing the dynamics and overall behavior of these systems.

In general, a source zone of small extent and magnitude develops under neutral ($\Pi_{J_y} = 0$) and losing ($\Pi_{J_y} < 0$) regional groundwater flow conditions. This zone is absent under gaining conditions ($\Pi_{J_y} > 0$). Under neutral conditions (third row in Figure 6.8), the source zone is smallest and roughly constrained to $\Pi_{C,c} \leq 10^{-1}$ and $10^2 \leq Da_O \leq 10^4$ and similar in shape for all sinuosity values. As the magnitude of the losing regional groundwater flow increases, the source zone extends lower Da_O values, reaching $Da_O = 1$. As mentioned, the magnitude of the biogeochemical potential within the source zone is close to zero. We hypothesize that the expansion of the source zone under losing conditions is caused by dispersive mixing along the hyporheic zone boundary, which interacts with channel-born flow paths recharging the alluvial aquifer. The opposite effect is observed for gaining conditions given the boundary conditions assumed for the alluvial aquifer boundary in our model. In general, this dispersive mixing along the hyporheic zone boundary represents a minor fraction of the overall mass flowing through the hyporheic zone (Hester and Gooseff, 2010, 2011; Hester et al., 2014; Gomez et al., 2012).

The $\Pi_{C,c} - Da_O$ zonation for pristine systems is consistent with our expectations based on the microbial reaction process represented in our model. For these scenarios, the concentrations of NO_3^- and NH_4^+ at the channel (and their corresponding dimensionless variables $\Pi_{NO,c}$ and $\Pi_{NH,c}$) are relatively small. Low Da_O values characterize systems where meanders take longer to reach anoxic conditions, constraining denitrification, or the small amounts of NH_4^+ cannot drive significant nitrification. These conditions likely result in meanders that preferentially transport NO_3^- with negligible transformations. As Da_O increases, this oxic constraint becomes weaker, and preferentially anoxic conditions develop to facilitate denitrification. As shown in Figure 6.8, the development of these conditions occurs for lower Da_O values when DOC limitations are unimportant (i.e., $\Pi_{C,c} > 1$).

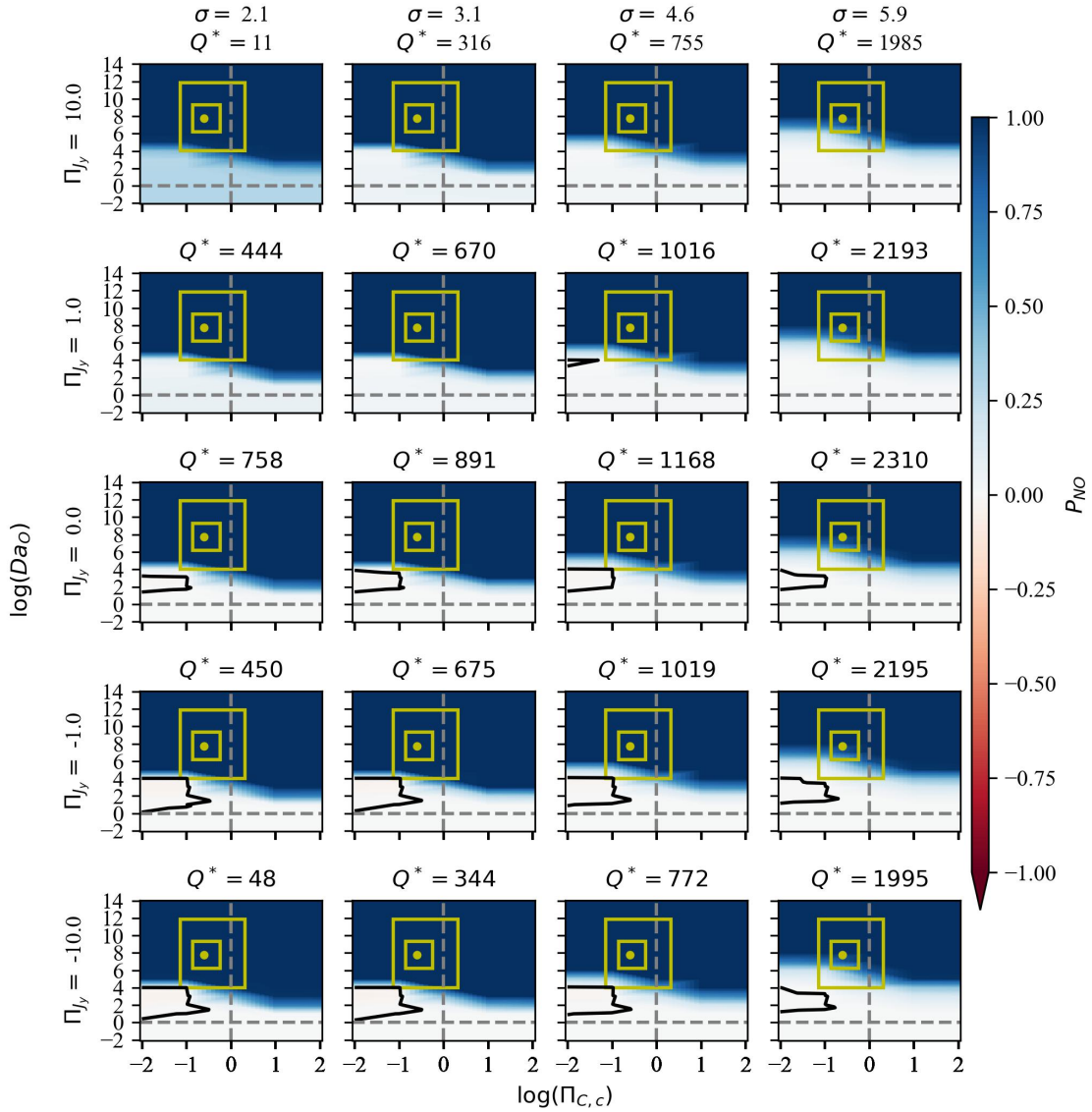


Figure 6.8: Potential of retention of nitrates for the pristine river channel case and $P_0 = 0.02\%$. The columns denote different meander topologies described by the sinuosity (σ). The rows separate the regional gradient Π_y . The colors show the potential for biogeochemical retention. The solid black line shows the zero contour line. The horizontal dashed line is the division between transport-limited ($\log(Da_O) > 0$) and reaction-limited systems ($\log(Da_O) < 0$). The vertical dashed line is the division between carbon-limited ($\Pi_{C,c} < 0$) and oxygen-limited systems ($\Pi_{C,c} > 0$). For reference, we include histograms for typical values of the dimensionless variables found across the Conterminous US and their corresponding 5%, 25%, 50%, 75%, and 95% percentiles (yellow boxes and point).

The effects of sinuosity can be explained by the dominant role of meander neck flow paths with shorter time scales. These flow paths move a larger proportion of total exchange as sinuosity increases. For example, oxic conditions extend a larger proportion of the meander neck due to shorter transport time scales, increasing the opportunities for nitrification while limiting denitrification. This effect explains the emergence of a source zone, which is mild due to the low supply of NH_4^+ that limits the production of NO_3^- through nitrification. As the sinuosity increases, and therefore the prevalence of short transport time scales characteristic of the meander neck, a higher Da_O value is needed to drive nitrification. This explains the upward migration of the strong sink transition in Figure 6.8.

Polluted systems. Similar to Zheng et al. (2016), our polluted scenarios increase channel NO_3^- and NH_4^+ concentrations and their corresponding dimensionless variables by approximately one order of magnitude relative to pristine systems. Figure 6.9 illustrates the simulations in the $\Pi_{C,c} - Da_O$ domain with POC of 0.02%. The polluted scenarios are characterized by the emergence of a pronounced source zone that marks a transition from mild sinks, for low Da_O values, to strong sinks as Da_O increases. For the scenarios in this figure, a small fraction of probable value ranges for meanders across CONUS falls within the source zone. The lower boundary, marking the transition from mild sinks to strong sources, occurs at $Da_O = 1$ for neutral and gaining conditions; however, it can extend to $Da_O < 1$ for losing conditions. Note that the meanders with the lowest sinuosity and the strongest gaining conditions explored (upper left corner in Figure 6.9) present a different behavior, where the source zone is limited to a small region where $10^2 \leq Da_O \leq 10^4$ and $\Pi_{C,c} \leq 0.1$. As explained before, this difference is likely driven by mixing along the boundary of a highly compressed hyporheic zone.

The upper limit marking the transition from a strong source to strong sink meanders varies primarily as a function of sinuosity. For example, under neutral conditions, the transition boundary migrates toward higher Da_O values with increasing sinuosity. This is consistent with the dominant role of short residence times in higher sinuosity systems where neck flow paths dominate the total exchange flux. In this case, transport residence times constrain the capacity of the hyporheic zone to denitrify, resulting in a dominant role of nitrification that leads to a net source of nitrate. Furthermore, the zone is larger in carbon-limited systems ($\Pi_{C,c} < 1$), where aerobic respiration is likely consuming a large proportion of the available DOC, which limits the progression of denitrification. Nitrate source conditions can also be found for oxygen-limited systems, highlighting a “hot spot” of residence times where nitrification is favored (McClain et al., 2003; Zarnetske et al., 2011b). As will be shown later, the dissolution of POC requires large enough Da_O to offset the DOC limitation and significantly activate the role of denitrification. This defines the location of the transition zone from source to sink as Da_O increases. Finally, as gaining fluxes increase ($\Pi_{J_y} > 0$), the source zone in the oxygen-limited quadrant disappears; this is consistent with the removal of neck flow

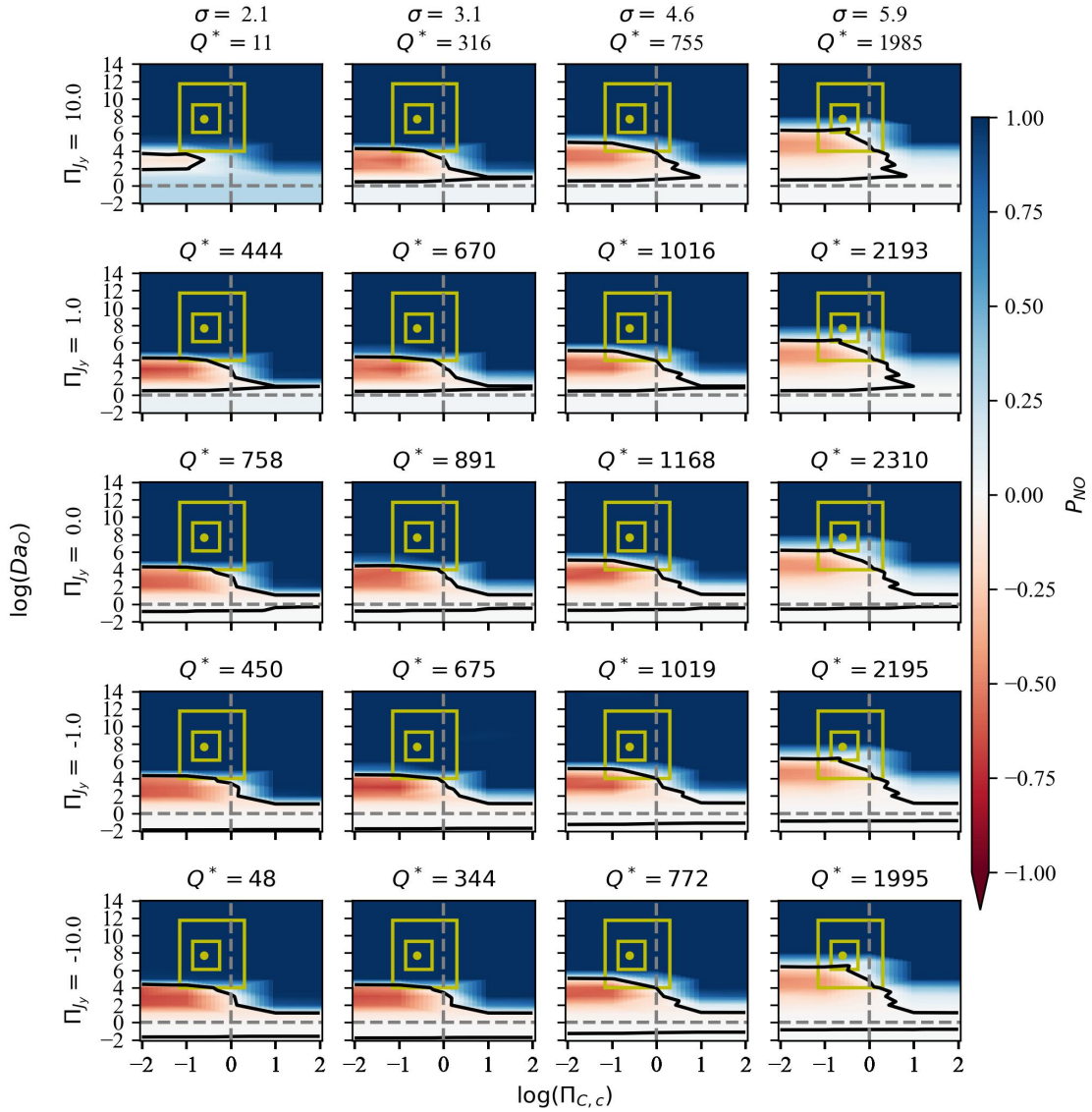


Figure 6.9: Potential of retention of nitrates for the polluted river channel case and $P_0 = 0.02\%$. The columns denote different meander topologies described by the sinuosity (σ). The rows separate the regional gradient Π_{J_y} . The colors show the potential for biogeochemical retention. The solid black line shows the zero contour line. The horizontal dashed line is the division between transport-limited ($\log(Da_O) > 0$) and reaction-limited systems ($\log(Da_O) < 0$). The vertical dashed line is the division between carbon-limited ($\Pi_{C,c} < 0$) and oxygen-limited systems ($\Pi_{C,c} > 0$). For reference, we include histograms for typical values of the dimensionless variables found across the Conterminous US and their corresponding 5%, 25%, 50%, 75%, and 95% percentiles (yellow boxes and point).

paths and a general increase in residence times, leading to enhancement of aerobic respiration and additional contact time under anoxic conditions, which ultimately enhances the role of denitrification. The net effect of these conditions is a transition to a net sink. This behavior is not consistent with losing conditions, given the mixing effects at the boundary of a thin hyporheic zone.

These findings have important implications for river restoration practices. If sinuosity is increased as a restoration strategy (e.g., Hester and Gooseff, 2010, 2011), the meander can act as a net source of nitrate, leading to adverse and unintended consequences from the perspective of nutrient retention. In fact, the overall negative impact increases with sinuosity, given that sinuosity significantly increases flux and, therefore, the overall contaminant load delivered from the hyporheic zone to the river. For example, the exchange increases by about two orders of magnitude when sinuosity is increased from 2.1 to 5.9 (Figure 6.9). As mentioned, this issue is driven by the dominant role of the meander neck as a control for the net flow and residence times within the meander's hyporheic zone.

6.3.2.2 The role of Particulate Organic Carbon

Labile POC is a key constraint for offsetting DOC limitations in our simulations. The importance of this offset depends on the amount of POC available (represented by the dimensionless variable Π_{P-C}) and the dimensionless POC linear distribution coefficient (represented by Π_{Kd}). Here, we illustrate the changes in the biogeochemical potential for NO_3^- transformations within the $\Pi_{C,c} - Da_O$ domain for three values of POC under pristine and contaminated conditions. These results are summarized in Figure 6.10 for a single meander ($\sigma = 3.1$) under neutral conditions. Note that the role of Π_{Kd} decreases as POC increases (see Appendix C for additional details), and therefore, we focus on Π_{P-C} , which is directly proportional to POC.

The systems without POC available to offset DOC limitations (first column of Figure 6.10) consume all the DOC available through aerobic respiration, which in turn constrains the role of denitrification because it needs DOC to proceed. When aerobic respiration is limited by the availability of DOC or short transport time scales, the oxygen remaining can promote nitrification and lead to the formation of a nitrate source zone (red areas in the $\Pi_{C,c} - Da_O$ domain). The nitrification reaction is then limited by the availability of NH_4^+ . In the case of the polluted river channels, the nitrate source zone is constrained to $\Pi_{C,c} \leq 0.1$ and $10^2 \leq Da_O \leq 10^7$. For polluted channels, the nitrate source zone extends the majority of the carbon-limited domain and some sections of the oxygen-limited domain, primarily for small Da_O values. The meanders from the CONUS analysis (yellow rectangles) will be within the source zone under polluted conditions, imposing a positive feedback cycle where the sinuosity-driven hyporheic zone may exacerbate the nitrate excess problems.

As the available POC increases to 0.002% and 0.2%, we see the emergence of a strong source zone for DOC (dark brown colors with $P_C < 0$). The DOC promotes aerobic respiration and denitrification while

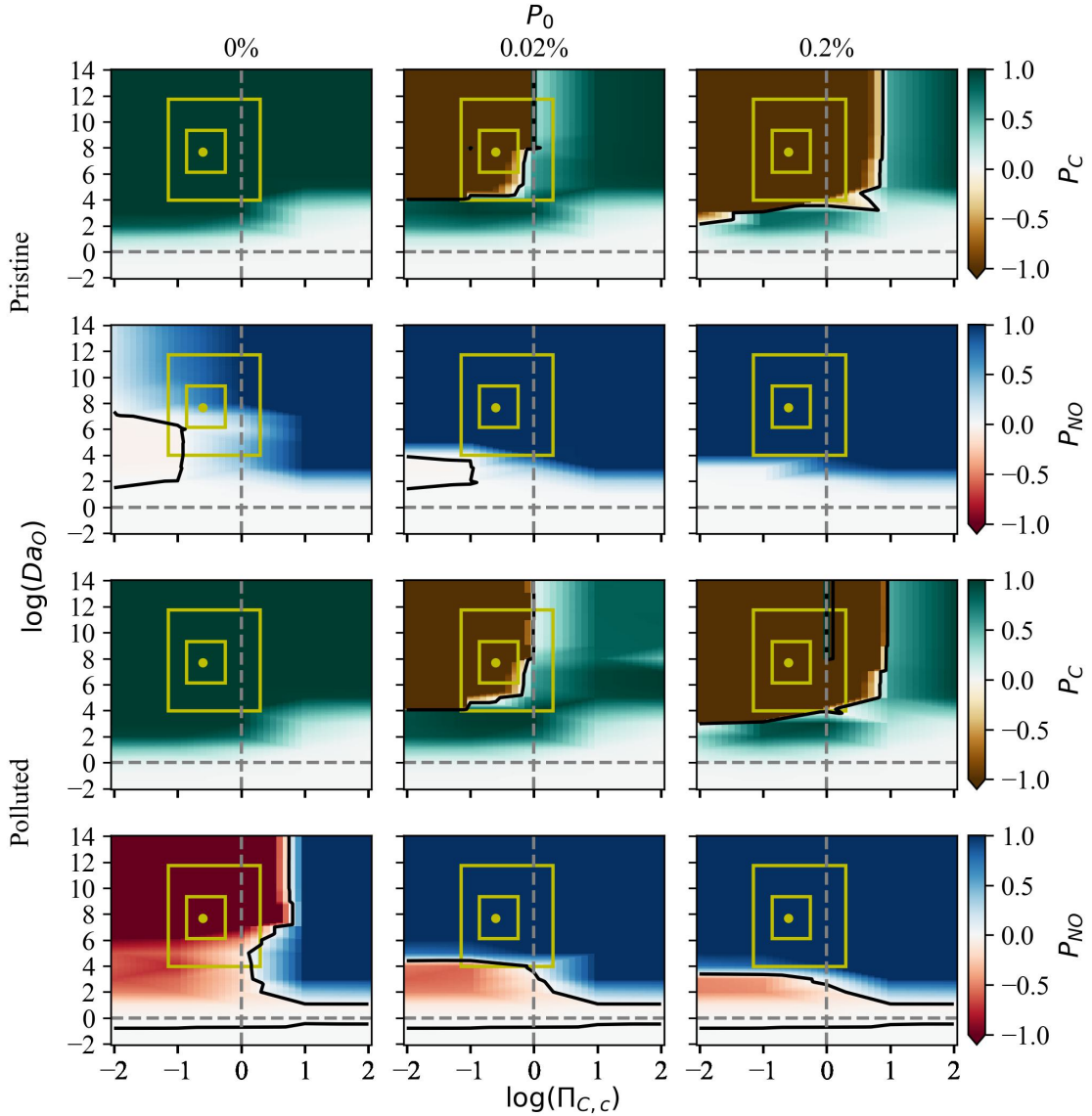


Figure 6.10: Effect on POC concentration in the biogeochemical potential for DOC and NO_3^- transformations for meanders of moderate sinuosity ($\sigma = 3.1$) and neutral regional groundwater flow ($\Pi_{J_y} = 0.0$). Columns correspond to labile POC of 0%, 0.02%, and 0.2%. The figure includes meanders under pristine (rows one and two) and polluted (rows three and four) channel conditions. The solid black line shows the zero contour line. The horizontal dashed line is the division between transport-limited ($\log(Da_O) > 0$) and reaction-limited systems ($\log(Da_O) < 0$). The vertical dashed lines is the division between carbon-limited ($\Pi_{C,c} < 0$) and oxygen-limited systems ($\Pi_{C,c} > 0$). For reference, we include histograms for typical values of the dimensionless variables found across the Conterminous US and their corresponding 5%, 25%, 50%, 75%, and 95% percentiles (yellow boxes and point).

suppressing nitrification. In other words, the overall effect of the dissolution of POC is to compress the nitrate source zone in the $\Pi_{C,c} - Da_O$ domain and to expand the zones classified as strong sinks. This effect is particularly important in polluted systems where the CONUS meanders transition to sinks of nitrate with POC

concentrations as small as 0.02%. Note, however, that the increases in POC do not completely eliminate the nitrate source zone, but it significantly decreases its extent. Hence, the availability and reactivity of organic carbon are likely a significant control on the fate of the nitrogen in meanders, and the reactivity of DOC remains an understudied area of field hyporheic research (Zarnetske et al., 2012).

6.4 Conclusions

Meanders in river channels provide a critical and underappreciated natural biogeochemical reactor. Our models and simulations provide a fundamental understanding of the role that first-order drivers (meander topology) and modulators (regional groundwater flow) play in the hydrodynamics, transport, and reactions taking place within sinuosity-driven hyporheic zones occurring in meanders. Furthermore, we reveal and propose a dimensionless framework to characterize these processes in terms of metrics that can be quantified by widely available remote sensing and water quality data. These metrics, at the same time, offer a first step toward the development of a new generation of surrogate models that explicitly include the role of meanders in water quality modeling efforts.

From the perspective of the hyporheic exchange hydrodynamics, meander topology, and in particular, the relative size of the meander neck (expressed as a funneling factor), emerges as a key variable controlling the total amount of exchange and the characteristic time scales for transport. As sinuosity increases, the funneling factor increases, leading to a hydrodynamic shielding effect that protects the sinuosity-driven hyporheic zone from the compressing effects of regional groundwater flow. This effect highlights the robust nature of this hyporheic exchange process along river corridors and shows that it can be more important and ubiquitous than previously thought (Cardenas, 2009a,b; Gomez et al., 2012; Gomez-Velez et al., 2015, 2017).

Meander topology also plays a key control in multiple biogeochemical transformations taking place within the hyporheic zone. Here, we focused on nitrogen transformation, and in particular on the fate of nitrate. However, other transformations of interest could be explored within a similar framework, especially those chemical transformations associated with oxidation-reduction (redox) processes and carbon utilization (e.g. Hedin et al., 1998; Burgin and Loecke, 2023). Our simulations show the complex interplay between transport and biogeochemical time scales, substrate availability, and sinuosity. Topology and regional groundwater flow determine the transport time scales, solute concentrations at the channel impose critical boundary conditions and limitations, alluvial aquifer biogeochemical parameters impose transformation time scales, and availability of particulate organic carbon becomes a critical factor to offset carbon limitations. All these factors can lead to similar meanders acting as net sources or sinks of nitrate. Understanding their role allows us to predict the potential implications of the exchange process and propose reasonable restoration strategies that take advantage of the natural potential of river corridors to remove excess nitrogen (e.g.,

Hester and Gooseff, 2010, 2011). For example, a practitioner interested in increasing sinuosity for channel restoration purposes could use field measurements and estimates of the expected post-restoration sinuosity to map scenarios into the $\Pi_{C,c} - Da_o$ domain (Figures 6.8, 6.9, 6.10). This mapping would provide a “back-of-the-envelope” prediction for the expected behavior of the meanders under the proposed restoration strategy. More generally, this framework offers general insight into the tight coupling of substrate availability, residence times, and channel topology.

Although our conceptual model is idealized, we are confident it captures the first-order controls for the exchange process, providing fundamental insight into the biogeochemical potential of meanders across river corridors. Furthermore, it provides a scalable framework to explore multiple meander topologies and regional groundwater conditions. Finally, our results stress the vital role of dissolved and particulate organic carbon content in the biogeochemical potential of sinuosity-driven hyporheic zones and, in particular, the need to better constrain POC content in stream sediments and alluvial aquifers.

It is important to note that the assumptions behind the reduced-complexity model carry important limitations, most of which can be relaxed in future applications. First, our model neglects the three-dimensional nature of groundwater flow and the nested nature of exchange processes. This three-dimensional structure can be particularly important near the channel (e.g., Boano et al., 2010a, 2014; Perez et al., 2021; Stonedahl et al., 2013; Wang et al., 2022), where convergent flow and the interplay of multiple morphologies driving hyporheic exchange are a first-order control for transport and reaction. Second, we assume a homogeneous and isotropic porous media, ignoring the important role of physical and biogeochemical heterogeneity (e.g., Arora et al., 2022; Song et al., 2020; Zhou et al., 2014), which plays a central role in the formation of biogeochemical hotspots (e.g., Briggs et al., 2018; Krause et al., 2022). The representation of POC heterogeneity (Sawyer, 2015) and its liability (Zheng et al., 2019) is of particular interest, which is ignored in the current conceptualization. Lastly, we assume a steady river stage and constituent concentration. As mentioned before, these boundary conditions covary over space and time (Creed et al., 2015), constraining exchange dynamics, residence times, and substrate supply (e.g., Dwivedi et al., 2018; Gomez-Velez et al., 2017; Song et al., 2020; Wu et al., 2021). Future work should consider the temporal dynamics and correlations of discharge and concentrations (e.g., Dwivedi et al., 2018; Gomez-Velez et al., 2017), the influence of heterogeneity in sediments (e.g., Sawyer, 2015), and the potential implications of including our conceptualization into reach-scale water quality models, where the effects of concentrations on reaction rates play a significant role (e.g., Schmadel et al., 2020).

CHAPTER 7

WigglyRivers: A Tool to Characterize the Multiscale Nature of Meandering Channels

This chapter is a modified version of a paper in preparation that will be sent to Environmental Modelling & Software. Gonzalez-Duque, D. & Gomez-Velez, J. D. (2024). *WigglyRivers: a tool to characterize the Multiscale Nature of Meandering Channels* (In preparation). Environmental Modelling & Software.

Abstract

Sinuuous channels are ubiquitous features along river networks. Their complex patterns span scales and influence morphodynamic processes, landscape evolution, and ecosystem services. Identifying and characterizing meandering features along river transects has been a challenge for traditional curvature-based algorithms. Here, we present *WigglyRivers*, a Python package that builds on existing work using wavelet-based methods to create an unsupervised identification tool. This tool allows the characterization of the multiscale nature of river transects and the identification of individual meandering features. The package uses any set of river coordinates and calculates the curvature and direction-angle to perform the characterization, and also leverages the use of the High-Resolution National Hydrography Dataset (NHDPlus HR) to assess river transects at a catchment scale. Additionally, the *WigglyRivers* package contains a supervised river identification tool that allows the visual selection of individual meandering features with satellite imagery in the background. Here, we provide examples in idealized river transects and show the capabilities of the *WigglyRivers* package at a catchment scale. We also use the supervised identification tool to validate the unsupervised identification on river transects across the US. The package presented here can provide crucial data that represents an essential step toward understanding the multiscale characteristics of river networks and the link between river geomorphology and river corridor connectivity.

7.1 Introduction

Meandering channels are prevalent features in river networks across landscapes (Leopold et al., 1992). Their irregular patterns vary across scales in both sedimentary and non-sedimentary environments (Seminara, 2006) and are developed from morphodynamical processes that involve the interaction between hydrology and geomorphological characteristics of the river channel (Schumm, 1985; Zolezzi and Seminara, 2001). Characterizing these river patterns at multiple scales can provide crucial information on processes occurring in the river channel and its surroundings. For instance, at a reach scale, the identification of meandering patterns in an evolving river planform allows the study of stability and self-organized behavior of rivers (Hooke, 2007,

2003), as well as the understanding of river meander migration (Lagasse et al., 2004; Dominguez Ruben et al., 2021), how it is linked to erosion heterogeneity (Güneralp and Rhoads, 2011), and how this process impacts landscapes and floodplain processes (Piégay et al., 2005; Van De Wiel et al., 2007; Odgaard, 1987), and ecosystem dynamics (Ward et al., 2002). At a local scale, the geometry and topology of a meander bend and the characteristics of the channel have been shown to impact the lateral hyporheic exchange fluxes (Cardenas, 2008; Stonedahl et al., 2013; Gonzalez-Duque et al., 2024b), affecting residence times and biogeochemical processes occurring within the hyporheic zone (Boano et al., 2010b; Revelli et al., 2008; Gomez et al., 2012; Gomez-Velez et al., 2017; Gonzalez-Duque et al., 2024b), and thus, impacting the ecosystem services the river corridor provides (Harvey et al., 2018).

The identification and posterior characterization of meandering channels has been a topic of interest among geomorphologists for decades (Leopold and Wolman, 1960). One of the most common identification processes involves finding the inflection points in the curvature of the river planform (Howard and Hemberger, 1991) as these points describe the starting and ending points of a single meander bend. This method, however, is highly sensitive to noise in the data. So, a smoothing of the planimetry is required to obtain a reasonable computation of the curvature (Güneralp and Rhoads, 2008). Another approach uses morphodynamic modeling of the river planimetry to locate the possible cutoffs of a given meander bend and then a tracking algorithm to detect the starting and ending points of a meander bend from these cutoffs (Schwenk et al., 2015). However, this method requires a morphodynamic model and a tracking algorithm that can be computationally expensive when applied to large river networks (Schwenk et al., 2015). An alternative to these two approaches is to leverage the use of wavelet-based methods to characterize meandering features in the curvature of the river planform, as performed by Vermeulen et al. (2016). This method is less sensitive to noise in the data and can provide a multiscale characterization of the river planimetry (Zolezzi and Güneralp, 2016; Vermeulen et al., 2016).

Wavelet-based methods, different from conventional spectral tools like Fourier transforms, are able to capture the multiscale nature of non-stationary signals like the ones produced by meandering rivers (Gutierrez and Abad, 2014). Among the numerous applications of these methods, we can see the study of El Niño-Southern Oscillation (ENSO) (Gu and Philander, 1995; Wang and Wang, 1996), how it impacts local meteorological dynamics (Díaz et al., 2022), and its association with influenza cases (Xiao et al., 2022); the study of the Madden-Julian Oscillation (MJO) variability by CMIP6 models (Le et al., 2021), the characterization of shoreline features (Vulis et al., 2023), and, more specifically to river networks, the determination of the predominant wavelengths and scales of rivers transects (Zolezzi and Güneralp, 2016; Gutierrez and Abad, 2014), among others. In particular, the work done by Vermeulen et al. (2016) has shown that applying a Continuous Wavelet Transform (CWT) to the curvature of the river planform can provide the location of

individual meander bends over long reaches and their associated scales.

In this work, we built on top of Vermeulen et al. (2016) multiscale algorithm to create the *WigglyRivers* Python package. This package allows the supervised and unsupervised identification of meandering bends along river transects across scales. Although *WigglyRivers* uses any given river planimetry, it also contains routines that leverage the use of the High-Resolution National Hydrography Dataset (NHDPlus HR) (Moore et al., 2019), allowing the identification of meander bends at catchment and basin scales. The package also contains an interactive tool that allows the manual identification of meander bends at a reach scale using Jupyter Notebooks that can be used as a validation set for the unsupervised identification routine. Lastly, *WigglyRivers* uses spectral metrics to characterize river transects similar to the ones described in Zolezzi and Güneralp (2016) and also calculates individual meander metrics, such as the radius of curvature, amplitude, asymmetry, funneling factor, and sinuosity for meander bend analysis like the ones provided in Leopold et al. (1992) and Howard and Hemberger (1991).

The use of this tool with the NHDPlus HR information can open the door for the study of the multi-scale nature of river networks across scales and environments and how they can be linked to hydrologic and geomorphologic processes. Furthermore, the identification of individual meander bend's geometry and topology can be used in sinuosity-driven hyporheic exchange models to have estimates of lateral exchange fluxes at catchment and basin scales, refining current estimates (i.e., Gomez-Velez and Harvey, 2014; Kiel and Bayani Cardenas, 2014).

7.2 The *WigglyRivers* tool

The *WigglyRivers* package offers a workflow that characterizes meandering features in rivers, providing two independent tools that allow the identification of meanders and the exploration of the multiscale nature of river networks. The first one provides routines for the supervised identification of meanders, where users can go through a reach on the network and manually select the beginning and ending points of meanders. The manual identification of meanders serves as a tool to validate the automatic detection performed by the second tool of the package. This second tool allows the automatic identification of meander bends at a reach scale using a Continuous Wavelet Transform (CWT) approach proposed by Vermeulen et al. (2016). Lastly, the routines and subroutines used in the automatic identification allow the user to assess the multiscale nature of the river network.

To achieve this functionality, we divided *WigglyRivers* into three fundamental classes, `RiverDataset`, `RiverTransect`, and `Meander`. The `RiverDataset` class contains all the subroutines to store, save, and load `RiverTransect` data. `RiverTransect` is the main class of the package; it stores all the information related to a specific river (coordinates, distance, curvature, CWT, meanders, among others). This

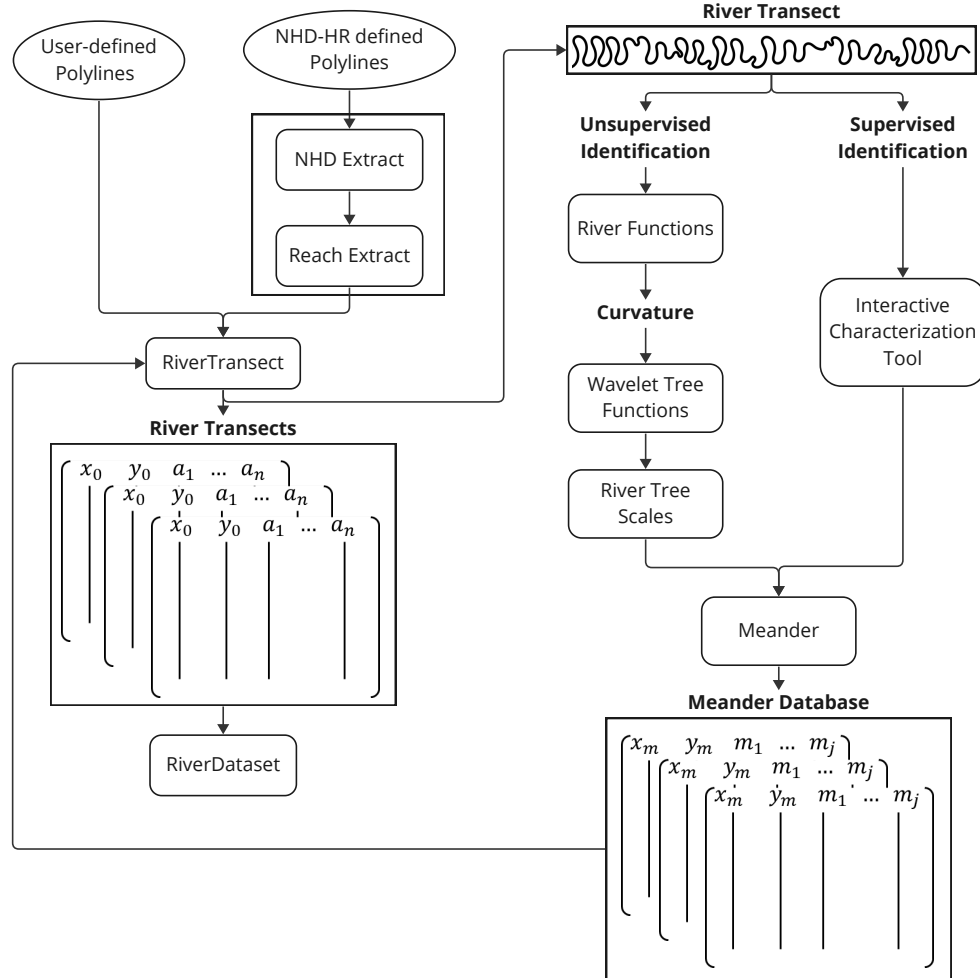


Figure 7.1: Structure of the *WigglyRivers* Python package. The blue boxes represent the main classes of the package. The yellow boxes represent the classes and functions that make river-related computations, such as river extractions, scaling, and resampling, among others. The red boxes represent wavelet-related functions, the magenta boxes represent plotting-related functions, and the green boxes are utility-based functions. The lines show the connection between the package sections and where to expect the computations to be made.

class also has the subroutines to perform the supervised and automatic detection of meanders. Lastly, the `Meander` class has information about each meander (coordinates, meander arlength, sinuosity, radius of curvature, amplitude, among others). The general rule in the package is that `RiverDatasets` contain individual `RiverTransect` that can hold several `Meander` features. The general package structure with classes, functions, and their relationships is shown in Figure 7.1.

In the following subsections, we will delve deeper into the process behind the characterization and detection tools and other functionalities crucial in understanding the underlying mechanisms of detecting meanders with the *WigglyRivers* python package.

7.2.1 Data preparation

The *WigglyRivers* package uses any set of $\mathbf{x}_o = [x_{o_1}, \dots, x_{o_n}]$ and $\mathbf{y}_o = [y_{o_1}, \dots, y_{o_n}]$ coordinates that represent the river transect centerline planimetry. It is important to consider that the package will calculate metrics with the given coordinates, such as distances, curvature, and meander lengths. Thus, using projected coordinates while using the tool to have a realistic computation of the different metrics is strongly recommended. Although the package uses any set of coordinates to perform the meander characterization, it also contains routines that allow the extraction and processing of river transects within the High-Resolution National Hydrography Dataset (NHDPlus HR). The processing of this information is explored in the following sub-subsection.

7.2.1.1 NHDPlus HR information processing

As mentioned above, the *WigglyRivers* package has built-in routines that allow the processing of the High-Resolution National Hydrography Dataset (NHDPlus HR) information (Moore et al., 2019). In this processing, the tool first loads the geodatabase, then it projects and extracts the `NHDFlowline` table and coordinates, and appends the `NHDPlusFlowlineVAA` and `NHDPlusEROMMA` tables that are needed in the construction of the river network. As an additional set, the package also takes into account the `NHDWaterbody` shapefile and includes a flag with ones where the specific reach is within a waterbody that will not be taken into account in the characterization of meandering features in the river transect. The extracted coordinates will be saved in *hdf5* format with the *NHDPlusID* as the key to access any individual reach. On the other hand, tables will be saved in either *CSV* or *feather* format to be accessed later by the `RiverDatasets` class.

Once the initial information pre-processing is performed, the package creates a `RiverDatsets` object and loads the extracted coordinates and tables. The object removes all the divergence paths and also the reach paths that have an *FCode* indicator of a coastline (56600) and pipelines (42800 through 42816), leaving the artificial paths and canals to have connectivity in the network. The remaining reach paths are then used by a routine that maps the river network using the *FromNode* and *ToNode* in the tables. This routine creates vectors of rivers that go from the headwaters to the outlet of the catchment or to the connecting path that has already been explored. Each vector is organized with Common Identifiers (ComIDs) ($comid = [comid_1, comid_2, \dots, comid_k]$) where each $comid_i$ is the *NHDPlusID* that is linked to a row in the NHDPlus HR table and a set of coordinates. The package then uses these vectors to extract and append all the coordinates for each list of ComIDs. In this process, the routine creates new vectors with all the coordinates, calculates the length of the river, and interpolates the drainage area (*DA*) of each link to estimate the width of the channel (*W*) using the relationship proposed by Wilkerson et al. (2014) (see Section E.1 in Appendix D).

The extracted information is saved files that the `RiverDatasets` can easily access. The user should keep in mind that the extraction process computational time scales with the number of headwaters nodes available in the catchment. Therefore, it is recommended that sections of the catchment extract the coordinates once the ComID lists are created. An example of performing the extraction is presented in a Jupyter Notebook within the *WigglyRivers* package files.

7.2.2 Transect characterization

7.2.2.1 Resampling and smoothing the river transect

A crucial part of characterizing meanders with the *WigglyRivers* tool is having a river planimetry that has equally spaced distance. This spacing allows a refined calculation of the curvature of the river and the computation of the Continuous Wavelet Transform (CWT) used to characterize meandering features in the river transect. We used a similar approach to the one proposed in Güneralp and Rhoads (2008) to achieve equally spaced points. In this case, the `RiverTransect` object uses the user's selected sampling distance (Δs). Otherwise, it will use either the minimum channel width, if available, or the geometric mean of the streamwise arclength (s). Once the sampling distance is selected, the `RiverTransect` object performs the following series of steps,

1. take the n projected coordinates of the river ($\mathbf{x}_o, \mathbf{y}_o$) and calculates the cumulative Euclidean distances, $\mathbf{s}_o = [0, D_1, D_1 + D_2, \dots, \sum_{i=1}^{n-1} D_i]$, where

$$D_i = \sqrt{(x_{i+1} - x_i)^2 + (y_{i+1} - y_i)^2}. \quad (7.1)$$

2. Then, fits 1-D splines of third order between each coordinate vector and the cumulative distance, such that $\mathbf{x}_o = S_x(\mathbf{s}_o, [sm])$ and $\mathbf{y}_o = S_y(\mathbf{s}_o, [sm])$, where sm is a smoothing parameter for the spline.
3. Finally, the routine creates the streamwise vector with the sampling distance $\mathbf{s} = [0, \Delta s, \dots, \sum_{i=1}^{n-1} \Delta s]$ and uses the splines to resample the coordinate on the new equally spaced distances, such that $\mathbf{x} = S_x(\mathbf{s}, [sm])$ and $\mathbf{y} = S_y(\mathbf{s}, [sm])$.

The `RiverTransect` class uses the `UnivariateSpline` function from the `Scipy` Python package (Virtanen et al., 2020) to fit the spline to the data. The `UnivariateSpline` function incorporates a smoothing parameter (sm) that increases the number of knots until the criterion $\sum_{i=1}^n (y_o - y)^2 \leq sm$ is satisfied. The selection of a good number for sm depends on the complexity of the given planimetry. An approach to estimate a reasonable value for sm is to use the expression $sm = n \times 10^p$, where p depends on the complexity of the river planimetry, testing values of p for noisy synthetic rivers yielded a range of values of

[0,4].

7.2.2.2 Characterization of planimetry curvature and direction-angle

The curvature has been widely used in the characterization of meandering features in rivers (Howard and Hemberger, 1991; Vermeulen et al., 2015; Gutierrez and Abad, 2014; Zolezzi and Güneralp, 2016; Güneralp and Rhoads, 2008). Following on these previous work, the *WigglyRivers* tool uses the curvature (C) to determine the starting and ending points of meandering features in the channel. The computation of the curvature depends on the estimation of first- and second-order derivatives of the planimetry coordinates and the cumulative distances (\mathbf{x}' , \mathbf{x}'' , \mathbf{y}' , \mathbf{y}''). This river variable can be calculated as follow (Güneralp and Rhoads, 2008),

$$C = \frac{\mathbf{x}'\mathbf{y}'' - \mathbf{y}'\mathbf{x}''}{[(\mathbf{x}')^2 + (\mathbf{y}')^2]^{3/2}} \quad (7.2)$$

Another variable used in the characterization of the multiple spatial frequencies in meandering rivers is the direction angle (θ) (Zolezzi and Güneralp, 2016). This variable can be calculated using the curvature of the channel as follows (Güneralp and Rhoads, 2008),

$$\theta = \theta_0 + \int_{s=0}^{s=s_n} C ds \quad (7.3)$$

Where θ_0 is the initial direction angle calculated as $\theta_0 = \tan^{-1}(y'_1/x'_1)$. As can be seen from the previous calculations, the computation of both the curvature and the direction angle depends on the first and second derivatives of the planimetry coordinate, making them highly sensitive to noise in the data (see Figure D.1 in Appendix D). Thus, the selection of a reasonable smoothing factor (sm) in the resampling steps is important to achieve a reasonable computation of these signals.

The use of spectral tools to analyze the dominant frequencies on these signals can yield different results. While the signal produced by the curvature is shifted to shorter harmonics, the direction-angle signal is shifted towards longer harmonics (Zolezzi and Güneralp, 2016). Although the *WigglyRivers* package contains sub-routines that calculate both of these metrics, we only use the curvature for the unsupervised detection of meanders. The direction-angle can be used to study the dominant wavelengths of the river planimetry, as will be seen later in Section 7.3.3.1.

7.2.2.3 River and meander bend definitions

Before we present the unsupervised and supervised detection, we use this subsection to present the definitions used in the *WigglyRivers* package. According to Howard and Hemberger (1991), a half-meander is defined as

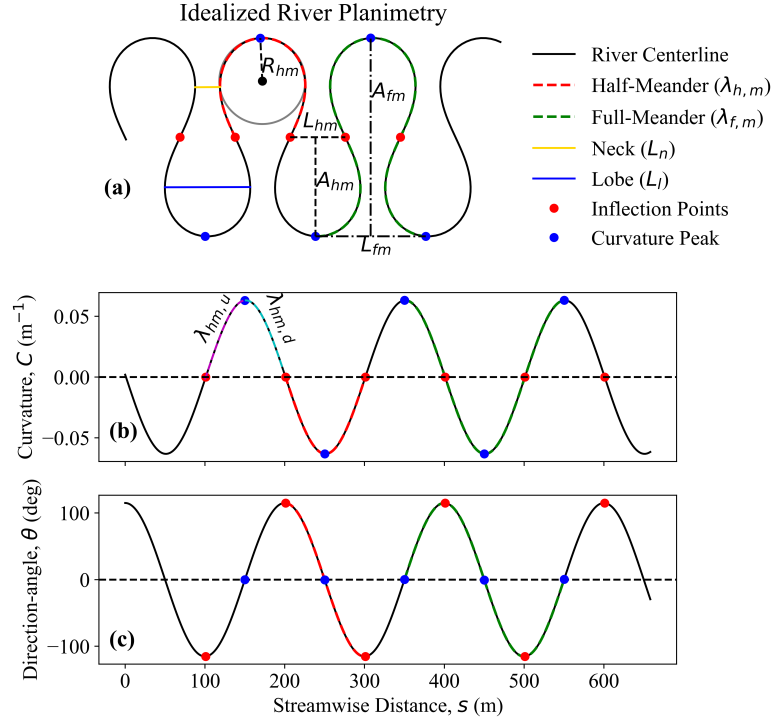


Figure 7.2: (a) Idealized river planimetry is shown in the black solid line in the first panel. (b) and (c) show the curvature and direction-angle calculated from the river planimetry. The half-meander is bounded by the inflection points (red dots and red dashed line), and the full-meander is bounded by the maximum points in the curvature (blue dots and green dashed line). The half-meander is characterized by the half-meander arc-wavelength (λ_{hm}), valley length (L_{hm}), and amplitude (A_{hm}). Similarly, the full-meander is characterized by the full-meander arc-wavelength (λ_{fm}), valley length (L_{fm}), and amplitude (A_{fm}). The radius of curvature (R_{hm}) is calculated for the half-meander. The gold solid line denotes the distance in the neck (L_n), and the solid magenta line denotes the largest distance within the meander lobe (L_l). The distances between the inflection points and the maximum points in the curvature upstream ($\lambda_{hm,u}$) and downstream ($\lambda_{hm,d}$) of the half-meander are denoted by the magenta and cyan lines.

the region between two inflection points in the curvature of the river planimetry (dashed red line in Figure 7.2). Furthermore, we consider a full-meander as the region between two curvature peaks encapsulating a half-meander (dashed green line in Figure 7.2). On each half-meander, the *WigglyRivers* package calculates the half- and full-meander arc-wavelengths (λ_{hm} and λ_{fm}), valley lengths (L_{hm} and L_{fm}), and amplitudes (A_{hm} and A_{fm}) (see dashed black lines Figure 7.2a). The package also calculates the half-meander radius of curvature (R_{hm} , gray circle in Figure 7.2a), the distance in the neck (L_n , gold solid line in Figure 7.2a), the largest distance within the meander lobe (L_l , blue solid line in Figure 7.2a), and the distances between the inflection points and the maximum points in the curvature upstream ($\lambda_{hm,u}$) and downstream ($\lambda_{hm,d}$) of the half-meander (magenta and cyan lines in Figure 7.2b). These variables will be used to calculate the half- and full-meander sinuosities (σ_{hm} and σ_{fm}) and the asymmetry (a_{hm} and a_{fm}), and the funneling factor (FF) of

the full-meander. The details about these calculations are presented in Section 7.2.5.

A common approach in the morphological studies of meandering planimetry is to use the channel width as a scaling parameter to non-dimensionalize the river variables (i.e., Zolezzi and Güneralp, 2016; Vermeulen et al., 2016; Gutierrez and Abad, 2014; Seminara et al., 2001; Zolezzi and Seminara, 2001). One of the purposes of the non-dimensionalization is to provide a comparable framework of river and meander metrics among river transects. The *WigglyRivers* package has the option to use the non-dimensional form of the planimetry variables by using the geometric mean of channel width as the scaling factor. The variables utilized in the package and their non-dimensional form are presented in Table D.1 in the Appendix D.

7.2.3 Unsupervised identification of meandering features

The unsupervised identification of meanders implemented in the *WigglyRivers* tool builds upon the process and MATLAB scripts created by Vermeulen et al. (2016). The process of identifying meanders has the following steps: (i) resample and smooth river coordinates (a in Figure 7.3), (ii) estimate the curvature of the planimetry using Equation (7.2) (b in Figure 7.3), (iii) compute the curvature continuous wavelet transform (CWT) (c in Figure 7.3), (iv) identify the multiscale meandering signal (d in Figure 7.3), and (vi) identify individual half-meanders (E in Figure 7.3). These steps will be described in detail below.

7.2.3.1 Continuous Wavelet Transform

The *WigglyRivers* package relies on the curvature's continuous wavelet transform (CWT) to characterize meandering features in river transect. The CWT provides mathematical tools that allow the mapping of temporal or spatial series to time-frequency or scale-frequency domains. The mathematical descriptions and some applications in geophysics can be found in Foufoula-Georgiou and Kumar (1994) and Torrence and Compo (1998). In general, the CWT ($W_n(l_s)$) of a discrete sequence $n = 1, 2, \dots, N$, where N is the total number of points, can be defined as presented below (Torrence and Compo, 1998).

$$W_n(l_s) = \sum_{n'=0}^{N-1} x_n \Psi^* \left[\frac{(n' - n)\Delta s}{l_s} \right] \quad (7.4)$$

where l_s is the wavelet scale, the superscript * denotes the complex conjugate, and the $\Psi(\eta)$ is the wavelet function. As is mentioned in Torrence and Compo (1998), the wavelet function is obtained by normalizing a selected mother wavelet ($\Psi_0(\eta)$) to represent unit energy, as follows,

$$\Psi(\eta) = \sqrt{\frac{2\pi l_s}{\Delta s}} \Psi_0(\eta) \quad (7.5)$$

Within the *WigglyRivers* package, we use the Python codes created by Evgeniya Predybaylo that are based

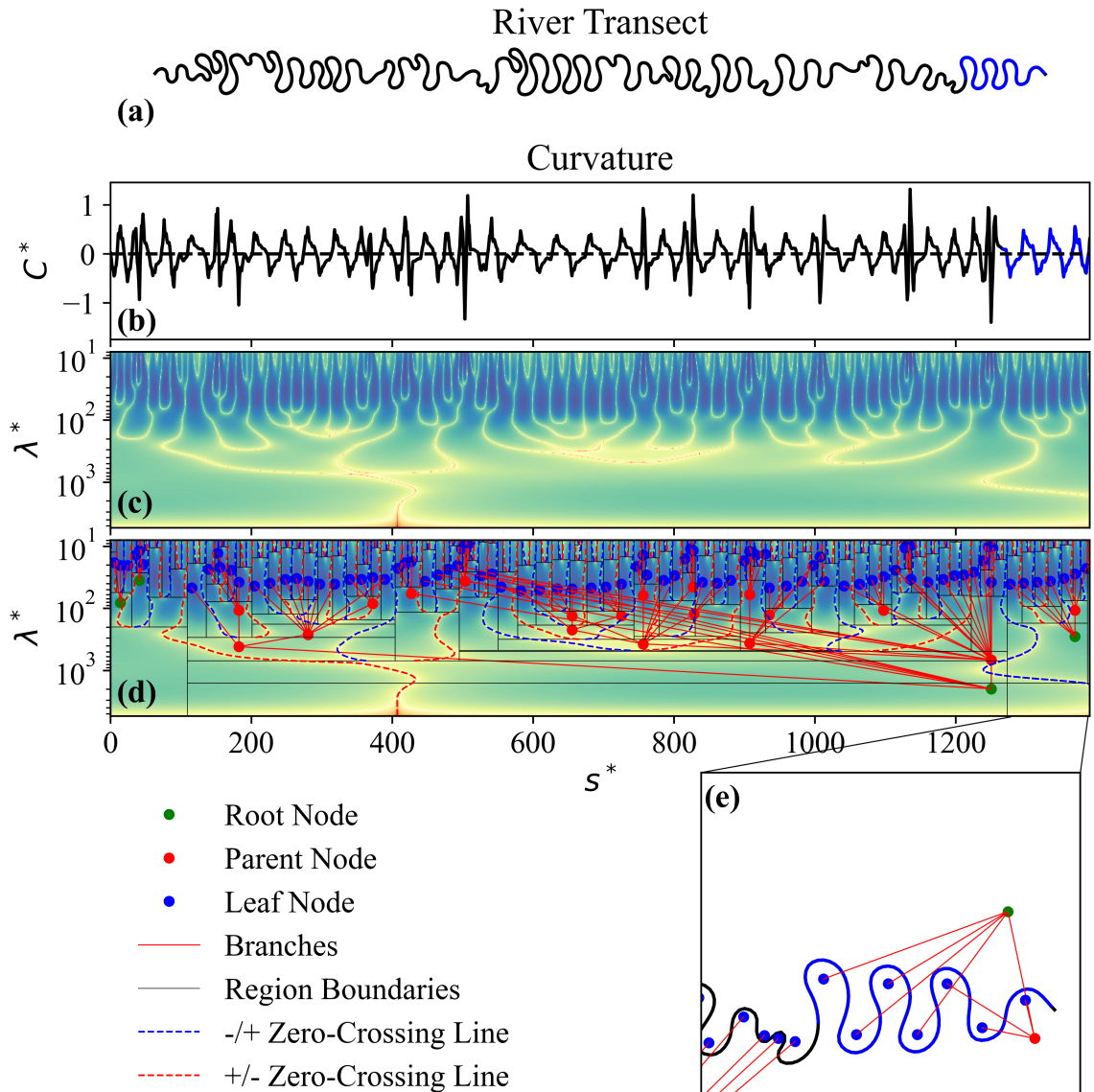


Figure 7.3: Process for automatic detection of meanders. (a) resampled and smoothed river planimetry. (b) curvature of the planimetry. (c) CWT of the curvature. (d) Construction of the scale space tree in the CWT plane. (e) zoomed in planimetry with the projected tree where individual half-meanders are identified. The blue lines in (a) and (b) denote the zoomed-in river section presented in (e).

on work done by Torrence and Compo (1998). These codes contain the Morlet and DOG (Derivatives of a Gaussian, also known as Mexican hat) mother wavelets. The mother wavelet selection depends on several factors mentioned in Torrence and Compo (1998). Among these factors are the trade-off between the spatial and scale resolutions and the use of real or complex wavelets. According to (Torrence and Compo, 1998), a narrow mother wavelet function will resolve smaller spatial features but have poor scale resolution and vice-versa for a wider function. Additionally, while real wavelets can detect sharp changes in amplitude, complex

wavelets are better for looking at the oscillatory behavior of the signal Torrence and Compo (1998). With the latter in mind and similar to Vermeulen et al. (2016), the *WigglyRivers* uses the DOG mother wavelet to perform the automatic detection of meanders in the rivers (C in Figure 7.3). That said, the user can also utilize the Morlet mother wavelet to assess the oscillatory behavior of the curvature and direction-angle signals, as done by other authors (e.g., Zolezzi and Güneralp, 2016; Gutierrez and Abad, 2014).

The resulting CWT plane of the curvature will provide a matrix with columns reflecting the distance along the channel and rows reflecting the scale of the wavelet. The package also calculates the Global Wavelet Spectrum (GWS) and the Scale-Averaged Wavelet Power (SAWP) to detect dominant wavelengths and the harmonic content of the river planimetry (Torrence and Compo, 1998; Zolezzi and Güneralp, 2016). The GWS and the SAWP can be calculated as follows,

$$GWS = \frac{1}{N} \sum_{n=0}^{N-1} |W_n(l_s)|^2 \quad (7.6)$$

$$SAWP = \frac{\delta_j \Delta s}{C_\delta} \sum_{j=j_0}^J \frac{|W_n(l_{s,j})|^2}{l_{s,j}} \quad (7.7)$$

where δ_j is the scale resolution, C_δ is the reconstruction factor, and $j = 0, 1, 2, \dots, J$ is the scale index with the largest scale J .

7.2.3.2 Multiscale meandering signal identification

A general approach to characterize meandering features in a river planimetry is by using the inflection points (zero-crossings) in the curvature signal (Howard and Hemberger, 1991). This approach is highly sensitive to the meander shapes and sampling of the river planimetry that are translated into the curvature signal, leading to a misidentification of half-meanders in river transects (Andrle, 1996; Güneralp and Rhoads, 2008). To overcome this limitation, Vermeulen et al. (2016) proposed using the CWT of the curvature to detect the dominant wavelengths in the river transect associated with half-meanders. In the CWT plane, the zero-crossing lines denote shape variations in the signal across scales, creating bounding regions at multiple scales (Mallat, 1991). The *WigglyRivers* package constructs a scale space tree that identifies the multiscale signal of meandering features, from half-meanders to large-scale variations in the river transect, the same approach that Vermeulen et al. (2016) uses.

The construction of the scale space tree in the CWT plane is done by detecting singular points between pairs of zero-crossing lines. The resulting partitioning creates regions in the CWT plane, which define the scale space tree or the ternary tree (Witkin, 1984; Rosin, 1998). The tree nodes are then obtained by estimating the maximum power in each region of the CWT plane, and the tree is constructed by linking the leaf nodes

(nodes at the smallest scales) to their corresponding parent nodes (nodes that contain the leaf nodes at larger scales) until we reach the root nodes (largest scales) (D in Figure 7.3).

Once the scale space trees are constructed in the CWT plane, the algorithm goes through each tree branch. It detects the local peaks (maximum or minimum) in the CWT plane using a hexagonal lattice technique that detects extremes and saddle points in a 2D field (Kuijper, 2004). While the local peaks in the CWT plane are associated with the dominant wavelengths in the curvature signal (i.e., half-meanders), the parent nodes of these peaks are associated with larger scales curvature variations in the river transect (i.e., “multiscale signal” or “multiple loop tree”) (Vermeulen et al., 2016). This iterative process removes nodes in tree branches where local peaks are not detected and the leaf nodes whose parent has a peak in the CWT plane (i.e., half-meander) as they are associated with noise in the curvature signal. The *WigglyRivers* also includes an additional pruning algorithm that allows a refinement in characterizing the meandering features in the river transect. This algorithm prunes the tree by peak power, where it goes through the branches, detects the parent nodes with higher power than the average power of the leaf nodes, and removes the leaf nodes with lower power, converting the parent node to a meander node. This process is helpful in river transects with multiple scales (i.e., river transects containing various stream orders) with a high noise level where the initial algorithm detects noise in the signal as individual half-meanders. This pruning routine is not included in the original MATLAB scripts created by Vermeulen et al. (2016) and has to be used after the initial identification.

The resulting pruned scale space tree is then used to map the half-meanders back to the river planimetry. This process is explained in the following section 7.2.3.3.

7.2.3.3 Meander identification

The half-meanders identified in the CWT plane are located in a specific wavelength value and are bounded by the zero-crossing lines (Vermeulen et al., 2016). These bounds are associated with the inflection points in the curvature signal and, thus, can be mapped back to the planimetry of the river by using the streamwise arc length (s) and the resampling splines. However, due to the river sampling, the zero-crossing line does not correspond to the exact location of the inflection points in the curvature. So, once the half-meander bounds are identified in the CWT plane, the *Wigglyrivers* package runs a sub-routine that estimates the location of the inflection point by interpolating the points in the curvature that passes through zero and then uses the resample splines to estimate the coordinates where the inflection points are located in the river planimetry. On the other hand, the tree nodes at each scale are projected to the planimetry (E in Figure 7.3) by circumscribing a circle between the bounding points and the middle point in the planimetry with a radius as the quarter of wavelength distance ($R = \lambda/4\pi$), similar to what was done in Vermeulen et al. (2016).

In addition to identifying the half-meanders by the inflection points, the *WigglyRivers* package also detects

the peaks of curvature adjacent to the half-meander signal, which allows the identification of the full-meander bend (green dotted line in Figure 7.2). This full-meander identification is crucial in the study of hyporheic exchange processes at the meander scale, as the neck in meanders has a hydrodynamic effect in the exchange zone impacting its residence times (Cardenas, 2008; Gonzalez-Duque et al., 2024b) and the biogeochemical processes occurring within (Revelli et al., 2008; Boano et al., 2010b; Gonzalez-Duque et al., 2024b). The extension of the meander bounds is optional in the identification process, and the user can select whether to bound meanders by the inflection points or the curvature peaks.

Once the bounds have been identified and corrected, the package saves each meander as a `Meander` class within the `RiverTransect` class and calculates the meander metrics described in section 7.2.5.

7.2.4 Supervised identification of meanders

To assess the performance of the automatic identification algorithm included in the *WigglyRivers* package, we provide a supervised identification tool that allows the user to select meanders in the river planimetry manually to create a validation set. The tool is built within the `RiverTransect` class, and it leverages the capabilities of interactive plots in Jupyter Notebooks using `plotly` (Plotly Technologies Inc., 2015) with the `Mapbox` integration. This integration allows the user to go through the river network with a satellite image as background, facilitating the manual selection of starting and ending points of full meanders through the network. Section 7.3.3.1 presents an example of the tool. Further details on how to use the tool are presented in the examples folder in the repository.

The manually identified meanders are also saved as `Meander` classes with a flag that indicates they were manually selected. This information is used by the validation routine that compares the overlapping sections (N_o) of the automatic (N_a) and manually (N_m) selected meanders and calculates the fraction of automatic overlaps (F_{oa}) and the fraction of manual overlaps (F_{ma}) as follows,

$$F_{oa} = \frac{N_o}{N_a} \quad F_{ma} = \frac{N_o}{N_m}. \quad (7.8)$$

The closer both overlapping fractions are to one, the better the automatic detection algorithm performs. With this in mind, the *WigglyRivers* package creates a 2D histogram plot (see the application in Section 7.3.3.1). It classifies the validation of the automatic identification into four zones: Zone I, or correctly identified, contains the meanders that have a high degree of overlapping ($F_{oa} \geq 0.75$ and $F_{ma} \geq 0.75$), Zone II, or sub-identified, contains the meanders where the automatic identification is only a portion of the manual identification ($F_{oa} < 0.75$ and $F_{ma} \geq 0.75$), Zone III, or over-identified, contains the meanders where the automatic identification is a superset of the manual identification ($F_{oa} \geq 0.75$ and $f_{ma} < 0.75$), and Zone

IV, or misidentified, contains the meanders where the automatic identification is not a subset of the manual identification ($F_{oa} < 0.75$ and $F_{ma} < 0.75$). The user can then use this information to assess the performance of the automatic identification algorithm and, if necessary, adjust the parameters used in the process.

The creation of the validation set through the manual identification tool can also serve as a training set for future training machine learning algorithms that detect meandering features within river networks using satellite imagery. Also, as the interactive capability is linked to NHDPlus HR, it allows the users to qualitatively assess how well the river network aligns with current satellite images.

7.2.5 Meander Metrics

Once the meanders have been identified from the supervised or unsupervised identification tools, the `Meander` class calculates the following metrics for each meander. These metrics provide morphological characteristics of meanders and serve as the basis for analyzing meanders at multiple scales. The metrics computed for each meander are the arc-wavelength (λ_{hm}), the valley length (L_{hm}), the radius of curvature (R_{hm}), the amplitude (A_{hm}), the asymmetry (a_{hm}), and the sinuosity (σ_{hm}). The calculation of each metric is explained below.

Length metrics: The `Meander` class starts by calculating the arc-wavelength (λ_{hm}) as the summation of the individual distance river sections from the starting to the ending point of the meander as follows,

$$\lambda_{hm} = \sum_{i=j}^k \sqrt{(x_{i+1} - x_i)^2 + (y_{i+1} - y_i)^2} \quad (7.9)$$

where j and k are the indices of the starting and ending points of the meander, respectively. The valley length (L_{hm}) is calculated as the Euclidean distance between the starting and the ending point of the meander as follows,

$$L_{hm} = \sqrt{(x_k - x_j)^2 + (y_k - y_j)^2}. \quad (7.10)$$

Suppose the user decides to include the points for the full-meander. The package also calculates the full-meander arc-wavelength (λ_{fm}) and the full-meander valley length (L_{fm}) by changing the range of values between j and k in equations (7.9) and (7.10) to include the extended bounds (see Figure 7.2A).

Sinuosity: The half-meander's sinuosity (σ_{hm}) is the fraction of the arc-wavelength (λ_{hm}) and the valley length (L_{hm}) and reflects the degree of wandering of a given half-meander bend. This dimensionless metric is calculated as follows,

$$\sigma_{hm} = \frac{\lambda_{hm}}{L}. \quad (7.11)$$

The subroutine also calculates the full-meander sinuosity (σ_{fm}) by using the extended arc-wavelength (λ_{fm}) and the extended valley length (L_{fm}).

Radius of Curvature: The radius of curvature of the half-meander (R_{hm} , see Figure 7.2a) is obtained by circumscribing a circle between the inflection points of the half-meander with a radius of $R_{hm} = \lambda/4\pi$, where λ is the dominant wavelength of the half-meander coming from the wavelet analysis, similar to the calculation performed in Vermeulen et al. (2016). In half-meanders selected manually, we assume that $\lambda_{fm} = \lambda$ and use the previous approach to calculate the radius of curvature.

Amplitude: The amplitude (A_{hm} , see Figure 7.2a) is estimated by rotating the half-meander coordinates to align the meander axis with the x -axis between its inflection points ($[\mathbf{x}, \mathbf{y}] \rightarrow [\mathbf{x}_r, \mathbf{y}_r]$) and calculating the difference between the maximum and minimum y -coordinates as follows,

$$A_{hm} = \max(y_r) - \min(y_r). \quad (7.12)$$

The subroutine also calculates the full-meander amplitude (A_{fm}) by using the extended bounds of the meander.

Asymmetry: For the half-meander asymmetry (a_{hm}) calculation, the package breaks the half-meander into two sections, the upstream ($\lambda_{hm,u}$) and downstream ($\lambda_{hm,d}$) arc-wavelengths, separated by the location of the maximum curvature (Figure 7.2b). Then, the subroutine estimates the asymmetry as follows (Howard and Hemberger, 1991),

$$a_{hm} = \frac{\lambda_{hm,u} - \lambda_{hm,d}}{\lambda_{hm}} \quad (7.13)$$

which ranges from -1 to 1, where negative values denote upstream asymmetry and positive values denote downstream asymmetry. The full-meander asymmetry (a_{fm}) is calculated by using the distance between peaks of curvature of the full-meander.

Funneling Factor: The funneling factor (FF) was defined by Gonzalez-Duque et al. (2024b) as the ratio between the minimum distances in the full-meander neck (L_n) and the maximum distance within the full-meander lobe (L_l) (see Figure 7.2). These lines are parallel to the line defined by the full-meander inflection points. The subroutine calculates the funneling factor as follows,

$$FF = \frac{L_n}{L_l} \quad (7.14)$$

This number has a minimum value of 1.0, where high FF values correspond to meanders with narrow necks and significant lobe space, and low FF values correspond to meanders with wider necks.

7.3 Applications

This section presents applications of the *WigglyRivers* package on idealized and natural systems. We start by looking into idealized river planimetries and then transition to natural river transects using the NHDPlus HR information. All of the applications presented here are saved as workflows within the *WigglyRivers* GitHub repository <https://github.com/gomezvelezlab/WigglyRivers>.

7.3.1 Periodic river transect example

As mentioned above, the *WigglyRivers* package can use any river planimetry coordinates. For the following applications, we will show the characterization of meandering features on idealized periodic river transects to explore the potential of the spectral tools incorporated in the package. Then, we will use the unsupervised detection tool to identify the meander bends present in the periodic river. In the first application, we use a *Kinoshita Curve* river planimetry that is a particular type of sine-generated curves that account for the fattening and skewing of meander loops (Kinoshita, 1961). The *WigglyRivers* package contains the version of the *Kinoshita Curve* presented in Zolezzi and Güneralp (2016), where the direction angle (θ) and the curvature (C) are dependent on $\kappa = 2\pi/\lambda$, the amplitude of the direction angle oscillation (θ_0), and the skewness (θ_s), and fatness (θ_f) coefficients as follows:

$$\theta = \theta_0 \cos(\kappa s) + \theta_s \sin(3\kappa s) + \theta_f \cos(3\kappa s) \quad (7.15)$$

$$C = \kappa[\theta_0 \sin(\kappa s) - 3\theta_s \cos(3\kappa s) + 3\theta_f \sin(3\kappa s)] \quad (7.16)$$

We first explored the spectral characteristics of three Kinoshita-type river transects by calculating the CWT on the curvature and the direction-angle, using a Morlet mother wavelength as performed by Zolezzi and Güneralp (2016). These transects have 20 full-meander bends that have the same wavelength ($\lambda = 100$ m), skewness ($\theta_s = 0.344$), and fatness ($\theta_f = 0.031$) but vary in the amplitude of the direction angle oscillation as $\theta_0 = [90^\circ, 115^\circ, 120^\circ]$. In all of the river transects, we calculated the CWT of the curvature and direction-angle and their respective global wavelet spectrum (GWS) and scaled-average wavelet power (SAWP) (b and c in Figure 7.4). The GWS of the curvature for the first river transect (b in Figure 7.4) shows two distinct power peaks, one in the $\lambda = 100$ m, as expected, and another one in the $\lambda = 37$ m, this behavior is lost in the CWT of the direction angle where we only see a strong peak at $\lambda = 100$ m (c in Figure 7.4). The multiple peaks in the CWT of the curvature are common in these systems because the CWT of the curvature tends to shift towards lower wavelengths than the direction-angle (Zolezzi and Güneralp, 2016). However, this behavior is reduced as the complexity of the river planform increases, where we can see an unimodal

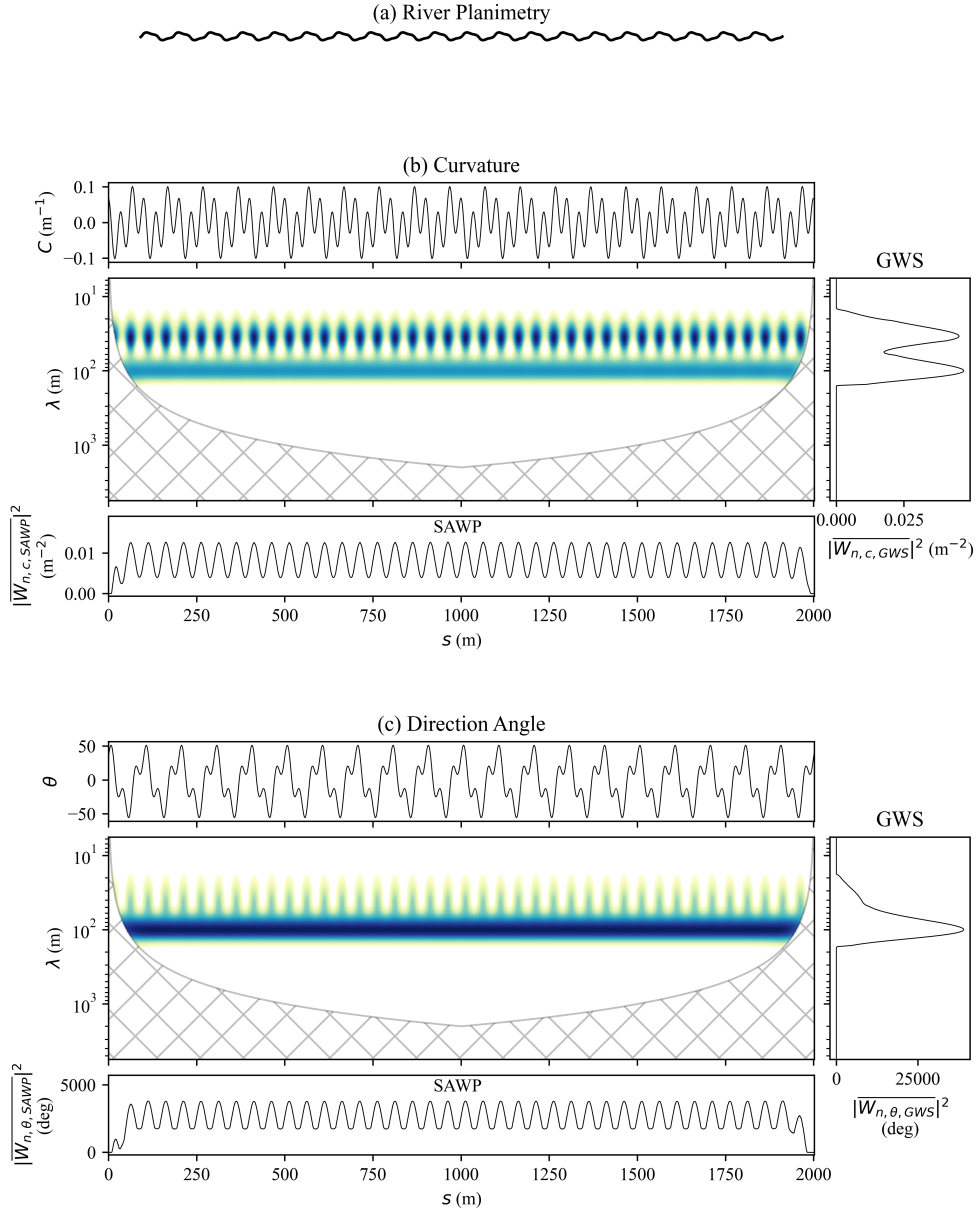


Figure 7.4: Spectral characterization of a regular river transect planform. (a) river transect generated with equation (7.15) with $\theta_0 = 37^\circ$, $\theta_s = 0.344$, $\theta_f = 0.031$, and $\lambda = 100$. (b) curvature calculated with equation (7.2), CWT of the curvature below, the GWS on the right is calculated with equation (7.6), and SAWP at the bottom is calculated with equation (7.7). The same arrangement is given on (c) direction-angle, calculated with equation (7.3). The hatch areas are the cone of influence of the CWT calculations.

power distribution at $\lambda = 100$ m in the GWS (Figure 7.4). In the case of SAWP, we see a periodic signal with a periodicity every 50 m associated with the half-meander arc wavelength in both river transects (see SAWP in b and c in Figures 7.4). The remaining river transects are presented in Figures D.2 and D.3 in the

Appendix D. Lastly, the comparison between the GWS of the three river transects shows a distinct peak in $\lambda = 100$ m for all the river transects and the curvature and the direction-angle (a and c in Figure 7.5), this behavior is expected as we selected the wavelength of the Kinoshita curve to be 100 meters. In the SAWP comparison, we see the same periodicity with increasing power as the complexity of the meandering planform increases (b and d in Figure 7.5).

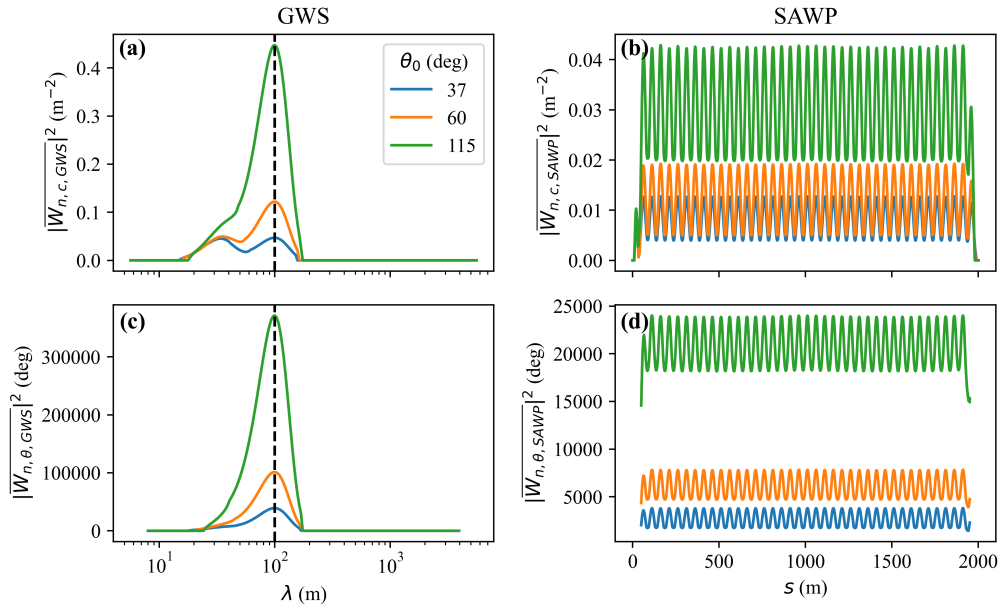


Figure 7.5: Comparison between GWS values (a) for curvature and (c) for direction-angle, and SAWP (b) for curvature and (d) for direction-angle on periodic river transects with a wavelength (λ) of 100 m (dashed line in a and c).

As the *WigglyRivers* explores the multiscale nature of the river transect, we wanted to see the spectral characteristics of a periodic network with changing an increasing wavelength. With that in mind, we created a river transect with a wavelength that increases as $\lambda = [50, 100, 200, 500]$ m every five full-meander bends with values of $\theta_0 = 115^\circ$, $\theta_s = 0.344$, and $\theta_f = 0.031$ (a in Figure 7.6). The CWT of the curvature for this system shows an apparent increase in the dominant wavelength as the river transect wavelength increases with the highest power shifted towards the small wavelengths (b in Figure 7.6). We see the opposite in the CWT of the direction-angle, where the power is shifted towards the larger wavelengths (c in Figure 7.6). The SAWP curves are different for both the curvature and the direction-angle. In contrast, the curvature SAWP shows oscillating signals for the meanders at $\lambda = 50$ m with decreasing power and extending oscillations as we move to larger wavelengths; the direction-angle SAWP oscillates around the same power with extended periodicity as we move to larger wavelengths. Additionally, the SAWP oscillations in meandering river transects without skewness and fatness tend to have smaller bumps in the spectrum (Figure D.4 in the Appendix D).

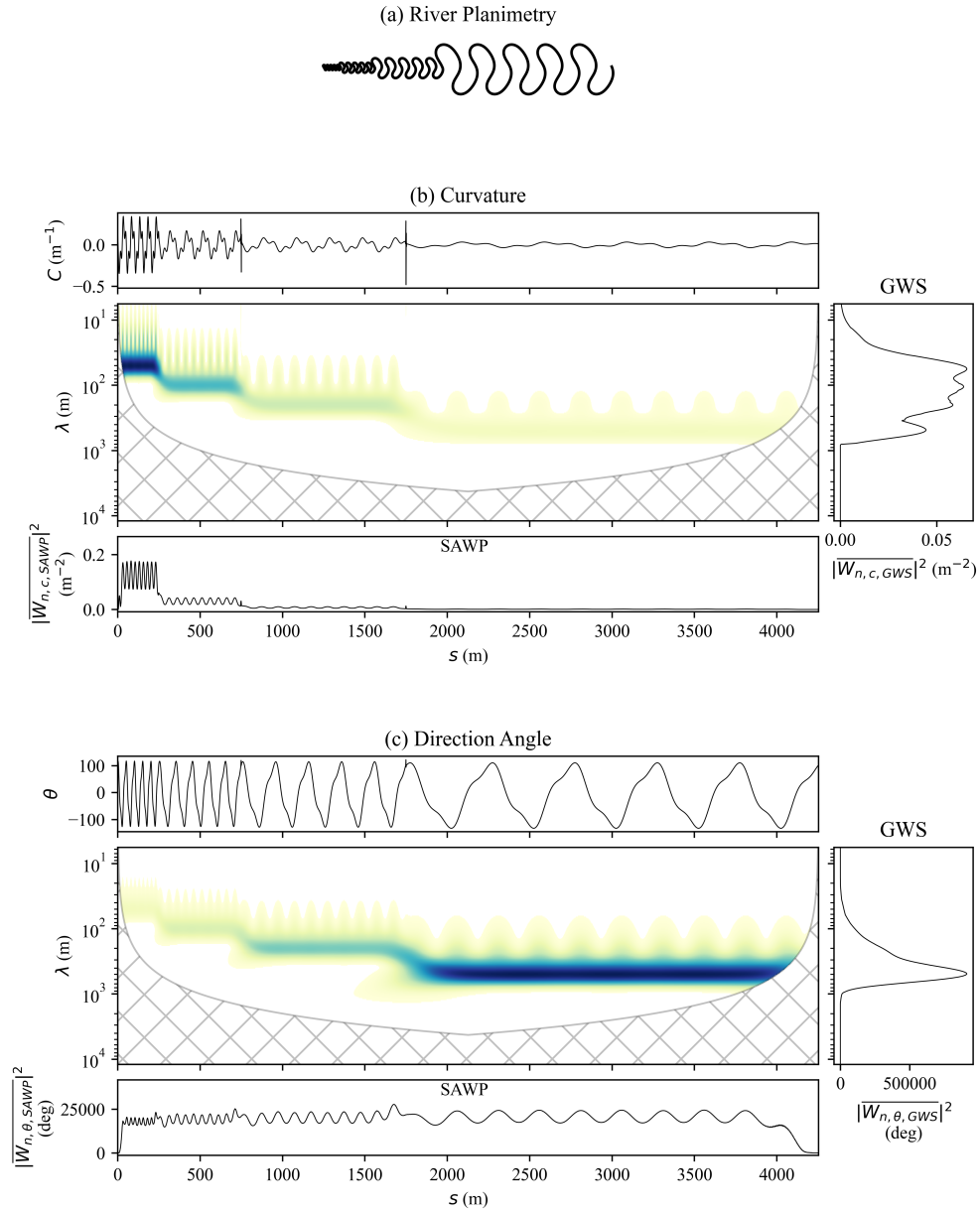


Figure 7.6: Spectral characterization of a regular river transect planform with changing wavelength ($\lambda = [50, 100, 200, 500]$). (a) river transect with $\theta_0 = 115^\circ$, $\theta_s = 0.344$, and $\theta_f = 0.031$. (b) curvature calculated with equation (7.2), CWT of the curvature below, the GWS on the right is calculated with equation (7.6), and SAWP at the bottom is calculated with equation (7.7). The same arrangement is given on (c) direction-angle, calculated with equation (7.3). The hatch areas are the cone of influence of the CWT calculations.

In summary, while CWT and the curvature allow the characterization of the dominant wavelengths at smaller scales, the CWT of the direction-angle is capable of identifying the dominant wavelengths at larger scales, similar to Zolezzi and Güneralp (2016). Furthermore, the GWS shows the distribution of dominant

wavelengths throughout the river transect, and the SAWP shows the power distribution across the river centerline, allowing the user to identify the periodicity along the river planimetry. All of this information can be used to characterize the multiscale nature of rivers.

For the last analysis on the Kinoshita-type river transects, we tested the unsupervised meander identification algorithm on the river presented in Figure 7.6. As can be seen, the algorithm constructs the scale space tree in the CWT domain and, from there, is capable of identifying 39 out of the 40 half-meander bends, with the last one missing due to its proximity to the boundary (Figure 7.7). The radius of curvature (R_{hm}) increases with the meander size from 4 to 40 m, the half-meander amplitude (A_{hm}) increases from 7 to 70 m, the half-meander sinuosity (σ_{hm}) has a constant value of 2.78, the funneling factor (FF) has a value of 2.4, except in the transitions between wavelength values, and the asymmetry (a_{hm}) has a constant value of -0.5, which is related to an asymmetry upstream (we assumed the river flows from left to right in this case).

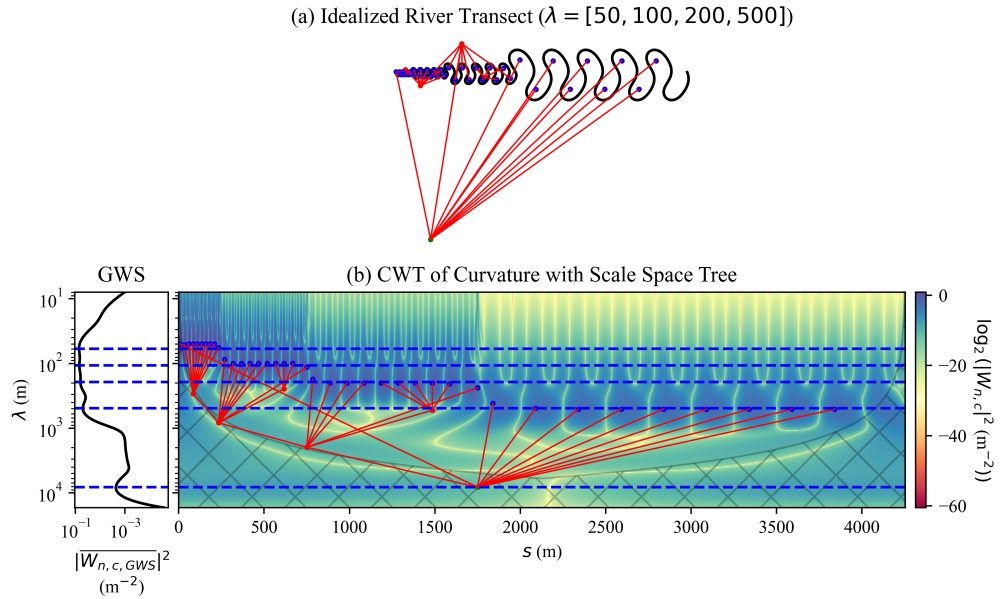


Figure 7.7: Unsupervised identification of meander bends in the regular river transect planform with changing wavelength ($\lambda = [50, 100, 200, 500]$). (a) river transect with $\theta_0 = 115^\circ$, $\theta_s = 0.344$, and $\theta_f = 0.031$ with the projected scale space tree. (b) CWT of the curvature with the scale space tree. The blue dots denote the location of the meander nodes, the red dots denote parent nodes, and the green node represents the root node. These nodes are connected by the branches (red lines). The blue dashed lines denote the peaks in the wavelength found in the GWS.

7.3.2 Idealized channel example

For the following example, we used the *meanderpy* Python package (Sylvester et al., 2019; Sylvester, 2023) to generate idealized meandering river planforms. This package is based on the numerical model described

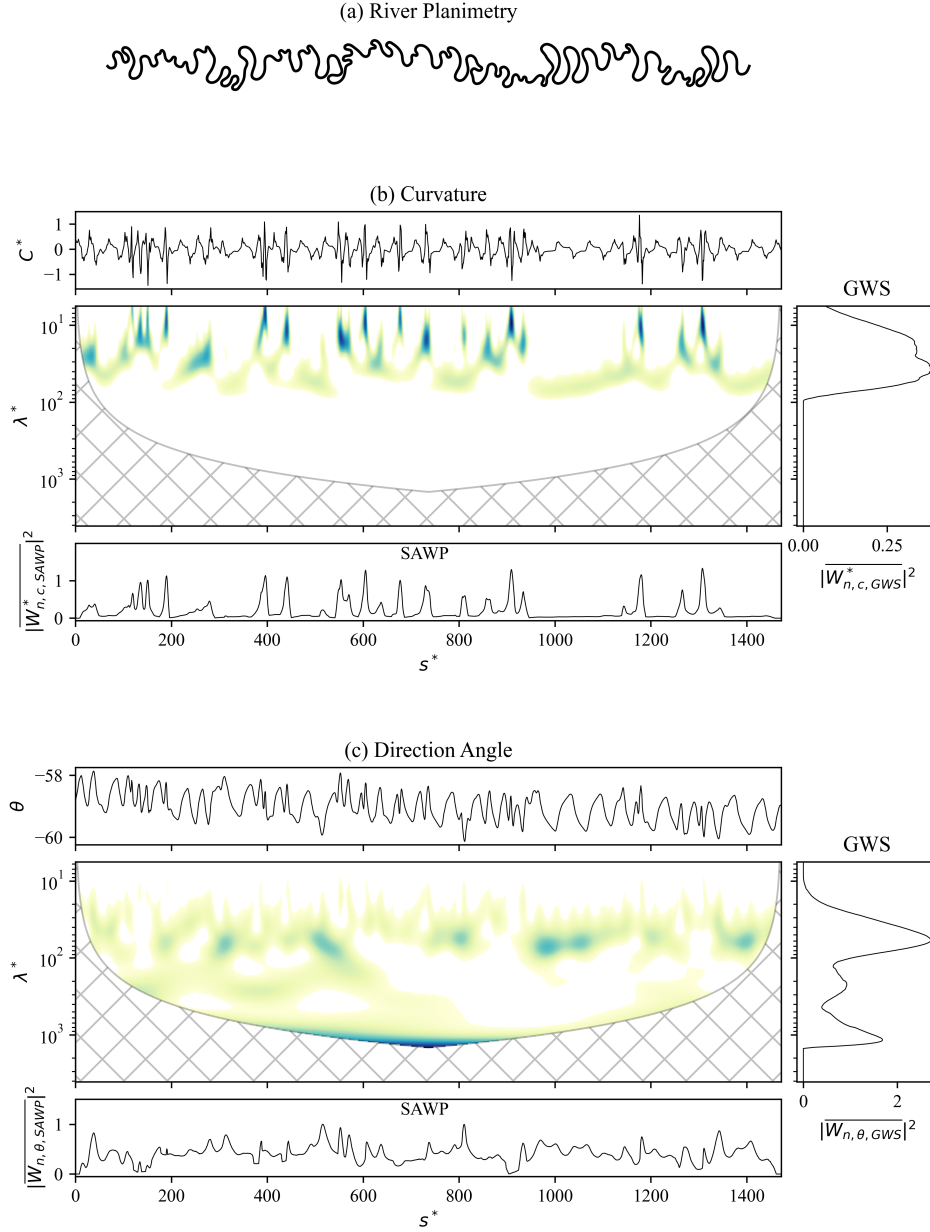


Figure 7.8: Spectral characterization of a river transect modeled with *meanderpy*. (a) river transect. (b) curvature calculated with equation (7.2), CWT of the curvature below, the GWS on the right is calculated with equation (7.6), and SAWP at the bottom is calculated with equation (7.7). The same arrangement is given on (c) direction-angle, calculated with equation (7.3). The hatch areas are the cone of influence of the CWT calculations.

by Howard and Knutson (1984). It creates evolving meander planforms that depend on the computation of migration rates based on the weighted sum of upstream curvatures (Sylvester et al., 2019). However, the simple kinematic model creates realistic meandering planforms that serve as a tool to test the functionality of

WigglyRivers. We ran one simulation assuming the default values of the example presented in *meanderpy* and took three river planforms that have increasing complexity. In this work, we present the results for the most complex planform in non-dimensional form, taking the width of the channel for the simulations ($W = 200$ m) (Figure 7.8). The remaining planforms are presented in the Appendix D (Figures D.5 and D.6).

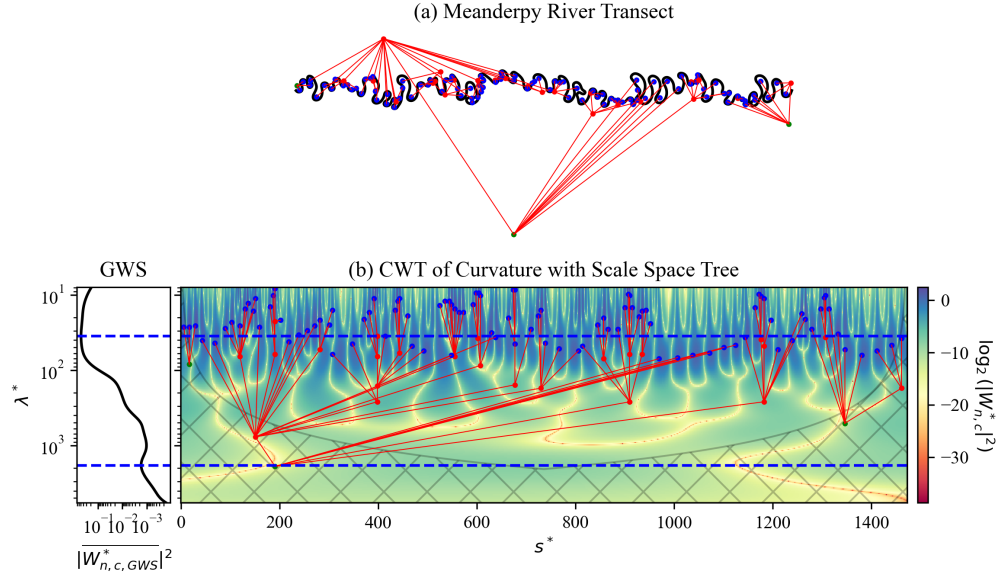


Figure 7.9: Unsupervised identification of meander bends of a river transect modeled with *meanderpy*. (A) river transect with the projected scale space tree. (B) CWT of the curvature with the scale space tree. The blue dots denote the location of the meander nodes, the red dots denote parent nodes, and the green node represents the root node. These nodes are connected by the branches (red lines). The blue dashed lines denote the peaks in the wavelength found in the GWS.

In the modeled river planimetry, we see meanders varying in complexity, from sinusoidal to highly skewed meander geometries. This complexity is reflected in the CWT of the curvature, where there is a broader range of dominant wavelengths in the GWS distribution that ranges from 10 to 42 river widths (b in Figure 7.8); these values are similar to the ones presented in (Gutierrez and Abad, 2014). Conversely, the direction-angle shows a multimodal distribution of the dominant wavelengths with the highest peak at 57 river widths and two other peaks at larger wavelengths close to the cone of influence. The presence of high powers close to the cone of influence is a known behavior for the direction-angle due to its tendency to capture higher wavelengths (Zolezzi and Güneralp, 2016). This behavior can have substantial implications while analyzing large river transects where the direction-angle would not be capable of detecting signals within the range of the meander bends. In both cases, the SAWP presents non-periodic fluctuations with power peaks close to small half-meander bends. Lastly, in Figure 7.9, we show the results of the unsupervised identification of meander

bends in the river planimetry. In this identification, the package detected 83 of the 89 half-meander bends in the river planimetry, capturing complex full-meander bends throughout the river planform. Different metrics show that the algorithm can capture simple and complex meander bends. For instance, the σ_{hm} varies from 1.01 to 4.88, and the FF ranges from 1 to 5.9, where small values of these metrics are related to sinusoidal geometries and higher values are related to complex geometries with closer necks. We will explore the range of these and the other meander metrics in natural river channels present in the next subsection.

7.3.3 Natural river channels examples

The following subsections explore the tool's potential in natural river systems using the NHDPlus HR information. We manually identify meanders in random river transects across the conterminous United States (CONUS) to test the automatic identification. Then, we analyze the spectral characteristics and the meander metrics of automatically identified meanders at a subregion level related to a 4-Digit Hydrologic Unit (HUC-4) according to Moore et al. (2019).

7.3.3.1 Validation of unsupervised detection

To validate the automatic identification of meanders, we manually selected 1313 full-meander bends in 35 random reaches of HUC-8 across CONUS. As was mentioned in section 7.2.4, the validation is performed by calculating the overlapping fractions (F_{oa} and F_{ma}) and dividing the resulting meanders into four zones. The resulting comparison (Figure 7.10a) shows that more than 53% of the automatically identified full-meander bends are in reasonable agreement with the manual identification (Zone I). The comparison also presents a 35% of the full-meander bends where either the automatic or manual identification is a subset of the other (Zone II and III). Finally, the remaining 11% of the full-meander bends are either misidentified or not identified (Zone IV). As an additional analysis, we include a histogram of the classification discretized by stream order (SO) (Figure 7.10b), where we can see that the automatic identification works well in middle to large stream orders (SO 3 to 8) and has more difficulties in small stream orders (SO 1 and 2) due to the lower resolution of the river planform. In summary, the results show that the automatic identification can capture most of the full-meander bends in the explored river planforms, where more than 88% of meanders are identified in the network.

7.3.4 Catchment analysis

As an example for the catchment characterization, we used the *WigglyRivers* tool to analyze the unsupervised identification results on the Tennessee River Region (HUCs-4 0601, 0602, 0603, and 0604) using the NHDPlus HR information. To do this, we used the NHD extraction tool built inside the package to obtain

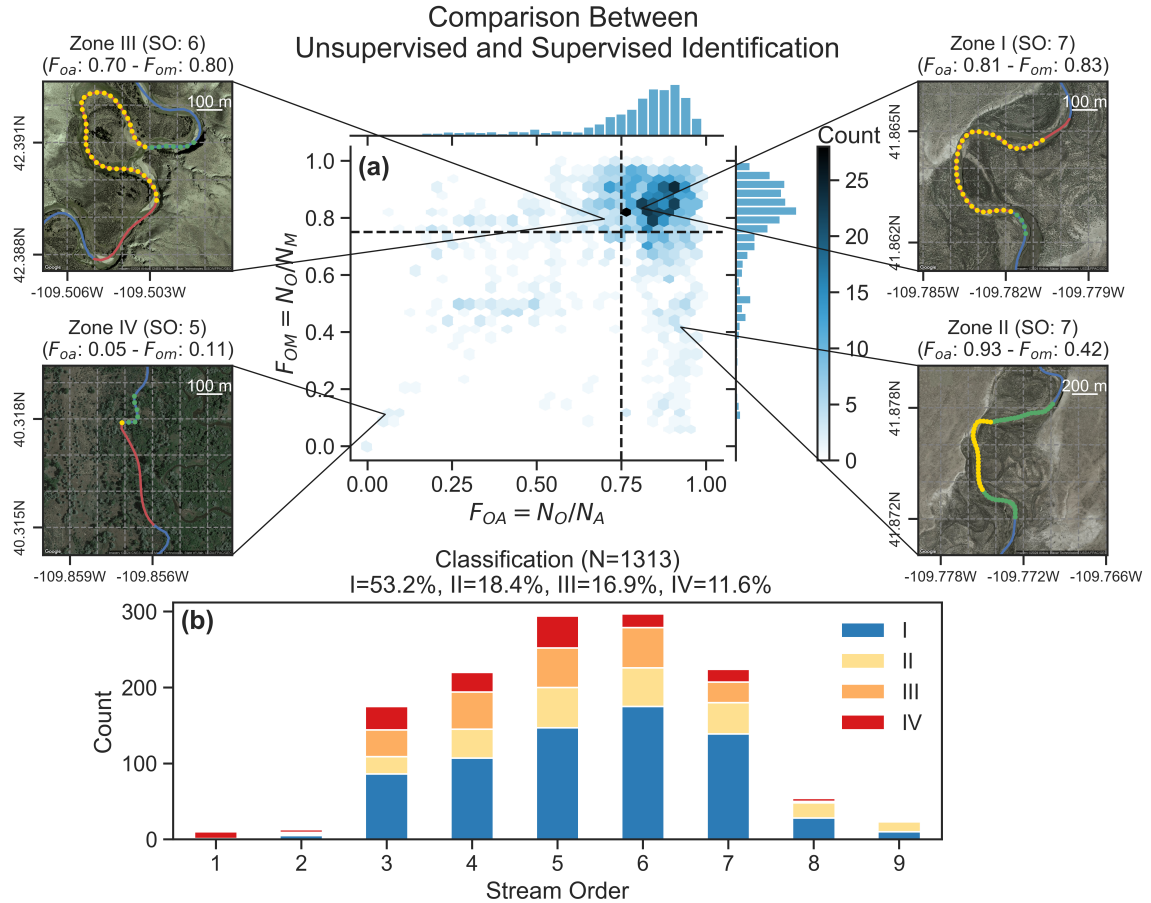


Figure 7.10: (a) hexbin plot of the overlapping fractions (F_{oa} and F_{ma}) of the automatic and manual identification of full-meander bends, calculated with equation (7.8). The color scale represents the number of full-meander bends in each hexbin. The dashed lines are the set thresholds for the zone separation. The insets show examples of the identification of meander for each zone, where the blue line is the river centerline, the red line is the automatic identification, the green dots show the manual identification, and the gold dots show the overlapping points. (b) histogram of the classification of the overlapping fractions discretized by stream order (SO).

the river transects from headwaters to the outlet of each subregion or an already explored path, generating around 180,000 reaches to analyze. First, we study the spectral behavior of one river transect that contains streams of order 1 to 7 within the 0602 subregion (Figure 7.11). The curvature of the river transect is highly fluctuating, with the highest amplitude variability at the start of the river transect, going in tandem with the CWT and SAWP powers. As we move downstream, the amplitude of the curvature decreases, as well as the power values in the CWT and SAWP (b in Figure 7.11). The range of fluctuations in the direction-angle is smaller than the curvature, presenting high variability throughout the SAWP and shifting the dominant wavelengths to the highest powers close to the cone of influence (c in Figure 7.11). The GWS of the curvature has one dominant wavelength at around 1,000 m with a small peak at 4,000 m, suggesting an overall increase

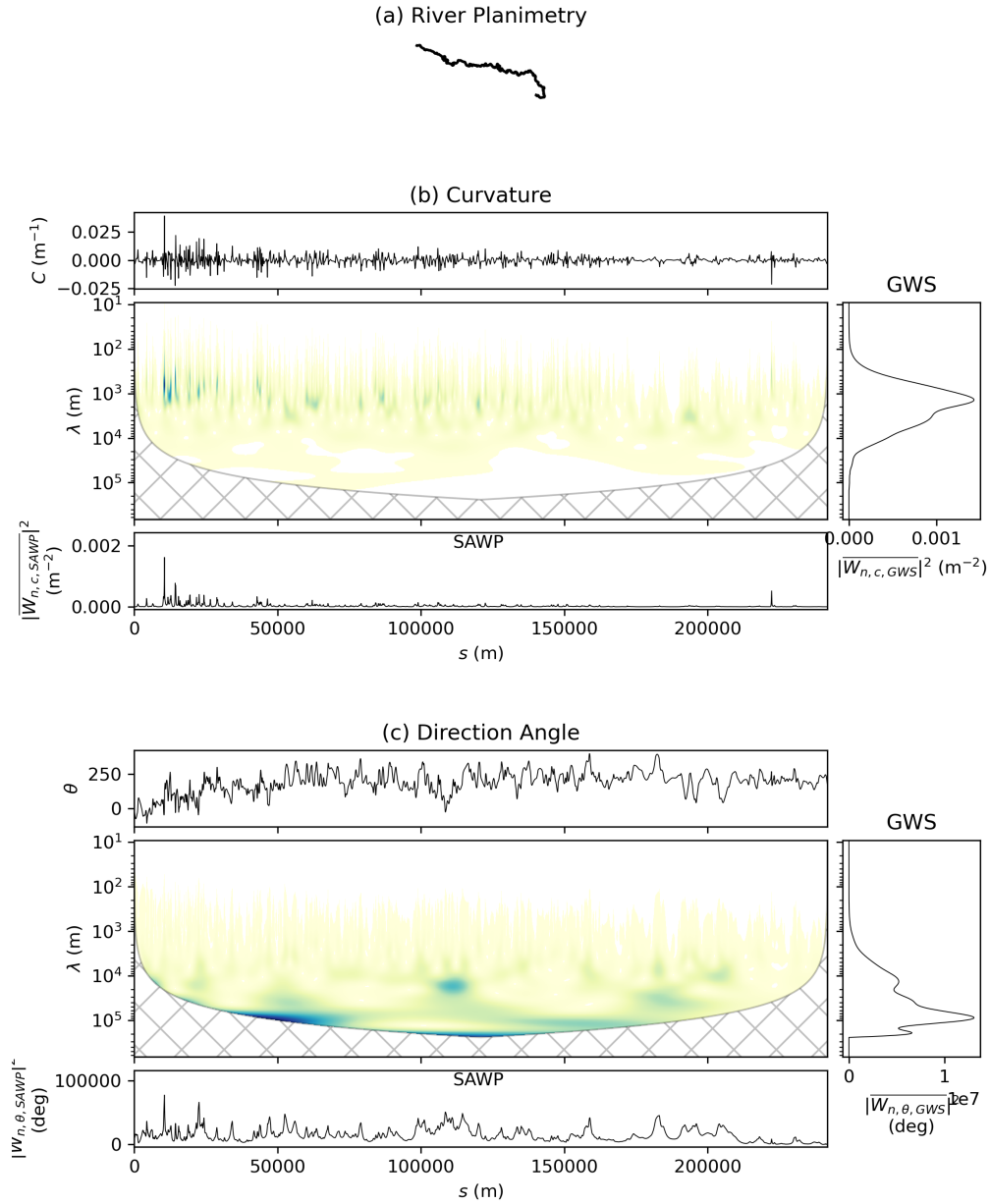


Figure 7.11: Spectral characterization of a river transect within the 0602 subregion river network. (a) river transect. (b) curvature calculated with equation (7.2), CWT of the curvature below, the GWS on the right is calculated with equation (7.6), and SAWP at the bottom is calculated with equation (7.7). The same arrangement is given on (c) direction-angle, calculated with equation (7.3). The hatch areas are the cone of influence of the CWT calculations.

in meander size as we move downstream, similar to the one presented in Figure D.3. On the other hand, the high peak in the GWS of the direction-angle is located at 60,000 m, which is close to the cone of influence of the CWT and masks the dominant wavelengths of meandering features in the network. A similar behavior is

shown in another river transect within the 0604 subregion (Figure D.7 in the Appendix D).

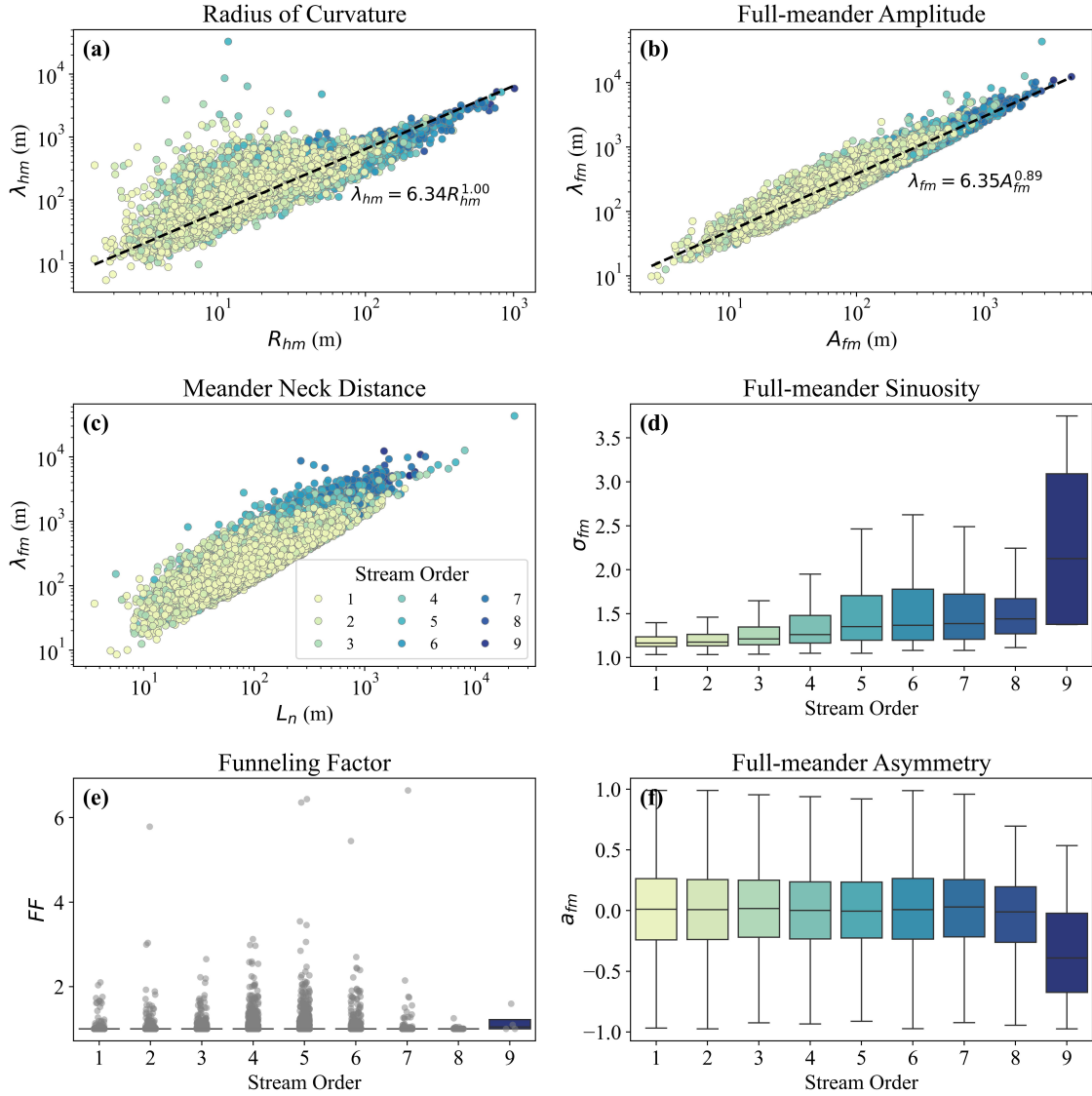


Figure 7.12: Relationships between meander length metrics and (a) radius of curvature (R_{fm}), (b) full-meander amplitude (A_{fm}), (c) meander neck distance (L_n), (d) full-meander sinuosity (σ_{fm}), (e) funnelling factor (FF), and (f) asymmetry (a_{fm}). The colors denote the stream order.

After performing the unsupervised identification, we obtained 55,593 full-meander bends across the Tennessee River Region. This information allows us to analyze the possible relationships between the meander metrics and the river characteristics. As an example, we relate the meander metrics for all the stream orders in the river network (Figure 7.12), and also show maps that contain the distribution of the analyzed metrics across the region (Figure 7.13). In our results we visualize a scaling relationship between the half-meander arc wavelength (λ_{hm}) and the radius of curvature (R_{hm}) and another relationship between the full-meander arc

wavelength (λ_{fm}) and the full-meander amplitude (A_{fm}) (A and B in Figure 7.12) that have scaling values similar to the ones reported in Leopold et al. (1992). From these relationships, we can see that the radius of curvature and amplitude increases with an increasing meander size with a scaling parameter of around 1.0. This relationship can also be seen in the distribution of meanders across the Tennessee River Region, where darker blue colors are close to the outlets of the subregions (a, b, and c in Figure 7.13). Another interesting relationship is the one between the full-meander arc wavelength and the full-meander neck length (L_n), where we see that the same neck length can be associated with different meander arc wavelengths (c in Figure 7.12), this explains why the funneling factor (FF) does not vary considerably over scales and across the region (e in Figure 7.12 and f in Figure 7.13). On the other hand, the sinuosity shows a tendency to increase with increasing stream order; however, there is a lot of variability in the sinuosity values across the region (d in Figure 7.12 and e in Figure 7.13), suggesting that large rivers can also produce simple meander geometries. Lastly, we see that the full-meander asymmetry (a_{fm}) is fairly constant over scales and across the region, with values that range between -1 and 1 for the majority of stream orders (f in Figure 7.12 and d in Figure 7.13). It is important to note that the box plot presented in Figure 7.12 for stream order nine was constructed with only four full-meander bends due to the limited information obtained for this stream order, so we cannot make inferences about this river scale.

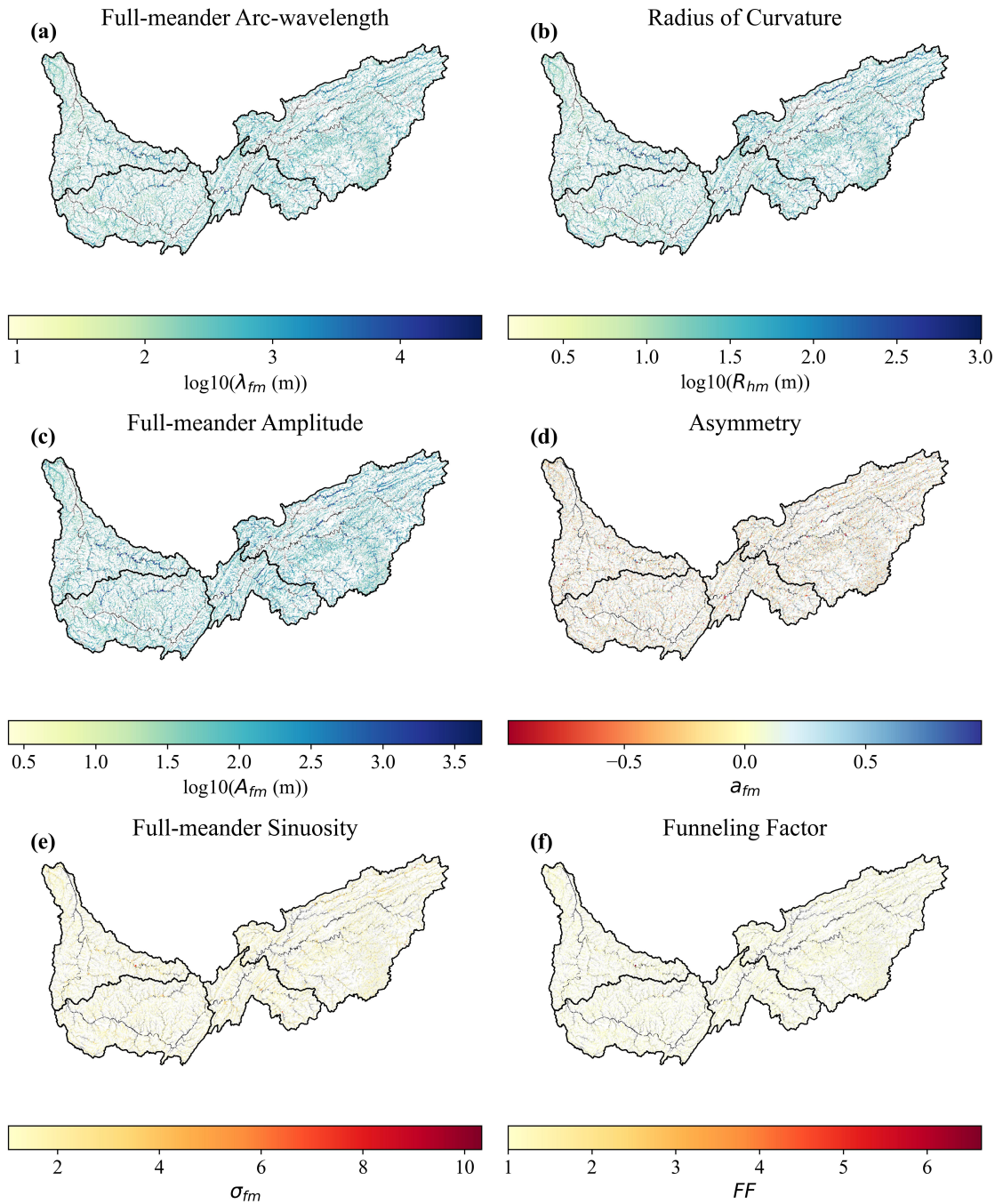


Figure 7.13: Tennessee River Region (HUCs-4 0601, 0602, 0603, and 0604) maps showing the distribution of (a) the full-meander arc-wavelength (λ_{fm}), (b) the radius of curvature (R_{hm}), (c) the full-meander amplitude (A_{fm}), (d) the full-meander asymmetry (a_{hm}), (e) the full-meander sinuosity (σ_{fm}), and (f) the funneling factor. The watershed outlet is located on the top left corner. Notice that the main stem was not captured by the unsupervised detection and is illustrated here in gray for representation purposes.

7.4 Conclusions

The *WigglyRivers* Python package provides tools that allow the analysis of the multiscale nature of river planforms and the exploration of relationships between the meander metrics and river characteristics. The package also contains supervised and unsupervised meander bend identification algorithms that characterize meandering geometries in river transects. We validate the package with idealized and natural river planforms using spectral and supervised identification tools, showing the potential of the package to capture the multiscale nature of river planimetry and the relationships between the meander metrics.

The incorporation of extraction tools for the NHDPlus HR information expands the scope of the package by allowing the extraction and subsequent analysis of river transects across CONUS. This NHDPlus HR information can also give additional river metrics, such as flow and slope, and can be connected to other databases that can expand the analysis on meandering bends. We show part of this potential by analyzing the Tennessee River Region's spectral characteristics and the meander metrics, where we found scaling relationships between the meander metrics and river characteristics.

CHAPTER 8

Conclusions and Future Work

In this part of the dissertation, we explore the role of the meander geometry and topology, the regional groundwater flow, and the availability of chemical constituents in the biogeochemical potential for denitrification within the hyporheic exchange zone (Chapter 6). We achieve this by conceptualizing a dimensionless framework using the groundwater flow and transport models. In this dimensionless framework, we proposed a set of master variables that describe the hydrodynamics of the system and the biogeochemical processes occurring in the hyporheic zone. Our results show how the neck of the meanders creates strong hydraulic gradients that shield the hyporheic zone from the compressing effect of the regional groundwater flow. This necking effect also impacts the residence times in the hyporheic zone, where meanders with a smaller neck tend to have shorter residence times due to the increase in velocities close to the neck. Lastly, our work explores the complex interplay between the transport of chemical constituents, the biogeochemical time scales, and substrate availability, illustrating the importance of carbon and oxygen as limiting factors in the denitrification process of the hyporheic exchange zone. Although the conceptualized model is idealized, it captures the first-order controls for the exchange process and provides insight into the biogeochemical potential of meanders to become net sinks or sources of nitrates across river corridors. Additionally, the model dimensionless framework allows the exploration of multiple meander topologies and geometries, providing a basis for future work that explores the biogeochemical potential of sinuosity-driven hyporheic exchange across scales.

One crucial concept not explored in Chapter 6 was the impact of physical and chemical heterogeneities of the porous matrix in the biogeochemical potential of denitrification. The heterogeneity of both properties in the porous matrix generates hotspots that show disproportionately high reaction rates relative to the surrounding matrix (McClain et al., 2003), which can produce important zonation in the biogeochemical processes within the hyporheic exchange zone and have implications for the management of ecosystem services and river restoration strategies (Arora et al., 2022). Furthermore, as Khurana et al. (2022) suggests, ignoring the spatial-terminal heterogeneities can exacerbate inaccurate estimations of nutrient export and microbial biomass. This problem is compounded by the fact that heterogeneities are site- and scale-dependent and can be assessed by integrating biogeochemical, hydrogeological, and geophysical data into the groundwater modeling approach (Scheibe et al., 2006). A way to approach the heterogeneity problem is to use simplified homogeneous models that capture the overall biogeochemical process (Sanz-Prat et al., 2015). An example of this approach is presented in Sanz-Prat et al. (2016), where the authors approximate the complexity of a

two-dimensional heterogeneous biogeochemical model into an equivalent uniform one-dimensional model by mapping the spatial exposure-time distribution and accounting for the time offset between exposure and travel time.

In our case, we are interested in looking at the overall denitrification potential for the complete sinuosity-driven hyporheic exchange zone. While heterogeneities within the meander can cause the zonation of biogeochemical reactions, we are confident that our modeling approach can provide reasonable estimates of the overall denitrification potential by mapping the chemical and hydraulic properties to equivalent variables. As an example, we created an idealized two-dimensional model that compares the denitrification potential between a heterogeneous and a homogeneous porous matrix (the model conceptualization is provided in Appendix E). In this model, we included 15 elongated lenses of a liable substrate at random locations (Figure 8.1a) and compared its denitrification potential (P_{NO}) to a homogeneous porous matrix that has an equivalent amount of particulate organic carbon (POC) (Figure 8.1b). Results show that even though the homogeneous model does not capture the spatial details of the heterogeneous model, both have the same integrated denitrification potential. These preliminary results suggest that we could be able to map the complexity of the biogeochemical process to equivalent variables to account for the heterogeneity of the hyporheic exchange zone in future work.

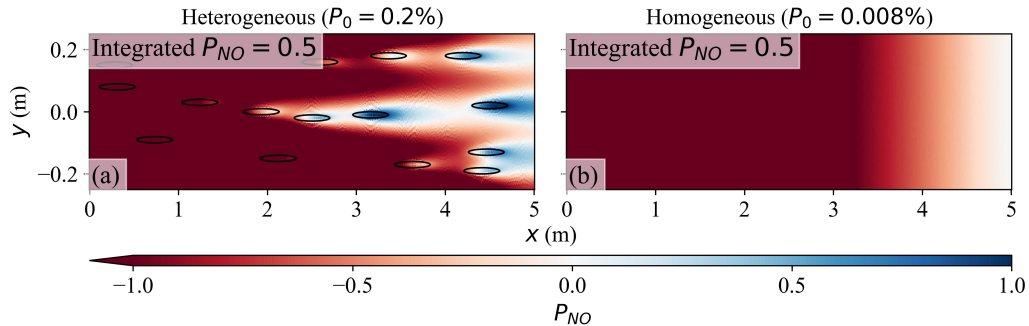


Figure 8.1: Denitrification potential comparison between (a) heterogeneous and (b) homogeneous porous matrix. The 15 black lenses in the heterogeneous system (a) are the location of liable particulate organic carbon (POC) where the dissolution of organic carbon will occur. The integrated denitrification potential is calculated with equation (6.18) using the integrated mass of nitrates coming from the left and the integrated mass of nitrates leaving the porous media on the right.

Besides heterogeneity, it is important to remember that the assumptions behind the reduced-complexity model carry other limitations that can be addressed in future work. First, our model neglects the three-dimensional nature of groundwater flow and the nested nature of exchange processes that can be important near the channel. Also, we assumed a steady river stage and chemical constituent concentration, as mentioned in Chapter 6, these boundary conditions have significant variations over space and time constraining the

exchange dynamics, residence times, and substrate supply.

The second piece of the puzzle on the road to characterizing the biogeochemical potential of sinuosity-driven hyporheic exchange at a national scale is the identification of meandering geometries along river transects. In the work presented in Chapter 7, we developed the *WigglyRivers* Python package, a river identification tool that characterizes meandering features in river transects. This Python package uses wavelet-based methods to explore the spectral characteristics of a given channel and uses this information to identify meander bends along the river. It also has an integration that leverages the NHDPlus HR information to extract river planforms across the Conterminous US (CONUS). Finally, this package also contains a supervised identification tool that allows the user to create a validation set for the unsupervised identification routines. The unsupervised identification was validated using information from rivers across the CONUS. This package opens the door for future characterization of meander geometries across CONUS that will be later used to estimate the contribution of lateral exchange processes to the total hyporheic exchange fluxes. Finally, the package also provides the basis for future morphodynamic characterization of rivers at a national scale.

In future work, we intend to create hyporheic exchange surrogate models using the meander geometries extracted from the NHDPlus HR and the conceptual hydrodynamic and biogeochemical model. These surrogate models can be trained using an active kriging approach (i.e., Jones and Schonlau, 1998; Bichon et al., 2008; Lam and Notz, 2008; Mo et al., 2019) and will allow the efficient estimation of hyporheic exchange fluxes across CONUS. Additionally, we aspire to use the spectral tools in the *WigglyRivers* package to explore the characteristics of rivers across CONUS and how they relate to morphodynamic and lithological variables.

Appendix A

Supplemental Material for Chapter 2: "Groundwater Circulation within the Mountain Block: Combining Flow and Transport Models with Magnetotelluric Observations to Untangle Its Nested Nature"

A.1 Additional Figures

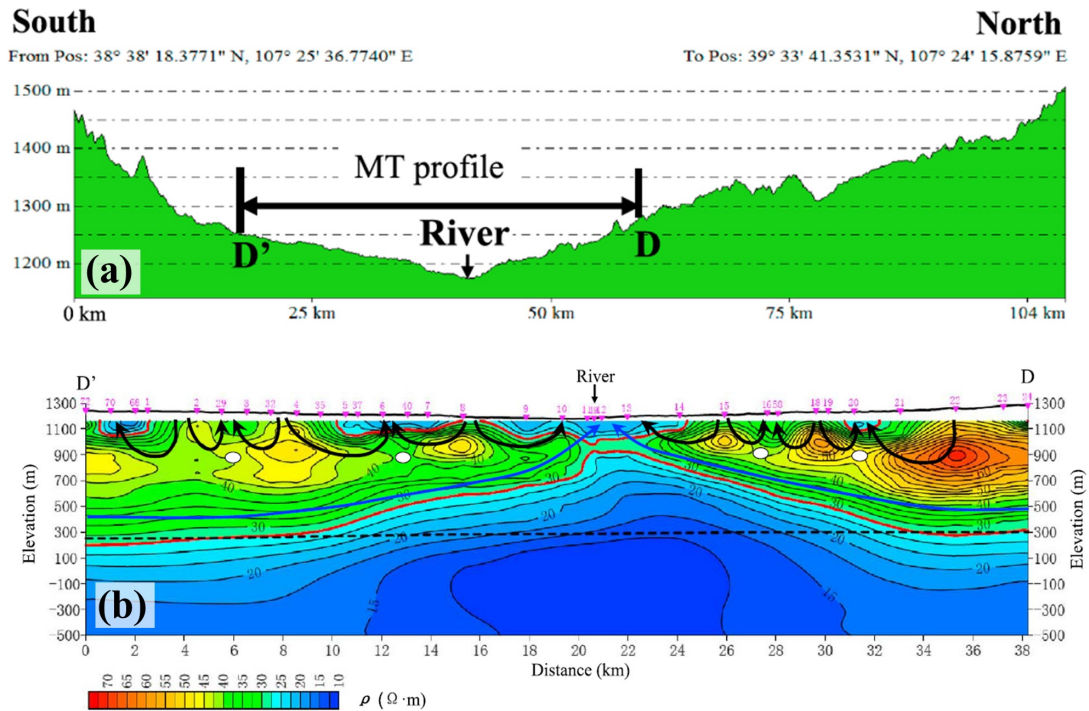


Figure A.1: MT survey crossing Dosit River, China. (a) topography and location of survey profile. (b) distribution of apparent resistivity and schematic streamlines along with profile DD', the pink numbers and triangles denote the location of MT stations, the black dashed line is the boundary of the Cretaceous and Jurassic formations, the solid black arrows are streamlines of local flow systems, the solid blue lines with arrows are streamlines of old regional flow systems, and the white circles are internal hydraulic traps (stagnation zones). Modified from Jiang et al. (2014).

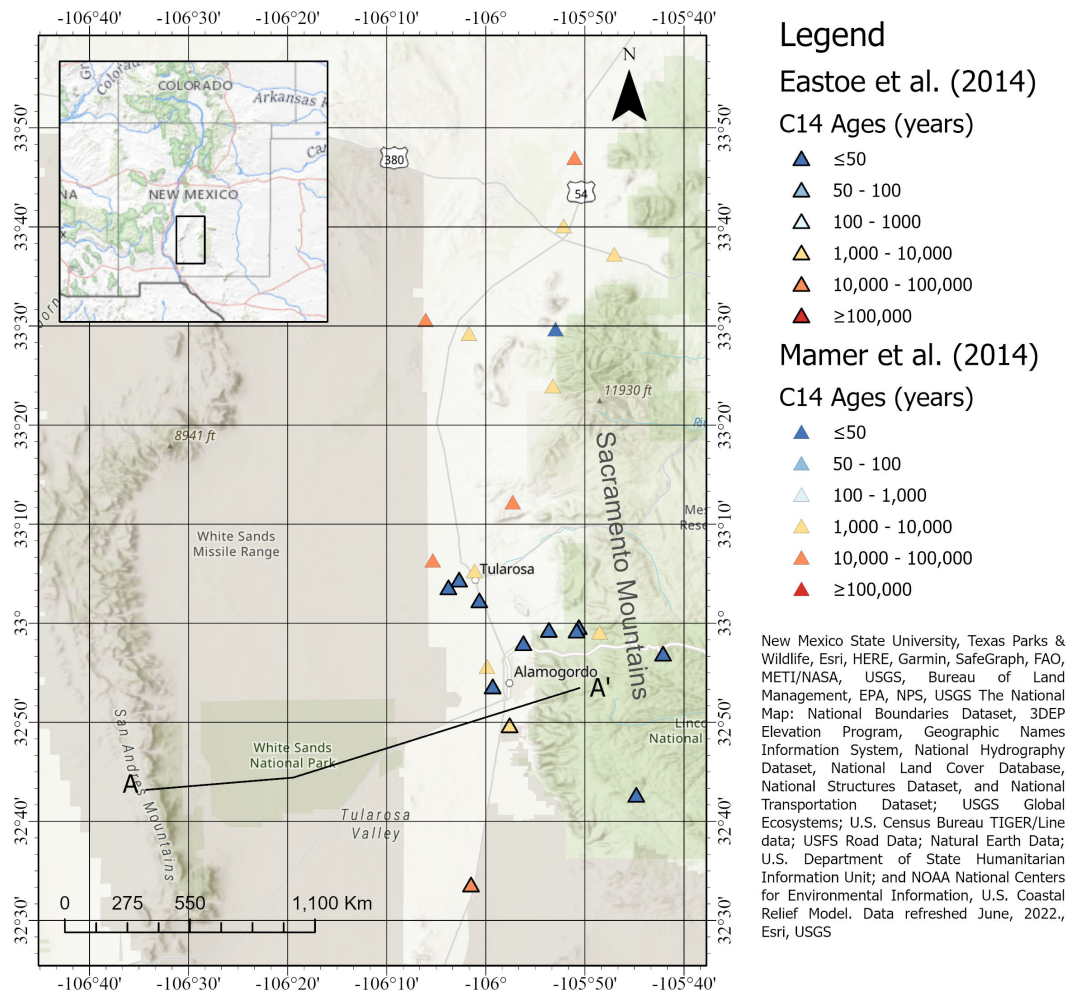


Figure A.2: Water quality and Carbon-14 measurements within the Tularosa Basin. The water quality measurements were provided by the New Mexico Environment Department (NMED), the New Mexico Bureau of Geology and Mineral Resources (NMBGMR), and the US Geological Survey (USGS). The information was downloaded from the NMBGMR interactive map (NMBGMR et al., 2016). The Carbon-14 age measurements were taken from Eastoe and Rodney (2014) and Mamer et al. (2014). The map shows old and saline groundwater systems in the basin west of the Sacramento Mountains mountain block. The geology of the cross-section profile A-A' is presented in Figure A.3.

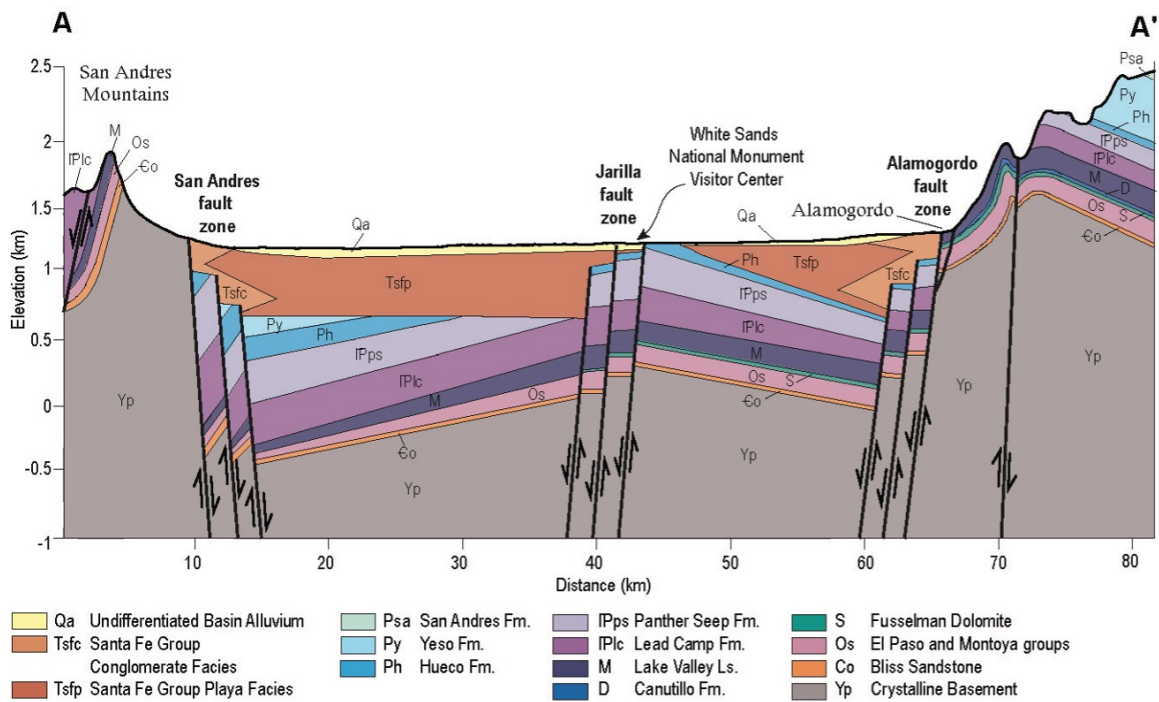


Figure A.3: Geologic cross-section through the Tularosa Basin. Modified from Newton and Land (2016).

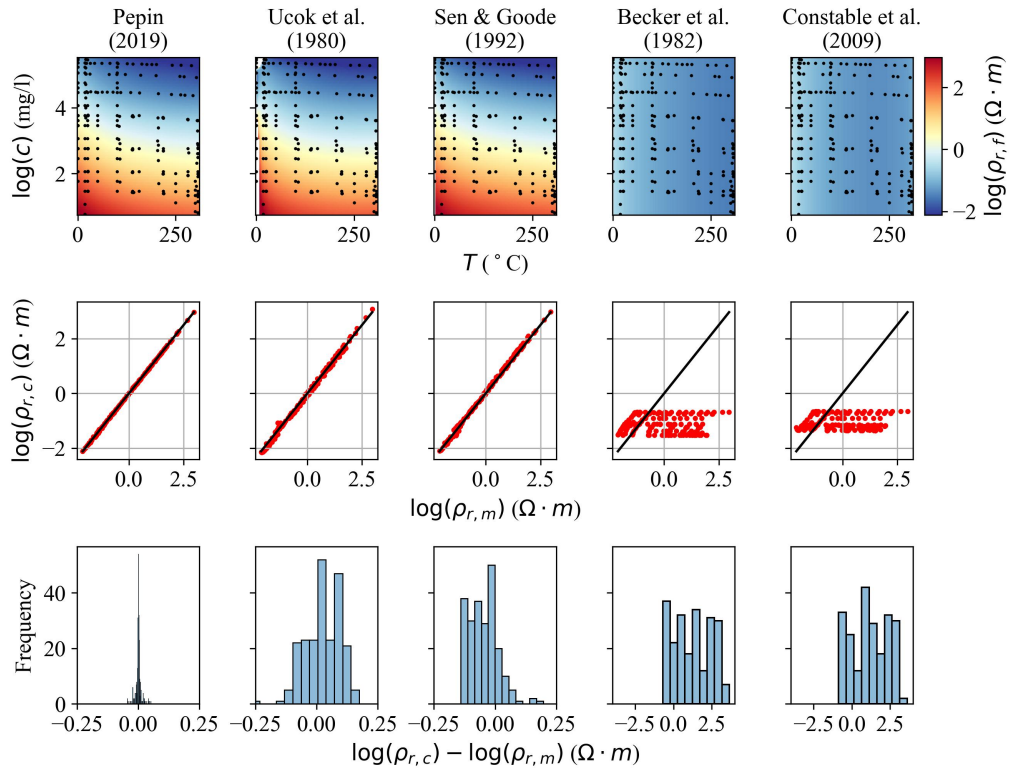


Figure A.4: Comparison between five empirical models for the fluid electrical resistivity. The first row shows the comparison between the models for a range of values of concentration of solutes (c) (NaCl, in this case) and temperature (T). The black dots denote the concentration and temperature location of the measured values for resistivity collected by Pepin (2019). The middle row compares calculated resistivity ($\rho_{r,c}$) and measured resistivity ($\rho_{r,m}$). The bottom row shows the histogram of the residuals between the calculated and measured resistivity. Notice that the scales of Pepin (2019), Ucok et al. (1980), and Sen and Goode (1992) have a different scale from the Becker et al. (1982) and Constable et al. (2009) models to provide a better comparison of the errors. The first three models reasonably fit the data, showing the importance of temperature variations in fluid resistivity.

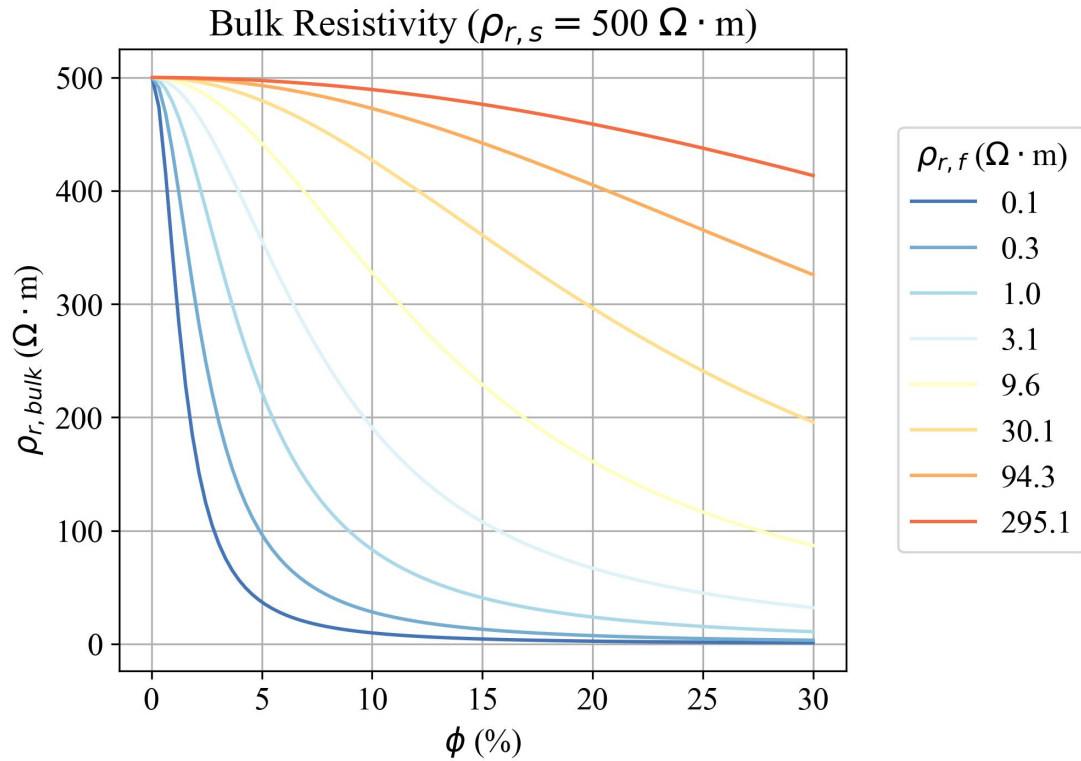


Figure A.5: Effective resistivity ($\rho_{r,bulk} = 1/\sigma_{r,bulk}$) resulting from variations in porosity (ϕ) and fluid resistivity ($\rho_{r,f}$) for Glover’s model $\sigma_{r,bulk} = \sigma_{r,f}\phi^{m_r} + \sigma_{r,s}(1 - \phi)^{p_r}$ (Glover et al., 2000). The solid resistivity is assumed to be $500 \Omega \cdot m$. Results show that low resistivity water (lower than $3.1 \Omega \cdot m$), associated with hot saline water, can be detected in systems porosities lower than 5%.

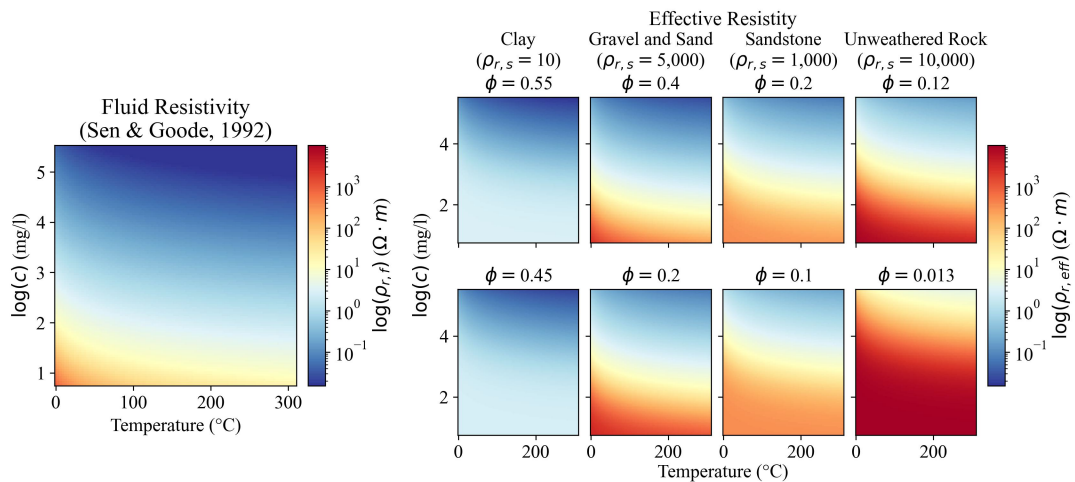


Figure A.6: (left) Fluid resistivity using the model by Sen and Goode (1992). (right) Effective resistivity calculated with Glover et al. (2000) for different rock groups and porosities within those values. High solid resistivity mediums provide a higher contrasting factor between fresh and saline water.

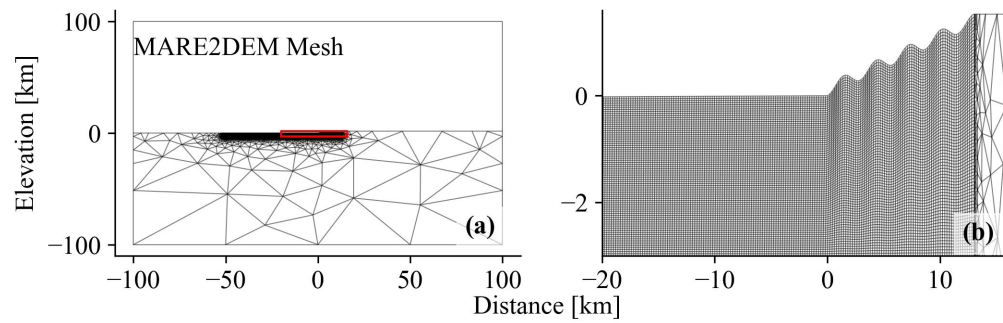


Figure A.7: The MARE2DEM forward and inverse MT simulations use a telescopic meshing approach to minimize artificial boundary effects. In this case, we combine an unstructured mesh outside the area of interest (panel a) and a structured mesh for the mountain-to-valley system (panel b). The red polygon in panel (a) corresponds to the location of the mountain-to-valley system.

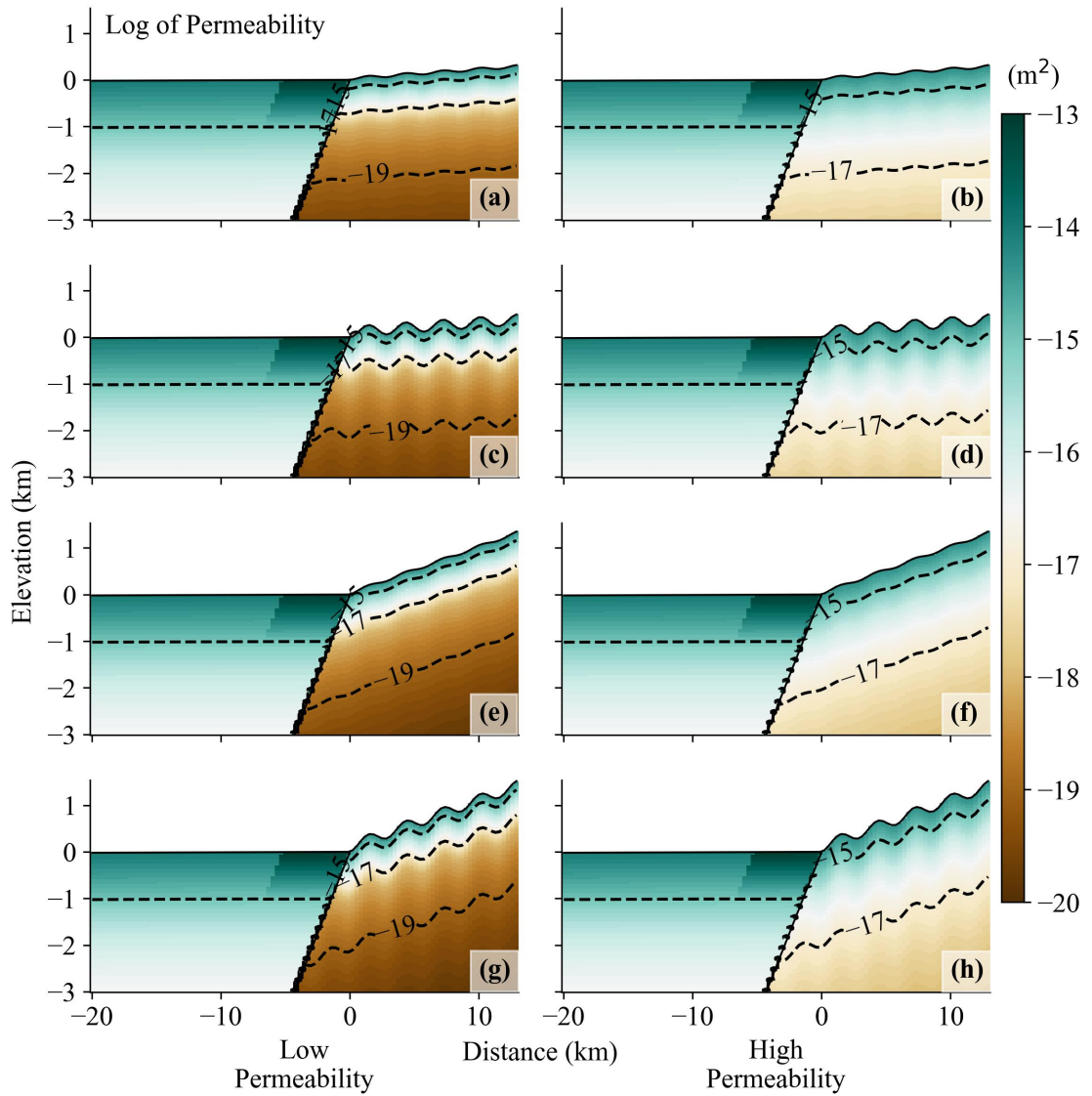


Figure A.8: Scenarios of permeability on the z direction (κ_z). The only changes in permeability are present in the mountain block.

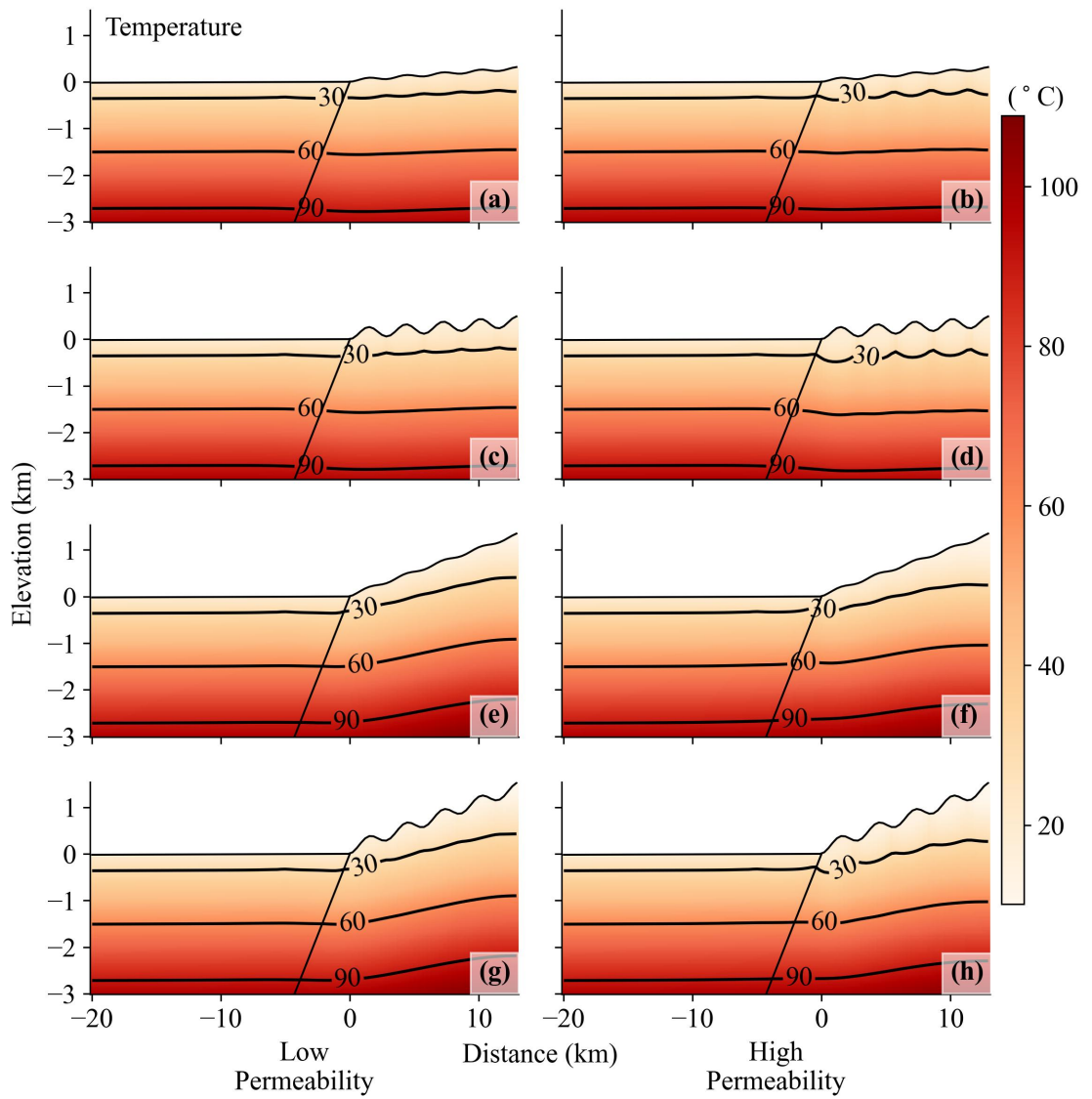


Figure A.9: Temperature fields of the mountain-to-valley transition systems. In the figure, the columns denote the two scenarios for permeability, increasing from left to right, the rows present different topographic relief systems, and the contours represent the isotherms. The temperature follows the multi-scale nature of flow in the mountain block and increases with depth, agreeing with previous studies (Gleeson and Manning, 2008; Jiang et al., 2009; Smith and Chapman, 1983; Tóth, 1963).

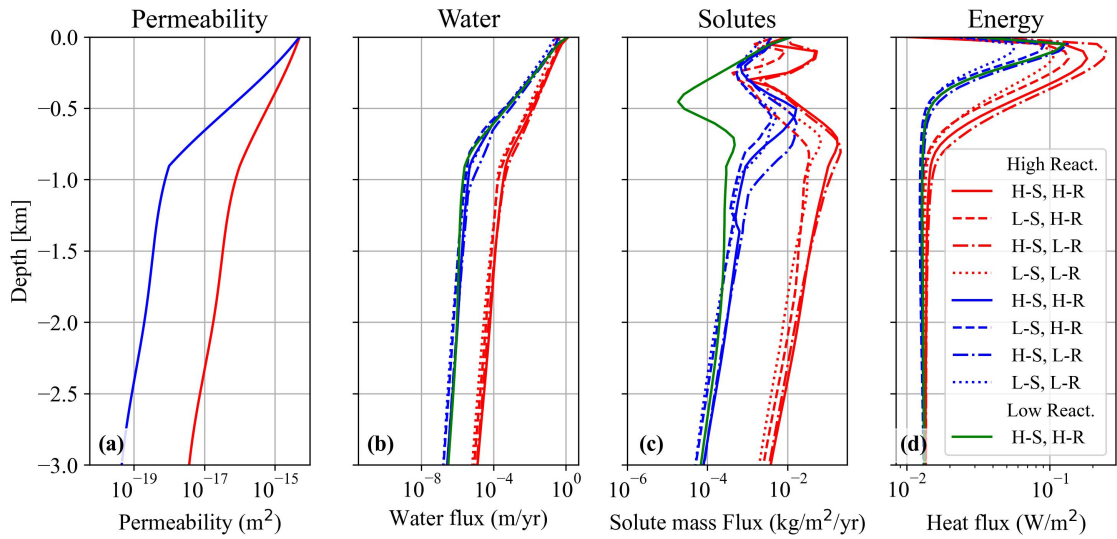


Figure A.10: Profiles of permeability, velocity, mass flux, and heat flux at the fault. The colors show the difference in permeability for the simulations. The line styles show the combination of systems with high regional slope and high relief (H-S, H-R), low regional slope and high relief (L-S, H-R), high regional slope and low relief (H-S, L-R), and low regional slope and low relief (L-S, L-S).

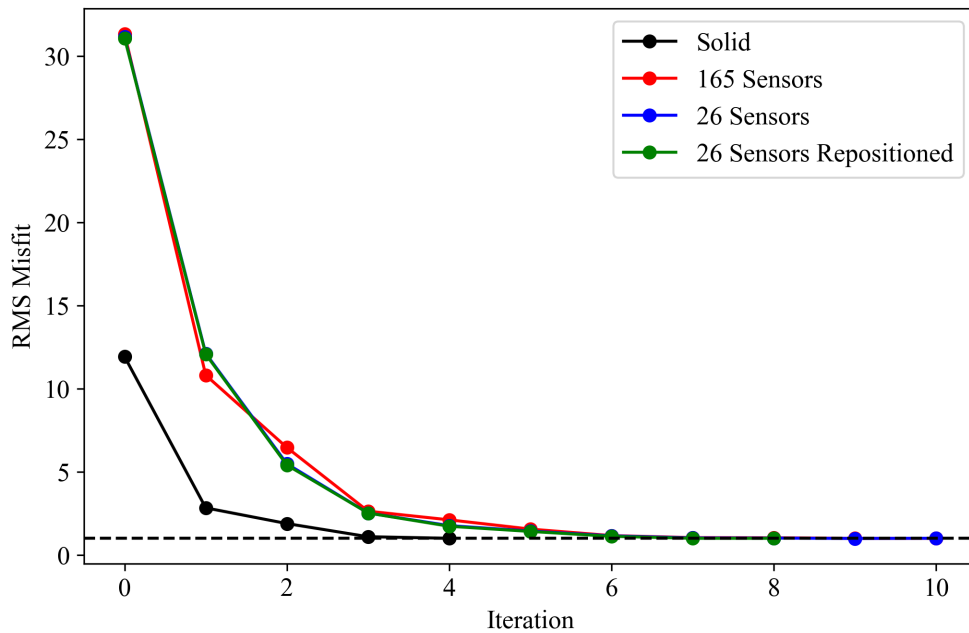


Figure A.11: RMS misfit for each iteration of all the inversions performed with MARE2DEM. The dashed line denotes the target misfit value of 1.0.

Appendix B

Supplemental Material for Chapter 3: "Exploring The Multiscale Nature of Flow in the Sacramento Mountains and Their Influence on Brackish Groundwater Resources Distribution in the Tularosa Basin in New Mexico"

B.1 Additional Figures

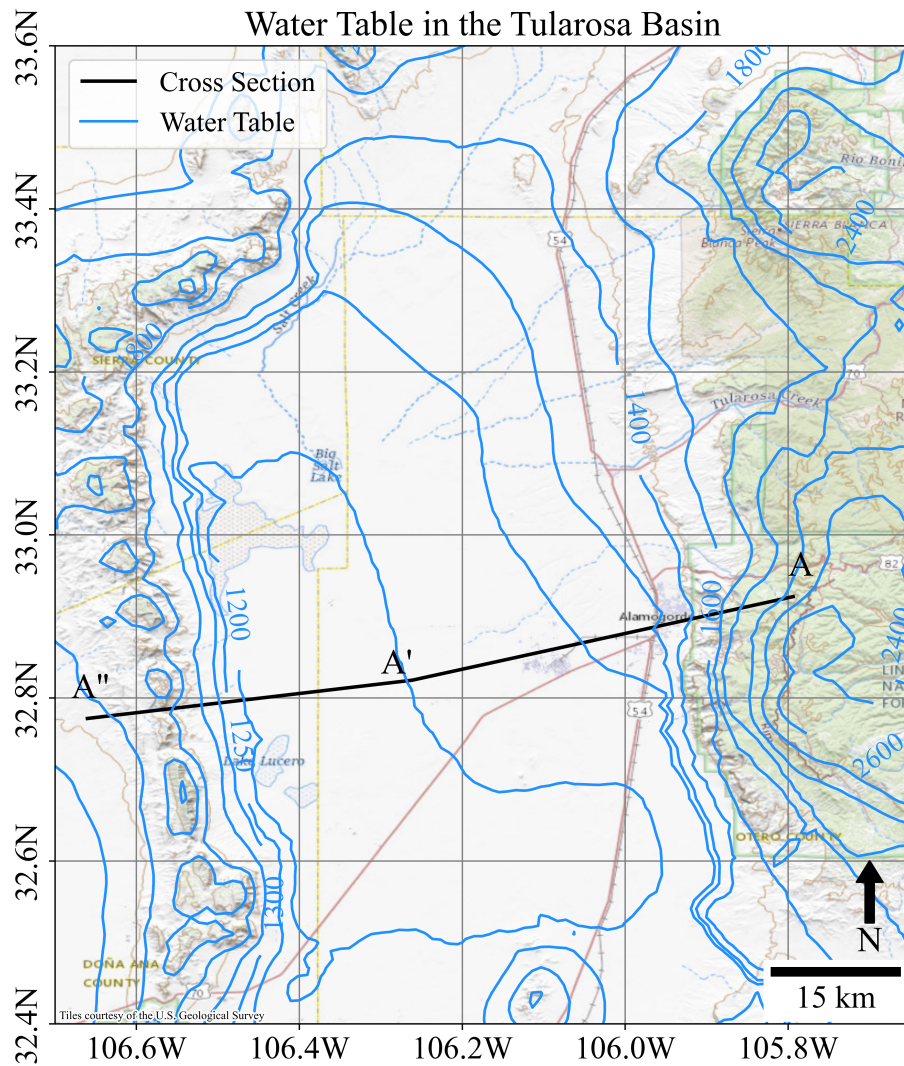


Figure B.1: Interpolated water table for the Tularosa Basin. The solid black line shows the cross-section A-A'-A'' used for the simulations. The water table was interpolated from water-level maps from the Sacramento Mountains (Land et al., 2014), the basin-fill (Embidi et al., 2011), and the San Andres Mountains (Horne, 2019).

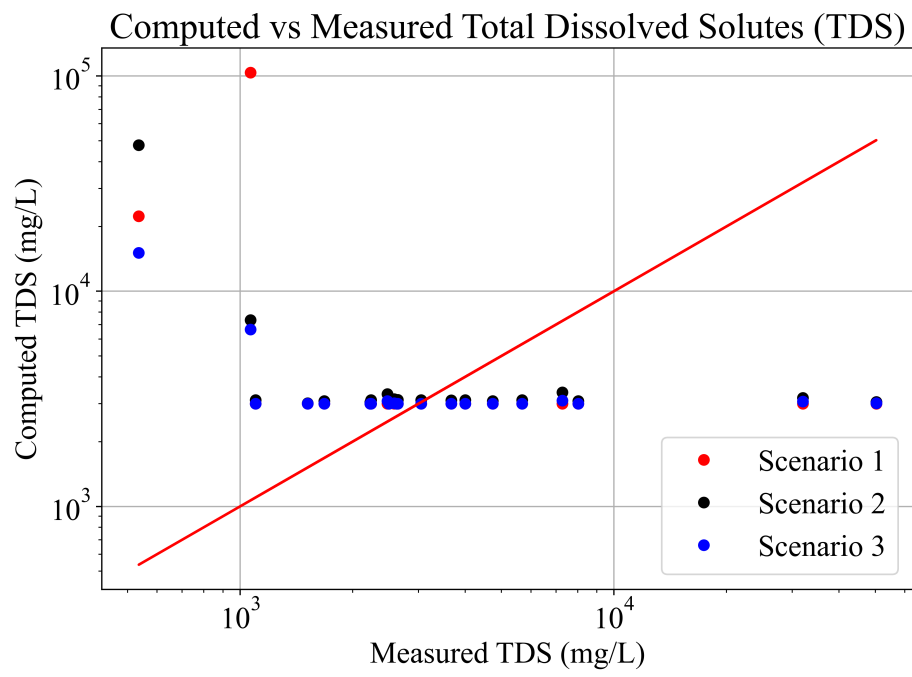


Figure B.2: Comparison between measured and computed total dissolved solutes (TDS). The measured salinities were obtained from NMBGMR et al. (2016). The computed information comes from the modeled Scenario 2.

B.2 Additional Tables

Table B.1: Parameter values used in the numerical simulations of the Tularosa Basin

Symbol	Variable Name	Values
T_a (°C)	Temperature at the Alluvium ^a	17
Γ (°C/km)	Thermal Lapse Rate	6.5
q_{Hb} (mW/m ²)	Basal Heat Flux ^b	60
μ_f (kg/(m·s))	Initial Fluid Viscosity	0.001
ρ_f	Initial Fluid Density	998.2
C_{pf} (J/(kg·K))	Fluid Specific Heat Capacity ^b	4,183
K_f (W/(m·K))	Fluid Thermal Capacity ^b	1
ρ_s (kg/m ³)	Solid (Rock) Density	2,600
C_{ps} (J/(kg·K))	Solid Specific Heat Capacity	836.8
K_s (W/(m·K))	Solid Thermal Capacity ^b	3
c_{max} (mg/L)	Maximum Salinity ^{c,d}	2.9×10^5
$c_{0,m}$ (mg/L)	Recharge Solute Concentration in the Mountains	9.98
$c_{0,WS}$ (mg/L)	Recharge Solute Concentration in White Sands ^e	5,000
$c_{0,A}$ (mg/L)	Recharge Solute Concentration in Alamogordo ^f	3,000
R_0 (kcal/(mol·K))	Ideal Gas Constant ^g	1.9871×10^{-3}
E_0 (kcal/mol)	Activation Energy ^g	10.0
$k_{mt_0,Q}$ (1/s)	Dissol. Rate of the Undifferentiated Basin Alluvium	1×10^{-18}
$k_{mt_0,TsfP}$ (1/s)	Dissol. Rate of the Santa Fe Group	1×10^{-12}
$k_{mt_0,TsfC}$ (1/s)	Dissol. Rate of the Santa Fe Conglomerate Facies	1×10^{-18}
$k_{mt_0,Py}$ (1/s)	Dissol. Rate of the Yeso Formation	2×10^{-6}
$k_{mt_0,Ph}$ (1/s)	Dissol. Rate of the Hueco Formation	1×10^{-12}
$k_{mt_0,Pps}$ (1/s)	Dissol. Rate of the Panther Seep Formation	1×10^{-16}
$k_{mt_0,Plc}$ (1/s)	Dissol. Rate of the Lead Camp Formation	1×10^{-16}
$k_{mt_0,M}$ (1/s)	Dissol. Rate of the Lake Valley	1×10^{-14}
$k_{mt_0,Os}$ (1/s)	Dissol. Rate of the El Paso de Montoya Group	1×10^{-14}
$k_{mt_0,b}$ (1/s)	Dissol. Rate of the Basement and Mountains	1×10^{-14}
α_L (m)	Longitudinal Dispersivity ^{h,i}	100
α_T (m)	Transversal Dispersivity ^{h,i}	10
M_{NaCl} (g/mol)	NaCl Molar Mass	58.442
$\rho_{r,Q}$ ($\Omega \cdot m$)	Solid Resistivity of the Undifferentiated Basin Alluvium ^j	20
$\rho_{r,TsfP}$ ($\Omega \cdot m$)	Solid Resistivity of the Santa Fe Group ^j	100
$\rho_{r,TsfC}$ ($\Omega \cdot m$)	Solid Resistivity of the Santa Fe Conglomerate Facies ^j	250
$\rho_{r,Py}$ ($\Omega \cdot m$)	Solid Resistivity of the Yeso Formation ^j	100
$\rho_{r,Ph}$ ($\Omega \cdot m$)	Solid Resistivity of the Hueco Formation ^j	100
$\rho_{r,Pps}$ ($\Omega \cdot m$)	Solid Resistivity of the Panther Seep Formation ^j	150

Continued on next page

Table B.1: Parameter values used in the numerical simulations of the Tularosa Basin (Continued)

Symbol	Variable Name	Values
$\rho_{r,Plc}$ ($\Omega \cdot m$)	Solid Resistivity of the Lead Camp Formation ^j	1000
$\rho_{r,M}$ ($\Omega \cdot m$)	Solid Resistivity of the Lake Valley ^j	1000
$\rho_{r,Os}$ ($\Omega \cdot m$)	Solid Resistivity of the El Paso de Montoya Group ^j	1000
$\rho_{r,b}$ ($\Omega \cdot m$)	Solid Resistivity of the Basement and Mountains ^j	1000

^aBourret (2015), ^bSmith and Chapman (1983), ^cLemieux et al. (2008b), ^dProvost et al. (2012),

^eNewton and Allen (2014), ^fNewton and Land (2016), ^gLangmuir (1997), ^hFetter (2001), ⁱGelhar et al. (1992),

^jPalacky (1988).

Appendix C

Supplemental Material for Chapter 6: "Sinuosity-driven Hyporheic Exchange: Hydrodynamics and Biogeochemical Potential"

C.1 Model Sensitivity Analysis

We conceptualize the modeling domain as an infinite series of meanders within an infinite alluvial belt. To mimic this conceptualization with a finite numerical modeling domain, we use (i) periodic boundary conditions for the upstream and downstream boundaries (i.e., $\partial\Omega_u$ and $\partial\Omega_d$) in a domain with a prescribed number of meanders and (ii) a valley-side boundary that is far enough from the meandering channel such that our simulations are unaffected by its location (i.e., $\partial\Omega_v$). We performed a series of exploratory simulations to select reasonable parameters. First, periodic boundary conditions can create numerical artifacts propagating within the domain, affecting the flow and solute concentration fields. These artifacts are more prevalent under dynamic flow conditions (see discussion in Gomez-Velez et al. (2017)). To minimize the potential presence of these artifacts, we refine the mesh around the boundaries and use high-order numerical schemes. Furthermore, to ensure that if the numerical instabilities form, they do not significantly affect our simulations, we model several channel meander cycles and focus our analyses on a bend far from the boundaries. Here, we balance the selection of a number of meander cycles that minimize the effects of potential instabilities while maintaining a reasonable computational cost. To this end, we performed a series of simulations with one, two, three, and four meanders (Figure C.1). We compared the flow and solute concentration fields for all these cases. In this case, and given the steady-state nature of flow, all cases result in the same solution and extent of the hyporheic zone. In the abundance of caution, we used three meanders and focused our analyses on the middle one.

To select the location of the valley-side boundary ($\partial\Omega_v$), we explored four values of the distance $B = 0.1L$, $0.2L$, $0.5L$, and L . As shown in Figure S C.2, the sensitivity of the modeling results to the boundary location is minimal for $B > 0.5L$. The smallest value of B constrains the formation of the alluvial hyporheic cell for the highest sinuosity under neutral regional groundwater conditions (the most challenging scenario) (see A in Figure S C.2). As we increased the value of B , this effect vanishes relatively fast. For example, the flow field near the meander for the simulations with $B = 0.5L$ and $B = L$ are unchanged (see B-D in Figure S C.2). In other words, we obtain a B -independent result for values of B larger than about $0.5L$. Like before, we selected $B = L$ with an abundance of caution, which resulted in a moderate increase in the computational burden.

C.2 Flow, Transport, and Reaction Models

C.2.1 Nondimensionalization of the flow model

As described in Chapter 6, the mathematical statement for the flow model is given by

$$\nabla \cdot \mathbf{Q} = 0 \quad \text{with} \quad \mathbf{Q} = -KH\nabla h \quad (\text{C.1})$$

$$h(\mathbf{x}) = H_c + (3L)J_x - \frac{J_x}{\sigma} s(\mathbf{x}) \quad \text{for } \mathbf{x} \in \partial\Omega_c \quad (\text{C.2})$$

$$h(x = 3L, y) = h(x = 0, y) - (3L)J_x \quad \text{for } \mathbf{x} \in \partial\Omega_u \vee \partial\Omega_d \quad (\text{C.3})$$

$$-\mathbf{n} \cdot \mathbf{Q} = KHJ_y \quad \text{for } \mathbf{x} \in \partial\Omega_v \quad (\text{C.4})$$

Here we nondimensionalize Eqns. C.1-C.4 to remove physical dimensions and aid interpretation and parameterization of scenarios. Let l_c and h_c be characteristic length scales for distance in the $x - y$ plane and hydraulic head, respectively, such that

$$\mathbf{x} = l_c \mathbf{x}^* \quad \nabla(\cdot) = \frac{\nabla^*(\cdot)}{l_c} \quad h = h_c h^* \quad (\text{C.5})$$

where the asterisk (*) makes reference to dimensionless quantities.

Using the above definitions, Eqns. C.1-C.4 are recast as

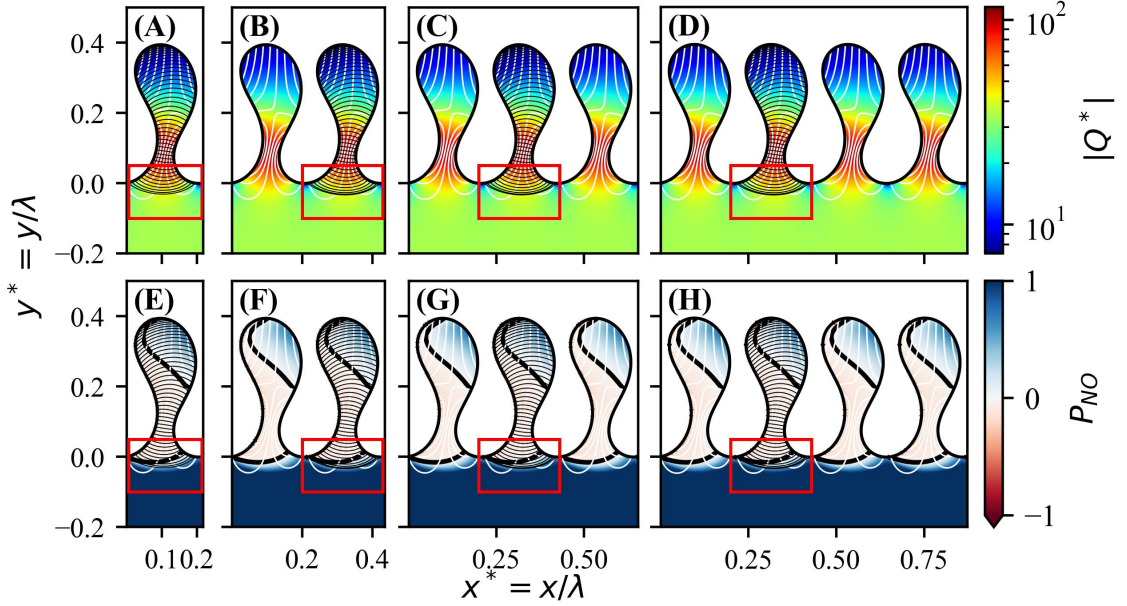


Figure C.1: Sensitivity analysis on the number of meanders. While panels (A) through (D) show the dimensionless vertical integrated fluxes (Q^*), panels (E) through (H) show the potential of denitrification (P_{NO}) for one, two, three, and four meander sequential bends. The black streamlines show the extent of the hyporheic zone, the black solid contour line shows the places where $P_{NO} = 0$, the white contour lines denote the dimensionless hydraulic head, and the red square boxes point to the extent of the hyporheic zone through the neck of the meander.

$$\nabla^* \cdot \mathbf{Q}^* = 0 \quad \text{with} \quad \mathbf{Q}^* = -H^* \nabla^* h^* \quad (\text{C.6})$$

$$h^*(\mathbf{x}^*) = \left(\frac{H_c}{h_c} \right) + 3 \left(\frac{J_x L}{h_c} \right) - \left(\frac{J_x l_c}{\sigma h_c} \right) s^*(\mathbf{x}^*) \quad \text{for } \mathbf{x}^* \in \partial \Omega_c \quad (\text{C.7})$$

$$h^*(x^* = 3(L/l_c), y^*) = h^*(x^* = 0, y^*) - 3 \left(\frac{J_x L}{h_c} \right) \quad \text{for } \mathbf{x}^* \in \partial \Omega_u \vee \partial \Omega_d \quad (\text{C.8})$$

$$-\mathbf{n} \cdot \mathbf{Q}^* = \frac{l_c J_y}{h_c} H^* \quad \text{for } \mathbf{x}^* \in \partial \Omega_v \quad (\text{C.9})$$

where $\mathbf{Q} = Q_c \mathbf{Q}^*$, with $Q_c = \frac{K h_c^2}{l_c}$; $\mathbf{q} = q_c \mathbf{q}^*$, with $q_c = \frac{K h_c}{l_c}$; $H = h_c(h^* - Z_b^*) = h_c H^*$, with $Z_b = h_c Z_b^*$; and $s(\mathbf{x}) = l_c s^*(\mathbf{x}^*)$. In particular, the relationship between the dimensional ($s(\mathbf{x})$) and dimensionless ($s^*(\mathbf{x}^*)$) arc length can be found by expressing the Kinoshita curve as a parametric curve within our modeling domain:

$$\mathbf{x}(\xi) = [x(\xi), y(\xi)] \quad \text{with} \quad \xi \in [0, 3\lambda]. \quad (\text{C.10})$$

In this case, $\mathbf{x}(\xi = 0) = [0, 0]$, and the arc length distance from the origin to any point \mathbf{x} along the curve such that $\mathbf{x} = \mathbf{x}(\eta)$ is given by

$$s(\mathbf{x}) = \int_0^\eta \sqrt{\left(\frac{dx}{d\xi} \right)^2 + \left(\frac{dy}{d\xi} \right)^2} d\xi \quad (\text{C.11})$$

Then, this expression can be recast in dimensionless terms as

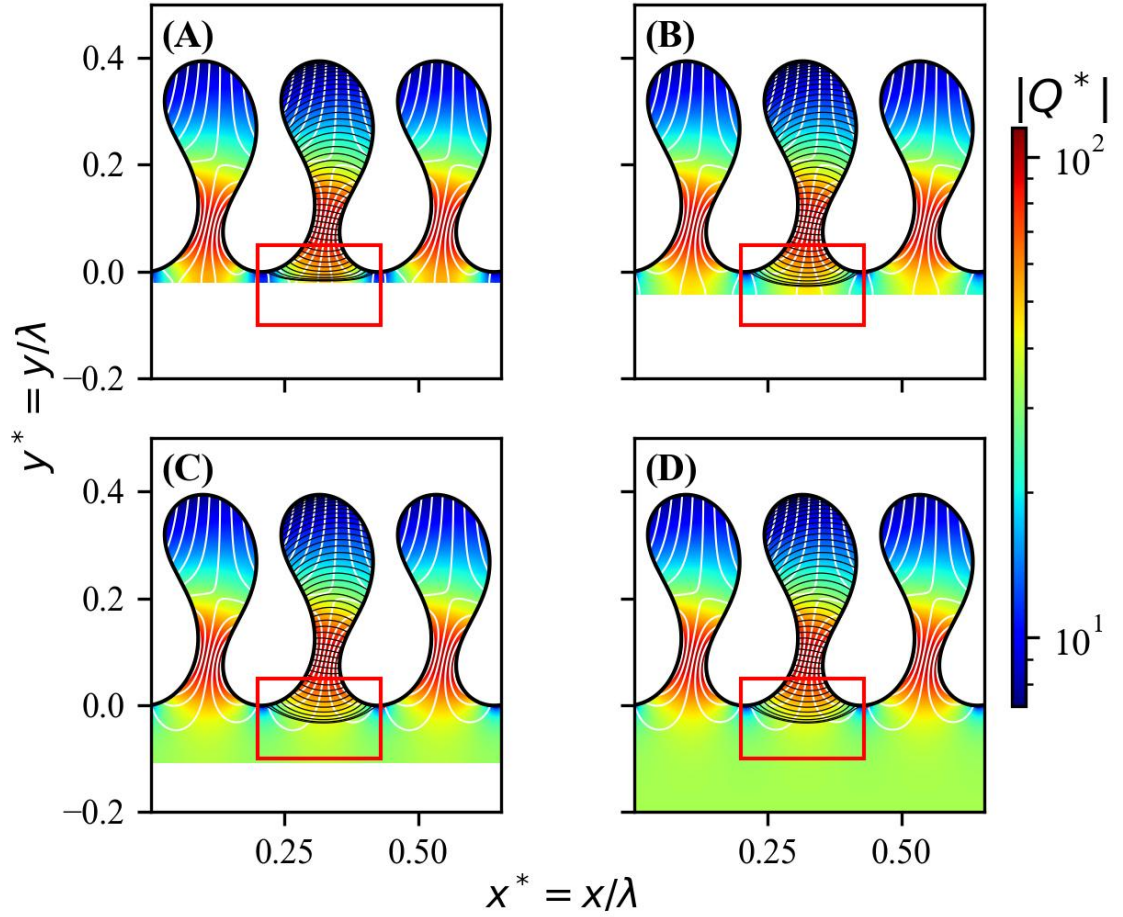


Figure C.2: Sensitivity analysis on the extent of the alluvial valley. The panels (A) through (D) show the dimensionless vertical integrated fluxes (Q^*) for $B = 0.1L, 0.2L, 0.5L,$ and L . The black streamlines show the extent of the hyporheic zone, the white contour lines denote the dimensionless hydraulic head, and the red square boxes point to the extent of the hyporheic zone through the neck of the meander.

$$s^*(\mathbf{x}^*) = \frac{s(\mathbf{x}/l_c)}{l_c} = \int_0^{\eta^*} \sqrt{\left(\frac{dx^*}{d\xi^*}\right)^2 + \left(\frac{dy^*}{d\xi^*}\right)^2} d\xi^*. \quad (\text{C.12})$$

Now, based on our physical intuition, we propose the following characteristic lengths:

$$l_c = \lambda \quad h_c = J_x \lambda \quad (\text{C.13})$$

In this case, the horizontal scale corresponds to the meander's wavelength and the vertical scale to the average head drop over a distance λ . With these definitions, the mathematical statement in Eqns. C.6-C.9 can be recast as

$$\nabla^* \cdot \mathbf{Q}^* = 0 \quad \text{with} \quad \mathbf{Q}^* = -H^* \nabla^* h^* \quad (\text{C.14})$$

$$h^*(\mathbf{x}^*) = \Pi_{H_c} + \sigma^{-1} [3 - s^*(\mathbf{x}^*)] \quad \text{for } \mathbf{x}^* \in \partial\Omega_c \quad (\text{C.15})$$

$$h^*(x^* = 3\sigma^{-1}, y^*) = h^*(x^* = 0, y^*) - 3\sigma^{-1} \quad \text{for } \mathbf{x}^* \in \partial\Omega_u \cup \partial\Omega_d \quad (\text{C.16})$$

$$-\mathbf{n} \cdot \mathbf{Q}^* = \Pi_{J_y} H^* \quad \text{for } \mathbf{x}^* \in \partial\Omega_v \quad (\text{C.17})$$

where $Q_c = KJ_x^2 \lambda$, $q_c = KJ_x$, $Z_b^* = 3\Pi_{\sigma}^{-1} - x^*$, $\Pi_{H_c} = \frac{H_c}{J_x \lambda}$, and $\Pi_{J_y} = \frac{J_y}{J_x}$. Notice that exploratory analyses (not shown) demonstrate that for the Kinoshita curve, the sinuosity σ is independent of λ and only depends on the parameters θ_0 , J_f , and J_s . This is also the case for the dimensionless arc length function $s^*(\mathbf{x}^*)$. To summarize, the dimensionless flow problem only depends on the values of the following five dimensionless parameters:

$$\sigma = \frac{\lambda}{L} = f(\theta_0, J_f, J_s), \quad \Pi_{H_c} = \frac{H_c}{J_x \lambda}, \quad \Pi_{J_y} = \frac{J_y}{J_x} \quad (\text{C.18})$$

C.2.2 Nondimensionalization of the Cumulative Age Distribution

The cumulative residence time distribution, $\Psi(\tau)$, is described by the following form of the advection-dispersion equation (ADE) Gomez et al. (2012); Gomez and Wilson (2013):

$$\frac{\partial(\varepsilon_p H \Psi)}{\partial \tau} = \nabla \cdot (\mathbf{D} \nabla \Psi) - \nabla \cdot (\mathbf{Q} \Psi) \quad (\text{C.19})$$

$$\Psi(\mathbf{x}) = 1 \quad \text{for } \mathbf{x} \in \partial\Omega_c \mid \mathbf{n} \cdot \mathbf{Q} \leq 0 \quad (\text{C.20})$$

$$\mathbf{D} \nabla \Psi = 0 \quad \text{for } \mathbf{x} \in \partial\Omega_c \mid \mathbf{n} \cdot \mathbf{Q} > 0 \quad (\text{C.21})$$

$$\Psi(x = 3L, y) = \Psi(x = 0, y) \quad \text{for } \mathbf{x} \in \partial\Omega_u \cup \partial\Omega_d \quad (\text{C.22})$$

$$\Psi = 1 - \exp\left(-\frac{\tau}{\tau_v}\right) \quad \text{for } \mathbf{x} \in \partial\Omega_v \quad (\text{C.23})$$

From our previous definitions, we know that $l_c = \lambda$, $h_c = J_x \lambda$, $Q_c = KJ_x^2 \lambda$, and $D_c = KJ_x^2 \lambda^2$. We also know that the cumulative residence time distribution (Ψ) is dimensionless, and it is already scaled from 0 to 1. Thus, we can assume a characteristic residence time $\tau_c = \lambda / (KJ_x)$ such that $\tau = \tau_c \tau^*$ and $\tau_v = \tau_c \tau_v^*$,

$$\frac{\partial(\varepsilon_p H^* \Psi^*)}{\partial \tau^*} = \nabla^* \cdot (\mathbf{D}^* \nabla^* \Psi^*) - \nabla^* \cdot (\mathbf{Q}^* \Psi^*) \quad (\text{C.24})$$

$$\Psi^*(\mathbf{x}^*) = 1 \quad \text{for } \mathbf{x}^* \in \partial\Omega_c \mid \mathbf{n} \cdot \mathbf{Q}^* \leq 0 \quad (\text{C.25})$$

$$\mathbf{D}^* \nabla^* \Psi^* = 0 \quad \text{for } \mathbf{x} \in \partial\Omega_c \mid \mathbf{n} \cdot \mathbf{Q}^* > 0 \quad (\text{C.26})$$

$$\Psi^*(x^* = 3\sigma^{-1}, y^*) = \Psi^*(x^* = 0, y^*) \quad \text{for } \mathbf{x}^* \in \partial\Omega_u \cup \partial\Omega_d \quad (\text{C.27})$$

$$\Psi^* = 1 - \exp\left(-\frac{\tau^*}{\tau_v^*}\right) \quad \text{for } \mathbf{x} \in \partial\Omega_v \quad (\text{C.28})$$

C.2.3 Nondimensionalization of Transport and Reaction Model

The complete mathematical statement for the transport model is given by

$$\frac{\partial(\varepsilon_p H C_i)}{\partial t} = \nabla \cdot (\mathbf{D} \nabla C_i) - \nabla \cdot (\mathbf{Q} C_i) + \varepsilon_p H R_i \quad (\text{C.29})$$

$$\begin{cases} C_i = C_{i,c}, & \text{for } \mathbf{x} \in \partial\Omega_c | \mathbf{n} \cdot \mathbf{Q} < 0 \\ -\mathbf{n} \cdot (-\mathbf{D} \nabla C_i) = 0, & \text{for } \mathbf{x} \in \partial\Omega_c | \mathbf{n} \cdot \mathbf{Q} > 0 \end{cases} \quad (\text{C.30})$$

$$C_i(x = 3L, y) = C_i(x = 0, y) \quad \text{for } \mathbf{x} \in \partial\Omega_u \cup \partial\Omega_d \quad (\text{C.31})$$

$$\begin{cases} C_i = C_{i,v}, & \text{for } \mathbf{x} \in \partial\Omega_v | \mathbf{n} \cdot \mathbf{Q} < 0 \\ -\mathbf{n} \cdot (-\mathbf{D} \nabla C_i) = 0, & \text{for } \mathbf{x} \in \partial\Omega_v | \mathbf{n} \cdot \mathbf{Q} > 0 \\ -\mathbf{n} \cdot (\mathbf{Q} C_i - \mathbf{D} \nabla C_i) = 0, & \text{for } \mathbf{x} \in \partial\Omega_v | \mathbf{n} \cdot \mathbf{Q} = 0 \end{cases} \quad (\text{C.32})$$

Let us assume a characteristic concentration for each species that corresponds to the oxygen channel concentration ($C_i = C_{O,c} C_i^*$) and a characteristic time scale $t_c = l_c/q_c = \lambda/(KJ_x)$ such that $t = t_c t^*$. Then, using these definitions and the ones defined previously, Eqs. C.29-C.32 can be recast in dimensionless form as

$$\frac{\partial(\varepsilon_p H^* C_i^*)}{\partial t^*} = \nabla^* \cdot (\mathbf{D}^* \nabla^* C_i^*) - \nabla^* \cdot (\mathbf{Q}^* C_i^*) + \varepsilon_p H^* R_i^* \quad (\text{C.33})$$

$$\begin{cases} C_i^* = \frac{C_{i,c}}{C_{O,c}}, & \text{for } \mathbf{x}^* \in \partial\Omega_c | \mathbf{n} \cdot \mathbf{Q}^* < 0 \\ -\mathbf{n} \cdot (-\mathbf{D}^* \nabla^* C_i^*) = 0, & \text{for } \mathbf{x}^* \in \partial\Omega_c | \mathbf{n} \cdot \mathbf{Q}^* > 0 \end{cases} \quad (\text{C.34})$$

$$C_i^*(x^* = 3\sigma^{-1}, y^*) = C_i^*(x^* = 0, y^*) \quad \text{for } \mathbf{x}^* \in \partial\Omega_u \cup \partial\Omega_d \quad (\text{C.35})$$

$$\begin{cases} C_i^* = \frac{C_{i,v}}{C_{O,c}}, & \text{for } \mathbf{x}^* \in \partial\Omega_v | \mathbf{n} \cdot \mathbf{Q}^* < 0 \\ -\mathbf{n} \cdot (-\mathbf{D}^* \nabla^* C_i^*) = 0, & \text{for } \mathbf{x}^* \in \partial\Omega_v | \mathbf{n} \cdot \mathbf{Q}^* > 0 \\ -\mathbf{n} \cdot (\mathbf{Q}^* C_i^* - \mathbf{D}^* \nabla^* C_i^*) = 0, & \text{for } \mathbf{x}^* \in \partial\Omega_v | \mathbf{n} \cdot \mathbf{Q}^* = 0 \end{cases} \quad (\text{C.36})$$

where the dispersion diffusion tensor can be expressed as $\mathbf{D} = Q_c \lambda \mathbf{D}^*$ with

$$D_{i,j}^* = \frac{D_{i,j}}{Q_c \lambda} = \alpha_T^* |\mathbf{Q}^*| \delta_{i,j} + (\alpha_L^* - \alpha_T^*) \frac{Q_i^* Q_j^*}{|\mathbf{Q}^*|} + \frac{\varepsilon_p H^*}{\eta} D_m^*, \quad (\text{C.37})$$

$D_m = KJ_x \lambda D_m^*$, $\alpha_T = \lambda \alpha_T^*$, $\alpha_L = \lambda \alpha_L^*$, $C_{i,c} = C_{i,c}/C_{O,c}$, $\Pi_{i,v} = C_{i,v}/C_{O,c}$, and $R_i = (C_{O,c}/t_c) R_i^* = (C_{O,c} q_c / \lambda) R_i^*$.

We define the Damhköler number for each reaction as $Da_i = V_i t_c$, $Da_P = \alpha t_c$, $P = P_0 P^*$, and $K_d = (P_0/C_{C,c}) K_d^*$.

The dimensionless reaction rates R_i^* are given by

$$\begin{aligned} R_O^* = -Da_O \left[y_O \left(\frac{X_{AR}}{C_{O,c}} \right) \left(\frac{C_C^*}{(K_C/C_{O,c}) + C_C^*} \right) \left(\frac{C_O^*}{(K_O/C_{O,c}) + C_O^*} \right) \right. \\ \left. + (1 - y_O) \left(\frac{X_{NIT}}{C_{O,c}} \right) \left(\frac{C_{NH}^*}{(K_{NH}/C_{O,c}) + C_{NH}^*} \right) \left(\frac{C_O^*}{(K_O/C_{O,c}) + C_O^*} \right) \right], \end{aligned} \quad (\text{C.38})$$

$$\begin{aligned}
R_{NH}^* = & -Da_{NH} \left[y_{NH} \left(\frac{X_{NIT}}{C_{O,c}} \right) \left(\frac{C_{NH}^*}{(K_{NH}/C_{O,c}) + C_{NH}^*} \right) \left(\frac{C_O^*}{(K_O/C_{O,c}) + C_O^*} \right) \right. \\
& \left. + (1 - y_{NH}) \left(\frac{X_{UP}}{C_{O,c}} \right) \left(\frac{C_{NH}^*}{(K_{NH}/C_{O,c}) + C_{NH}^*} \right) \left(\frac{C_C^*}{(K_C/C_{O,c}) + C_C^*} \right) \right], \tag{C.39}
\end{aligned}$$

$$\begin{aligned}
R_{NO}^* = & Da_{NH} y_{NH} \left(\frac{X_{NIT}}{C_{O,c}} \right) \left(\frac{C_{NH}^*}{(K_{NH}/C_{O,c}) + C_{NH}^*} \right) \left(\frac{C_O^*}{(K_O/C_{O,c}) + C_O^*} \right) \\
& - Da_{NO} \left(\frac{X_{DN}}{C_{O,c}} \right) \left(\frac{(K_I/C_{O,c})}{(K_I/C_{O,c}) + C_O^*} \right) \left(\frac{C_C^*}{(K_C/C_{O,c}) + C_C^*} \right) \left(\frac{C_{NO}^*}{(K_{NO}/C_{O,c}) + C_{NO}^*} \right), \tag{C.40}
\end{aligned}$$

$$\begin{aligned}
R_C^* = & -Da_O y_O \left(\frac{X_{AR}}{C_{O,c}} \right) \left(\frac{C_C^*}{(K_C/C_{O,c}) + C_C^*} \right) \left(\frac{C_O^*}{(K_O/C_{O,c}) + C_O^*} \right) \\
& - Da_{NO} \left(\frac{X_{DN}}{C_{O,c}} \right) \left(\frac{(K_I/C_{O,c})}{(K_I/C_{O,c}) + C_O^*} \right) \left(\frac{C_C^*}{(K_C/C_{O,c}) + C_C^*} \right) \left(\frac{C_{NO}^*}{(K_{NO}/C_{O,c}) + C_{NO}^*} \right) \\
& - Da_{NH} (1 - y_{NH}) \left(\frac{X_{UP}}{C_{O,c}} \right) \left(\frac{C_{NH}^*}{(K_{NH}/C_{O,c}) + C_{NH}^*} \right) \left(\frac{C_C^*}{(K_C/C_{O,c}) + C_C^*} \right) \\
& + Da_P \left(\frac{\rho_b P_0}{\varepsilon_p C_{O,c}} \right) \left(P^* - \left(\frac{K_d C_{O,c}}{P_0} \right) C_C^* \right) \tag{C.41}
\end{aligned}$$

The dissolution of particulate organic carbon (POC, P) is described by a first-order mass transfer coefficient:

$$\frac{\partial P^*}{\partial t^*} = -Da_P \left(P^* - \left(\frac{K_d C_{O,c}}{P_0} \right) C_C^* \right) \tag{C.42}$$

As part of this nondimensionalization, we used the channel oxygen concentration as a characteristic concentration given its widespread availability. Zarnetske et al. (2012) assumed $X_{AR} = C_{O,c}$, $X_{NIT} = C_{NH,c}$, $X_{DN} = C_{NO,c}$, and $X_{UP} = C_{NH,c}$. Under these assumptions, we can recast Eqns. C.38-C.41 as

$$\begin{aligned}
R_O^* = & -Da_O \left[y_O \left(\frac{C_C^*}{\Pi_{K_C} + C_C^*} \right) \left(\frac{C_O^*}{\Pi_{K_O} + C_O^*} \right) \right. \\
& \left. + (1 - y_O) \Pi_{NH,c} \left(\frac{C_{NH}^*}{\Pi_{K_{NH}} + C_{NH}^*} \right) \left(\frac{C_O^*}{\Pi_{K_O} + C_O^*} \right) \right], \tag{C.43}
\end{aligned}$$

$$\begin{aligned}
R_{NH}^* = & -Da_{NH} \left[y_{NH} \Pi_{NH,c} \left(\frac{C_{NH}^*}{\Pi_{K_{NH}} + C_{NH}^*} \right) \left(\frac{C_O^*}{\Pi_{K_O} + C_O^*} \right) \right. \\
& \left. + (1 - y_{NH}) \Pi_{NH,c} \left(\frac{C_{NH}^*}{\Pi_{K_{NH}} + C_{NH}^*} \right) \left(\frac{C_C^*}{\Pi_{K_C} + C_C^*} \right) \right], \tag{C.44}
\end{aligned}$$

$$\begin{aligned}
R_{NO}^* = & Da_{NH} y_{NH} \Pi_{NH,c} \left(\frac{C_{NH}^*}{\Pi_{K_{NH}} + C_{NH}^*} \right) \left(\frac{C_O^*}{\Pi_{K_O} + C_O^*} \right) \\
& - Da_{NO} \Pi_{NO,c} \left(\frac{\Pi_{K_I}}{\Pi_{K_I} + C_O^*} \right) \left(\frac{C_C^*}{\Pi_{K_C} + C_C^*} \right) \left(\frac{C_{NO}^*}{\Pi_{K_{NO}} + C_{NO}^*} \right),
\end{aligned} \tag{C.45}$$

$$\begin{aligned}
R_C^* = & -Da_O y_O \left(\frac{C_C^*}{\Pi_{K_C} + C_C^*} \right) \left(\frac{C_O^*}{\Pi_{K_O} + C_O^*} \right) \\
& - Da_{NO} \Pi_{NO,c} \left(\frac{\Pi_{K_I}}{\Pi_{K_I} + C_O^*} \right) \left(\frac{C_C^*}{\Pi_{K_C} + C_C^*} \right) \left(\frac{C_{NO}^*}{\Pi_{K_{NO}} + C_{NO}^*} \right) \\
& - Da_{NH} (1 - y_{NH}) \Pi_{NH,c} \left(\frac{C_{NH}^*}{\Pi_{K_{NH}} + C_{NH}^*} \right) \left(\frac{C_C^*}{\Pi_{K_C} + C_C^*} \right) \\
& + Da_P \Pi_{P-C} (P^* - \Pi_{K_d} C_C^*)
\end{aligned} \tag{C.46}$$

$$\frac{\partial P^*}{\partial t^*} = -Da_P (P^* - \Pi_{K_d} C_C^*) \tag{C.47}$$

Based on the dimensionless form of the biogeochemical model, and in addition to the dimensionless parameters defined in Eq. C.18, the solution to this fully-coupled system of PDEs only depends on the values of the following dimensionless parameters:

$$\begin{aligned}
Da_O = \frac{V_O \lambda}{K J_x}, Da_{NO} = \frac{V_{NO} \lambda}{K J_x}, Da_{NH} = \frac{V_{NH} \lambda}{K J_x}, Da_P = \frac{\alpha \lambda}{K J_x}, \\
\Pi_{K_C} = \frac{K_C}{C_{O,c}}, \Pi_{K_O} = \frac{K_O}{C_{O,c}}, \Pi_{K_{NH}} = \frac{K_{NH}}{C_{O,c}}, \\
\Pi_{K_{NO}} = \frac{K_{NO}}{C_{O,c}}, \Pi_{K_I} = \frac{K_I}{C_{O,c}}, \Pi_{K_d} = \frac{K_d C_{O,c}}{P_0} \\
\Pi_{C,c} = \frac{C_{C,c}}{C_{O,c}}, \Pi_{NH,c} = \frac{C_{NH,c}}{C_{O,c}}, \Pi_{NO,c} = \frac{C_{NO,c}}{C_{O,c}}, \Pi_{P-C} = \frac{\rho_b P_0}{\varepsilon_p C_{C,c}} \\
\Pi_{O,v} = \frac{C_{O,v}}{C_{O,c}}, \Pi_{C,v} = \frac{C_{C,v}}{C_{O,c}}, \Pi_{NH,v} = \frac{C_{NH,v}}{C_{O,c}}, \Pi_{NO,v} = \frac{C_{NO,v}}{C_{O,c}}
\end{aligned} \tag{C.48}$$

C.3 Additional Figures

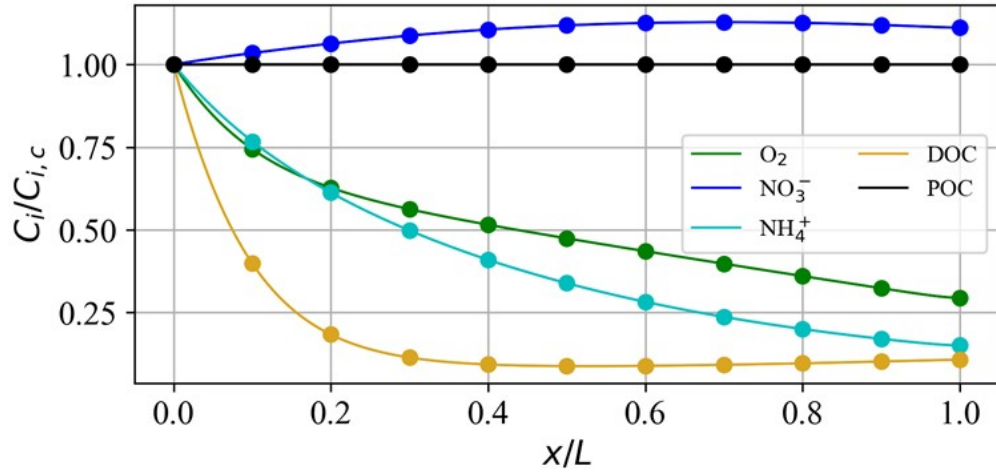


Figure C.3: Comparison of the numerical solutions for the transient (solid lines) and steady-state (dots) versions of the reactive transport model in equations (6.7)-(6.11) from Chapter 6. In this case, we use relative concentrations in a one-dimensional domain. The transient solution corresponds to the long-term relative concentrations predicted by the system of PDEs from equations (6.7)-(6.11), which are transient in nature and account for the coupled dissolution of POC. The steady-state solution corresponds to the relative concentrations predicted by the system of PDEs from equations (6.7)-(6.11) when $\partial(\varepsilon_p H C_i)/\partial t \rightarrow 0$ and $P(t) = P_0$.

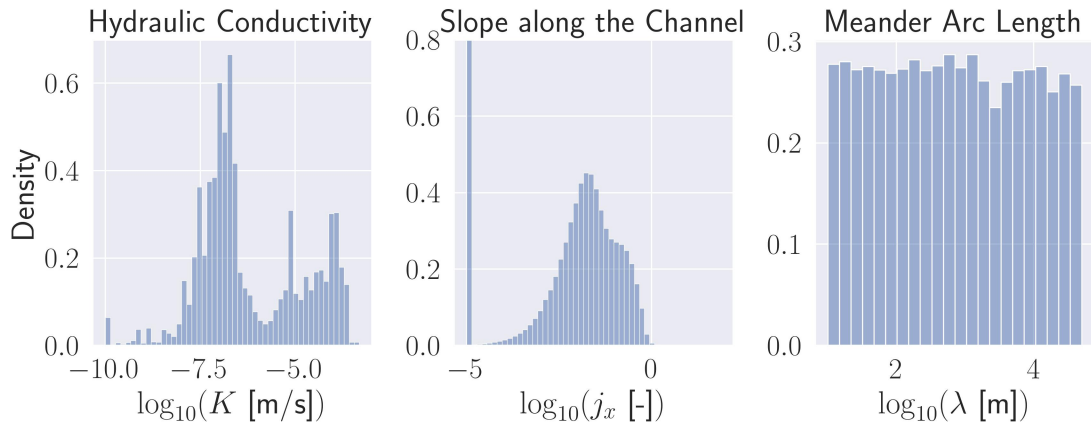


Figure C.4: Monte Carlo simulations of hydraulic conductivity (K), slope (J_x), and meander arc length (λ). The hydraulic conductivity was obtained from the `Hydr1CondCat` variable in the `StreamCat` dataset (Hill et al., 2016), the slope was obtained from the `NHDPlus High-Resolution` dataset (Moore et al., 2019), and we assumed a uniform distribution in log space from 10 meters to 50 kilometers for the arc length of the meanders, similar to what can be found from exploration in river planimetries in satellite images.

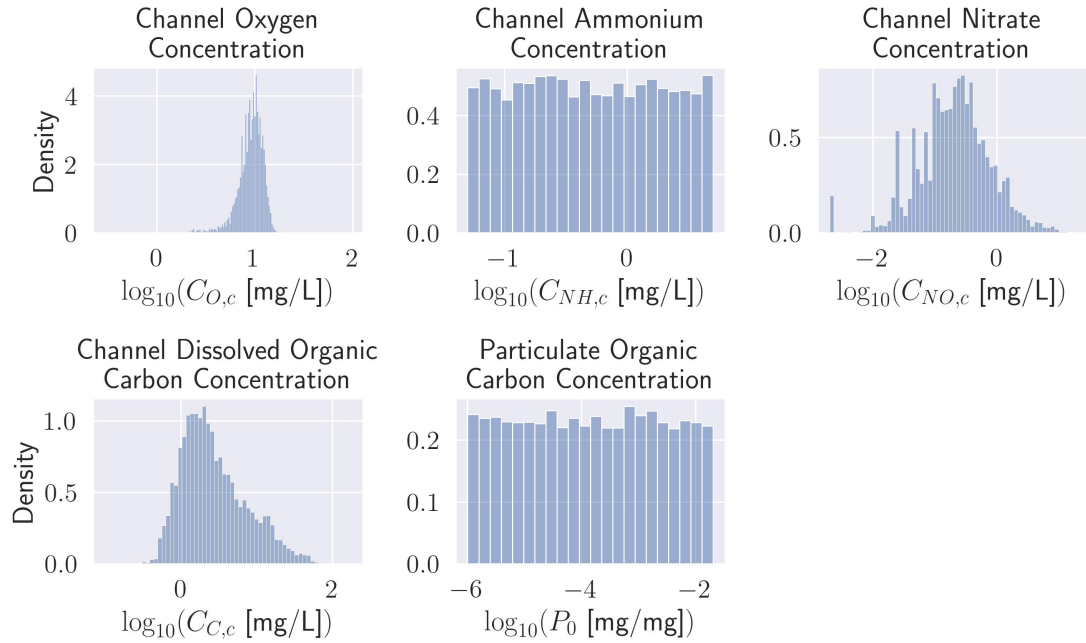


Figure C.5: Monte Carlo simulations of channel concentration in oxygen ($C_{O,c}$), ammonium ($C_{NH,c}$), nitrate ($C_{NO,c}$), dissolved organic carbon (DOC, $C_{C,c}$), and particulate organic carbon (POC, P_0). We use CAMELS-Chem dataset, provided in Sterle et al. (2022), for oxygen, DOC, and nitrate. The ammonium concentration was assumed uniform with a range between pristine and polluted streams, presented in Zheng et al. (2016), with values of $C_{NH,c}$ between (0.05, 5). Finally, we assumed a uniform distribution in log space for the particulate organic carbon exploring ranges where POC is low 1×10^{-6} , and where is high 1×10^{-2} .

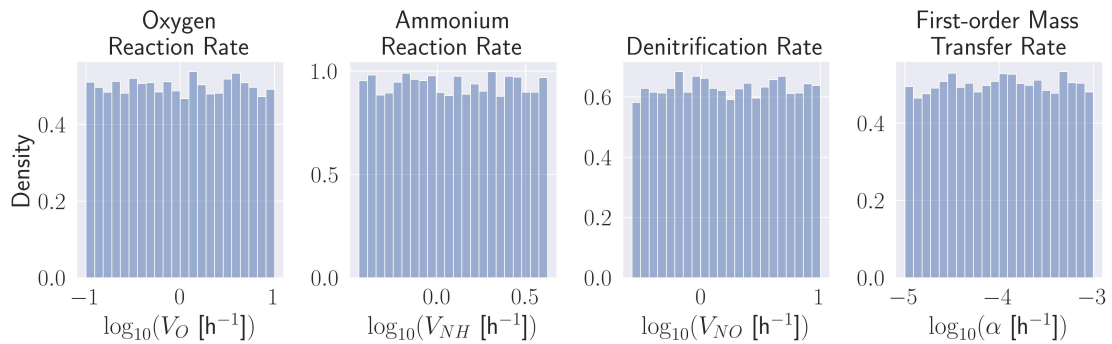


Figure C.6: Monte Carlo simulations of reaction rates for oxygen (V_O), ammonium (V_{NH}), and nitrates (C_{NO}), and the first-order mass transfer rate to dissolve organic carbon (α). We assumed a uniform distribution for all the rates with the ranges presented in Zarnetske et al. (2012).

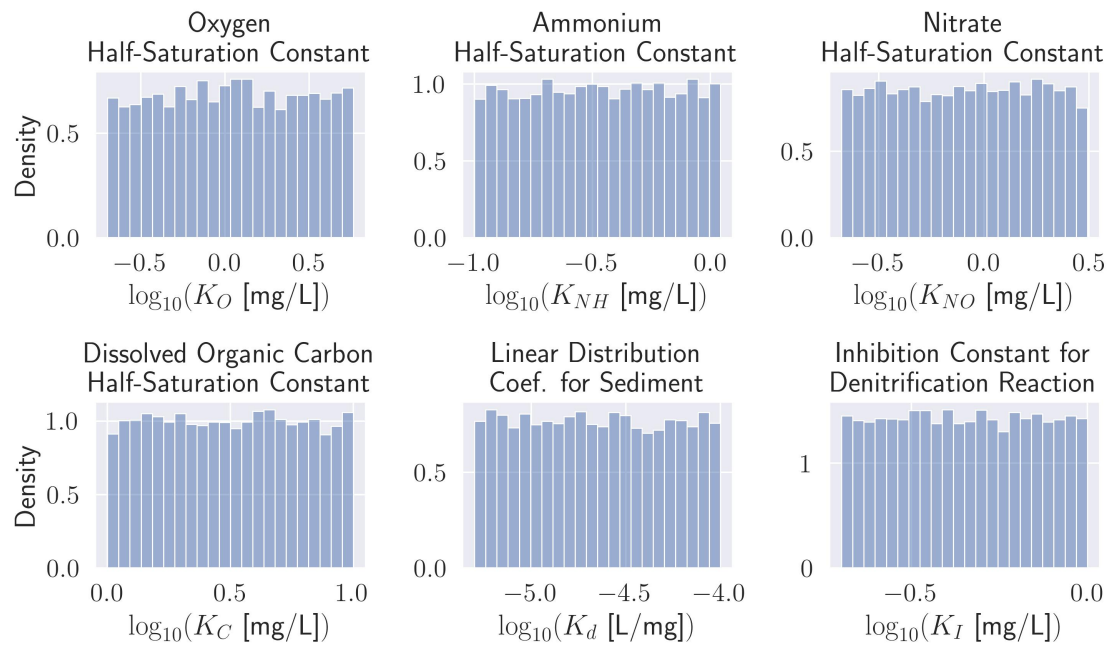


Figure C.7: Monte Carlo simulations of high-saturation constant for oxygen (K_O), ammonium (K_{NH}), nitrates (K_{NO}), and dissolved organic carbon (DOC, K_C), and histogram of the linear distribution of coefficient for sediments (K_d) and the inhibition constant for denitrification (K_I). We assumed a uniform distribution for all the concentration constants with the ranges presented in Zarnetske et al. (2012).

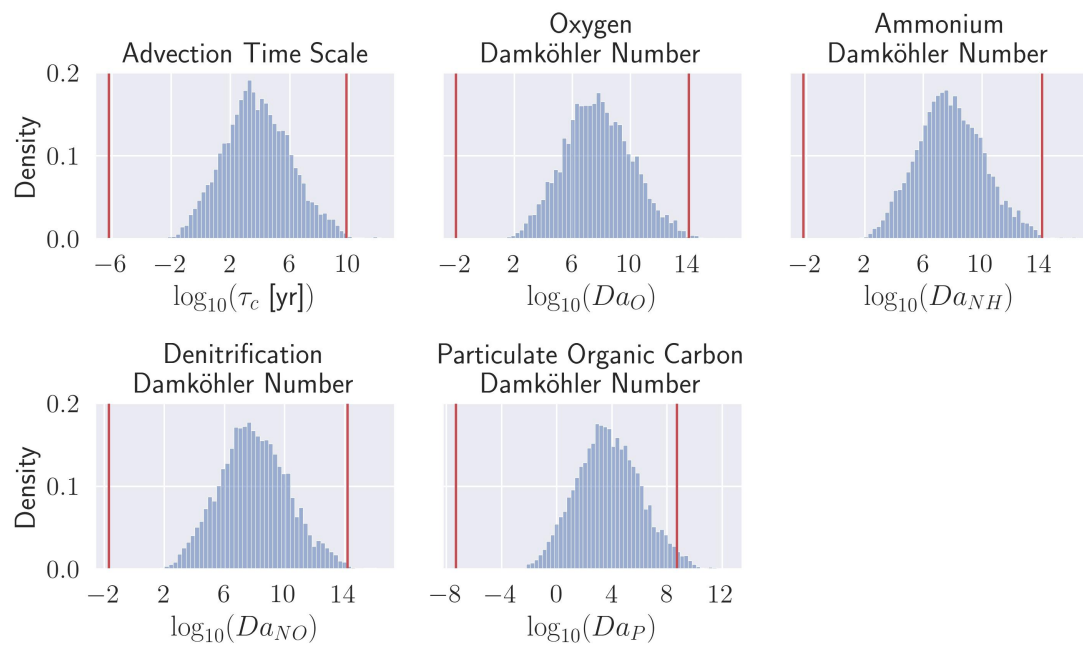


Figure C.8: Monte Carlo simulations for the advection time scale (τ_c), and the Damköhler numbers for oxygen (Da_O), ammonium (Da_{NH}), nitrates (Da_{NO}), and the particulate organic carbon (POC, Da_P). The values within the red lines show the range of values explored in the biogeochemical simulations.

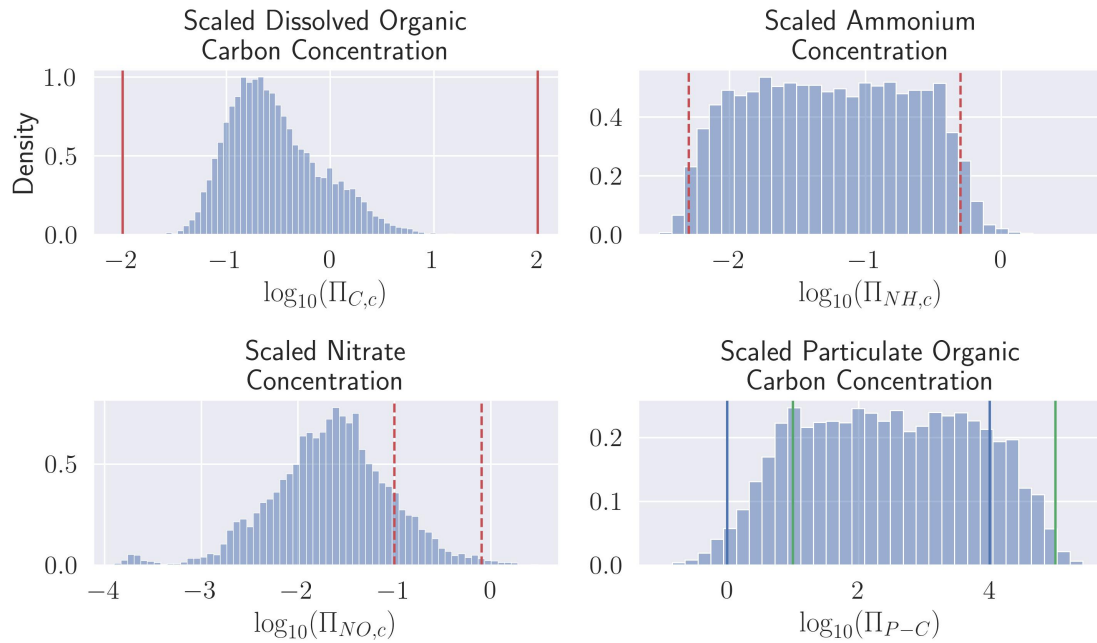


Figure C.9: Monte Carlo simulations for the scaled concentrations of dissolved organic carbon (DOC, $\Pi_{C,c}$), ammonium ($\Pi_{NH,c}$), nitrate ($\Pi_{NO,c}$), and particulate organic carbon (POC, Π_{P-C}). The solid red lines show the range of values explored in the biogeochemical simulations. The dashed lines show the values explored for pristine and polluted streams in ammonium and nitrates. Finally, the solid green and blue lines show the ranges of values explored for POC cases.

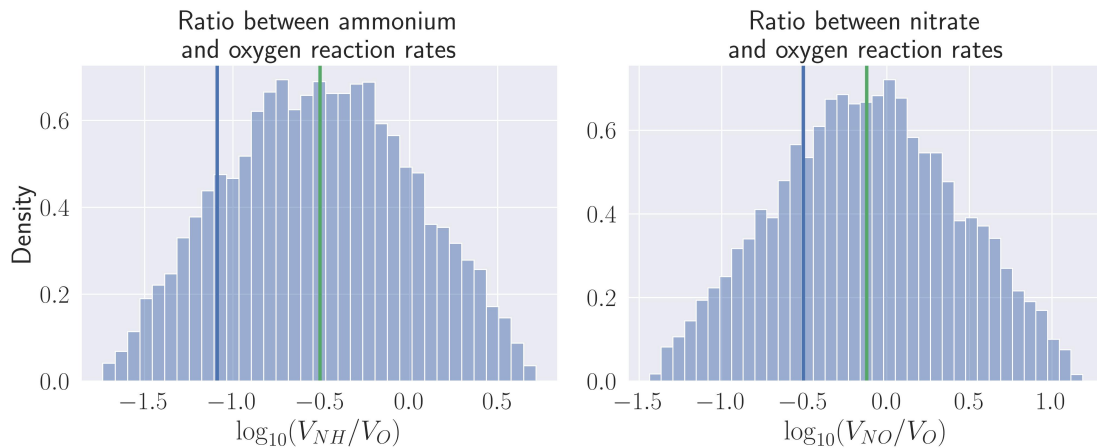


Figure C.10: Monte Carlo simulations for the ratios of reaction rates of ammonium (V_{NH}/V_O) and nitrate (V_{NO}/V_O). The green solid line shows the mean, and the blue line is the ratio from the values used in Zarnetske et al. (2012).

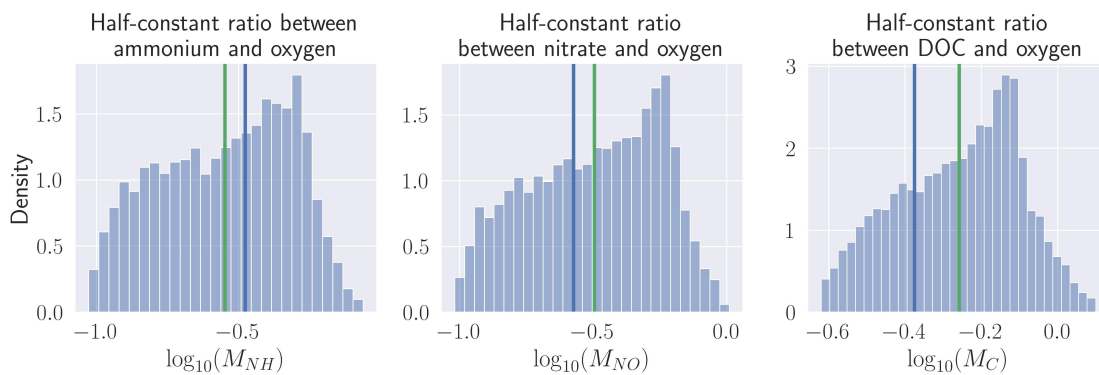


Figure C.11: Monte Carlo simulations for the ratios of reaction rates of ammonium (M_{NH}) and nitrate (M_{NO}). The green solid line shows the mean, and the blue line is the ratio from the values used in Zarnetske et al. (2012).

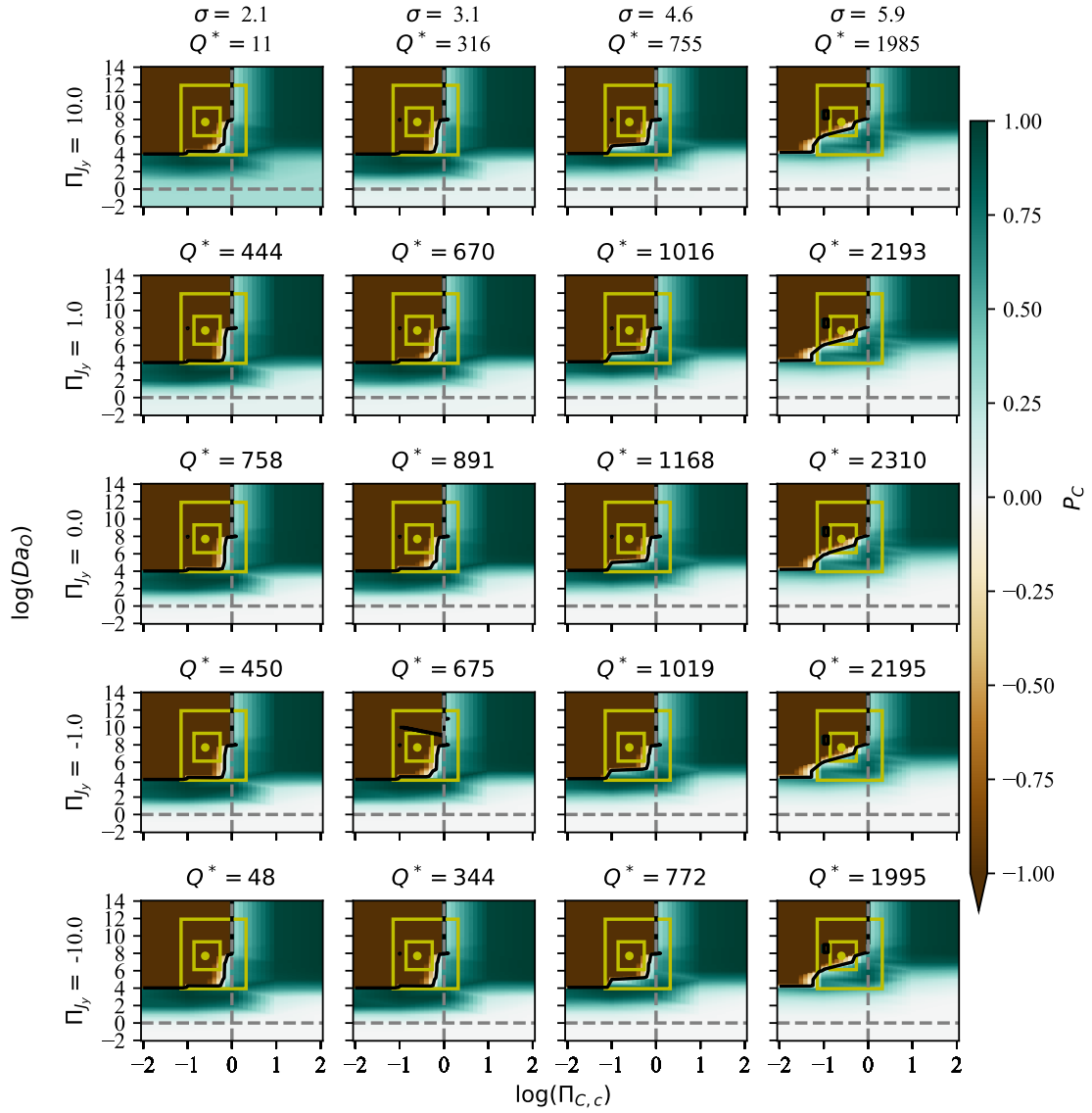


Figure C.12: Potential of retention of dissolved organic carbon for the pristine case and $P_0 = 0.02\%$. The columns denote different meander topologies described by the sinuosity (σ). The rows separate the regional gradient Π_y . The colors show the potential for biogeochemical retention. The solid black line shows the zero contour line. The horizontal dashed line is the division between transport-limited ($\log(Da_O) > 0$) and reaction-limited systems ($\log(Da_O) < 0$). The vertical dashed lines are the divisions between carbon-limited ($\Pi_{C,c} < 0$) and oxygen-limited systems ($\Pi_{C,c} > 0$). For reference, we include histograms for typical values of the dimensionless variables found across the Conterminous US and their corresponding 5%, 25%, 50%, 75%, and 95% percentiles (yellow boxes and point).

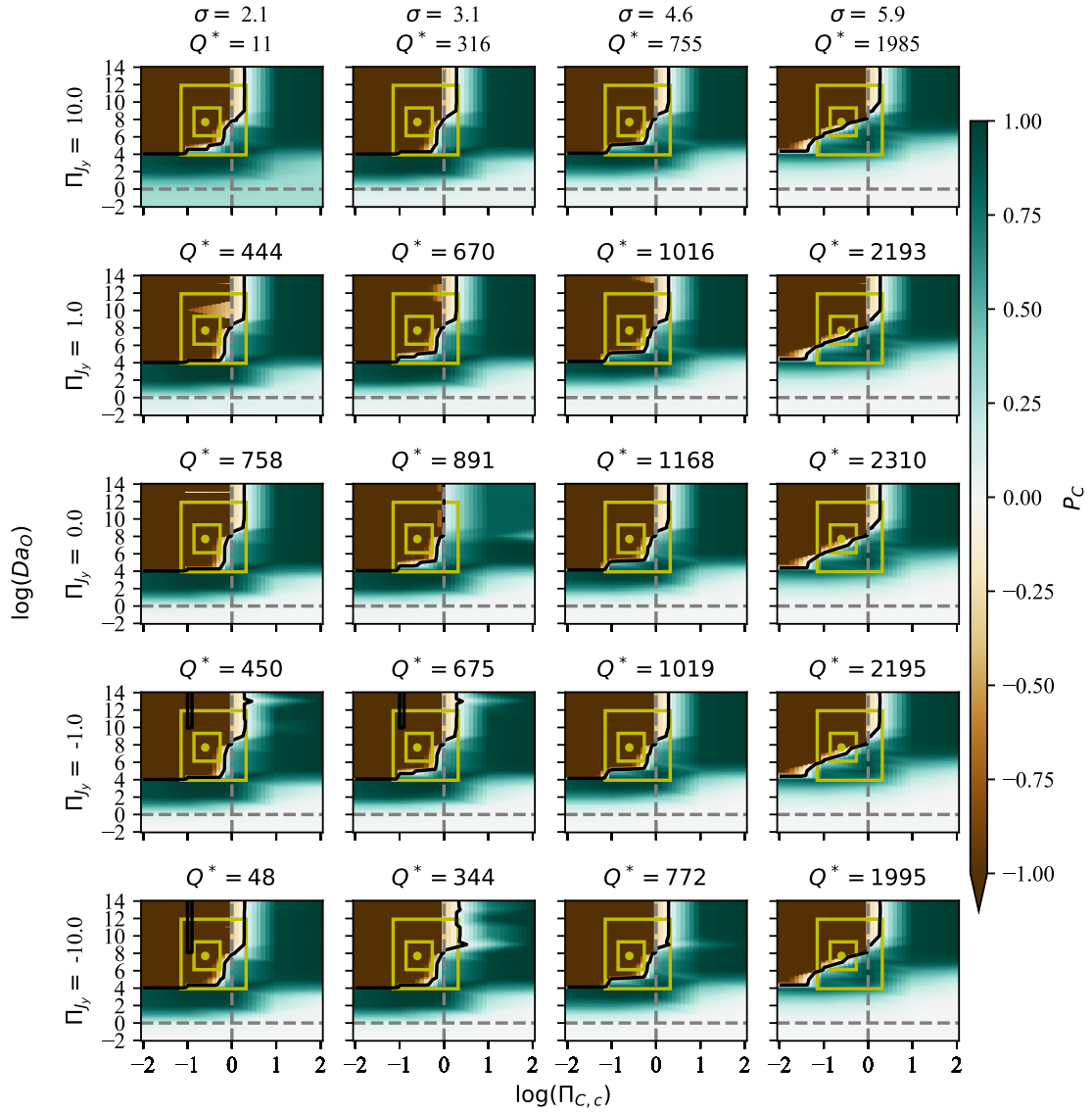


Figure C.13: Potential of retention of dissolved organic carbon for the polluted case and $P_0 = 0.02\%$. The columns denote different meander topologies described by the sinuosity (σ). The rows separate the regional gradient Π_y . The colors show the potential for biogeochemical retention. The solid black line shows the zero contour line. The horizontal dashed line is the division between transport-limited ($\log(Da_O) > 0$) and reaction-limited systems ($\log(Da_O) < 0$). The vertical dashed lines is the division between carbon-limited ($\Pi_{C,c} < 0$) and oxygen-limited systems ($\Pi_{C,c} > 0$). For reference, we include histograms for typical values of the dimensionless variables found across the Conterminous US and their corresponding 5%, 25%, 50%, 75%, and 95% percentiles (yellow boxes and point).

Appendix D

Supplemental Material for Chapter 7: "WigglyRivers: A Tool to Characterize the Multiscale Nature of Meandering Channels"

D.1 Interpolation of drainage area and channel width

The drainage area is interpolated on each link using the total drainage area ($TotDASqKm, DA_T$), the incremental drainage area ($AreaSqKm, DA_{inc}$), and the headwaters drainage area ($HWNodeSqKm, DA_{HW}$) available in the NHDPlus HR tables. At the start of the river, we use the following criteria to start the drainage area (DA_0). If the starting node is a headwater,

$$DA_0 = \begin{cases} DA_{HW} & \text{if } DA_{HW} > 0 \\ DA_{inc} & \text{if } DA_{inc} \neq DA_T \\ 0.1DA_T & \text{otherwise} \end{cases} \quad (\text{D.1})$$

If the starting node is not a headwater,

$$DA_0 = \begin{cases} DA_T - DA_{inc} & \text{if } DA_{inc} > 0 \\ DA_T & \text{of upstream otherwise} \end{cases} \quad (\text{D.2})$$

Finally, the `RiveDatasets` routine performs an estimate of bankfull width (w_{bf}) of the channel using the relationship proposed by Wilkerson et al. (2014), where

$$W_{bf} = \begin{cases} 2.18DA_i^{0.191} & \text{if } \ln(DA_i) < 1.600 \\ 1.41DA_i^{0.462} & \text{if } 1.600 \leq \ln(DA_i) < 5.820 \\ 7.18DA_i^{0.183} & \text{if } \ln(DA_i) \geq 5.820 \end{cases} \quad (\text{D.3})$$

D.2 Additional Tables

Table D.1: River and meander variables used in the *WigglyRivers* package with their dimensionless form.

Symbol	Variable Name	Units	Dimensionless Notation
W	Geometric Mean Channel Width	[L]	1
$\mathbf{x}_0, \mathbf{y}_0$	Original Planimetry Coordinates	[L]	$\mathbf{x}_0^* = \mathbf{x}_0/W$ $\mathbf{y}_0^* = \mathbf{y}_0/W$
\mathbf{x}, \mathbf{y}	Resampled Planimetry Coordinates	[L]	$\mathbf{x}^* = \mathbf{x}/W$ $\mathbf{y}^* = \mathbf{y}/W$
s	Arc-length	[L]	$s^* = 2s/W$
C	Curvature	[L ⁻¹]	$C^* = CW$
θ	Direction-angle	[·]	θ
l_s	Wavelet scale	[L]	$l_s^* = l_s/W$
λ	Wavelength	[L]	$\lambda^* = \lambda/W$
k	Wavenumber	[L ⁻¹]	$k^* = 2\pi W/\lambda$
r	Radius of Curvature	[L]	$r^* = r/W$
R_{hm}	Half-meander Radius of Curvature	[L]	$R_{hm}^* = R_{hm}/W$
λ_{hm}	Half-meander arc-wavelength	[L]	$\lambda_{hm}^* = \lambda_{hm}/W$
L_{hm}	Half-meander Valley Length	[L]	$L_{hm}^* = L_{hm}/W$
A_{hm}	Half-Meander Amplitude	[L]	$A_{hm}^* = A_{hm}/W$
a_{hm}	Half-meander Asymmetry	[·]	a_{hm}
σ_{hm}	Half-meander Sinuosity	[·]	σ_{hm}
λ_{fm}	Full-meander arc-wavelength	[L]	$\lambda_{fm}^* = \lambda_{fm}/W$
L_{fm}	Full-meander Valley Length	[L]	$L_{fm}^* = L_{fm}/W$
A_{fm}	Full-Meander Amplitude	[L]	$A_{fm}^* = A_{fm}/W$
a_{fm}	Full-meander Asymmetry	[·]	a_{fm}
σ_{fm}	Full-meander Sinuosity	[·]	σ_{fm}
FF	Funneling Factor	[·]	FF

D.3 Additional Figures

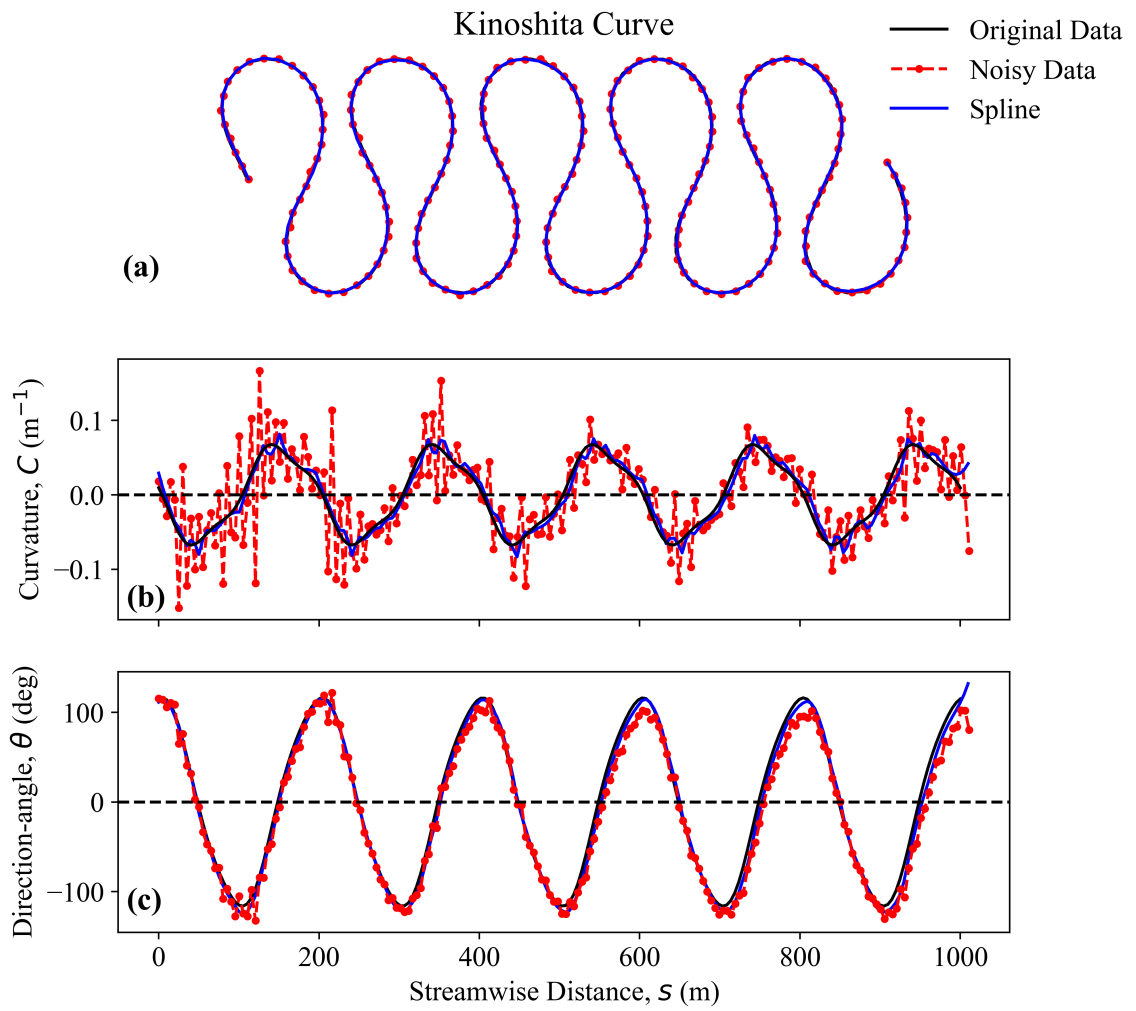


Figure D.1: Computation of curvature and direction angle. Comparison between normal, noisy, and spline-fitted planimetry coordinates in a kinoshita-type river.

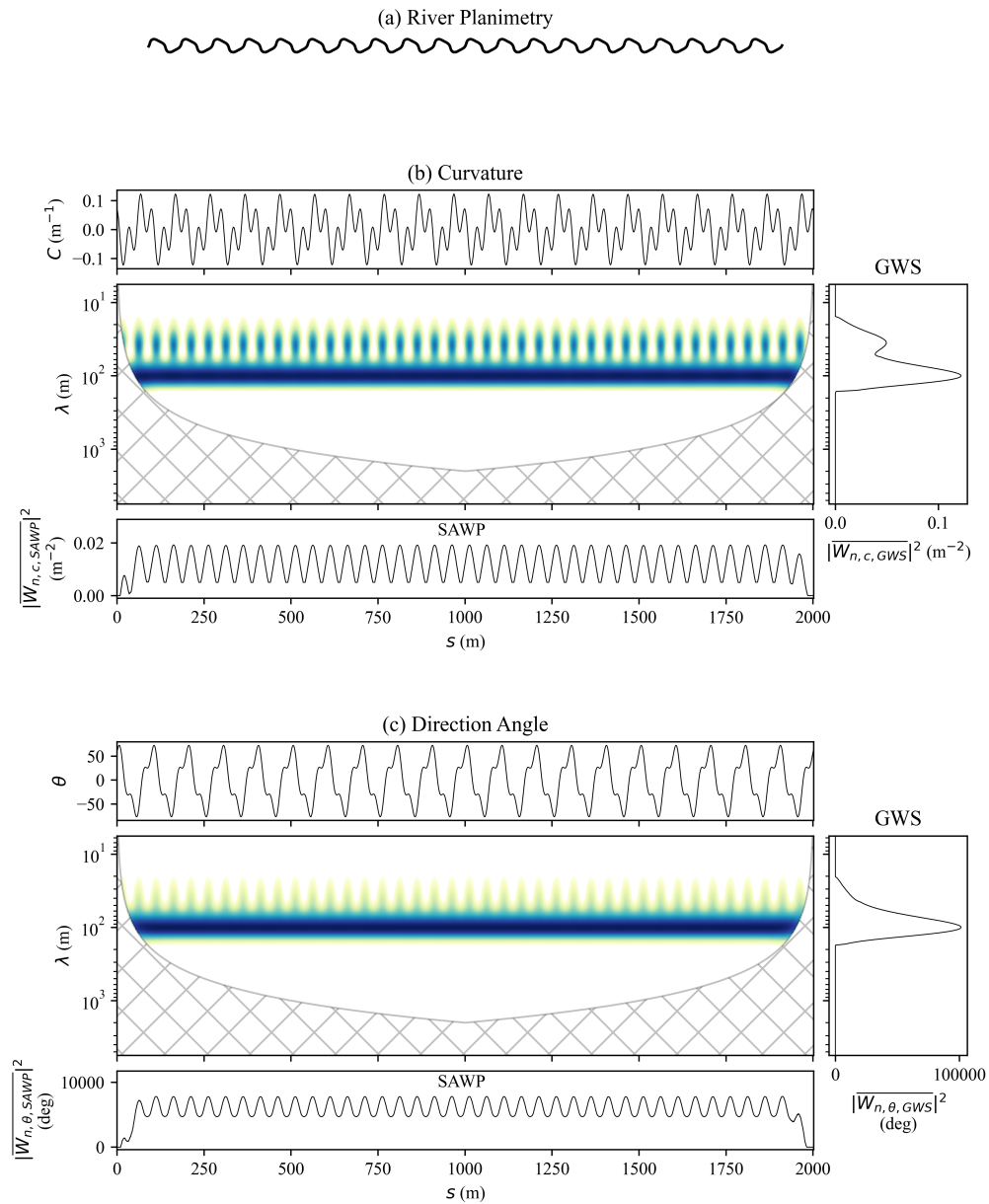


Figure D.2: Spectral characterization of a regular river transect planform. (a) river transect generated with equation (7.15) with $\theta_0 = 115$, $\theta_s = 0.344$, $\theta_f = 0.031$, and $\lambda = 100$. (b) curvature, CWT of the curvature below, the GWS on the right, and SAWP at the bottom. The same arrangement is given on (c) direction-angle. The hatch areas are the cone of influence of the CWT calculations.

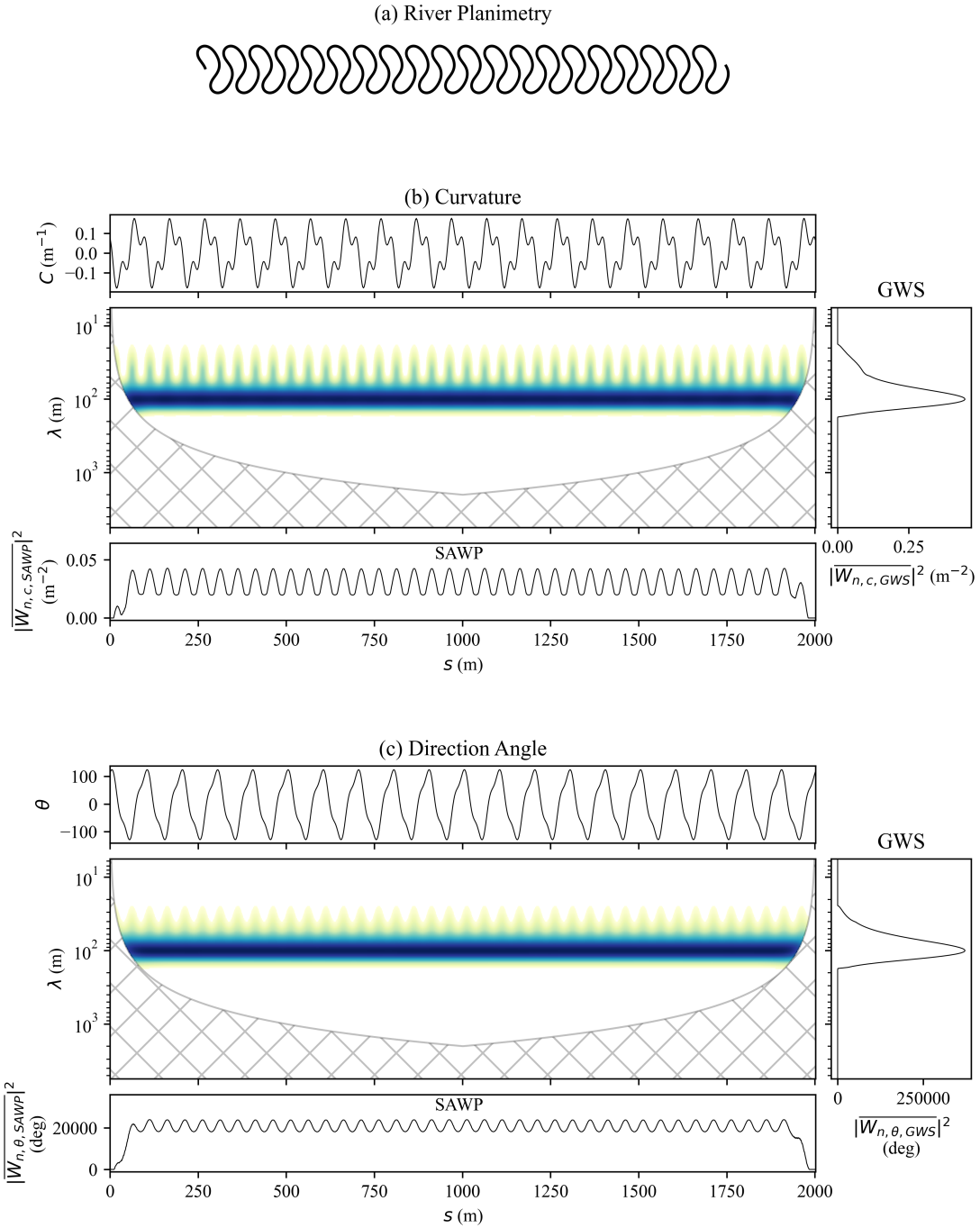


Figure D.3: Spectral characterization of a regular river transect planform. (a) river transect generated with equation (7.15) with $\theta_0 = 115^\circ$, $\theta_s = 0.344$, $\theta_f = 0.031$, and $\lambda = 100$. (b) curvature calculated with equation (7.2), CWT of the curvature below, the GWS on the right is calculated with equation (7.6), and SAWP at the bottom is calculated with equation (7.7). The same arrangement is given on (c) direction-angle, calculated with equation (7.3). The hatch areas are the cone of influence of the CWT calculations.

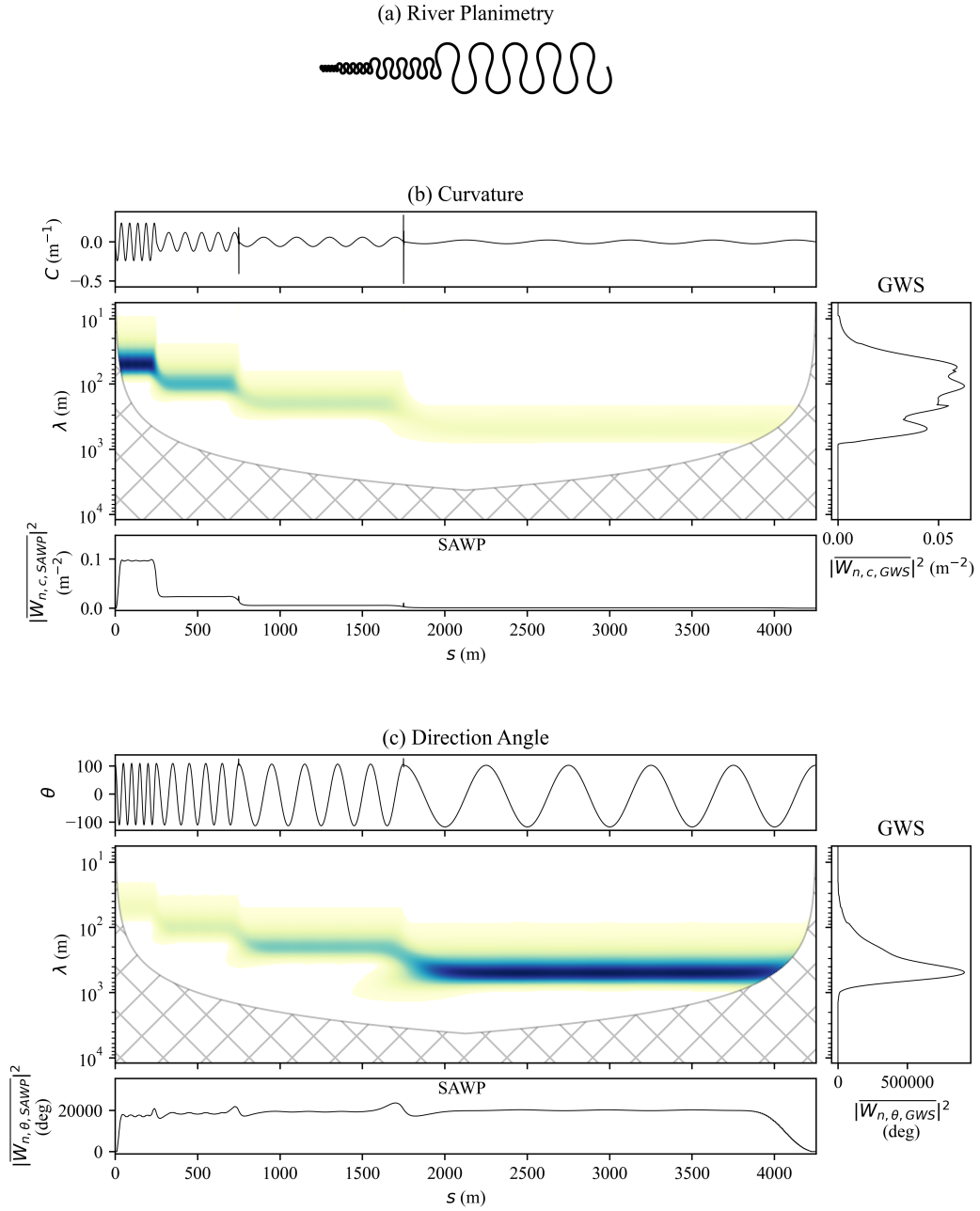


Figure D.4: Spectral characterization of a regular river transect planform with changing wavelength ($\lambda = [50, 100, 200, 500]$). (a) river transect with $\theta_0 = 115^\circ$, $\theta_s = 0$, and $\theta_f = 0$. (b) curvature and CWT of the curvature. The same arrangement is given on (c) direction-angle. The hatch areas are the cone of influence of the CWT calculations.

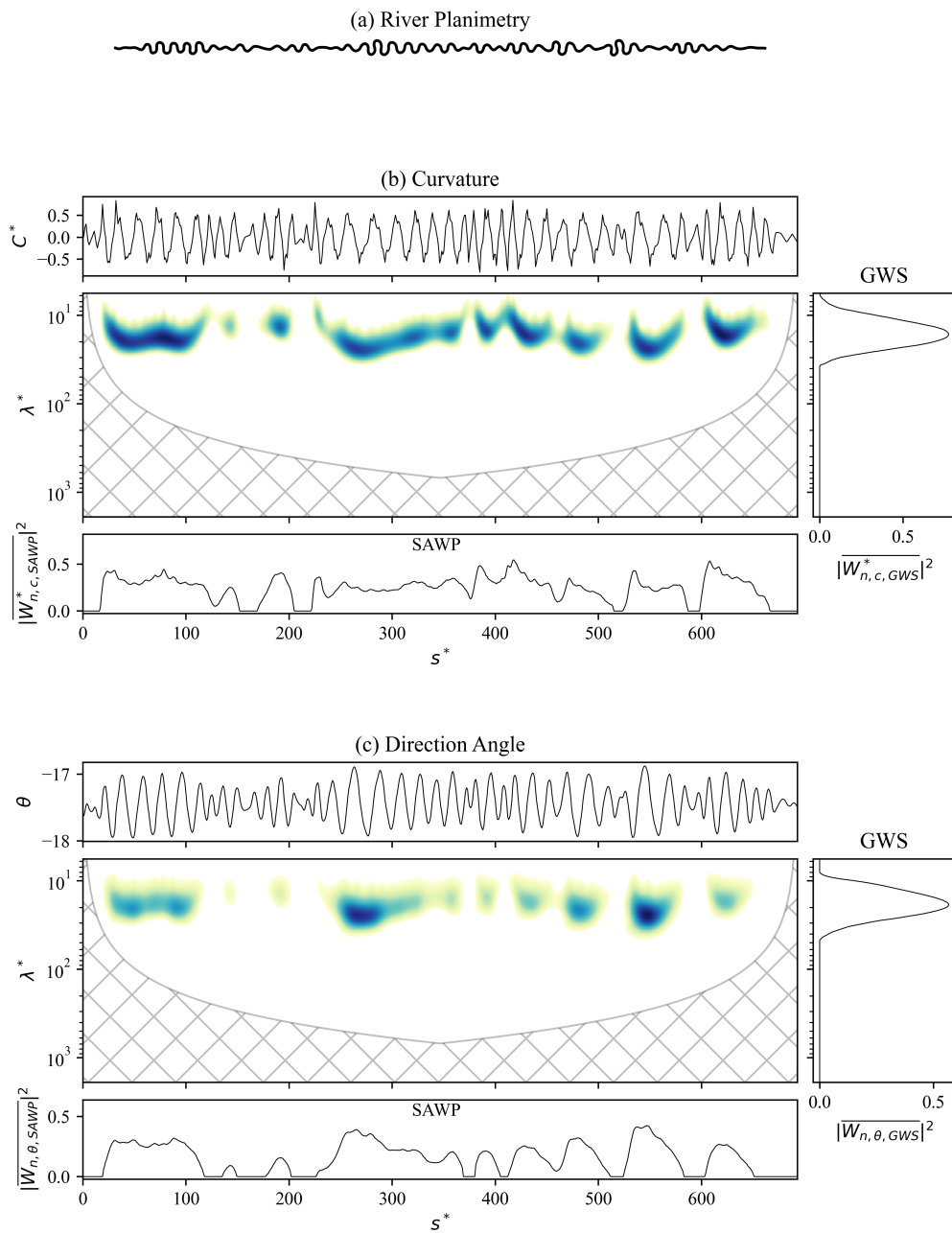


Figure D.5: Spectral characterization of a river transect modeled with *meanderpy*. (a) river transect. (b) curvature, CWT of the curvature below, the GWS on the right, and SAWP at the bottom. The same arrangement is given on (c) direction-angle. The hatch areas are the cone of influence of the CWT calculations.

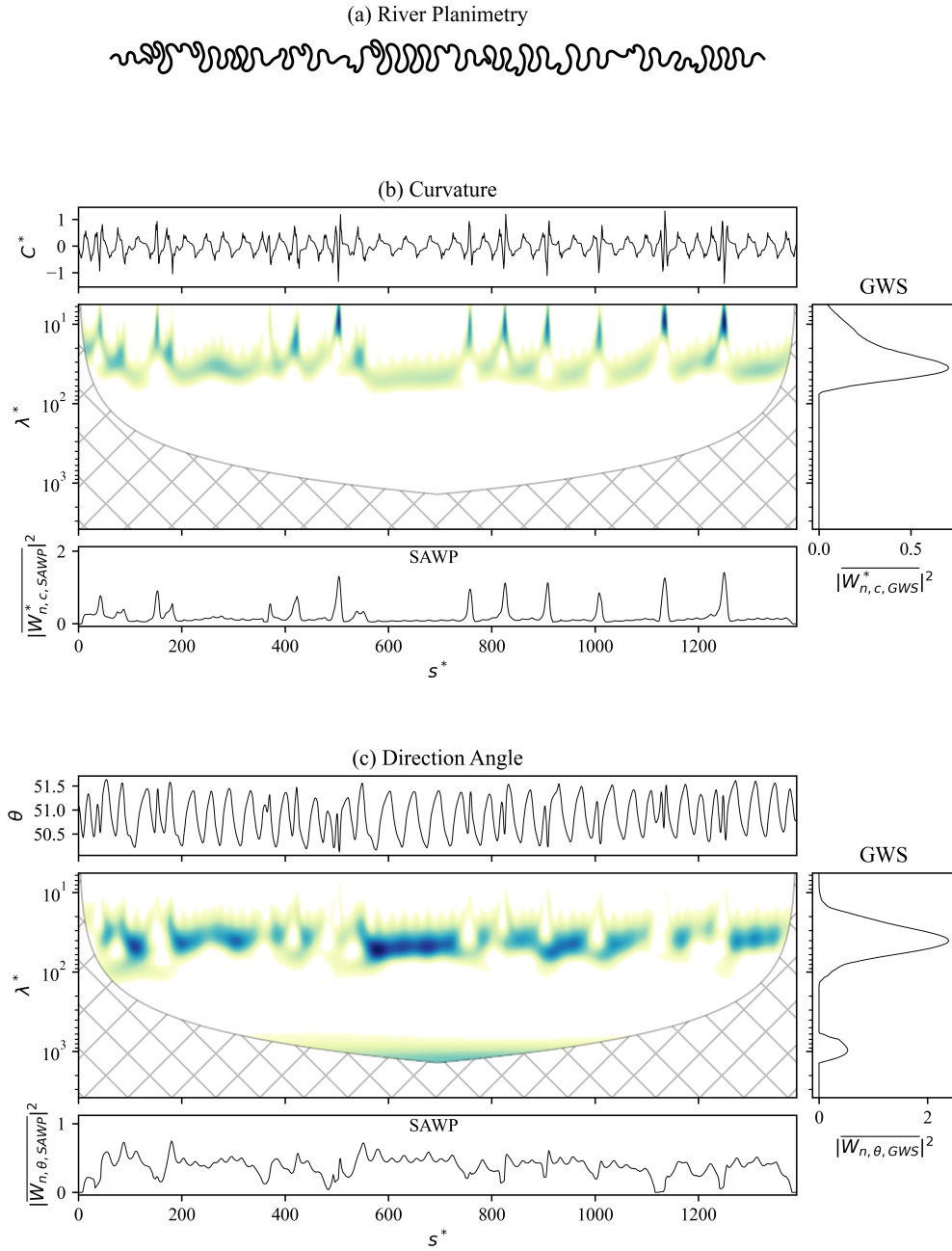


Figure D.6: Spectral characterization of a river transect modeled with *meanderpy*. (a) river transect. (b) curvature, CWT of the curvature below, the GWS on the right, and SAWP at the bottom. The same arrangement is given on (c) direction-angle. The hatch areas are the cone of influence of the CWT calculations.

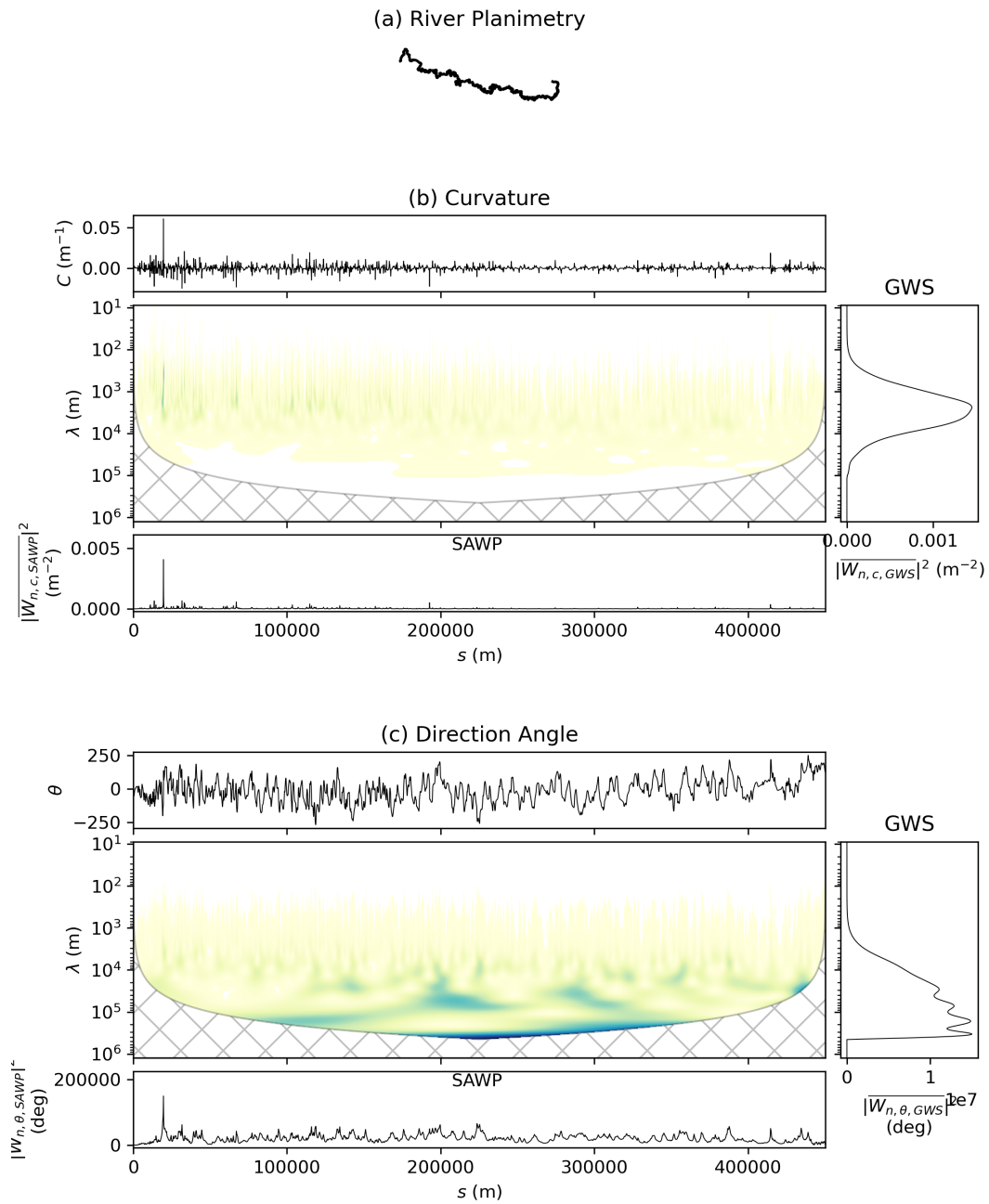


Figure D.7: Spectral characterization of a river transect within the 0604 subregion river network. (a) river transect. (b) curvature, CWT of the curvature below, the GWS on the right, and SAWP at the bottom. The same arrangement is given on (c) direction-angle. The hatch areas are the cone of influence of the CWT calculations.

Appendix E

Supplemental Material for Chapter 8: 2D Heterogeneous and Homogeneous Model Conceptualization

E.1 Model Conceptualization

To compare the effect of heterogeneity in the porous matrix on the denitrification potential, we created a two-dimensional model that compares the denitrification potential between a heterogeneous and a homogeneous porous matrix (Figure E.1). The model is a simplified version of the conceptual model presented in Chapter 6 and is described by the following equations for flow (Bear, 1972; Bear and Cheng, 2010).

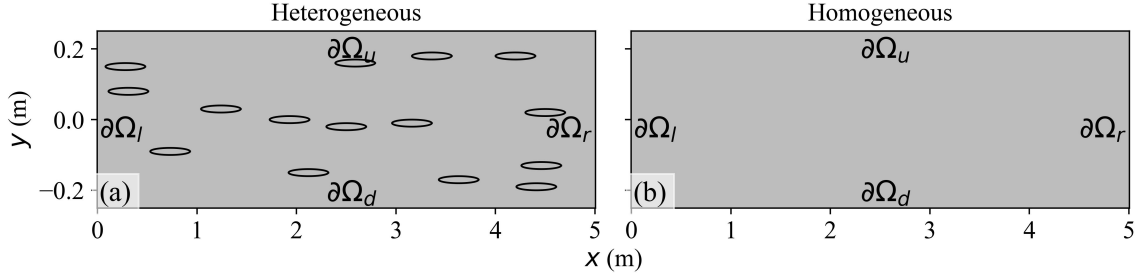


Figure E.1: Conceptualization of the 2D model for the (a) heterogeneous and (b) homogeneous porous matrix. The 15 black lenses in the heterogeneous system (a) are the location of liable particulate organic carbon (POC) where the dissolution of organic carbon will occur.

$$\begin{aligned}
 \nabla \cdot \mathbf{Q} &= 0 \text{ with } \mathbf{Q} = -KH\nabla h & (E.1) \\
 -\mathbf{n} \cdot \rho \mathbf{Q} &= 0 \text{ on } \partial\Omega_u \wedge \partial\Omega_d \\
 p(x=0, y) &= \rho g(J_x \lambda) \text{ on } \partial\Omega_l \\
 p(x=\lambda, y) &= 0 \text{ on } \partial\Omega_r
 \end{aligned}$$

where $\mathbf{Q}(\mathbf{x}) = -KH\nabla h$ is the vertically integrated flux [L^2T^{-1}], $\mathbf{q}(\mathbf{x}) = \mathbf{Q}(\mathbf{x})/H = -K\nabla h$ is the Darcy flux [LT^{-1}], $\mathbf{x} = [x, y]$ is the spatial coordinate vector [L], $K = 1 \times 10^{-6}$ is the homogeneous hydraulic conductivity [LT^{-1}], $H(\mathbf{x}) = h - Z_b$ is the saturated thickness [L], and $Z_b(x)$ is the vertical location of the impermeable layer elevation with respect to a reference datum $z = 0$ [L]. For simplicity, and without loss of generality, we assume $Z_b(x) = J_x(\lambda - x)$, with $J_x = 0.1425$ [-] and $\lambda = 5$ m [L] the slope and the system length (x -direction), respectively. In this model, the groundwater moves from left to right, driven by the hydraulic gradient J_x . The up-and-down boundaries ($\partial\Omega_u$ and $\partial\Omega_d$) are no-flow boundaries, and we imposed constant hydraulic head boundary conditions to the left and right boundaries ($\partial\Omega_l$ and $\partial\Omega_r$).

Similar to the model described in Chapter 6, we recast the biogeochemical model used by Zarnetske et al. (2012) for the microbially mediated reactions in Table 6.1 for a vertically-integrated domain:

$$\begin{aligned}
 \frac{\partial(\varepsilon_p H C_i)}{\partial t} &= \nabla \cdot (\mathbf{D} \nabla C_i) - \nabla \cdot (\mathbf{Q} C_i) + \varepsilon_p H R_i & (E.2) \\
 C_i(\mathbf{x}, t=0) &= 0 \\
 -\mathbf{n} \cdot (\mathbf{D} \nabla C_i - \mathbf{Q} C_i) &= 0 \text{ on } \partial\Omega_u \wedge \partial\Omega_d \\
 C_i(x=0, y) &= C_{i,c} \text{ on } \partial\Omega_l \\
 -\mathbf{n} \cdot \mathbf{D} \nabla C_i &= 0 \text{ on } \partial\Omega_r
 \end{aligned}$$

where $C_i(\mathbf{x}, t)$ and R_i are the concentration [ML^{-3}] and reaction rate [$ML^{-3}T^{-1}$] for species i ($i = NO, NH, O$, or C), defined in equations (6.8)-(6.12), ε_p is porosity [-] and $\mathbf{D} = \{D_{i,j}\}$ is the vertically-integrated

dispersion-diffusion tensor $[L^3T^{-1}]$, defined in (6.5). In both systems, we assumed a no flux boundary condition for the up-and-down boundaries ($\partial\Omega_u$ and $\partial\Omega_d$), a constant polluted concentration ($C_{NO,c} = 8$ mg/L, $C_{NH,c} = 5$ mg/L, $C_{O,c} = 10$ mg/L, and $C_{C,c} = 0.831$ mg/L) boundary conditions in the left boundary ($\partial\Omega_l$), and an outflow boundary condition in the right boundary ($\partial\Omega_r$). For the heterogeneous system, we assume the concentration of POC in the lenses is $P_0 = 0.2\%$ mg/L and $P_0 = 0$ mg/L everywhere else, and for the homogeneous system, we assume $P_0 = 0.008\%$ mg/L everywhere. The rest of the reaction variables are the same as the ones used in Chapter 6.

References

- Abad, J. D. and Garcia, M. H. (2009). Experiments in a high-amplitude Kinoshita meandering channel: 1. Implications of bend orientation on mean and turbulent flow structure: KINOSHITA CHANNEL, 1. *Water Resources Research*, 45(2).
- Ackerer, J., Ranchoux, C., Lucas, Y., Viville, D., Clément, A., Fritz, B., Lerouge, C., Schäfer, G., and Chabaux, F. (2021). Investigating the role of deep weathering in critical zone evolution by reactive transport modeling of the geochemical composition of deep fracture water. *Geochimica et Cosmochimica Acta*, 312:257–278.
- Adams, J. J. and Bachu, S. (2002). Equations of state for basin geofluids: algorithm review and intercomparison for brines. *Geofluids*, 2(4):257–271.
- Ahdab, Y. D. and Lienhard, J. H. (2021). Desalination of brackish groundwater to improve water quality and water supply. In *Global Groundwater*, pages 559–575. Elsevier.
- Allen, B. D., Love, D. W., and Myers, R. G. (2009). Evidence for late Pleistocene hydrologic and climatic change from Lake Otero, Tularosa Basin, south-central New Mexico. *New Mexico Geology*, 31(1):9–25.
- Alt-Epping, P., Diamond, L. W., Wanner, C., and Hammond, G. E. (2021). Effect of Glacial/Interglacial Recharge Conditions on Flow of Meteoric Water Through Deep Orogenic Faults: Insights Into the Geothermal System at Grimsel Pass, Switzerland. *Journal of Geophysical Research: Solid Earth*, 126(7):e2020JB021271. eprint: <https://onlinelibrary.wiley.com/doi/pdf/10.1029/2020JB021271>.
- An, R., Jiang, X.-W., Wang, J.-Z., Wan, L., Wang, X.-S., and Li, H. (2014). A theoretical analysis of basin-scale groundwater temperature distribution. *Hydrogeology Journal*, pages 1–8.
- Anderson, R. S. and Anderson, S. P. (2010). *Geomorphology: The Mechanics and Chemistry of Landscapes*. Cambridge University Press.
- Anderson, S. P., von Blanckenburg, F., and White, A. F. (2007). Physical and Chemical Controls on the Critical Zone. *Elements*, 3(5):315–319.
- Andrews, A. G. and Croskrey, A. (2019). Brackish Groundwater Production Zone Recommendations for the Blossom Aquifer, Texas. Open File Report 19-01, Texas Water Development Board, Texas, United States.
- Andrle, R. (1996). Measuring Channel Planform of Meandering Rivers. *Physical Geography*, 17(3):270–281. Publisher: Taylor & Francis eprint: <https://doi.org/10.1080/02723646.1996.10642585>.
- Anning, D. W., Beisner, K. R., Paul, A. P., Stanton, J. S., and Thiros, S. A. (2018). Brackish Groundwater and its Potential as a Resources in Southwestern United States. Fact Sheet 2018-3010, U.S. Geological Survey. Series: Fact Sheet.
- Aparicio, J., Candela, L., Alfranca, O., and García-Aróstegui, J. L. (2017). Economic evaluation of small desalination plants from brackish aquifers. Application to Campo de Cartagena (SE Spain). *Desalination*, 411:38–44.
- Armadillo, E., Rizzello, D., Pasqua, C., Pisani, P., Ghirotto, A., Kabaka, K., Mnjokava, T., Mwano, J., Didas, M., and Tumbu, L. (2020). Geophysical constraints on the Luhoi (Tanzania) geothermal conceptual model. *Geothermics*, 87:101875.
- Arora, B., Briggs, M. A., Zarnetske, J. P., Stegen, J., Gomez-Velez, J. D., Dwivedi, D., and Steefel, C. (2022). Hot Spots and Hot Moments in the Critical Zone: Identification of and Incorporation into Reactive Transport Models. In Wymore, A. S., Yang, W. H., Silver, W. L., McDowell, W. H., and Chorover, J., editors, *Biogeochemistry of the Critical Zone*, Advances in Critical Zone Science, pages 9–47. Springer International Publishing, Cham.

- Arps, J. (1953). The Effect of Temperature on the Density and Electrical Resistivity of Sodium Chloride Solutions. *Journal of Petroleum Technology*, 5(10):17–20.
- Arrigoni, A. S., Poole, G. C., Mertes, L. A. K., O’Daniel, S. J., Woessner, W. W., and Thomas, S. A. (2008). Buffered, lagged, or cooled? Disentangling hyporheic influences on temperature cycles in stream channels. *Water Resources Research*, 44(9). eprint: <https://agupubs.onlinelibrary.wiley.com/doi/pdf/10.1029/2007WR006480>.
- Aster, R. C., Borchers, B., and Thurber, C. H. (2016). *Parameter Estimation and Inverse Problems*. Amsterdam Heidelberg.
- Baker, M., Dahm, C., and Valett, H. (1999). Acetate retention and metabolism in the hyporheic zone of a mountain stream. *Limnology and oceanography*, 44(6):1530–1539.
- Barroll, M. W. and Reiter, M. (1990). Analysis of the Socorro hydrogeothermal system: Central New Mexico. *Journal of Geophysical Research: Solid Earth*, 95(B13):21949–21963. eprint: <https://agupubs.onlinelibrary.wiley.com/doi/pdf/10.1029/JB095iB13p21949>.
- Bear, J. (1972). *Dynamics of Fluids in Porous Media*. American Elsevier Publishing, New York.
- Bear, J. and Cheng, A. H.-D. (2010). *Modeling Groundwater Flow and Contaminant Transport*. Number 23 in Theory and Applications of Transport in Porous Media. Springer Netherlands, 1 edition.
- Becker, K., Von Herzen, R. P., Francis, T. J. G., Anderson, R. N., Honnorez, J., Adamson, A. C., Alt, J. C., Emmermann, R., Kempton, P. D., Kinoshita, H., Laverne, C., Mottl, M. J., and Newmark, R. L. (1982). In situ electrical resistivity and bulk porosity of the oceanic crust Costa Rica Rift. *Nature*, 300(5893):594–598. Number: 5893 Publisher: Nature Publishing Group.
- Behroozmand, A. A., Auken, E., and Knight, R. (2019). Assessment of Managed Aquifer Recharge Sites Using a New Geophysical Imaging Method. *Vadose Zone Journal*, 18(1):1–13.
- Bekins, B. A., Warren, E., and Godsy, E. M. (1998). A Comparison of Zero-Order, First-Order, and Monod Biotransformation Models. *Groundwater*, 36(2):261–268. eprint: <https://onlinelibrary.wiley.com/doi/pdf/10.1111/j.1745-6584.1998.tb01091.x>.
- Bencala, K. E. (2011). 2.20 - Stream–Groundwater Interactions. In Wilderer, P., editor, *Treatise on Water Science*, pages 537–546. Elsevier, Oxford.
- Bernabé, Y., Mok, U., and Evans, B. (2003). Permeability-porosity Relationships in Rocks Subjected to Various Evolution Processes. *pure and applied geophysics*, 160(5-6):937–960.
- Bernard, J. (2003). Short Note on the Depth of Investigation of Electrical Methods. Technical report, Iris Instruments.
- Bichon, B. J., Eldred, M. S., Swiler, L. P., Mahadevan, S., and McFarland, J. M. (2008). Efficient Global Reliability Analysis for Nonlinear Implicit Performance Functions. *AIAA Journal*, 46(10):2459–2468.
- Binley, A., Cassiani, G., and Deiana, R. (2010). Hydrogeophysics: opportunities and challenges. *Bollettino di Geofisica Teorica ed Applicata*, 51(4):267–287.
- Binley, A., Hubbard, S. S., Huisman, J. A., Revil, A., Robinson, D. A., Singha, K., and Slater, L. D. (2015). The emergence of hydrogeophysics for improved understanding of subsurface processes over multiple scales. *Water Resources Research*, 51(6):3837–3866.
- Blake, S., Henry, T., Muller, M. R., Jones, A. G., Moore, J. P., Murray, J., Companyà, J., Vozar, J., Walsh, J., and Rath, V. (2016). Understanding hydrothermal circulation patterns at a low-enthalpy thermal spring using audio-magnetotelluric data: A case study from Ireland. *Journal of Applied Geophysics*, 132:1–16.
- Boano, F., Camporeale, C., and Revelli, R. (2010a). A linear model for the coupled surface-subsurface flow in a meandering stream. *Water Resources Research*, 46(7).

- Boano, F., Camporeale, C., Revelli, R., and Ridolfi, L. (2006). Sinuosity-driven hyporheic exchange in meandering rivers. *Geophysical Research Letters*, 33(18).
- Boano, F., Demaria, A., Revelli, R., and Ridolfi, L. (2010b). Biogeochemical zonation due to intrameander hyporheic flow. *Water Resources Research*, 46(2). eprint: <https://agupubs.onlinelibrary.wiley.com/doi/pdf/10.1029/2008WR007583>.
- Boano, F., Harvey, J. W., Marion, A., Packman, A. I., Revelli, R., Ridolfi, L., and Wörman, A. (2014). Hyporheic flow and transport processes: Mechanisms, models, and biogeochemical implications. *Reviews of Geophysics*, 52(4):603–679.
- Bourret, S. M. (2015). MULTI-SCALE HYDROLOGIC MODELING OF THE WHITE SANDS DUNE FIELD AND SURROUNDING TULAROSA BASIN, NEW MEXICO. Master's thesis, New Mexico Institute of Mining and Technology.
- Briggs, M. A., Day-Lewis, F. D., Dehkordy, F. M. P., Hampton, T., Zarnetske, J. P., Scruggs, C. R., Singha, K., Harvey, J. W., and Lane, J. W. (2018). Direct Observations of Hydrologic Exchange Occurring With Less-Mobile Porosity and the Development of Anoxic Microzones in Sandy Lakebed Sediments. *Water Resources Research*, 54(7):4714–4729. eprint: <https://onlinelibrary.wiley.com/doi/pdf/10.1029/2018WR022823>.
- Buffington, J. M., Montgomery, D. R., and Greenberg, H. M. (2004). Basin-scale availability of salmonid spawning gravel as influenced by channel type and hydraulic roughness in mountain catchments. *Canadian Journal of Fisheries and Aquatic Sciences*. 61(11): 2085-2096., page 2085.
- Buffington, J. M. and Tonina, D. (2009). Hyporheic Exchange in Mountain Rivers II: Effects of Channel Morphology on Mechanics, Scales, and Rates of Exchange: Channel morphology and hyporheic exchange. *Geography Compass*, 3(3):1038–1062.
- Buono, R. M., Zodrow, K. R., Alvarez, P. J. J., and Li, Q. (2016). A new frontier in Texas: managing and regulating brackish groundwater. *Water Policy*, 18(3):727–749.
- Bureau of Reclamation (2022). Brackish Groundwater National Desalination Research Facility.
- Burgin, A. J. and Loecke, T. D. (2023). The biogeochemical redox paradox: how can we make a foundational concept more predictive of biogeochemical state changes? *Biogeochemistry*, 164(2):349–370.
- Camporeale, C., Perona, P., Porporato, A., and Ridolfi, L. (2007). Hierarchy of models for meandering rivers and related morphodynamic processes. *Reviews of Geophysics*, 45(1). eprint: <https://onlinelibrary.wiley.com/doi/pdf/10.1029/2005RG000185>.
- Cardenas, M. and Jiang, X.-W. (2010). Groundwater flow, transport, and residence times through topography-driven basins with exponentially decreasing permeability and porosity. *Water Resources Research*, 46(W11538).
- Cardenas, M. B. (2008). The effect of river bend morphology on flow and timescales of surface water–groundwater exchange across pointbars. *Journal of Hydrology*, 362(1-2):134–141.
- Cardenas, M. B. (2009a). A model for lateral hyporheic flow based on valley slope and channel sinuosity. *Water Resources Research*, 45(1).
- Cardenas, M. B. (2009b). Stream-aquifer interactions and hyporheic exchange in gaining and losing sinuous streams. *Water Resources Research*, 45(6).
- Cardenas, M. B. (2015). Hyporheic zone hydrologic science: A historical account of its emergence and a prospectus. *Water Resources Research*, 51(5):3601–3616. eprint: <https://agupubs.onlinelibrary.wiley.com/doi/pdf/10.1002/2015WR017028>.

- Carroll, R. W. H., Manning, A. H., Niswonger, R., Marchetti, D., and Williams, K. H. (2020). Baseflow Age Distributions and Depth of Active Groundwater Flow in a Snow-Dominated Mountain Headwater Basin. *Water Resources Research*, 56(12):e2020WR028161. eprint: <https://onlinelibrary.wiley.com/doi/pdf/10.1029/2020WR028161>.
- Cassiani, G., Godio, A., Stocco, S., Villa, A., Deiana, R., Frattini, P., and Rossi, M. (2009). Monitoring the hydrologic behaviour of a mountain slope via time-lapse electrical resistivity tomography. *Near Surface Geophysics*, 7(5-6):475–486.
- Cayan, D. R., Das, T., Pierce, D. W., Barnett, T. P., Tyree, M., and Gershunov, A. (2010). Future dryness in the southwest US and the hydrology of the early 21st century drought. *Proceedings of the National Academy of Sciences*, 107(50):21271–21276. Publisher: National Academy of Sciences Section: Research Articles.
- Chave, A. D., Jones, A. G., Mackie, R., and Rodi, W. (2012). *The Magnetotelluric Method: Theory and Practice*. Cambridge University Press, Cambridge.
- COMSOL AB (2024). COMSOL Multiphysics® [Software].
- Condon, L. E., Atchley, A. L., and Maxwell, R. M. (2020a). Evapotranspiration depletes groundwater under warming over the contiguous United States. *Nature Communications*, 11(1):873. Bandiera_abtest: a Cc_license_type: cc_by Cg_type: Nature Research Journals Number: 1 Primary_atype: Research Publisher: Nature Publishing Group Subject_term: Climate change;Hydrology Subject_term_id: climate-change;hydrology.
- Condon, L. E., Markovich, K. H., Kelleher, C. A., McDonnell, J. J., Ferguson, G., and McIntosh, J. C. (2020b). Where Is the Bottom of a Watershed? *Water Resources Research*, 56(3):e2019WR026010. eprint: <https://agupubs.onlinelibrary.wiley.com/doi/pdf/10.1029/2019WR026010>.
- Constable, S., Key, K., and Lewis, L. (2009). Mapping offshore sedimentary structure using electromagnetic methods and terrain effects in marine magnetotelluric data. *Geophysical Journal International*, 176(2):431–442.
- Constable, S. C., Parker, R. L., and Constable, C. G. (1987). Occam's inversion: a practical algorithm for generating smooth models from electromagnetic sounding data. *Geophysics*, 52(3):289–300.
- Cook, P. G., Walker, G. R., Buselli, G., Potts, I., and Dodds, A. R. (1992). The application of electromagnetic techniques to groundwater recharge investigations. *Journal of Hydrology*, 130(1):201–229.
- Creed, I. F., McKnight, D. M., Pellerin, B. A., Green, M. B., Bergamaschi, B. A., Aiken, G. R., Burns, D. A., Findlay, S. E., Shanley, J. B., Striegl, R. G., Aulenbach, B. T., Clow, D. W., Laudon, H., McGlynn, B. L., McGuire, K. J., Smith, R. A., and Stackpoole, S. M. (2015). The river as a chemostat: fresh perspectives on dissolved organic matter flowing down the river continuum. *Canadian Journal of Fisheries and Aquatic Sciences*, 72(8):1272–1285. Publisher: NRC Research Press.
- Croskrey, A., Syudam, A., Robinson, M. C., and Meyer, J. (2019). Brackish Groundwater Production Zone Recommendations for the Nacatoch Aquifer, Texas. Open File Report 19-02, Texas Water Development Board, Texas, United States.
- Cuthbert, M. O., Gleeson, T., Moosdorf, N., Befus, K. M., Schneider, A., Hartmann, J., and Lehner, B. (2019). Global patterns and dynamics of climate–groundwater interactions. *Nature Climate Change*, 9(2):137–141. Bandiera_abtest: a Cg_type: Nature Research Journals Number: 2 Primary_atype: Research Publisher: Nature Publishing Group Subject_term: Climate sciences;Hydrology;Water resources Subject_term_id: climate-sciences;hydrology;water-resources.
- Cáñez, T. T. (2019). *MAPPING FRESH AND BRACKISH GROUNDWATER TO INFORM BETTER MANAGEMENT OF DECREASING GROUNDWATER LEVELS IN THE WILLCOX BASIN, SE ARIZONA*. Bachelor Thesis, University of Arizona.

- Dahm, C., Grimm, N., Marmonier, P., Valett, H., and Vervier, P. (1998). Nutrient dynamics at the interface between surface waters and groundwaters. *Freshwater Biology*, 40(3):427–451.
- Daily, W. and Ramirez, A. (1995). Electrical resistance tomography during in-situ trichloroethylene remediation at the Savannah River Site. *Journal of Applied Geophysics*, 33(4):239–249.
- Deming, J. W. and Baross, J. A. (1993). Deep-sea smokers: Windows to a subsurface biosphere? *Geochimica et Cosmochimica Acta*, 57(14):3219–3230.
- Deng, F., Hou, L., Liu, M., Zheng, Y., Yin, G., Li, X., Lin, X., Chen, F., Gao, J., and Jiang, X. (2015). Dissimilatory nitrate reduction processes and associated contribution to nitrogen removal in sediments of the Yangtze Estuary. *Journal of Geophysical Research: Biogeosciences*, 120(8):1521–1531. .eprint: <https://onlinelibrary.wiley.com/doi/pdf/10.1002/2015JG003007>.
- Dent, C. L., Grimm, N. B., and Fisher, S. G. (2001). Multiscale effects of surface–subsurface exchange on stream water nutrient concentrations. *Journal of the North American Benthological Society*, 20(2):162–181. Publisher: The University of Chicago Press.
- Dent, C. L., Schade, J. D., Grimm, N. B., and Fisher, S. G. (2000). 16 - Subsurface Influences on Surface Biology. In Jones, J. B. and Mulholland, P. J., editors, *Streams and Ground Waters*, Aquatic Ecology, pages 381–402. Academic Press, San Diego.
- Diamond, J. S., Pinay, G., Bernal, S., Cohen, M. J., Lewis, D., Lupon, A., Zarnetske, J., and Moatar, F. (2023). Light and hydrologic connectivity drive dissolved oxygen synchrony in stream networks. *Limnology and Oceanography*, 68(2):322–335. .eprint: <https://onlinelibrary.wiley.com/doi/pdf/10.1002/lno.12271>.
- Dodds, W. K., Perkin, J. S., and Gerken, J. E. (2013). Human Impact on Freshwater Ecosystem Services: A Global Perspective. *Environmental Science & Technology*, 47(16):9061–9068.
- Dominguez Ruben, L., Naito, K., Gutierrez, R. R., Szupiany, R., and Abad, J. D. (2021). Meander Statistics Toolbox (MStat): A toolbox for geometry characterization of bends in large meandering channels. *SoftwareX*, 14:100674.
- Dwivedi, D., Arora, B., Steefel, C. I., Dafflon, B., and Versteeg, R. (2018). Hot Spots and Hot Moments of Nitrogen in a Riparian Corridor. *Water Resources Research*, 54(1):205–222. .eprint: <https://onlinelibrary.wiley.com/doi/pdf/10.1002/2017WR022346>.
- Décamps, H., Fortuné, M., Gazelle, F., and Pautou, G. (1988). Historical influence of man on the riparian dynamics of a fluvial landscape. *Landscape Ecology*, 1(3):163–173.
- Díaz, D., Villegas, N., Díaz, D., and Villegas, N. (2022). Wavelet coherence between ENSO indices and two precipitation databases for the Andes region of Colombia. *Atmósfera*, 35(2):237–271. Publisher: Centro de Ciencias de la Atmósfera, UNAM.
- Earth Resources Observation And Science (EROS) Center (2017). Shuttle Radar Topography Mission (SRTM) 1 Arc-Second Global. Medium: tiff.
- Eastoe, C. and Rodney, R. (2014). Isotopes as Tracers of Water Origin in and Near a Regional Carbonate Aquifer: The Southern Sacramento Mountains, New Mexico. *Water*, 6(2):301–323.
- Egbert, G. D., Yang, B., Bedrosian, P. A., Key, K., Livelybrooks, D. W., Schultz, A., Kelbert, A., and Parris, B. (2022). Fluid transport and storage in the Cascadia forearc influenced by overriding plate lithology. *Nature Geoscience*, 15(8):677–682. Number: 8 Publisher: Nature Publishing Group.
- Embid, E. H., Finch, S. T., and Shomaker, J. (2011). WHITE SANDS NATIONAL MONUMENT INVENTORY OF WATER RIGHTS AND GROUNDWATER EVALUATION DATA. Technical report.
- Fan, Y. (2015). Groundwater in the Earth’s critical zone: Relevance to large-scale patterns and processes. *Water Resources Research*, 51(5):3052–3069. .eprint: <https://onlinelibrary.wiley.com/doi/pdf/10.1002/2015WR017037>.

- Fan, Y. (2019). Are catchments leaky? *Wiley Interdisciplinary Reviews: Water*, 6.
- Ferré, T., Bentley, L., Binley, A., Linde, N., Kemna, A., Singha, K., Holliger, K., Huisman, J. A., and Minsley, B. (2009). Critical Steps for the Continuing Advancement of Hydrogeophysics. *Eos, Transactions American Geophysical Union*, 90(23):200–200. eprint: <https://onlinelibrary.wiley.com/doi/pdf/10.1029/2009EO230004>.
- Fetter, C. (2001). *Applied Hydrogeology: Fourth Edition*. Prentice Hall, Upper Saddle River, N.J., 4 edition.
- Flerchinger, G. N. and Cooley, K. R. (2000). A ten-year water balance of a mountainous semi-arid watershed. *Journal of Hydrology*, 237(1):86–99.
- Forster, C. and Smith, L. (1988). Groundwater flow systems in mountainous terrain 2. Controlling factors. *Water Resources Research*, 24(7).
- Foufoula-Georgiou, E. and Kumar, P. (1994). Wavelet Analysis in Geophysics: An Introduction. In Foufoula-Georgiou, E. and Kumar, P., editors, *Wavelet Analysis and Its Applications*, volume 4 of *Wavelets in Geophysics*, pages 1–43. Academic Press.
- Freeze, R. A. and Witherspoon, P. A. (1967). Theoretical analysis of regional groundwater flow: 2. Effect of water-table configuration and subsurface permeability variation. *Water Resources Research*, 3(2):623–634. eprint: <https://onlinelibrary.wiley.com/doi/pdf/10.1029/WR003i002p00623>.
- Frisbee, M. D., Phillips, F. M., White, A. F., Campbell, A. R., and Liu, F. (2013a). Effect of source integration on the geochemical fluxes from springs. *Applied Geochemistry*, 28:32–54.
- Frisbee, M. D., Tolley, D. G., and Wilson, J. L. (2017). Field estimates of groundwater circulation depths in two mountainous watersheds in the western U.S. and the effect of deep circulation on solute concentrations in streamflow. *Water Resources Research*, 53(4):2693–2715.
- Frisbee, M. D., Wilson, J. L., Gomez-Velez, J. D., Phillips, F. M., and Campbell, A. R. (2013b). Are we missing the tail (and the tale) of residence time distributions in watersheds? *Geophysical Research Letters*, pages 4633–4637.
- Fujimoto, M., Ohte, N., Kawasaki, M., Osaka, K., Itoh, M., Ohtsuka, I., and Itoh, M. (2016). Influence of bedrock groundwater on streamflow characteristics in a volcanic catchment. *Hydrological Processes*, 30(4):558–572. eprint: <https://onlinelibrary.wiley.com/doi/pdf/10.1002/hyp.10558>.
- Gabrielli, C., McDonnell, J., and Jarvis, W. (2012). The role of bedrock groundwater in rainfall–runoff response at hillslope and catchment scales. *Journal of Hydrology*, 450–451:117–133.
- Garven, G. and Freeze, R. A. (1984). Theoretical analysis of the role of groundwater flow in the genesis of stratabound ore deposits; 2, Quantitative results. *American Journal of Science*, 284(10):1125–1174.
- Gelhar, L. W., Welty, C., and Rehfeldt, K. (1992). A critical review of data on field-scale dispersion in aquifers. *Water Resources Research*, 28(7):1955–1974.
- Ghermandi, A. and Minich, T. (2017). Analysis of farmers’ attitude toward irrigation with desalinated brackish water in Israel’s Arava Valley. *DESALINATION AND WATER TREATMENT*, 76:328–331.
- Ginn, T. R. (1999). On the distribution of multicomponent mixtures over generalized exposure time in subsurface flow and reactive transport: Foundations, and formulations for groundwater age, chemical heterogeneity, and biodegradation. *Water Resources Research*, 35(5):1395–1407. <https://agupubs.onlinelibrary.wiley.com/doi/pdf/10.1029/1999WR900013>.
- Gleeson, T. and Manning, A. H. (2008). Regional groundwater flow in mountainous terrain: Three-dimensional simulations of topographic and hydrogeologic controls. *Water Resources Research*, 44(10).
- Gleeson, T., Marklund, L., Smith, L., and Manning, A. H. (2011). Classifying the water table at regional to continental scales: WATER TABLE AT CONTINENTAL SCALES. *Geophysical Research Letters*, 38(5):n/a–n/a.

- Glover, P. W. J., Hole, M. J., and Pous, J. (2000). A modified Archie's law for two conducting phases. *Earth and Planetary Science Letters*, 180(3):369–383.
- Gomez, J. D. and Wilson, J. L. (2013). Age distributions and dynamically changing hydrologic systems: Exploring topography-driven flow. *Water Resources Research*, 49(3):1503–1522.
- Gomez, J. D., Wilson, J. L., and Cardenas, M. B. (2012). Residence time distributions in sinuosity-driven hyporheic zones and their biogeochemical effects: RTD IN HYPORHEIC ZONES AND BIOGEOCHEMICAL EFFECTS. *Water Resources Research*, 48(9).
- Gomez-Velez, J. D. (2013). *On Residence Time Distributions and Dynamically Changing Hydrologic Systems*. PhD Dissertation, New Mexico Institute of Mining and Technology, Socorro, New Mexico.
- Gomez-Velez, J. D. and Harvey, J. W. (2014). A hydrogeomorphic river network model predicts where and why hyporheic exchange is important in large basins. *Geophysical Research Letters*, 41(18):6403–6412. [_eprint: https://onlinelibrary.wiley.com/doi/pdf/10.1002/2014GL061099](https://onlinelibrary.wiley.com/doi/pdf/10.1002/2014GL061099).
- Gomez-Velez, J. D., Harvey, J. W., Cardenas, M. B., and Kiel, B. (2015). Denitrification in the Mississippi River network controlled by flow through river bedforms. *Nature Geoscience*, 8(12):941–945. Number: 12 Publisher: Nature Publishing Group.
- Gomez-Velez, J. D., Krause, S., and Wilson, J. L. (2014). Effect of low-permeability layers on spatial patterns of hyporheic exchange and groundwater upwelling. *Water Resources Research*, pages 5196–5215.
- Gomez-Velez, J. D., Wilson, J. L., Cardenas, M. B., and Harvey, J. W. (2017). Flow and Residence Times of Dynamic River Bank Storage and Sinuosity-Driven Hyporheic Exchange: BANK STORAGE AND HYPORHEIC EXCHANGE. *Water Resources Research*, 53(10):8572–8595.
- Gonzalez-Duque, D., Gomez-Velez, J. D., Person, M. A., Kelley, S., Key, K., and Lucero, D. (2024a). Deep Circulation in Hydrologic Systems: Their Nested Nature and the Importance of Coupling Physical, Solute, and Thermal Processes (Accepted). *Water Resources Research*.
- Gonzalez-Duque, D., Gomez-Velez, J. D., Zarnetske, J. P., Chen, X., and Scheibe, T. D. (2024b). Sinuosity-driven Hyporheic Exchange: Hydrodynamics and Biogeochemical Potential (Accepted). *Water Resources Research*.
- Gothäll, H. (2022). How to Inspect Your Mesh in COMSOL Multiphysics®.
- Graham, C. B., van Verseveld, W., Barnard, H. R., and McDonnell, J. J. (2010). Estimating the deep seepage component of the hillslope and catchment water balance within a measurement uncertainty framework. *Hydrological Processes*, 24(25):3631–3647. [_eprint: https://onlinelibrary.wiley.com/doi/pdf/10.1002/hyp.7788](https://onlinelibrary.wiley.com/doi/pdf/10.1002/hyp.7788).
- Graham, J. S. (2015). Brackish and Saline Groundwater in New Mexico. *New Mexico Earth Matters*, 15(2):6.
- Green, C. T., Liao, L., Nolan, B. T., Juckem, P. F., Shope, C. L., Tesoriero, A. J., and Jurgens, B. C. (2018). Regional variability of nitrate fluxes in the unsaturated zone and groundwater, Wisconsin, USA. *Water Resources Research*, 54(1):301322. Code: Water Resources Research Type: Journal Article IP-086033.
- Gu, C., Anderson, W., and Maggi, F. (2012). Riparian biogeochemical hot moments induced by stream fluctuations. *Water Resources Research*, 48(9). [_eprint: https://onlinelibrary.wiley.com/doi/pdf/10.1029/2011WR011720](https://onlinelibrary.wiley.com/doi/pdf/10.1029/2011WR011720).
- Gu, C., Hornberger, G. M., Herman, J. S., and Mills, A. L. (2008a). Effect of freshets on the flux of groundwater nitrate through streambed sediments. *Water Resources Research*, 44(5). [_eprint: https://onlinelibrary.wiley.com/doi/pdf/10.1029/2007WR006488](https://onlinelibrary.wiley.com/doi/pdf/10.1029/2007WR006488).
- Gu, C., Hornberger, G. M., Herman, J. S., and Mills, A. L. (2008b). Influence of stream-groundwater interactions in the streambed sediments on NO₃- flux to a low-relief coastal stream. *Water Resources Research*, 44(11). [_eprint: https://onlinelibrary.wiley.com/doi/pdf/10.1029/2007WR006739](https://onlinelibrary.wiley.com/doi/pdf/10.1029/2007WR006739).

- Gu, C., Hornberger, G. M., Mills, A. L., Herman, J. S., and Flewelling, S. A. (2007). Nitrate reduction in streambed sediments: Effects of flow and biogeochemical kinetics. *Water Resources Research*, 43(12). [.eprint: https://agupubs.onlinelibrary.wiley.com/doi/pdf/10.1029/2007WR006027](https://agupubs.onlinelibrary.wiley.com/doi/pdf/10.1029/2007WR006027).
- Gu, D. and Philander, S. G. H. (1995). Secular Changes of Annual and Interannual Variability in the Tropics during the Past Century. *Journal of Climate*, 8(4):864–876. Publisher: American Meteorological Society Section: Journal of Climate.
- Güneralp, I. and Rhoads, B. L. (2008). Continuous Characterization of the Planform Geometry and Curvature of Meandering Rivers. *Geographical Analysis*, 40(1):1–25. [.eprint: https://onlinelibrary.wiley.com/doi/pdf/10.1111/j.0016-7363.2007.00711.x](https://onlinelibrary.wiley.com/doi/pdf/10.1111/j.0016-7363.2007.00711.x).
- Güneralp, I. and Rhoads, B. L. (2011). Influence of floodplain erosional heterogeneity on planform complexity of meandering rivers. *Geophysical Research Letters*, 38(14). [.eprint: https://agupubs.onlinelibrary.wiley.com/doi/pdf/10.1029/2011GL048134](https://agupubs.onlinelibrary.wiley.com/doi/pdf/10.1029/2011GL048134).
- Gustafson, C., Key, K., and Evans, R. L. (2019). Aquifer systems extending far offshore on the U.S. Atlantic margin. *Scientific Reports*, 9(1):8709.
- Gustafson, C. D., Key, K., Siegfried, M. R., Winberry, J. P., Fricker, H. A., Venturelli, R. A., and Michaud, A. B. (2022). A dynamic saline groundwater system mapped beneath an Antarctic ice stream. *Science*, 376(6593):640–644. Publisher: American Association for the Advancement of Science.
- Gutierrez, R. R. and Abad, J. D. (2014). On the analysis of the medium term planform dynamics of meandering rivers. *Water Resources Research*, 50(5):3714–3733. [.eprint: https://agupubs.onlinelibrary.wiley.com/doi/pdf/10.1002/2012WR013358](https://agupubs.onlinelibrary.wiley.com/doi/pdf/10.1002/2012WR013358).
- Hancock, P. J. (2002). Human Impacts on the Stream-Groundwater Exchange Zone. *Environmental Management*, 29(6):763–781.
- Hare, D. K., Helton, A. M., Johnson, Z. C., Lane, J. W., and Briggs, M. A. (2021). Continental-scale analysis of shallow and deep groundwater contributions to streams. *Nature Communications*, 12(1):1450. Bandiera_abtest: a Cc_license_type: cc_by Cg_type: Nature Research Journals Number: 1 Primary_atype: Research Publisher: Nature Publishing Group Subject_term: Ecology;Hydrology Subject_term_id: ecology;hydrology.
- Harvey, J., Gomez-Velez, J., Schmadel, N., Scott, D., Boyer, E., Alexander, R., Eng, K., Golden, H., Kettner, A., Konrad, C., Moore, R., Pizzuto, J., Schwarz, G., Soulsby, C., and Choi, J. (2018). How Hydrologic Connectivity Regulates Water Quality in River Corridors. *JAWRA Journal of the American Water Resources Association*.
- Harvey, J. and Gooseff, M. (2015). River corridor science: Hydrologic exchange and ecological consequences from bedforms to basins. *Water Resources Research*, 51(9):6893–6922. [.eprint: https://agupubs.onlinelibrary.wiley.com/doi/pdf/10.1002/2015WR017617](https://agupubs.onlinelibrary.wiley.com/doi/pdf/10.1002/2015WR017617).
- Harvey, J. W. and Schmadel, N. M. (2021). The River Corridor’s Evolving Connectivity of Lotic and Lentic Waters. *Frontiers in Water*, 2.
- Hedin, L. O., von Fischer, J. C., Ostrom, N. E., Kennedy, B. P., Brown, M. G., and Robertson, G. P. (1998). Thermodynamic Constraints on Nitrogen Transformations and Other Biogeochemical Processes at Soil-Stream Interfaces. *Ecology*, 79(2):684–703. Publisher: Ecological Society of America.
- Herckenrath, D., Auken, E., Christiansen, L., Behroozmand, A. A., and Bauer-Gottwein, P. (2012). Coupled hydrogeophysical inversion using time-lapse magnetic resonance sounding and time-lapse gravity data for hydraulic aquifer testing: Will it work in practice? *Water Resources Research*, 48(1). [.eprint: https://agupubs.onlinelibrary.wiley.com/doi/pdf/10.1029/2011WR010411](https://agupubs.onlinelibrary.wiley.com/doi/pdf/10.1029/2011WR010411).
- Herckenrath, D., Odlum, N., Nenna, V., Knight, R., Auken, E., and Bauer-Gottwein, P. (2013). Calibrating a Salt Water Intrusion Model with Time-Domain Electromagnetic Data. *Groundwater*, 51(3):385–397. [.eprint: https://ngwa.onlinelibrary.wiley.com/doi/pdf/10.1111/j.1745-6584.2012.00974.x](https://ngwa.onlinelibrary.wiley.com/doi/pdf/10.1111/j.1745-6584.2012.00974.x).

- Hester, E. and Gooseff, M. (2010). Moving Beyond the Banks: Hyporheic Restoration Is Fundamental to Restoring Ecological Services and Functions of Streams. *Environ. Sci. Technol.*, 44(5):1521–1525.
- Hester, E. T. and Gooseff, M. N. (2011). Hyporheic restoration in streams and rivers. In Simon, A., Bennett, B., and Castro, J., editors, *Stream Restoration in Dynamic Fluvial Systems: Scientific Approaches, Analyses, and Tools*, volume 194 of *AGU Geophysical Monograph*, pages 167–187. American Geophysical Union, Washington DC.
- Hester, E. T., Young, K. I., and Widdowson, M. A. (2014). Controls on mixing-dependent denitrification in hyporheic zones induced by riverbed dunes: A steady state modeling study. *Water Resources Research*, 50(11):9048–9066. [_eprint: https://onlinelibrary.wiley.com/doi/pdf/10.1002/2014WR015424](https://onlinelibrary.wiley.com/doi/pdf/10.1002/2014WR015424).
- Hill, R. A., Weber, M. H., Leibowitz, S. G., Olsen, A. R., and Thornbrugh, D. J. (2016). The Stream-Catchment (StreamCat) Dataset: A Database of Watershed Metrics for the Conterminous United States. *JAWRA Journal of the American Water Resources Association*, 52(1):120–128. [_eprint: https://onlinelibrary.wiley.com/doi/pdf/10.1111/1752-1688.12372](https://onlinelibrary.wiley.com/doi/pdf/10.1111/1752-1688.12372).
- Hinnell, A. C., Ferré, T. P. A., Vrugt, J. A., Huisman, J. A., Moysey, S., Rings, J., and Kowalsky, M. B. (2010). Improved extraction of hydrologic information from geophysical data through coupled hydrogeophysical inversion. *Water Resources Research*, 46(4). [_eprint: https://agupubs.onlinelibrary.wiley.com/doi/pdf/10.1029/2008WR007060](https://agupubs.onlinelibrary.wiley.com/doi/pdf/10.1029/2008WR007060).
- Ho, P. C., Bianchi, H., Palmer, D. A., and Wood, R. H. (2000). Conductivity of Dilute Aqueous Electrolyte Solutions at High Temperatures and Pressures Using a Flow Cell. *Journal of Solution Chemistry*, 29(3):217–235.
- Holbrook, W. S., Riebe, C. S., Elwaseif, M., Hayes, J. L., Basler-Reeder, K., Harry, D. L., Malazian, A., Dosseto, A., Hartsough, P. C., and Hopmans, J. W. (2014). Geophysical constraints on deep weathering and water storage potential in the Southern Sierra Critical Zone Observatory. *Earth Surface Processes and Landforms*, 39(3):366–380. [_eprint: https://onlinelibrary.wiley.com/doi/pdf/10.1002/esp.3502](https://onlinelibrary.wiley.com/doi/pdf/10.1002/esp.3502).
- Holmes, R. (2000). The Importance of Ground Water to Stream Ecosystem Function. In Jones, J. B. and Mulholland, P. J., editors, *Streams and Ground Waters*, Aquatic ecology series, pages 137–148.
- Hooke, J. (2003). River meander behaviour and instability: a framework for analysis. *Transactions of the Institute of British Geographers*, 28(2):238–253. Publisher: John Wiley & Sons, Ltd.
- Hooke, J. M. (2007). Complexity, self-organisation and variation in behaviour in meandering rivers. *Geomorphology*, 91(3):236–258.
- Horne, M. M. (2019). Assessing the Rincon Geothermal System Using Transient Electromagnetics and Hydrothermal Modeling. Master's thesis, New Mexico Institute of Mining and Technology, United States – New Mexico. ISBN: 9781392844571.
- Howard, A. D. and Hemberger, A. T. (1991). Multivariate characterization of meandering. *Geomorphology*, 4(3-4):161–186.
- Howard, A. D. and Knutson, T. R. (1984). Sufficient conditions for river meandering: A simulation approach. *Water Resources Research*, 20(11):1659–1667.
- Hu, Z., Ao, D., and Mahadevan, S. (2017). Calibration experimental design considering field response and model uncertainty. *Computer Methods in Applied Mechanics and Engineering*, 318:92–119.
- Huff, G. F. (2002). Apparent age of ground water near the southeastern margin of the Tularosa Basin, Otero County, New Mexico. In *Geology of White Sands*, pages 303–307. New Mexico Geological Society.
- Huff, G. F. (2004). An Overview of the Hydrogeology of Saline Groundwater in New Mexico. Technical Report Water Desalination and Reuse Strategies for New Mexico, New Mexico Water Resources Research Institute, New Mexico, United States.

- Huff, G. F. (2005). Simulation of Ground-Water Flow in the Basin-Fill Aquifer of the Tularosa Basin, South-Central New Mexico, Predevelopment through 2040. Scientific Investigations Report, U.S. Geological Survey, Reston, Virginia. Series: Scientific Investigations Report.
- Hunter, K. S., Wang, Y., and Van Cappellen, P. (1998). Kinetic modeling of microbially-driven redox chemistry of subsurface environments: coupling transport, microbial metabolism and geochemistry. *Journal of Hydrology*, 209(1):53–80.
- Ingebritsen, S. E. and Manning, C. E. (2010). Permeability of the continental crust: dynamic variations inferred from seismicity and metamorphism. *Geofluids*.
- Jardine, P. M., Dunnivant, F. M., Selim, H. M., and McCarthy, J. F. (1992). Comparison of Models for Describing the Transport of Dissolved Organic Carbon in Aquifer Columns. *Soil Science Society of America Journal*, 56(2):393–401. eprint: <https://onlinelibrary.wiley.com/doi/pdf/10.2136/sssaj1992.03615995005600020009x>.
- Jiang, X.-W. (2012). A quantitative study on accumulation of age mass around stagnation points in nested flow systems. *Water Resources Research*.
- Jiang, X.-W., Wan, L., Cardenas, M., and Ge, S. (2010). Simultaneous rejuvenation and aging of groundwater in basins due to depth-decaying hydraulic conductivity and porosity. *Geophysical Research . . .*
- Jiang, X.-W., Wan, L., Wang, J.-Z., Yin, B.-X., Fu, W.-X., and Lin, C.-H. (2014). Field identification of groundwater flow systems and hydraulic traps in drainage basins using a geophysical method. *Geophysical Research Letters*, 41(8):2014GL059579.
- Jiang, X.-W., Wan, L., Wang, X.-S., Ge, S., and Liu, J. (2009). Effect of exponential decay in hydraulic conductivity with depth on regional groundwater flow. *Geophysical Research Letters*, 36(24):L24402.
- Jiang, X.-W., Wang, X.-S., Wan, L., and Ge, S. (2011). An analytical study on stagnation points in nested flow systems in basins with depth-decaying hydraulic conductivity. *Water Resources Research*, 47(1):n/a–n/a.
- Jones, D. R. and Schonlau, M. (1998). Efficient Global Optimization of Expensive Black-Box Functions. *Journal of Global Optimization*, 13(4):455–492.
- Kang, M. and Jackson, R. B. (2016). Salinity of deep groundwater in California: Water quantity, quality, and protection. *Proceedings of the National Academy of Sciences*, 113(28):7768–7773. Publisher: National Academy of Sciences Section: Physical Sciences.
- Kelley, S., Edwardsngler, T., Cather, M., Pokorny, C., Yang, C.-H., Mamer, E., Hoffman, G., Wilch, J., Johnson, P., and Zeigler, K. (2014a). Hydrologic assessment of oil and gas resource development of the Mancos Shale in the San Juan Basin, New Mexico. Open-File Report 566, New Mexico Bureau of Geology and Mineral Resources, Socorro, New Mexico.
- Kelley, S., Koning, D. J., and Allen, B. (2014b). Preliminary Geologic Map of the Tularosa and Bent Region, northeastern Tularosa Basin, Otero County, New Mexico. Open File Report 564, New Mexico Bureau of Geology and Mineral Resources, Socorro, New Mexico.
- Kestin, J., Khalifa, H. E., and Correia, R. J. (1981). Tables of the dynamic and kinematic viscosity of aqueous KCl solutions in the temperature range 25–150 °C and the pressure range 0.1–35 MPa. *Journal of Physical and Chemical Reference Data*, 10(1):71–81.
- Key, K. (2016). MARE2DEM: a 2-D inversion code for controlled-source electromagnetic and magnetotelluric data. *Geophysical Journal International*, 207(1):571–588.
- Khurana, S., Heße, F., Hildebrandt, A., and Thullner, M. (2022). Predicting the impact of spatial heterogeneity on microbially mediated nutrient cycling in the subsurface. *Biogeosciences*, 19(3):665–688. Publisher: Copernicus GmbH.

- Kiel, B. A. and Bayani Cardenas, M. (2014). Lateral hyporheic exchange throughout the Mississippi River network. *Nature Geoscience*, 7(6):413–417. Number: 6 Publisher: Nature Publishing Group.
- Kim, J.-H., Ferguson, G., Person, M., Jiang, W., Lu, Z.-T., Ritterbusch, F., Yang, G.-M., Tyne, R., Bailey, L., Ballentine, C., Reiners, P., and McIntosh, J. (2022a). Krypton-81 Dating Constrains Timing of Deep Groundwater Flow Activation. *Geophysical Research Letters*, 49(11):e2021GL097618. [_eprint: https://agupubs.onlinelibrary.wiley.com/doi/pdf/10.1029/2021GL097618](https://agupubs.onlinelibrary.wiley.com/doi/pdf/10.1029/2021GL097618).
- Kim, J.-H., Ferguson, G., Person, M. A., Jiang, W., Lu, Z.-T., Ritterbusch, F., Yang, G.-M., Tyne, R., Bailey, L., Ballentine, C., Reiners, P., and McIntosh, J. (2022b). Krypton-81 Dating Constrains Timing of Deep Groundwater Flow Activation. *Geophysical Research Letters*, 49(11):e2021GL097618. [_eprint: https://onlinelibrary.wiley.com/doi/pdf/10.1029/2021GL097618](https://onlinelibrary.wiley.com/doi/pdf/10.1029/2021GL097618).
- Kinoshita, R. (1961). Investigation of channel deformation in Ishikari River. *Report of Bureau of Resources*, 174. Publisher: Department of Science and Technology.
- Kinoshita, R. and Miwa, H. (1974). River channel formation which prevents downstream translation of transverse bars. *ShinSabo*, 94:12–17.
- Kirsch, R. (2009). *Groundwater Geophysics: A Tool for Hydrogeology*. Springer-Verlag, Berlin Heidelberg, 2 edition.
- Kocurek, G., Carr, M., Ewing, R., Havholm, K. G., Nagar, Y. C., and Singhvi, A. K. (2007). White Sands Dune Field, New Mexico: Age, dune dynamics and recent accumulations. *Sedimentary Geology*, 197(3):313–331.
- Koning, D. J., Kelley, S., and Goff, F. (2014). Preliminary Geologic Map of the northeastern Tularosa Basin and Western Sierra Blanca Basin, Lincoln and Otero Counties, New Mexico. Open-File Report 563, New Mexico Bureau of Geology and Mineral Resources.
- Kottowski, F. E. (1975). Stratigraphy of the San Andres Mountains in south-central New Mexico. In *Las Cruces Country*, pages 95–104. New Mexico Geological Society.
- Krause, S., Abbott, B. W., Baranov, V., Bernal, S., Blaen, P., Datry, T., Drummond, J., Fleckenstein, J. H., Velez, J. G., Hannah, D. M., Knapp, J. L. A., Kurz, M., Lewandowski, J., Martí, E., Mendoza-Lera, C., Milner, A., Packman, A., Pinay, G., Ward, A. S., and Zarnetzke, J. P. (2022). Organizational Principles of Hyporheic Exchange Flow and Biogeochemical Cycling in River Networks Across Scales. *Water Resources Research*, 58(3):e2021WR029771. [_eprint: https://agupubs.onlinelibrary.wiley.com/doi/pdf/10.1029/2021WR029771](https://agupubs.onlinelibrary.wiley.com/doi/pdf/10.1029/2021WR029771).
- Kruegler, J., Gomez-Velez, J., Lautz, L. K., and Endreny, T. A. (2020). Dynamic Evapotranspiration Alters Hyporheic Flow and Residence Times in the Intrameander Zone. *Water*, 12(2):424.
- Kuijper, A. (2004). On detecting all saddle points in 2D images. *Pattern Recognition Letters*, 25(15):1665–1672.
- Lagasse, P. F., Spitz, W. J., Zevenbergen, L. W., and Zachmann, D. W. (2004). Handbook for Predicting Stream Meander Migration and Supporting Software. Technical Report 533, National Cooperative Highway Research Program, Washington, D.C. Pages: 23346.
- Lam, C. Q. and Notz, W. I. (2008). Sequential adaptive designs in computer experiments for response surface model fit. page 28.
- Land, L. (2016). Overview of Fresh and Brackish Water Quality in New Mexico. Technical Report Open-file Report 583, New Mexico Bureau of Geology and Mineral Resources.
- Land, L., Felix, B., and Newton, T. (2014). Regional water table map of the northeastern Tularosa Basin region, Otero and Lincoln counties, New Mexico. Open File Report 561, New Mexico Bureau of Geology and Mineral Resources, New Mexico, United States.

- Land, L. and Timmons, S. (2016). New Mexico: A Brackish Water Data Assessment. Fact Sheet, New Mexico Bureau of Geology and Mineral Resources.
- Langford, R. P. (2003). The Holocene history of the White Sands dune field and influences on eolian deflation and playa lakes. *Quaternary International*, 104(1):31–39.
- Langmuir, D. (1997). *Aqueous Environmental Geochemistry*. Prentice-Hall, Upper Saddle River, New Jersey.
- Larkin, R. G. and Sharp JR, J. M. (1992). On the relationship between river-basin geomorphology, aquifer hydraulics, and ground-water flow direction in alluvial aquifers. *Geological Society Of America Bulletin*, 104(12):1608–1620.
- Lazarus, E. D. and Constantine, J. A. (2013). Generic theory for channel sinuosity. *Proceedings of the National Academy of Sciences*, 110(21):8447–8452.
- Le, P. V. V., Guilloteau, C., Mamalakis, A., and Foufoula-Georgiou, E. (2021). Underestimated MJO Variability in CMIP6 Models. *Geophysical Research Letters*, 48(12):e2020GL092244. [eprint: https://agupubs.onlinelibrary.wiley.com/doi/pdf/10.1029/2020GL092244](https://agupubs.onlinelibrary.wiley.com/doi/pdf/10.1029/2020GL092244).
- Ledo, J. (2006). 2-D Versus 3-D Magnetotelluric Data Interpretation. *Surveys in Geophysics*, 27(1):111–148.
- Ledo, J., Queralt, P., and Pous, J. (1998). Effects of galvanic distortion on magnetotelluric data over a three-dimensional regional structure. *Geophysical Journal International*, 132(2):295–301.
- Lemieux, J.-M., Sudicky, E. A., Peltier, W. R., and Tarasov, L. (2008a). Simulating the impact of glaciations on continental groundwater flow systems: 1. Relevant processes and model formulation. *Journal of Geophysical Research: Earth Surface*, 113(F3):F03017.
- Lemieux, J.-M., Sudicky, E. A., Peltier, W. R., and Tarasov, L. (2008b). Simulating the impact of glaciations on continental groundwater flow systems: 2. Model application to the Wisconsinian glaciation over the Canadian landscape. *Journal of Geophysical Research: Earth Surface*, 113(F3):F03018.
- Leopold, L. B., Wolman, G., and Miller, J. P. (1992). *Fluvial processes in geomorphology*. A Series of books in geology. Dover Publications Inc., New York, 1 edition.
- Leopold, L. B. and Wolman, M. G. (1960). River Meanders. *Geological Society of America Bulletin*, 71(6):769.
- Lewandowski, J., Arnon, S., Banks, E., Batelaan, O., Betterle, A., Broecker, T., Coll, C., Drummond, J. D., Garcia, J. G., Galloway, J., Gomez-Velez, J., Grabowski, R. C., Herzog, S. P., Hinkelmann, R., Höhne, A., Hollender, J., Horn, M. A., Jaeger, A., Krause, S., Prats, A. L., Magliozzi, C., Meinikmann, K., Mojarrad, B. B., Mueller, B. M., Peralta-Maraver, I., Popp, A. L., Posselt, M., Putschew, A., Radke, M., Raza, M., Riml, J., Robertson, A., Rutere, C., Schaper, J. L., Schirmer, M., Schulz, H., Shanafield, M., Singh, T., Ward, A. S., Wolke, P., Wörman, A., and Wu, L. (2019). Is the Hyporheic Zone Relevant beyond the Scientific Community? *Water*, 11(11):2230.
- Liao, L., Green, C. T., Bekins, B. A., and Böhlke, J. K. (2012). Factors controlling nitrate fluxes in groundwater in agricultural areas. *Water Resources Research*, 48(6). [eprint: https://onlinelibrary.wiley.com/doi/pdf/10.1029/2011WR011008](https://onlinelibrary.wiley.com/doi/pdf/10.1029/2011WR011008).
- Lide, D. R. and Haynes, W. M. (2009). CRC Handbook of Chemistry and Physics, 2009-2010, 90th ed. *Journal of the American Chemical Society*, 131(35):12862–12862.
- Lindsey, B. D., Phillips, S., Donnelly, C. A., Speiran, G. K., Plummer, N., Bohlke, J. K., Focazio, M. J., Burton, W. C., and Busenberg, E. (2003). Residence times and nitrate transport in ground water discharging to streams in the Chesapeake Bay Watershed. USGS Numbered Series 2003-4035, U.S. Geological Survey. Code Number: 2003-4035 Code: Residence times and nitrate transport in ground water discharging to streams in the Chesapeake Bay Watershed Publication Title: Residence times and nitrate transport in ground water discharging to streams in the Chesapeake Bay Watershed Reporter: Residence times and nitrate transport in ground water discharging to streams in the Chesapeake Bay Watershed Series: Water-Resources Investigations Report.

- Lozinsky, R. P. and Bauer, P. W. (1991). Structure and Basin-fill Units of the Tularosa Basin. In *Geology of the Sierra Blanca, Sacramento, and Capitan Ranges, New Mexico*, pages 7–11, New Mexico, United States. New Mexico Geological Society.
- Machette, M. N. (1987). Preliminary assessment of paleoseismicity at White Sands Missile Range, southern New Mexico: Evidence for recency of faulting, fault segmentation, and repeat intervals for major earthquakes in the region. Open-File Report, U.S. Geological Survey, Denver, Colorado, USA. Series: Open-File Report.
- Magnuson, M. L., Valdez, J. M., Lawler, C. R., Nelson, M., and Petronis, L. (2019). New Mexico Water Use by Categories 2015. Technical Report 55, New Mexico Office of the State Engineer, New Mexico, United States.
- Mailloux, B. J., Person, M., Kelley, S., Dunbar, N., Cather, S., Strayer, L., and Hudleston, P. (1999). Tectonic controls on the hydrogeology of the Rio Grande Rift, New Mexico. *Water Resources Research*, 35(9):2641–2659.
- Mallat, S. (1991). Zero-crossings of a wavelet transform. *IEEE Transactions on Information Theory*, 37(4):1019–1033. Conference Name: IEEE Transactions on Information Theory.
- Mamer, E., Newton, B. T., Koning, D. J., Timmons, S. S., and Kelley, S. (2014). Northeastern Tularosa Basin Regional Hydrogeology Study, New Mexico. Open File Report 561, New Mexico Bureau of Geology and Mineral Resources, New Mexico, United States.
- Manning, C. E. and Ingebritsen, S. E. (1999). Permeability of the continental crust: Implications of geothermal data and metamorphic systems. *Reviews of Geophysics*, 37(1):127–150.
- Markovich, K. H., Manning, A. H., Condon, L. E., and McIntosh, J. C. (2019). Mountain-Block Recharge: A Review of Current Understanding. *Water Resources Research*, 55(11):8278–8304. eprint: <https://onlinelibrary.wiley.com/doi/pdf/10.1029/2019WR025676>.
- Marwan, M., Yanis, M., Nugraha, G. S., Zainal, M., Arahman, N., Idroes, R., Dharma, D. B., Saputra, D., and Gunawan, P. (2021). Mapping of Fault and Hydrothermal System beneath the Seulawah Volcano Inferred from a Magnetotellurics Structure. *Energies*, 14(19):6091. Number: 19 Publisher: Multidisciplinary Digital Publishing Institute.
- Mayo, A. L., Morris, T. H., Peltier, S., Petersen, E. C., Payne, K., Holman, L. S., Tingey, D., Fogel, T., Black, B. J., and Gibbs, T. D. (2003). Active and inactive groundwater flow systems: Evidence from a stratified, mountainous terrain. *GSA Bulletin*, 115(12):1456–1472.
- McClain, M. E., Boyer, E. W., Dent, C. L., Gergel, S. E., Grimm, N. B., Groffman, P. M., Hart, S. C., Harvey, J. W., Johnston, C. A., Mayorga, E., McDowell, W. H., and Pinay, G. (2003). Biogeochemical Hot Spots and Hot Moments at the Interface of Terrestrial and Aquatic Ecosystems. *Ecosystems*, 6(4):301–312.
- McGavock, E. and Montgomery, E. L. (2016). Opportunities for Desalination of Brackish Groundwater in Arizona. Technical report, Errol L. Montgomery & Associates, Inc.
- McGuire, K. and McDonnell, J. (2006). A review and evaluation of catchment transit time modeling. *Journal of Hydrology*, 330(3-4):543–563.
- McIntosh, J. C. and Ferguson, G. (2021). Deep Meteoric Water Circulation in Earth's Crust. *Geophysical Research Letters*, 48(5):e2020GL090461. eprint: <https://onlinelibrary.wiley.com/doi/pdf/10.1029/2020GL090461>.
- McLean, J. S. (1970). Saline ground-water resources of the Tularosa Basin, New Mexico. Open File Report, United States Department of the Interior Geological Survey.
- Meqbel, N. M. M., Ritter, O., and Group, D. (2013). A magnetotelluric transect across the Dead Sea Basin: electrical properties of geological and hydrological units of the upper crust. *Geophysical Journal International*, 193(3):1415–1431.

- Messerli, B., Viviroli, D., and Weingartner, R. (2004). Mountains of the World: Vulnerable Water Towers for the 21st Century. *Ambio*, pages 29–34. Publisher: [Springer, Royal Swedish Academy of Sciences].
- Meyers, Z. P., Frisbee, M. D., Rademacher, L. K., and Stewart-Maddox, N. S. (2021). Old groundwater buffers the effects of a major drought in groundwater-dependent ecosystems of the eastern Sierra Nevada (CA). *Environmental Research Letters*, 16(4):044044. Publisher: IOP Publishing.
- Millington, R. J. and Quirk, J. P. (1961). Permeability of porous solids. *Transactions of the Faraday Society*, 57(0):1200–1207.
- Mo, S., Shi, X., Lu, D., Ye, M., and Wu, J. (2019). An adaptive Kriging surrogate method for efficient uncertainty quantification with an application to geological carbon sequestration modeling. *Computers & Geosciences*, 125:69–77.
- Molz, F. J., Widdowson, M. A., and Benefield, L. D. (1986). Simulation of Microbial Growth Dynamics Coupled to Nutrient and Oxygen Transport in Porous Media. *Water Resources Research*, 22(8):1207–1216. [_eprint: https://onlinelibrary.wiley.com/doi/pdf/10.1029/WR022i008p01207](https://onlinelibrary.wiley.com/doi/pdf/10.1029/WR022i008p01207).
- Montgomery, K. (1996). Sinuosity and Fractal Dimension of Meandering Rivers. *Area*, 28(4):491–500. Publisher: [Royal Geographical Society (with the Institute of British Geographers), Wiley].
- Moore, R. B., McKay, L. D., Rea, A. H., Bondelid, T. R., Price, C. V., Dewald, T. G., and Johnston, C. M. (2019). User’s Guide for the National Hydrography Dataset Plus (NHDPlus) High Resolution. Open-File Report 2019-1096, U.S. Geological Survey, Reston, Virginia. Series: Open-File Report.
- Mosley, M. P. (1979). Streamflow generation in a forested watershed, New Zealand. *Water Resources Research*, 15(4):795–806. [_eprint: https://agupubs.onlinelibrary.wiley.com/doi/pdf/10.1029/WR015i004p00795](https://agupubs.onlinelibrary.wiley.com/doi/pdf/10.1029/WR015i004p00795).
- National Research Council (1930). *International Critical Tables of Numerical Data, Physics, Chemistry and Technology*.
- Newton, B. T. and Allen, B. (2014). Hydrologic Investigation at White Sands National Monument. Open-File Report 559, New Mexico Bureau of Geology and Mineral Resources, New Mexico, United States.
- Newton, B. T. and Land, L. (2016). Brackish Water Assessment in the Eastern Tularosa Basin, New Mexico. Open-file Report 582, New Mexico Bureau of Geology and Mineral Resources.
- Nield, D. A. and Bejan, A. (2013). *Convection in Porous Media*. Springer New York, New York, NY.
- NMBGMR, USGS, and NMED (2016). New Mexico Bureau of Geology and Mineral Resources Map.
- Nordstrom, D. K., Ball, J. W., Donahoe, R. J., and Whittimore, D. (1989a). Groundwater chemistry and water-rock interactions at Stripa. *Geochimica et Cosmochimica Acta*, 53(8):1727–1740.
- Nordstrom, D. K., Lindblom, S., Donahoe, R. J., and Barton, C. C. (1989b). Fluid inclusions in the Stripa granite and their possible influence on the groundwater chemistry. *Geochimica et Cosmochimica Acta*, 53(8):1741–1755.
- Noyes, A. A. A. A. (1907). *The electrical conductivity of aqueous solutions. A report*. Washington, D.C., Carnegie institution of Washington.
- Odgaard, A. J. (1987). Streambank erosion along two rivers in Iowa. *Water Resources Research*, 23(7):1225–1236. [_eprint: https://agupubs.onlinelibrary.wiley.com/doi/pdf/10.1029/WR023i007p01225](https://agupubs.onlinelibrary.wiley.com/doi/pdf/10.1029/WR023i007p01225).
- Oldham, C. E., Farrow, D. E., and Peiffer, S. (2013). A generalized Damköhler number for classifying material processing in hydrological systems. *Hydrology And Earth System Sciences*, 17(3):1133–1148.
- Orr, B. R. and Myers, R. G. (1986). Water Resources in Basin-Fill Deposits in The Tularosa Basin, New Mexico. Report 85-4219, U.S. Geological Survey, Albuquerque, New Mexico.

- Palacky, G. J. (1988). Resistivity Characteristics of Geologic Targets. In *Electromagnetic Methods in Applied Geophysics: Volume 1, Theory*. Society of Exploration Geophysicists.
- Paola, C., Heller, P. L., and Angevine, C. L. (1992). The large-scale dynamics of grain-size variation in alluvial basins, 1: Theory. *Basin Research*, 4(2):73–90. eprint: <https://onlinelibrary.wiley.com/doi/pdf/10.1111/j.1365-2117.1992.tb00145.x>.
- Peacock, J. R., Earney, T. E., Mangan, M. T., Schermerhorn, W. D., Glen, J. M., Walters, M., and Hartline, C. (2020). Geophysical characterization of the Northwest Geysers geothermal field, California. *Journal of Volcanology and Geothermal Research*, 399:106882.
- Peacock, J. R., Mangan, M. T., McPhee, D., and Wannamaker, P. E. (2016). Three-dimensional electrical resistivity model of the hydrothermal system in Long Valley Caldera, California, from magnetotellurics. *Geophysical Research Letters*, 43(15):7953–7962. eprint: <https://onlinelibrary.wiley.com/doi/pdf/10.1002/2016GL069263>.
- Pepin, J. (2019). *NEW APPROACHES TO GEOTHERMAL RESOURCE EXPLORATION AND CHARACTERIZATION*. Ph.D. Dissertation, New Mexico Institute of Mining and Technology, Socorro, New Mexico.
- Pepin, J., Person, M., Phillips, F., Kelley, S., Timmons, S., Owens, L., Witcher, J., and Gable, C. (2014). Deep fluid circulation within crystalline basement rocks and the role of hydrologic windows in the formation of the Truth or Consequences, New Mexico low-temperature geothermal system. *Geofluids*.
- Perez, G., Gomez-Velez, J. D., Chen, X., Scheibe, T., Chen, Y., and Bao, J. (2021). Identification of Characteristic Spatial Scales to Improve the Performance of Analytical Spectral Solutions to the Groundwater Flow Equation. *Water Resources Research*, 57(12):e2021WR031044. eprint: <https://onlinelibrary.wiley.com/doi/pdf/10.1029/2021WR031044>.
- Person, M. and Garven, G. (1994). A sensitivity study of the driving forces on fluid flow during continental-rift basin evolution. *GSA Bulletin*, 106(4):461–475.
- Person, M. A., McIntosh, J., Kim, J.-H., Noyes, C., Bailey, L., Lingrey, S., Krantz, R., Lucero, D., Reiners, P., and Ferguson, G. (2024). Hydrologic windows into the crystalline basement and their controls on groundwater flow patterns across the Paradox Basin, western USA. *GSA Bulletin*.
- Person, M. A. and Sazeed, N. (2022). Continental Brackish Groundwater Resources. In Qadir, M., Smakhtin, V., Koo-Oshima, S., and Guenther, E., editors, *Unconventional Water Resources*, pages 111–128. Springer International Publishing, Cham.
- Peterson, E. W. and Sickbert, T. B. (2006). Stream water bypass through a meander neck, laterally extending the hyporheic zone. *Hydrogeology Journal*, 14(8):1443–1451.
- Pimentel, D., Bailey, O., Kim, P., Mullaney, E., Calabrese, J., Walman, L., Nelson, F., and Yao, X. (1999). Will Limits of the Earth's Resources Control Human Numbers? *Environment, Development and Sustainability*, 1(1):19–39.
- Piégay, H., Darby, S. E., Mosselman, E., and Surian, N. (2005). A review of techniques available for delimiting the erodible river corridor: a sustainable approach to managing bank erosion. *River Research and Applications*, 21(7):773–789. eprint: <https://onlinelibrary.wiley.com/doi/pdf/10.1002/rra.881>.
- Plotly Technologies Inc. (2015). Collaborative data science.
- Pollock, D. and Cirpka, O. A. (2012). Fully coupled hydrogeophysical inversion of a laboratory salt tracer experiment monitored by electrical resistivity tomography. *Water Resources Research*, 48(1). eprint: <https://agupubs.onlinelibrary.wiley.com/doi/pdf/10.1029/2011WR010779>.
- Poole, G. C., Stanford, J. A., Running, S. W., and Frissell, C. A. (2006). Multiscale geomorphic drivers of groundwater flow paths: subsurface hydrologic dynamics and hyporheic habitat diversity. *Journal of the North American Benthological Society*, 25(2):288–303. Publisher: [The University of Chicago Press, Society for Freshwater Science].

- Pringle, C. (2003). What is hydrologic connectivity and why is it ecologically important? *Hydrological Processes*, 17(13):2685–2689. [.eprint: https://onlinelibrary.wiley.com/doi/pdf/10.1002/hyp.5145](https://onlinelibrary.wiley.com/doi/pdf/10.1002/hyp.5145).
- Pringle, C. M. (2001). Hydrologic Connectivity and the Management of Biological Reserves: A Global Perspective. *Ecological Applications*, 11(4):981–998. [.eprint: https://esajournals.onlinelibrary.wiley.com/doi/pdf/10.1890/1051-0761%282001%29011%5B0981%3AH%20CATMO%5D2.0.CO%3B2](https://esajournals.onlinelibrary.wiley.com/doi/pdf/10.1890/1051-0761%282001%29011%5B0981%3AH%20CATMO%5D2.0.CO%3B2).
- Provost, A. M., Voss, C. I., and Neuzil, C. E. (2012). Glaciation and regional groundwater flow in the Fennoscandian shield. *Geofluids*, 12(1):79–96.
- Qadir, M., Sharma, B. R., Bruggeman, A., Choukr-Allah, R., and Karajeh, F. (2007). Non-conventional water resources and opportunities for water augmentation to achieve food security in water scarce countries. *Agricultural Water Management*, 87(1):2–22.
- Qi, S. L. and Harris, A. C. (2017). Geochemical Database for the Brackish Groundwater Assessment of the United States.
- Quist, A. S. and Marshall, W. L. (1968). Electrical conductances of aqueous sodium chloride solutions from 0 to 800.degree. and at pressures to 4000 bars. *The Journal of Physical Chemistry*, 72(2):684–703.
- Revelli, R., Boano, F., Camporeale, C., and Ridolfi, L. (2008). Intra-meander hyporheic flow in alluvial rivers. *Water Resources Research*, 44(12). [.eprint: https://onlinelibrary.wiley.com/doi/pdf/10.1029/2008WR007081](https://onlinelibrary.wiley.com/doi/pdf/10.1029/2008WR007081).
- Riebe, C. S., Hamm, W. J., and Brantley, S. L. (2017). Controls on deep critical zone architecture: a historical review and four testable hypotheses. *Earth Surface Processes and Landforms*, 42(1):128–156. [.eprint: https://onlinelibrary.wiley.com/doi/pdf/10.1002/esp.4052](https://onlinelibrary.wiley.com/doi/pdf/10.1002/esp.4052).
- Rijsberman, F. R. (2006). Water scarcity: Fact or fiction? *Agricultural Water Management*, 80(1):5–22.
- Rizzello, D., Armadillo, E., Pasqua, C., Pisani, P., Principe, C., Lelli, M., Didas, M., Giordan, V., Mnjokava, T., Kabaka, K., Tumbu, L., and Marini, L. (2022). Assessment of the Kiejo-Mbaka geothermal field by three-dimensional geophysical modelling. *Geomechanics and Geophysics for Geo-Energy and Geo-Resources*, 8(5):143.
- Robertson, D. M. and Saad, D. A. (2019). Spatially referenced models of streamflow and nitrogen, phosphorus, and suspended-sediment loads in streams of the midwestern United States. USGS Numbered Series 2019-5114, U.S. Geological Survey, Reston, VA. Code Number: 2019-5114 Code: Spatially referenced models of streamflow and nitrogen, phosphorus, and suspended-sediment loads in streams of the midwestern United States Publication Title: Spatially referenced models of streamflow and nitrogen, phosphorus, and suspended-sediment loads in streams of the midwestern United States Reporter: Spatially referenced models of streamflow and nitrogen, phosphorus, and suspended-sediment loads in streams of the midwestern United States Series: Scientific Investigations Report IP-103244.
- Robertson, W. D. and Cherry, J. A. (1995). In Situ Denitrification of Septic-System Nitrate Using Reactive Porous Media Barriers: Field Trials. *Groundwater*, 33(1):99–111. [.eprint: https://onlinelibrary.wiley.com/doi/pdf/10.1111/j.1745-6584.1995.tb00266.x](https://onlinelibrary.wiley.com/doi/pdf/10.1111/j.1745-6584.1995.tb00266.x).
- Robinson, D. A., Binley, A., Crook, N., Day-Lewis, F. D., Ferré, T. P. A., Grauch, V. J. S., Knight, R., Knoll, M., Lakshmi, V., Miller, R., Nyquist, J., Pellerin, L., Singha, K., and Slater, L. (2008). Advancing process-based watershed hydrological research using near-surface geophysics: a vision for, and review of, electrical and magnetic geophysical methods. *Hydrological Processes*, 22(18):3604–3635.
- Robinson, M. C., Deeds, N. E., and Lupton, D. M. (2019). Identification of Potential Brackish Groundwater Production Areas – Northern Trinity Aquifer. Technical Note 19-1, Texas Water Development Board, Texas, United States.
- Rosin, P. L. (1998). Determining local natural scales of curves. *Pattern Recognition Letters*, 19(1):63–75.

- Rowe, A. M. and Chou, J. C. S. (1970). Pressure-volume-temperature-concentration relation of aqueous sodium chloride solutions. *Journal of Chemical & Engineering Data*, 15(1):61–66.
- Roy, S. B., Chen, L., Girvetz, E. H., Maurer, E. P., Mills, W. B., and Grieb, T. M. (2012). Projecting Water Withdrawal and Supply for Future Decades in the U.S. under Climate Change Scenarios. *Environmental Science & Technology*, 46(5):2545–2556.
- Rubin, Y. and Hubbard, S. S. (2005). *Hydrogeophysics*, volume 50. Springer, Netherlands.
- Saar, M. O. and Manga, M. (2004). Depth dependence of permeability in the Oregon Cascades inferred from hydrogeologic, thermal, seismic, and magmatic modeling constraints. *Journal of Geophysical Research*, 109(B4).
- Sanz-Prat, A., Lu, C., Amos, R. T., Finkel, M., Blowes, D. W., and Cirpka, O. A. (2016). Exposure-time based modeling of nonlinear reactive transport in porous media subject to physical and geochemical heterogeneity. *Journal of Contaminant Hydrology*, 192:35–49.
- Sanz-Prat, A., Lu, C., Finkel, M., and Cirpka, O. A. (2015). On the validity of travel-time based nonlinear bioreactive transport models in steady-state flow. *Journal of Contaminant Hydrology*, 175-176:26–43.
- Sawyer, A. H. (2015). Enhanced removal of groundwater-borne nitrate in heterogeneous aquatic sediments. *Geophysical Research Letters*, 42(2):403–410. _eprint: <https://agupubs.onlinelibrary.wiley.com/doi/pdf/10.1002/2014GL062234>.
- Scanlon, B. R., Faunt, C. C., Longuevergne, L., Reedy, R. C., Alley, W. M., McGuire, V. L., and McMahon, P. B. (2012a). Groundwater depletion and sustainability of irrigation in the US High Plains and Central Valley. *Proceedings of the National Academy of Sciences*, 109(24):9320–9325.
- Scanlon, B. R., Keese, K. E., Flint, A. L., Flint, L. E., Gaye, C. B., Edmunds, W. M., and Simmers, I. (2006). Global synthesis of groundwater recharge in semiarid and arid regions. *Hydrological Processes*, 20(15):3335–3370. _eprint: <https://onlinelibrary.wiley.com/doi/pdf/10.1002/hyp.6335>.
- Scanlon, B. R., Longuevergne, L., and Long, D. (2012b). Ground referencing GRACE satellite estimates of groundwater storage changes in the California Central Valley, USA. *Water Resources Research*, 48(4). _eprint: <https://agupubs.onlinelibrary.wiley.com/doi/pdf/10.1029/2011WR011312>.
- Schaller, M. F. and Fan, Y. (2009). River basins as groundwater exporters and importers: Implications for water cycle and climate modeling. *Journal of Geophysical Research: Atmospheres*, 114(D4). _eprint: <https://agupubs.onlinelibrary.wiley.com/doi/pdf/10.1029/2008JD010636>.
- Scheibe, T. D., Fang, Y., Murray, C. J., Roden, E. E., Chen, J., Chien, Y.-J., Brooks, S. C., and Hubbard, S. S. (2006). Transport and biogeochemical reaction of metals in a physically and chemically heterogeneous aquifer. *Geosphere*, 2(4):220.
- Schmadel, N. M., Harvey, J. W., Alexander, R. B., Boyer, E. W., Schwarz, G. E., Gomez-Velez, J. D., Scott, D., and Konrad, C. P. (2020). Low threshold for nitrogen concentration saturation in headwaters increases regional and coastal delivery. *Environmental Research Letters*, 15(4):044018. Publisher: IOP Publishing.
- Schumm, S. A. (1985). Patterns of Alluvial Rivers. *Annual Review of Earth and Planetary Sciences*, 13(1):5–27. _eprint: <https://doi.org/10.1146/annurev.ea.13.050185.000253>.
- Schwenk, J., Lanzoni, S., and Fofoula-Georgiou, E. (2015). The life of a meander bend: Connecting shape and dynamics via analysis of a numerical model. *Journal of Geophysical Research: Earth Surface*, 120(4):690–710.
- Schön, J. H. (2015). *Physical Properties of Rocks: Fundamentals and Principles of Petrophysics*. Elsevier, Amsterdam, Netherlands, 2nd edition edition.

- Seager, R., Feldman, J., Lis, N., Ting, M., Williams, A. P., Nakamura, J., Liu, H., and Henderson, N. (2017). Whither the 100th Meridian? The Once and Future Physical and Human Geography of America's Arid-Humid Divide. Part II: The Meridian Moves East. *Earth Interactions*, 22(5):1–24. Publisher: American Meteorological Society.
- Seager, R., Ting, M., Held, I., Kushnir, Y., Lu, J., Vecchi, G., Huang, H.-P., Harnik, N., Leetmaa, A., Lau, N.-C., Li, C., Velez, J., and Naik, N. (2007). Model Projections of an Imminent Transition to a More Arid Climate in Southwestern North America. *Science*, 316(5828):1181–1184.
- Seminara, G. (2006). Meanders. *Journal of Fluid Mechanics*, 554:271–297.
- Seminara, G., Zolezzi, G., Tubino, M., and Zardi, D. (2001). Downstream and upstream influence in river meandering. Part 2. Planimetric development. *Journal of Fluid Mechanics*, 438:213–230.
- Sen, P. N. and Goode, P. A. (1992). Influence of temperature on electrical conductivity on shaly sands. *GEOPHYSICS*, 57(1):89–96.
- Smith, L. and Chapman, D. S. (1983). On the thermal effects of groundwater flow: 1. Regional scale systems. *Journal of Geophysical Research: Solid Earth*, 88(B1):593–608.
- Smith, R. A., Alexander, R. B., and Schwarz, G. E. (2003). Natural Background Concentrations of Nutrients in Streams and Rivers of the Conterminous United States. *Environmental Science & Technology*, 37(14):3039–3047. Publisher: American Chemical Society.
- Snow, R. S. (1989). Fractal sinuosity of stream channels. *pure and applied geophysics*, 131(1):99–109.
- Somers, L. D. and McKenzie, J. M. (2020). A review of groundwater in high mountain environments. *WIREs Water*, 7(6):e1475. eprint: <https://onlinelibrary.wiley.com/doi/pdf/10.1002/wat2.1475>.
- Song, X., Chen, X., Zachara, J. M., Gomez-Velez, J. D., Shuai, P., Ren, H., and Hammond, G. E. (2020). River Dynamics Control Transit Time Distributions and Biogeochemical Reactions in a Dam-Regulated River Corridor. *Water Resources Research*, 56(9):e2019WR026470. eprint: <https://onlinelibrary.wiley.com/doi/pdf/10.1029/2019WR026470>.
- Spies, B. R. (1989). Depth of investigation in electromagnetic sounding methods. *GEOPHYSICS*, 54(7):872–888. Publisher: Society of Exploration Geophysicists.
- Stanton, J. S., Anning, D. W., Brown, C. J., Moore, R. B., McGuire, V. L., Qi, S. L., Harris, A. C., Dennehy, K. F., McMahon, P. B., Degnan, J. R., and Böhlke, J. K. (2017). *Brackish groundwater in the United States*. Number 1833 in Professional paper. U.S. Department of the Interior, U.S. Geological Survey, Reston, Virginia.
- Stanton, J. S. and Dennehy, K. F. (2017). Brackish Groundwater and its Potential to Augment Freshwater Supplies. Fact Sheet, U.S. Geological Survey.
- Stelzer, R. S. and Bartsch, L. (2012). Nitrate removal in deep sediments of a nitrogen-rich river network: A test of a conceptual model. *Journal of Geophysical Research: Biogeosciences*, 117(G2). Code: Journal of Geophysical Research: Biogeosciences Type: Journal Article IP-036248.
- Stelzer, R. S., Scott, J. T., and Bartsch, L. A. (2015). Buried particulate organic carbon stimulates denitrification and nitrate retention in stream sediments at the groundwater–surface water interface. *Freshwater Science*, 34(1):161–171.
- Stephens, D. B. (2015). Technical Memorandum Brackish Water Desalination for Public Water Supply in Las Cruces, New Mexico. Technical report, Daniel B. Steohens & Associates, Inc., Albuquerque, New Mexico.
- Sterle, G., Perdrial, J., Kincaid, D. W., Underwood, K. L., Rizzo, D. M., Haq, I. U., Li, L., Lee, B. S., Adler, T., Wen, H., Middleton, H., and Harpold, A. A. (2024). CAMELS-Chem: augmenting CAMELS (Catchment Attributes and Meteorology for Large-sample Studies) with atmospheric and stream water chemistry data. *Hydrology and Earth System Sciences*, 28(3):611–630. Publisher: Copernicus GmbH.

- Sterle, G., Perdrial, J., Li, L., Adler, T., Underwood, K., Rizzo, D., Wen, H., and Harpold, A. (2022). CAMELS-Chem: Augmenting CAMELS (Catchment Attributes and Meteorology for Large-sample Studies) with Atmospheric and Stream Water Chemistry Data. preprint, Biogeochemical processes/Instruments and observation techniques.
- Stober, I. and Bucher, K. (2007). Hydraulic properties of the crystalline basement. *Hydrogeology Journal*, 15(2):213–224.
- Stonedahl, S. H., Harvey, J. W., and Packman, A. I. (2013). Interactions between hyporheic flow produced by stream meanders, bars, and dunes. *Water Resources Research*, 49(9):5450–5461. eprint: <https://onlinelibrary.wiley.com/doi/pdf/10.1002/wrcr.20400>.
- Sylvester, Z. (2023). meanderpy. original-date: 2018-11-21T21:50:58Z.
- Sylvester, Z., Durkin, P., and Covault, J. A. (2019). High curvatures drive river meandering. *Geology*, 47(3):263–266.
- Szynkiewicz, A., Moore, C. H., Glamoclija, M., and Pratt, L. M. (2009). Sulfur isotope signatures in gypsiferous sediments of the Estancia and Tularosa Basins as indicators of sulfate sources, hydrological processes, and microbial activity. *Geochimica et Cosmochimica Acta*, 73(20):6162–6186.
- Tani, M. (1997). Runoff generation processes estimated from hydrological observations on a steep forested hillslope with a thin soil layer. *Journal of Hydrology*, 200(1):84–109.
- The National Drought Mitigation Center (2019). Summary | United States Drought Monitor.
- Tonina, D. and Buffington, J. M. (2009). Hyporheic Exchange in Mountain Rivers I: Mechanics and Environmental Effects: Mechanics of hyporheic exchange. *Geography Compass*, 3(3):1063–1086.
- Torrence, C. and Compo, G. P. (1998). A Practical Guide to Wavelet Analysis. *Bulletin of the American Meteorological Society*, 79(1):61–78.
- Troch, P. A., Berne, A., Bogaart, P., Harman, C., Hilberts, A. G. J., Lyon, S. W., Paniconi, C., Pauwels, V. R. N., Rupp, D. E., Selker, J. S., Teuling, A. J., Uijlenhoet, R., and Verhoest, N. E. C. (2013). The importance of hydraulic groundwater theory in catchment hydrology: The legacy of Wilfried Brutsaert and Jean-Yves Parlange. *Water Resources Research*, 49(9):5099–5116.
- Tromp-van Meerveld, H. J., Peters, N. E., and McDonnell, J. J. (2007). Effect of bedrock permeability on subsurface stormflow and the water balance of a trenched hillslope at the Panola Mountain Research Watershed, Georgia, USA. *Hydrological Processes*, 21(6):750–769. eprint: <https://onlinelibrary.wiley.com/doi/pdf/10.1002/hyp.6265>.
- Tóth, J. (1963). A theoretical analysis of groundwater flow in small drainage basins. *Journal of Geophysical Research*, 68(16):4795–4812.
- Tóth, J. (2009). *Gravitational systems of groundwater flow: Theory, Evaluation, Utilization*. Cambridge University Press.
- Ucok, H., Ershaghi, I., and Olhoef, G. R. (1980). Electrical Resistivity of Geothermal Brines. *Journal of Petroleum Technology*, 32(04):717–727.
- UNU-INWEH (2019). Uncover Resource: Alleviating global water scarcity through unconventional water resources and technology. Technical report, United Nations University, Canada.
- US Government (1972). Clean Water Act.
- U.S. National Park Service (2020). Geology of White Sands - White Sands National Park (U.S. National Park Service).

- Van De Wiel, M. J., Coulthard, T. J., Macklin, M. G., and Lewin, J. (2007). Embedding reach-scale fluvial dynamics within the CAESAR cellular automaton landscape evolution model. *Geomorphology*, 90(3-4):283–301.
- Vermeulen, B., Hoitink, A. J. F., and Labeur, R. J. (2015). Flow structure caused by a local cross-sectional area increase and curvature in a sharp river bend. *Journal of Geophysical Research: Earth Surface*, 120(9):1771–1783. [.eprint: https://agupubs.onlinelibrary.wiley.com/doi/pdf/10.1002/2014JF003334](https://agupubs.onlinelibrary.wiley.com/doi/pdf/10.1002/2014JF003334).
- Vermeulen, B., Hoitink, A. J. F., Zolezzi, G., Abad, J. D., and Aalto, R. (2016). Multiscale structure of meanders. *Geophysical Research Letters*, page 2016GL068238.
- Virtanen, P., Gommers, R., Oliphant, T. E., Haberland, M., Reddy, T., Cournapeau, D., Burovski, E., Peterson, P., Weckesser, W., Bright, J., van der Walt, S. J., Brett, M., Wilson, J., Millman, K. J., Mayorov, N., Nelson, A. R. J., Jones, E., Kern, R., Larson, E., Carey, C. J., Polat, İ., Feng, Y., Moore, E. W., VanderPlas, J., Laxalde, D., Perktold, J., Cimrman, R., Henriksen, I., Quintero, E. A., Harris, C. R., Archibald, A. M., Ribeiro, A. H., Pedregosa, F., van Mulbregt, P., and SciPy 1.0 Contributors (2020). SciPy 1.0: Fundamental Algorithms for Scientific Computing in Python. *Nature Methods*, 17:261–272.
- Viviroli, D., Archer, D. R., Buytaert, W., Fowler, H. J., Greenwood, G. B., Hamlet, A. F., Huang, Y., Koboltschnig, G., Litaor, M. I., López-Moreno, J. I., Lorentz, S., Schädler, B., Schreier, H., Schwaiger, K., Vuille, M., and Woods, R. (2011). Climate change and mountain water resources: overview and recommendations for research, management and policy. *Hydrology and Earth System Sciences*, 15(2):471–504.
- Viviroli, D., Dürr, H. H., Messerli, B., Meybeck, M., and Weingartner, R. (2007). Mountains of the world, water towers for humanity: Typology, mapping, and global significance: MOUNTAINS AS WATER TOWERS FOR HUMANITY. *Water Resources Research*, 43(7).
- Viviroli, D., Kummu, M., Meybeck, M., Kallio, M., and Wada, Y. (2020). Increasing dependence of lowland populations on mountain water resources. *Nature Sustainability*, 3(11):917–928. Number: 11 Publisher: Nature Publishing Group.
- Voeckler, H. M., Allen, D. M., and Alila, Y. (2014). Modeling coupled surface water – Groundwater processes in a small mountainous headwater catchment. *Journal of Hydrology*, 517:1089–1106.
- Vorosmarty, C. J. (2000). Global Water Resources: Vulnerability from Climate Change and Population Growth. *Science*, 289(5477):284–288.
- Vulis, L., Tejedor, A., Ma, H., Nienhuis, J. H., Broaddus, C., Brown, J., Edmonds, D. A., Rowland, J. C., and Foufoula-Georgiou, E. (2023). River delta morphotypes emerge from multiscale characterization of shorelines. preprint, Preprints.
- Vušanović, I. and Voller, V. R. (2021). Reduced complexity solidification models. *International Journal of Heat and Mass Transfer*, 169:120923.
- Wang, B. and Wang, Y. (1996). Temporal Structure of the Southern Oscillation as Revealed by Waveform and Wavelet Analysis. *Journal of Climate*, 9(7):1586–1598. Publisher: American Meteorological Society Section: Journal of Climate.
- Wang, C., Gomez-Velez, J. D., and Wilson, J. L. (2022). Dynamic coevolution of baseflow and multiscale groundwater flow system during prolonged droughts. *Journal of Hydrology*, 609:127657.
- Ward, A. S. and Packman, A. I. (2019). Advancing our predictive understanding of river corridor exchange. *WIREs Water*, 6(1):e1327.
- Ward, J. V., Tockner, K., Arscott, D. B., and Claret, C. (2002). Riverine landscape diversity. *Freshwater Biology*, 47(4):517–539. [.eprint: https://onlinelibrary.wiley.com/doi/pdf/10.1046/j.1365-2427.2002.00893.x](https://onlinelibrary.wiley.com/doi/pdf/10.1046/j.1365-2427.2002.00893.x).
- Waxman, M. and Smits, L. (1968). Electrical Conductivities in Oil-Bearing Shaly Sands. *Society of Petroleum Engineers Journal*, 8(02):107–122.

- Welch, L. A. and Allen, D. M. (2012). Consistency of groundwater flow patterns in mountainous topography: Implications for valley bottom water replenishment and for defining groundwater flow boundaries. *Water Resources Research*, 48(5):W05526.
- Welch, L. A. and Allen, D. M. (2014). Hydraulic conductivity characteristics in mountains and implications for conceptualizing bedrock groundwater flow. *Hydrogeology Journal*, 22(5):1003–1026.
- Welch, L. A., Allen, D. M. M., and Meerveld, H. J. I. v. (2012). Topographic Controls on Deep Groundwater Contributions to Mountain Headwater Streams and Sensitivity to Available Recharge. *Canadian Water Resources Journal / Revue canadienne des ressources hydriques*, 37(4):349–371.
- White, A., Ma, L., Moravec, B., Chorover, J., and McIntosh, J. (2021). U-series and Sr isotopes as tracers of mineral weathering and water routing from the deep Critical Zone to streamflow in a high-elevation volcanic catchment. *Chemical Geology*, 570:120156.
- White, A., Moravec, B., McIntosh, J., Olshansky, Y., Paras, B., Sanchez, R. A., Ferré, T. P. A., Meixner, T., and Chorover, J. (2019). Distinct stores and the routing of water in the deep critical zone of a snow-dominated volcanic catchment. *Hydrology and Earth System Sciences*, 23(11):4661–4683. Publisher: Copernicus GmbH.
- White, D. S., Elzinga, C. H., and Hendricks, S. P. (1987). Temperature Patterns within the Hyporheic Zone of a Northern Michigan River. *Journal of the North American Benthological Society*, 6(2):85–91. Publisher: The University of Chicago Press.
- Wilkerson, G. V., Kandel, D. R., Perg, L. A., Dietrich, W. E., Wilcock, P. R., and Whiles, M. R. (2014). Continental-scale relationship between bankfull width and drainage area for single-thread alluvial channels. *Water Resources Research*, 50.
- Wilson, J. L. and Guan, H. (2004). Mountain-Block Hydrology and Mountain-Front Recharge. In Hogan, J. F., Phillips, F. M., and Scanlon, B. R., editors, *Groundwater Recharge in a Desert Environment: The Southwestern United States*, pages 113–137. American Geophysical Union.
- Witkin, A. (1984). Scale-space filtering: A new approach to multi-scale description. In *ICASSP '84. IEEE International Conference on Acoustics, Speech, and Signal Processing*, volume 9, pages 150–153.
- Wu, L., Gomez-Velez, J. D., Krause, S., Singh, T., Wörman, A., and Lewandowski, J. (2020). Impact of Flow Alteration and Temperature Variability on Hyporheic Exchange. *Water Resources Research*, 56(3):e2019WR026225. _eprint: <https://onlinelibrary.wiley.com/doi/pdf/10.1029/2019WR026225>.
- Wu, L., Gomez-Velez, J. D., Krause, S., Wörman, A., Singh, T., Nützmänn, G., and Lewandowski, J. (2021). How daily groundwater table drawdown affects the diel rhythm of hyporheic exchange. *Hydrology and Earth System Sciences*, 25(4):1905–1921. Publisher: Copernicus GmbH.
- Xiao, J., Gao, M., Huang, M., Zhang, W., Du, Z., Liu, T., Meng, X., Ma, W., and Lin, S. (2022). How do El Niño Southern Oscillation (ENSO) and local meteorological factors affect the incidence of seasonal influenza in New York state. *Hygiene and Environmental Health Advances*, 4:100040.
- Zarnetske, J. P., Haggerty, R., Wondzell, S. M., and Baker, M. A. (2011a). Dynamics of nitrate production and removal as a function of residence time in the hyporheic zone. *Journal of Geophysical Research: Biogeosciences*, 116(G1). _eprint: <https://onlinelibrary.wiley.com/doi/pdf/10.1029/2010JG001356>.
- Zarnetske, J. P., Haggerty, R., Wondzell, S. M., and Baker, M. A. (2011b). Labile dissolved organic carbon supply limits hyporheic denitrification. *Journal of Geophysical Research*, 116(G4):G04036.
- Zarnetske, J. P., Haggerty, R., Wondzell, S. M., Bokil, V. A., and González-Pinzón, R. (2012). Coupled transport and reaction kinetics control the nitrate source-sink function of hyporheic zones. *Water Resources Research*, 48(11):W11508.

- Zheng, J., Thornton, P. E., Painter, S. L., Gu, B., Wulfschleger, S. D., and Graham, D. E. (2019). Modeling anaerobic soil organic carbon decomposition in Arctic polygon tundra: insights into soil geochemical influences on carbon mineralization. *Biogeosciences*, 16(3):663–680. Publisher: Copernicus GmbH.
- Zheng, L., Cardenas, M. B., and Wang, L. (2016). Temperature effects on nitrogen cycling and nitrate removal-production efficiency in bed form-induced hyporheic zones. *Journal of Geophysical Research: Biogeosciences*, 121(4):1086–1103. .eprint: <https://onlinelibrary.wiley.com/doi/pdf/10.1002/2015JG003162>.
- Zhou, Y., Ritzi Jr., R. W., Soltanian, M. R., and Dominic, D. F. (2014). The Influence of Streambed Heterogeneity on Hyporheic Flow in Gravelly Rivers. *Groundwater*, 52(2):206–216. .eprint: <https://onlinelibrary.wiley.com/doi/pdf/10.1111/gwat.12048>.
- Zimmerman, G. H., Gruskiewicz, M. S., and Wood, R. H. (1995). New Apparatus for Conductance Measurements at High Temperatures: Conductance of Aqueous Solutions of LiCl, NaCl, NaBr, and CsBr at 28 MPa and Water Densities from 700 to 260 kg m⁻³. *The Journal of Physical Chemistry*, 99(29):11612–11625.
- Zohdy, A. A. R., Jackson, D. B., Mattick, R. E., and Peterson, D. L. (1969). Geophysical surveys for ground water at White Sands Missile Range, New Mexico. *Open-File Report*. Number: 69-326.
- Zolezzi, G. and Güneralp, I. (2016). Continuous wavelet characterization of the wavelengths and regularity of meandering rivers. *Geomorphology*, 252:98–111.
- Zolezzi, G. and Seminara, G. (2001). Downstream and upstream influence in river meandering. Part 1. General theory and application to overdeepening. *Journal of Fluid Mechanics*, 438:183–211. Publisher: Cambridge University Press.